UNIVERSITAT POLITÈCNICA DE CATALUNYA BARCELONATECH

PhD program in Construction Engineering

Structural behaviour of stainless steel frames. Safety against accidental seismic actions

Doctoral thesis by:

Isabel González de León

Thesis advisors:

Itsaso Arrayago Luquin

Esther Real Saladrigas

Escola Tècnica Superior d'Enginyeria de Camins, Canals i Ports
Department of Civil and Environmental Engineering

Barcelona, May 2023

ABSTRACT

Stainless steel is one of the most promising construction materials due to its long service life, low maintenance requirements, excellent mechanical properties and high residual value. Nevertheless, for a safe and efficient design with stainless steel, it is fundamental to account for the nonlinear effects of the material at all structural levels and for all load types. Research over the last couple of decades has significantly improved the scope of application of current stainless steel design codes, although they are still far from being as comprehensive as the ones for carbon steel, on which they are generally based. While the latest advances have focused on the material, cross-section and member behaviour, there has been little progress in the design of stainless steel structural systems subjected to static forces, and even less in the seismic design of stainless steel structures, for which no standard exists in Europe or the US. This thesis constitutes a significant step towards the understanding of the performance of stainless steel systems under different loading types, addressing aspects of the global behaviour of stainless steel structures under static and seismic forces with the aim of proposing design expressions that guarantee more optimised and safer structures.

Thus, this thesis presents the first known comprehensive experimental programme on stainless steel systems, in which four austenitic portal frames were tested under vertical and horizontal loading, and a detailed explanation of the different problems encountered in the planning and testing process is given in the document. The obtained results made it possible to validate, with experimental evidence, the design prescriptions included the Eurocode for the consideration of second order effects accounting for the influence of the nonlinear response of the material through the amplification of the horizontal forces.

In addition, an alternative design method for the in-plane design of stainless steel structures under static loading is presented. The method is based on performing a second order structural analysis, and the material nonlinearities and different structural imperfections are considered by reducing the stiffness of the members through a set of proposed factors, requiring only cross-section checks to be performed. In

contrast to the commonly adopted European approach, where a first order nonlinear material analysis is performed, this alternative design approach is typical of the US regulatory framework.

Regarding the cyclic behaviour of stainless steel structures, this thesis investigates experimentally and numerically the performance of stainless steel cold-formed rectangular hollow section members under cyclic loading, focusing on the rotation capacities. The correct estimation of the rotation capacity is of paramount importance from an assessment point of view, because it allows establishing the actual capacity of the structure. Based on the results, a simple formulation to estimate the rotation capacity is proposed in terms of the local slenderness, and calibrated for the three main stainless steel families, which in turn allows the description of the full moment-rotation curves.

Furthermore, this thesis studies the seismic performance of stainless steel moment resisting frames designed according to the new European design rules for carbon steel systems. Design adaptations and a new design formula to effectively account for material nonlinearities in the seismic design of these structures are proposed. The actual behaviour factors of stainless steel frames are also assessed from a number of case studies, and new values of the behaviour factors for stainless steel moment resisting frames in the European and US design frameworks are recommended.

Finally, this thesis investigates the post-necking behaviour of stainless steels under monotonic loading and proposes preliminary values for the key parameters of two common ductile fracture models to provide a material model that defines the response of stainless steels up to failure. One possible application of such model would be in the simulation of joint failure, which can be implemented in new design approaches that study structures as a whole, such as the Direct Design Method.

Everyone should have bosses like mine,
at least once in their lives.

ACKNOWLEDGEMENTS

This thesis would not be possible without the guidance, trust and affection of my supervisors Prof. Itsaso Arrayago and Prof. Esther Real. Anyone who knows them can imagine how grateful and fortunate I feel. They have welcomed me into their *inox-team* from the very beginning and during all these years they have kept the promise they made to me the day we met "we work very hard, but we also have a lot of fun". They have become my family in Barcelona.

I would also like to thank the steel department, especially Prof. Enrique Mirambell, who has shown great willingness to help me, and Guillermo Segura, for all the coffees, laughs and frustrations we have shared during this journey.

I am very grateful to the technicians of the Laboratori de Tecnologia d'Estructures Luís Agulló. In particular, the assistance received from Tomàs García and Carlos Hurtado was essential for the frame tests.

Likewise, I would like to thank Prof. Elide Nastri and her team (University of Salerno) for hosting me for three months, and Dr. Bonaventura Tagliafierro (University of Wisconsin-Madison) and Prof. Atsushi Sato (Nagoya Institute of Technology) for their guidance in seismic design. My sincere thanks to Prof. Enrique de Justo (University of Seville), because he was the first to trust in my research capabilities.

This thesis has been funded by the European Commission and the Ministry of Science, Innovation and Universities through the FPI-MINECO PhD grant Ref. BES-2017-082958, which is also gratefully acknowledged.

Finally, I would like to thank the unconditional support and love I have received from my family and Alejandro, who have always encouraged me to do what I really like and celebrate my achievements more than I do myself. This thesis is dedicated to them.

PUBLICATIONS

The peer-review publications developed in the framework of this thesis are listed below.

Journal publications

Arrayago I., González-de-León I., Real E. and Mirambell E. (2020). Tests on stainless steel frames. Part I: Preliminary tests and experimental set-up. *Thin-Walled Structures*, 157, 107005. https://doi.org/10.1016/j.tws.2020.107005

Arrayago I., González-de-León I., Real E. and Mirambell E. (2020). Tests on stainless steel frames. Part II: Results and analysis. *Thin-Walled Structures*, 157, 107006. https://doi.org/10.1016/j.tws.2020.107006

González-de-León I., Arrayago I., Real E. and Mirambell E. (2022). A stiffness reduction method for the in-plane design of stainless steel members and frames according with EN 1993-1-4. *Engineering Structures*, 253, 113740. https://doi.org/10.1016/j.engstruct.2021.113740

González-de-León I., Arrayago I., Real E. and Nastri E. (2022). Rotation capacity of cold-formed stainless steel RHS beams under cyclic loading. *Journal of Constructional Steel Research*, 192, 107199. https://doi.org/10.1016/j.jcsr.2022.107199

González-de-León I., Nastri E., Arrayago I., Montuori R., Piluso V. and Real E. (2022). Experimental study on stainless steel tubular members under cyclic loading. *Thin-Walled Structures*, 181, 109969. https://doi.org/10.1016/j.tws.2022.109969

González-de-León I., Arrayago I., Real E. and Sato A. (2023). Design of stainless steel moment resisting frames according to the second generation of Eurocode 8. *Submitted to Engineering Structures.*

Conference publications

Arrayago I., Real E., Mirambell E. and González-de-León I. (2019). Experimental study on the general behaviour of stainless steel frames. *Proceedings of the SDSS, International Colloquia on Stability and Ductility of Steel Structures*, Prague, Czech Republic, 124–132. http://hdl.handle.net/2117/171044

González-de-León I., Arrayago I. and Real E. (2021). Interaction of geometric and material nonlinearities in stainless steel frames. *Proceedings of the Eurosteel, European Conference on Steel and Composite Structures*, Sheffield, United Kingdom, 2149–2157. https://doi.org/10.1002/cepa.1533

González-de-León I., Arrayago I., Nastri E. and Real E. (2022). Ductile fracture simulation of stainless steel coupons under monotonic tensile forces. *Proceedings of the SDSS, International Colloquia on Stability and Ductility of Steel Structures*, Aveiro, Portugal, 520–526. https://doi.org/10.1002/cepa.1785

CONTENTS

CHAPTER 1

Introduction

1.1. Background

Stainless steels are iron alloys characterised by a minimum chromium content of 10.5%. This chemical element is the responsible for the corrosion resistance capacity that characterises stainless steels, since when the chromium is in contact with the oxygen, a transparent layer that protects the steels from further corrosion is formed on its surface. The other chemical elements that may be added to the alloy, such as nickel, molybdenum, titanium and copper, determine the mechanical resistance and other physical properties of the material, leading to countless types of stainless steel alloys that can meet almost any need. The correct selection of the stainless steel grade depends on the corrosivity of the environment, the mechanical properties and aesthetic appearance required in the project, the availability of fabrication and the foreseen level of maintenance of the structure.

Stainless steels can be classified into five groups according to their chemical composition: austenitic, duplex, ferritic, martensitic and precipitation hardening stainless steels, being the first two the most widely used for structural purposes because of their higher corrosion resistance, excellent ductility and

strain hardening (more pronounced in the austenitic alloys) properties, and remarkably high strength capabilities (in the duplex alloys). Ferritic stainless steels have good mechanical properties but they are the least corrosion resistant; however, they are also the ones with the lowest and more stable price, which makes them an attractive alternative to austenitic and duplex grades. Compared to structural carbon steels, stainless steels have better toughness and fatigue properties, and their high ductility is associated with a higher energy dissipation capacity, which can be useful in seismic design.

All types of stainless steel exhibit nonlinear stress-strain responses, which is why the design requirements for carbon steel should not be applied directly and should be adapted to account for the material nonlinearities, and the interaction of the effects of these nonlinearities with the effects of geometric nonlinearity.

1.2. Structural applications of stainless steel alloys

The use of stainless steel as structural material has increased since its development – dated in the early 1910s –, due to the mechanical properties, corrosion and heat resistance, aesthetic appearance and residual value of this material. From the early stages, it should be highlighted the use of stainless steel in the supporting structure of the dome of St. Paul's Cathedral in London (1925), in the cladding of the Chrysler Building in New York (1929), and in the Gateway Arch in St. Louis, Missouri (1960s).

More recent structural applications demonstrate the great versatility of stainless steel as a construction material. These include the Thames Gateway Treatment Works structure in London (2010), the structural enclosure of the Taronga Zoo Chimpanzee Sanctuary in Sydney (2012), the use of stainless steel in reinforcement bars and load-bearing structures in the Sagrada Familia in Barcelona since 2014, the Garrison Crossing pedestrian bridge in Toronto (2019), the Knight Architects' road bridge at Pooley Bridge, Cumbria (2020), the 3D printed MX3D Bridge in Amsterdam (2021), or the use of stainless steel to clad the façade and roof of the Santiago Bernabeu Stadium in Madrid (2023).

Although more and more structures are being built in stainless steel, some aspects of its structural behaviour are still unknown, especially at the global response level, and therefore the current stainless steel standards have many shortcomings. Further research is needed to provide more effective design standards.

1.3. Research objectives

In this context, the main objectives of this thesis are to understand the overall behaviour of stainless steels portal frames under static and seismic forces, and to provide expressions according to the European design framework for the efficient and safe design of stainless steel structures. The general and specific objectives are detailed as follows.

1.3.1. General objectives

The safe design of structures is one of the main requirements in design practice, together with the optimised use of material for an efficient use of natural resources. For this to be achieved, it is fundamental to understand the behaviour of the materials and how it influences its structural response. Stainless steel structures are more susceptible to instability phenomena than carbon steel structures due to the combination of material and geometric nonlinearities, so ignoring these effects can lead to unsafe designs. In addition, the capacity of stainless steels after yielding tends to be significantly higher than that of carbon steel alloys, and not accounting for this strength means higher tonnage of material usage and costs. With the aim of promoting more efficient, economical and sustainable stainless steel structures, this thesis investigated the overall behaviour of stainless steel portal frames first, focusing on the influence that the interaction of geometrical and material nonlinearities has on the capacity of structures and on design. Within the framework of this thesis, the first tests on stainless steel frames subjected to vertical and horizontal static forces were carried out. Based on these experimental results, an approach for the design of in-plane structures that accounts for material nonlinearities was proposed.

Furthermore, a safe design includes a reasonable behaviour of structures under unexpected conditions and accidental situations, such as earthquakes. Studies on the seismic behaviour of stainless steel structures, which are practically inexistent at date, would allow the derivation of seismic prescriptions that take into account the nonlinear behaviour and dissipation capacity of stainless steels. The second part of this thesis thus focuses on providing such guidance, carrying out relevant studies to understand the response of stainless steel structures under cyclic loads, and propose, for the first time, criteria for the seismic design of stainless steel moment resisting frames.

1.3.2. Specific objectives

In the framework of the previous general goals, this thesis addressed the following specific objectives, which can be grouped into three main topics or parts:

Part I – Performance of stainless steel structures under static loads

- To strengthen the available experimental data on austenitic stainless steel material, cross-sections, members and structures by conducting an experimental programme to better understand their overall behaviour considering all sources of nonlinearity effects.

- To provide experimental evidence of the applicability of the recently developed approach for the in-plane design of stainless steel structures under sway forces based on the experimental results.

- To develop a new and alternative approach for the design of in-plane stainless steel structures according to the Eurocode provisions that takes into account the effects of geometric nonlinearity by reducing the stiffness of members.

Part II – Performance of stainless steel structures under cyclic loads

- To develop a new expression to estimate the rotation capacity of stainless steel members subjected to cyclic forces and a novel model to describe the full moment-rotation curves, which are the fundamental characteristics defining the seismic behaviour of structures.

- To strengthen the available experimental data on austenitic members subjected to cyclic loading by carrying out an experimental programme, to better understand their seismic behaviour.

- To assess the applicability of current seismic design prescriptions for carbon steel included in the upcoming version of the Eurocode to stainless steel structures.

- To adapt the force-based method approach, which is considered to be the main seismic design method, for carbon steel structures included in the upcoming version of Eurocode to stainless steel moment resisting frames, by calibrating new values of the behaviour factors.

Part III – Towards the consideration of material degradation

- To calibrate a ductile fracture model for the accurate description of the material degradation of stainless steels for the development of a full-range constitutive material model that includes the fracture response to contribute to the implementation of advanced direct design approaches in the future.

1.4. Methodology

A summary of the methodology used in this thesis to achieve the objectives listed in the previous section is presented below.

1. Literature review. Review of the state of the art in stainless steel research. Due to the originality of the topics, the revision has been extended to other steel materials. The main topics reviewed have been: experimental programmes on systems, tests of members under cyclic loading, the numerical simulation of the nonlinear behaviour of stainless steels considering cyclic loading and strength degradation, and design methods under static and seismic forces prescribed in different normative frameworks.

Part I – Performance of stainless steel structures under static loads

2. Experimental programme on stainless steel portal frames.

2.1. Previous experimental works to characterise the behaviour of the specimens at different levels: tensile tests on flat and corner coupons, compression tests on stub column specimens, four-point bending tests, and flexural buckling tests on columns.
2.2. Conceptualization and definition of the test configuration for the frames.
2.3. Instrumentation of the frame specimens.
2.4. Execution of the tests, data curation and processing.

3. Analysis of the tests results and assessment of design approaches for stainless steel structures.
3.1. Analysis of the experimental results.
3.2. Development of advanced numerical models of the portal frames Validation of the models against experimental results.
3.3. Assessment of the design approaches provided in the current codes and the literature.

4. Development of a new design approach for the in-plane design of stainless steel structures.
4.1. Development and validation of the numerical models of the structural members and portal frames. Definition and execution of the parametric study.
4.2. Development of a new design approach for the design of stainless steel members and systems through geometric nonlinear analyses that consider material nonlinearities and imperfections through reduced stiffness properties.
4.3. Assessment of the proposal by comparison with results obtained from codified design approaches.

Part II – Performance of stainless steel structures under cyclic loads

5. Development of an expression for predicting the rotation capacity of stainless steel member under cyclic loading.
5.1. Development and validation of the numerical models of members under cyclic loading. Definition and execution of the parametric study.
5.2. Analysis of the results.
5.3. Development of a new expression for predicting rotation capacity of stainless steel members under cyclic bending in terms of the local slenderness and proposal of a novel model to describe the full moment-rotation curves.
5.4. Assessment of the proposals by comparison with results obtained from numerical analyses.

6. Experimental programme on stainless steel tubular members under cyclic loading.
6.1. Conceptualization and definition of the test configuration.
6.2. Instrumentation of the specimens.
6.3. Execution of the tests, data curation and processing.
6.4. Analysis of the experimental results.

7. Assessment of the suitability of seismic provisions for carbon steel structures for the seismic design of stainless steel frames. Proposal of new design rules and values for the behaviour factor if necessary.

7.1. Assessment of the current seismic design rules for carbon steel moment resisting frames.
7.2. Definition of the parametric study. Performance of the analyses. Analysis of the results.
7.3. Adaptation of the rules to account for the interaction between material nonlinearities and second order effects in seismic design.
7.4. Definition of the criteria to describe the behaviour factors.
7.5. Proposal of behaviour factors for the seismic design of stainless steel moment resisting frames. Comparison with the factors prescribed in other codes, and possible extensions.

Part III – Towards the consideration of material degradation

8. Calibration of a ductile fracture model for the accurate modelling of the post buckling behaviour of stainless steels through finite element software.
   8.1. Experimental data collection (raw of stress-strain curves).
   8.2. Development of advanced finite element models.
   8.3. Calibration of the ductile fracture material parameters through comparison with coupon tests.
   8.4. Proposal of fracture parameters for stainless steels.

1.5. Financial support

The research carried out in this thesis was developed in the frame of the Project BIA2016-75678-R, AEI/FEDER, UE "Comportamiento estructural de pórticos de acero inoxidable. Seguridad frente a acciones accidentales de sismo y fuego", funded by MINECO (Spain). The author of this thesis was financially supported by the FPI-MINECO PhD fellowship, with Ref. BES-2017-082958, from December 2018 to April 2023.

1.6. Thesis outline

This chapter outlines the framework of this thesis, briefly introducing structural stainless steels, their applications and fundamental properties. The general and specific objectives addressed in this thesis are also provided, as well as the methodology adopted to achieve them, and the financial support received.

Chapter 2 introduces an overview of the different design approaches prescribed in the main codes for steel and stainless steel structures, in addition to those found in the literature that are relevant for the studies covered in this thesis.

Part I – Performance of stainless steel structures under static loads

Chapter 3 provides a detailed description of the experimental programme carried out on stainless steel frames, including results from preliminary tests on material coupons and members, definition of the

loading protocol, the description of the set-up and the instrumentation adopted in the tests, and measurement of initial imperfections of the specimens.

Chapter 4 presents the result from the frame tests, and as well as an assessment of the design approaches prescribed in the European code for the in-plane design of stainless steel structures through experimental and numerical results.

Chapter 5 describes the development of a new approach for the in-plane design of stainless steel structures through geometric nonlinear analysis and consideration of material nonlinearities and imperfections through stiffness reductions.

Part II – Performance of stainless steel structures under cyclic loads

Chapter 6 features the development of the formula proposed for the prediction of the rotation capacity of stainless steel members under cyclic loading and the proposal of the model that describes the full moment-rotation curves through advanced finite element simulation. The development and validation of the numerical models is described in detail, and the predicted rotation capacities are assessed by comparison with numerical results.

Chapter 7 describes the experimental programme on stainless steel tubular members under cyclic loading, including the loading protocol, adopted instrumentation and the assessment of experimental results.

Chapter 8 presents the study on the seismic behaviour of stainless steel moment resisting frames designed according to the European design rules for carbon steel systems. Design adaptations and a new design formula are shown to effectively account for material nonlinearities in the seismic design of these structures. Finally, the actual behaviour factors of stainless steel frames are assessed, and new values are suggested for the behaviour factors of stainless steel moment resisting frames.

Part III – Towards the consideration of material degradation

Chapter 9 presents the study on the ductile fracture of stainless steels under monotonic loading. Through the comparison of experimental and numerical results, values of the main fracture parameters are recommended for stainless steel alloys.

Finally, Chapter 10 provides a general overview of the concluding remarks given through this thesis and presents possible future research paths to achieve a consistent and efficient design framework for stainless steel structures.

CHAPTER 2

Literature review

2.1. Introduction

This chapter presents a literature review on the topics on which this thesis is based. In particular, this chapter provides an overview of the main international steel and stainless steel design standards considered in this thesis, the most common material model used to simulate the behaviour of stainless steels, alternative design methods for the optimised design of stainless steel structural members, and the approaches available for designing stainless steel structures under static actions accounting for the effect of geometric and material nonlinearities. A summary of the studies carried out to date on the behaviour of stainless steel members under cyclic loading and the current status of standards for the seismic design of steel structures are also provided.

2.2. Structural design standards for stainless steel

The earliest normative for the structural design on stainless steel was the “Specification for the Design of Light Gauge Cold-Formed Stainless Steel Structural Members” published by the American Iron and

Steel Institute (AISI) in 1968, and updated 1974. Following revisions of this standard were published as "Specification for the Design of Cold-Formed Stainless Steel Structural Members", ASCE 8, by the American Society of Civil Engineers (ASCE) in 1990 and 2002, and the latest version of this specification has been just published in 2022. Likewise, the American Institute of Steel Construction has recently published the first edition of the "Specification for Structural Stainless Steel Buildings", AISC 370 (2021).

In the European framework, the first stainless steel standard, namely "Design Manual for Structural Stainless Steel", was published by Euro Inox in 1994. In 2006 the first European standard was launched, EN 1993-1-4, being updated in 2015 and 2021. The updated EN 1993-1-4 (2015) specification is the current code for designing in stainless steel. As most of the standards for stainless steel, EN 1993-1-4 (2015) is based on the carbon steel standard EN 1993-1-1 (2005) and provides supplementary rules that consider the singularities of stainless steel alloys (austenitic, ferritic and duplex) on the design of cross-sections and structural members.

Despite having undergone some minor updates and amendments since the early 2000s, most of European standards are now under a major revision process. Thus, prEN 1993-1-4 (2021) includes, for the first time, simple rules for the global design of structures under static forces considering the nonlinear behaviour of stainless steels. Likewise, prEN 1993-1-14 (2021) gives rules for assisting the design of steel and stainless steel structures using finite element models, tools that are essential to accurately consider the interaction between geometric and material nonlinearities on the overall behaviour of structures.

It should be noted that none of the US or European standards address the seismic design of stainless steel structural members and systems specifically. Only the "The Building Standard Law of Japan" (BCJ 2016) features regulations for the earthquake-resistant design of stainless steel systems.

2.3. Material response and modelling of stainless steel alloys

In contrast to the bilinear stress-strain behaviour of carbon steel, stainless steel alloys show a rounded stress-strain response even for low strain values. Since the nonlinear behaviour interacts with geometric nonlinearities and second order effects, an accurate prediction of this response is crucial for the correct design of stainless steel members and structural systems (Arrayago et al. 2020c; Arrayago et al. 2020d; Walport et al. 2021a). Among the constitutive models developed to describe the nonlinear stress-strain behaviour of metallic materials, the two-stage Ramberg-Osgood model (Arrayago et al. 2015a) is the most widely used for stainless steels and the one adopted by the European codes prEN 1993-1-4 (2021) and prEN 1993-1-14 (2021), and the US code AISC 370 (2021). This model uses one equation to define the stress-strain behaviour up to the yield stress, considered as the stress corresponding to a 0.2% plastic

strain (Eq. 2.1), and another equation to define the behaviour between the yield stress and the ultimate strength (Eq. 2.2). In Eq. 2.1 and Eq. 2.2, ε is the strain, σ is the stress, E is the Young's modulus, f_y and f_u are the yield stress and ultimate tensile strength, respectively, ε_u is the ultimate strain, n and m are the strain hardening exponents and E_y is the tangent modulus at the yield stress, given in Eq. 2.3.

$$\varepsilon = \frac{\sigma}{E} + 0.002\left(\frac{\sigma}{E}\right)^n \quad \text{for} \quad \sigma \leq f_y \qquad \text{Eq. 2.1}$$

$$\varepsilon = 0.002 + \frac{f_y}{E} + \frac{\sigma - f_y}{E_y} + \varepsilon_u\left(\frac{\sigma - f_y}{f_u - f_y}\right)^m \quad \text{for} \quad f_y < \sigma \leq f_u \qquad \text{Eq. 2.2}$$

$$E_y = \frac{E}{1 + 0.002n\frac{E}{f_y}} \qquad \text{Eq. 2.3}$$

Figure 2.1 shows the typical stress-strain responses exhibited by austenitic, ferritic and duplex stainless steels, and by S355 carbon steel. As shown, the strain-stress response of austenitic stainless steel is characterised by a high ductility, while the highest strengths are exhibited by the duplex stainless steel. It can be also observed that ferritic stainless steels have a similar response to carbon steel, exhibiting the lowest ductility and strain hardening capacities. These remarkable high resistance, ductility and strain hardening properties make stainless steel a suitable construction material for structures subjected to accidental loads such as seismic events (Baddoo 2008; Cashell and Baddoo 2014).

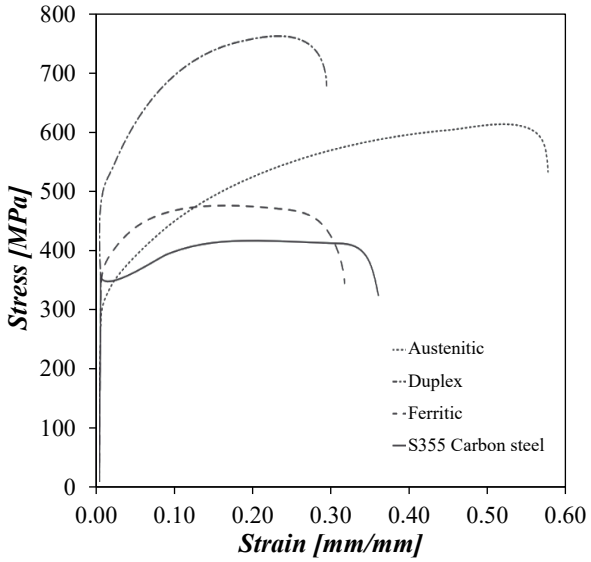

Figure 2.1. Typical stress-strain responses of the stainless steel alloys used in this study, and comparison with carbon steel S355 (SCI 2017).

It should be noted, though, that the two-stage Ramberg-Osgood model only describes the behaviour of stainless steel alloys up to the ultimate tensile strength, without considering the fracture that happens afterwards. As in other steels, the failure of stainless steel alloys is ductile and is originated by void growth and coalescence (Zhang et al. 2022). Since 1960, several ductile fracture models have been

developed for steels under monotonic loading, however, no specific prescriptions or adaptations have been provided yet to define the ductile fracture of stainless steels under monotonic loading.

One of the most common stainless steel product types are cold-formed sections, which combine the excellent corrosion resistant properties of these alloys with the remarkably high strength-to-weight features of these products. In the particular case of cold-formed specimens, the material properties at the corner parts of the cross-sections exhibit higher levels of strength than those shown by the flat parts, due to the cold-working process. To account for this effect in these cross-sections, it is advisable to assign different material properties along the cross-section. According to Gardner and Nethercot (2004b), the enhanced (corner part) material properties should be assigned to the shaded corner regions shown in Figure 2.2, which comprise the round regions (R_{ext}) plus an extension on the adjoining flat parts equal to two times the thickness ($2t$) of the cross-section. The enhanced properties can be directly obtained from monotonic tensile tests on coupons extracted from the corner parts of the specimen or through expressions based on the flat material properties and the cross-section geometry (Rasmussen 2003; Ashraf et al. 2005; Rossi et al. 2013). Another option to consider the effect of cold-working is to assign the weighted average material properties to the entire cross-section (Hradil and Talja 2013; Arrayago et al. 2017a).

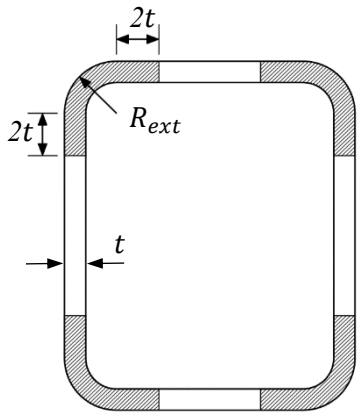

Figure 2.2. Extents of flat and corner parts in a typical RHS according to Gardner and Nethercot (2004b).

Finally, it should be noted that the material properties obtained through tensile tests on cold-formed sections already account for, implicitly, the effect of residual stresses. Residual stresses in cold-formed specimens are mainly caused during the fabrication processes by non-uniform plastic deformations, and they can significantly affect the response and resistance of stainless steel members. Residual stresses can be generally classified in membrane and bending residual stresses. While membrane residual stresses are low in magnitude and have been shown to have a negligible influence on structural response, bending residual stresses are more important in cold-formed stainless steel hollow sections (Jandera et al. 2008; Gardner and Cruise 2009). When cut from the cold-formed tubes, considerable curvatures can be observed in the coupons as a result of the relieved bending residual stresses, which are approximately

re-introduced in the coupons once they return to their original shape when gripped and loaded in the tensile testing machine. Thus, it can be considered that the obtained stress-strain curves inherently include the influence of bending residual stresses (Rasmussen and Hancock 1993a; Jandera et al. 2008).

2.4. Cross-section and member design rules

In the recent decades, research efforts have focused on the characterisation of the nonlinear stress-strain response of stainless steel alloys (Huang and Young 2014; Arrayago et al. 2015a; Afshan et al. 2019), and on the development of more accurate design expressions for stainless steel cross-sections (Gardner and Theofanous 2008; Afshan and Gardner 2013a; Arrayago and Real 2015, 2016) and structural members (Zhou and Young 2005; Arrayago et al. 2016; Buchanan et al. 2018; Sarquis et al. 2020). As a result, design standards for structural stainless steel – such as prEN 1993-1-4 (2021) in Europe –, based on those prescribed for carbon steel – prEN 1993-1-1 (2021) –, are progressively more specific and comprehensive, and are aimed at designing more efficient structures. In addition, more accurate deformation-based design approaches including strain hardening effects have been developed for stainless steel elements to fully exploit the cross-sectional capacity have been developed, such as the Continuous Strength Method (CSM).

2.4.1. Traditional European approach

As given in the carbon steel standard EN 1993-1-1 (2005), the traditional design approach prescribed by prEN 1993-4 (2021) is based on the cross-section classification, associating different criteria to estimate the resistance of a cross-section depending on their susceptibility to local buckling. Eurocode establishes four different cross-section classes, and the criteria are given in prEN 1993-4 (2021). As for carbon steel, it is assumed that class 1 stainless steel cross-sections reach their full plastic bending moment capacity M_{pl}, and that their rotation capacity is sufficient to be used in global plastic design. Class 2 and class 3 cross-sections are limited to their plastic M_{pl} and elastic M_{el} bending moment capacities, respectively. Finally, class 4 cross-sections are limited to the effective moment capacity M_{eff} through the use of the effective width method.

The traditional design approach prescribed in prEN 1993-1-4 (2021) includes formulae for predicting the cross-section resistance subjected to pure (and combined) axial loads, shear forces and bending moments. Similarly, there are also rules for estimating the resistance of stainless steel structural members under pure compression, shear and bending moments, as well as under the interaction of these forces. Note that the traditional formulae provided in prEN 1993-1-4 (2021) is based on the carbon steel provisions, and thus adopt elastic properties, ignoring the strain hardening exhibited by stainless steels after the yield stress f_y. Thus, the plastic and elastic bending moment capacity are computed as the products of $W_{pl} \cdot f_y$ and $W_{el} \cdot f_y$, respectively, being W_{pl} the plastic and W_{el} the elastic section moduli.

For the case of stainless steel members, reduction functions similar to those given for carbon steel are adopted, although buckling curves and interaction factors specific to stainless steel products have been developed and prescribed, which in general neglect the interaction between geometric and material nonlinearities.

2.4.2. Continuous Strength Method

The Continuous Strength method (CSM) is an alternativity approach for the design of stainless steel cross-sections and members. The CSM is based on the cross-section deformation capacity and provides more accurate predictions of the ultimate cross-section and member resistance than the traditional approach because strain hardening effects are considered in the equations.

The CSM formulation relies on a base curve which relates the maximum strain ε_{csm} that a cross-section can experience prior to buckling to its local slenderness $\bar{\lambda}_{p,i}$, normalised by the yield strain ε_y, which is calculated from $\varepsilon_y = f_y/E$. Eq. 2.4 shows the CSM base curve for fully-effective stainless steel cross-sections, as given in prEN 1993-1-4 (2021), where C_1 is a material coefficient that adopts a value of C_1 = 0.10 for austenitic and duplex alloys and C_1 = 0.40 for ferritic stainless steel grades, and Ω is a project specific parameter that defines the maximum permissible level of plastic strain in the structure. According to prEN 1993-1-4 (2021), the recommended value for Ω is 15. Local slenderness $\bar{\lambda}_{p,i}$ values can be calculated from $\bar{\lambda}_{p,i} = \sqrt{f_y/\sigma_{cr,l}}$, where $\sigma_{cr,l}$ is the elastic local buckling stress of the full cross-section under the appropriate stress distribution, obtained using software such as CUFSM (Li and Schafer 2010).

$$\frac{\varepsilon_{csm}}{\varepsilon_y} = \frac{0.25}{\bar{\lambda}_{p,i}^{3,6}} \leq \min\left(\Omega, \frac{C_1 \varepsilon_u}{\varepsilon_y}\right) \qquad \text{for} \quad \bar{\lambda}_{p,i} \leq 0.68 \qquad \text{Eq. 2.4}$$

The CSM was first developed for stocky cross-sections (Afshan and Gardner 2013b; Bock et al. 2015), and later extended to slender cross-sections (Zhao et al. 2017) and members (Arrayago et al. 2020d, 2021). As in the traditional approach, CSM formulae are available to predict cross-section and member strengths when subjected to almost any type of monotonic actions (both in isolation and in combination). These formulae can be found in the main stainless steel design standards and guides, such as prEN 1993-1-4 (2021), AISC 370 (2021), and the Structural Design Manual (SCI 2017). Thus, the CSM cross-section compression resistance for fully-effective stainless steel Rectangular Hollow Section (RHS) is given in Eq. 2.5, where f_{csm} is the design stress corresponding to ε_{csm}, and the CSM bending moment resistance for fully-effective stainless steel Rectangular Hollow Section (RHS) is given in Eq. 2.6. In both equations, E_{sh} is the strain hardening modulus given by Eq. 2.7 and in which C_2 is a material coefficient that adopts a value of C_2 = 0.16 for austenitic and duplex alloys and C_2 = 0.45 for ferritic stainless steels.

$$N_{csm} = Af_{csm} = A\left[f_y + E_{sh}\varepsilon_y\left(\frac{\varepsilon_{csm}}{\varepsilon_y} - 1\right)\right] \quad \text{for} \quad \bar{\lambda}_p \leq 0.68 \qquad \text{Eq. 2.5}$$

$$M_{csm} = W_{pl}f_y\left[1 + \frac{E_{sh}}{E}\frac{W_{el}}{W_{pl}}\left(\frac{\varepsilon_{csm}}{\varepsilon_y} - 1\right) - \left(1 - \frac{W_{el}}{W_{pl}}\right)\left(\frac{\varepsilon_{csm}}{\varepsilon_y}\right)^{-2}\right] \quad \text{for} \quad \bar{\lambda}_p \leq 0.68 \qquad \text{Eq. 2.6}$$

$$E_{sh} = \frac{f_u - f_y}{C_2\varepsilon_u - \varepsilon_y} \qquad \text{Eq. 2.7}$$

CSM has recently been extended to advanced structural system design, through what is known as the CSM strain limit approach. The CSM strain limit method was first developed for carbon steel structures (Fieber et al. 2019; Gardner et al. 2019) and then adapted to stainless steel frames by Walport et al. (2019b). The CSM strain limit approach allows to estimate the local failure of the structural members defined by beam-type Finite Elements (FE), which are unable to reproduce local buckling per se, by ensuring that the average deformation exhibited by the most critical cross-section in a length equal to the local buckling length does not exceed certain value. The limiting deformation ε_{csm} is obtained using the CSM base curve, which provides the maximum strains defined by Eq. 2.8 in the case of fully-effective stainless steel cross-sections. This method has shown to provide results equivalent to models featuring shell-type FE, and avoid conducting cross-section or member resistance checks (Walport et al. 2019b, 2023).

$$\frac{\varepsilon_{csm}}{\varepsilon_y} = \frac{0.25}{\bar{\lambda}_{p,i}^{3,6}} + \frac{0.002}{\varepsilon_y} \leq \min\left(\Omega, \frac{C_1\varepsilon_u}{\varepsilon_y}\right) \quad \text{for} \quad \bar{\lambda}_{p,i} \leq 0.68 \qquad \text{Eq. 2.8}$$

The CSM strain limit approach has been included in the prEN 1993-1-14 (2021) and AISC 370 (2021) specifications for the design of stainless steel structures by beam-type FE analysis.

2.5. In-plane design of stainless steel structures

The global behaviour of a structural system is affected by geometric and material nonlinearities. The consideration of these nonlinearities in design, when combined with the input of initial imperfections, results in five different methods for analysing steel structures: linear analysis or first order elastic analysis (LA), geometrically nonlinear analysis or second order elastic analysis (GNA), materially nonlinear analysis or first order plastic analysis (MNA), geometrically and materially nonlinear analysis or second order plastic analysis (GNA), and geometrically and materially nonlinear analysis with bow imperfections (GMNIA). Figure 2.3 shows the different load-displacement paths obtained from a typical stainless steel sway frame when considering these five analysis methods, showing significant differences. It is worth noting that the comparison of the responses obtained from GNA and LA analyses

allows estimating the influence of geometric nonlinearities on the global structural behaviour, while the comparison between MNA and LA responses shows the influence of material nonlinearities.

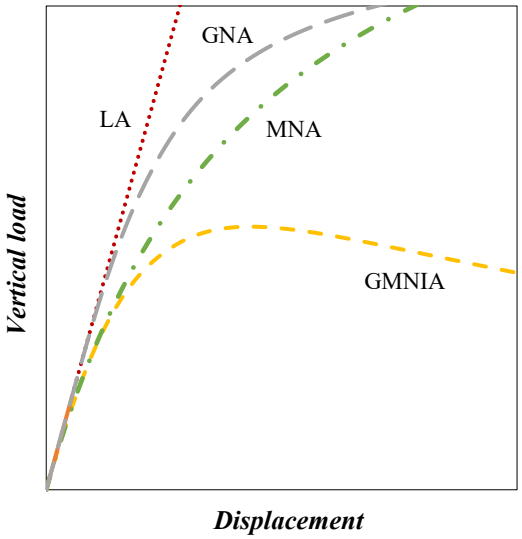

Figure 2.3. Typical load-displacement responses obtained from different methods of structural analysis.

Current stainless steel standards, such as ASCE 8 (2022) and the European EN 1993-1-4 (2015) code, do not provide specific provisions for the global analysis or design of stainless steel structures, although recent studies have highlighted the need of accounting for material nonlinearities in order to design safer structures (Walport et al. 2021a). Therefore, research is now being focused on understanding the global behaviour of stainless steel structures (Arrayago et al. 2020c) and on proposing global design expressions that consider the effects of material nonlinearity (Shen and Chacón 2020) and combined material and geometric nonlinearities (Walport et al. 2021a). In addition, the forthcoming publication of the European standard prEN 1993-1-14 (2021), which regulates the design of steel structures through numerical methods, will allow all types of stainless steel structures to be designed by directly considering geometrical and material nonlinearities and initial imperfections in the analysis (i.e., through GMNIA analysis). Nevertheless, GMNIA analyses require advanced software that is not always available to designers, so European researchers have tended to prescribe alternative global design approaches that account indirectly for the geometric nonlinearities, while research in the US has focused on providing alternative design approaches that account indirectly for material nonlinearities.

2.5.1. Geometric nonlinearity and Eurocode design approaches for in-plane structures

The susceptibility to second order effects is evaluated in EN 1993-1-1 (2005) by means of the factor $\alpha_{cr,sw}$, which represent the ratio between the applied design loads F_{Ed} and the elastic critical in-plane flexural buckling loads for a global (sway) buckling mode F_{cr}, as per Eq. 2.9. According to prEN 1993-1-1 (2021) for the global analysis of carbon steel structures, second order effects can be neglected for frames showing $\alpha_{cr,sw} \geq 10$ for elastic analysis. For multi-storey steel frames governed by the in-plane sway mode and showing $10 > \alpha_{cr,sw} \geq 3$, second order sway effects can be accounted for in an elastic

analysis by amplifying the horizontal forces by the factor k_{sw} given by Eq. 2.10 (prEN 1993-1-1 2021). In case of $\alpha_{cr,sw} < 3$, it is mandatory to carry out a second order analysis.

$$\alpha_{cr,sw} = \frac{F_{Ed}}{F_{cr}} \quad \text{Eq. 2.9}$$

$$k_{sw} = \frac{1}{1 - \frac{1}{\alpha_{cr,sw}}} \quad \text{for } 10 > \alpha_{cr,sw} \geq 3 \quad \text{Eq. 2.10}$$

According to prEN 1993-1-4 (2021), the susceptibility of stainless steel structures to second order effects should be evaluated using $\alpha_{cr,sw,ss}$, as per Eq. 2.11, where Y is a factor that approximates the further loss of stiffness, whose values are provided in Table 2.1, and the ratio K_s/K is the comparison between the stiffness of the structure obtained from a first order elastic analysis (LA) and that obtained from a first order plastic analysis (MNA) at the design load level. This new definition of the $\alpha_{cr,sw,ss}$ factor allows the consideration of material nonlinearities when evaluating the lateral stability of stainless steel structures, and was proposed by Walport et al. (2019b). As for carbon steel structures, in-plane stainless steel MRFs with $10 > \alpha_{cr,sw,ss} \geq 3$ can be designed considering second order effects by performing a first order MNA analysis if the horizontal forces are magnified by the $k_{sw,ss}$ factor given in Eq. 2.12. Similarly, second order effects can be neglected if $\alpha_{cr,sw,ss} \geq 10$, and shall be explicitly considered when $\alpha_{cr,sw,ss} < 3$.

$$\alpha_{cr,sw,ss} = Y \frac{K_s}{K} \alpha_{cr,sw} \quad \text{Eq. 2.11}$$

$$k_{sw,ss} = \frac{1}{1 - \frac{1}{\alpha_{cr,sw,ss}}} \quad \text{for } 10 > \alpha_{cr,sw,ss} \geq 3 \quad \text{Eq. 2.12}$$

Table 2.1. Y factor given in prEN 1993-1-4 (2021).

Stainless steel	Single storey frames	Multi-storey frames
Austenitic	0.80	0.55
Ferritic	0.90	0.65
Duplex	0.85	0.60

2.5.2. Material nonlinearity and AISC design approach for in-plane structures

Alternatively, the design approach adopted in the US framework for the in-plane design of steel frames is referred to as the Stiffness Reduction Method (SRM), and are design methods that account indirectly for material nonlinearities through the concept of reduced stiffness, but require second order analyses to be carried out.

The strategy of reducing the stiffness of the members to account for material nonlinearities in the design of structures is widely accepted due to its simplicity and accuracy. Traditionally, the SRM has been developed to be used in conjunction with plastic hinge-based analysis (Liew and Chen 1993a, 1993b;

Kim and Chen 1996a, 1996b; Ziemian and McGuire 2002; Zubydan 2010, 2011), and generally involves the modelling of geometric imperfections (Liew and Chen 1993a, 1993b; Zubydan 2010, 2011). Surovek-Maleck and White (2004a, 2004b) proposed a SRM in which the prediction of the capacity of steel structures is achieved through a second order elastic analysis where only global imperfections are introduced. To account for the spread of plasticity, including the effect of residual stresses, the stiffnesses of the members were reduced through analytical stiffness reduction factors.

With slight modifications, this approach was first adopted in 2005 as an annex of the AISC 360 and referred to as the Direct Analysis Method (DM). In the following editions of AISC 360 (2016, 2022), the DM has become the preferred design method and has been incorporated in the main body of the specification because it provides accurate estimates of the load effects in all types of steel structural systems and eliminates the need of calculating effective buckling lengths (Ziemian 2010). In the DM, the estimations of strengths are obtained from a second order elastic analysis, where the spread of plasticity is taken into account by reducing the stiffness of the members by two reduction factors: a general stiffness factor applied to the whole structure, and an additional factor only affecting the flexural stiffness of the members contributing to the stability of the structure. Initial global imperfections (out-of-plumbness of columns) should always be included in the analysis by means of notional loads or by modelling them directly, while different alternatives exist regarding initial member (out-of-straightness) imperfections: (1) they do not need to be explicitly included in the structural analysis, but they are accounted for by carrying out member checks, or (2) they can be explicitly included in the structural analysis, and therefore only cross-section checks are necessary.

The first edition of the American Specification for Structural Stainless Steel Buildings AISC 370 (2021) has recently adapted the DM approach previously developed for carbon steel to stainless steel structures by calibrating new values of the two reduction factors (Walport at el. 2021b). In line with the carbon steel approach, one of these factors corresponds to a general reduction in stiffness of all members due to the development and propagation of plasticity and assumes a constant value of 0.7 for all stainless steel members. The other factor applies only to the elements contributing to the stability of the structure and has been derived from the Ramberg-Osgood expression. The other requirements of the DM have remained unchanged, i.e., the consideration of initial global imperfections and the verification of member or cross-section strength depending on the approach adopted for the inclusion of member imperfections in the structural analysis. Note that cross-section strength verifications in AISC 370 are carried out using linear CSM cross-section interaction equations with a reduced maximum allowable level of plastic strain.

Having a Stiffness Reduction Method, similar to the DM but in line with the European code would be useful from a practical point of view, since most design software allow nonlinear geometric analyses to be carried out, but nonlinear material analyses are not always possible. Moreover, although the

prescription of a general reduction factor and the linear strength interaction equations proposed in AISC 370 facilitate the application of the DM, it would be interesting to study the possibility of having stiffness reduction factors more adjusted to each family of stainless steels and to use the interaction equations proposed in the Eurocode, which are more precise, to verify the cross-section resistances.

2.6. Seismic design of stainless steel structures

2.6.1. Seismic performance of stainless steel structures

Stainless steel has an excellent potential in seismic design due to its ductility, strain hardening, energy dissipation capacity and fire resistance properties (CSI 2017). Although research on the seismic behaviour of the most popular stainless steel alloys (austenitic, ferritic and duplex) is still at an early stage, some experimental studies on their hysteretic stress-strain behaviour are noteworthy (Ye et al. 2006; Nip et al. 2010a; Wang et al. 2014; Zhou and Li 2016; Chacón et al. 2018; Lázaro and Chacón 2022).

At member level, experimental studies on the hysteretic behaviour of austenitic and duplex (Nip et al. 2010b; Zhou et al. 2018; Fang et al. 2018; Kim et al. 2021; Chen et al. 2022) members under cyclic loading (subjected to either axial, bending loads, or to a combination of both) are worth mentioning, as well as numerical studies proposing expressions to estimate the ultimate rotation and axial displacement of such elements as a function of the width-to-thickness ratio (Fang et al. 2018; Zhou et al. 2018). Note that these expressions were only valid for the loading combinations considered in the corresponding studies.

Regarding the global behaviour of stainless steel structures under seismic forces, the literature presents a very limited research. The studies carried out by Di Sarno et al. (2003, 2006, 2008) can be highlighted, which revealed a considerable increase in the ultimate strength of carbon steel systems (moment resisting, braced and eccentrically braced frames) when introducing stainless steel dissipative elements.

2.6.2. Seismic design of steel and stainless steel frames according to Eurocode

The next revision of Eurocode 8 will include remarkable changes on both the general rules – prEN 1998-1-1 (2021) – and the rules for new buildings – prEN 1998-1-2 (2021). One of the major novelties the publication of a specific chapter – Chapter 15 (prEN 1998-1-2 2021) – devoted to the seismic design of certain aluminium structures, which also exhibit remarkably nonlinear stress-strain relationships.

However, as a consequence of the lack of research, the future edition of the European standard for the design of structures for earthquake resistance prEN 1998-1-2 (2021) does not include specific design provisions for stainless steel structures, despite the significantly different hysteretic response of these

alloys (Nip et al. 2010a, 2010b), and therefore the guidance provided for steel structures should be adopted. It should be noted that recommendations for stainless steel already exist in the Japanese code (BCJ 2016).

The most extended approach in Eurocode 8 for the seismic design of steel Moment Resisting Frames (MRFs) is the force-based approach. The force-based approach is based on the performance of an elastic analysis of the structure, where the nonlinear deformations and energy dissipation are considered by reducing the design seismic forces using tabulated behaviour factors, and the adequate performance of the frame under seismic actions is guaranteed by the fulfilment of several requirements related to the lateral stability, drift limitations and the application of certain capacity design rules (prEN 1998-1-1 2021). The values of the behaviour factors depend on the level of dissipation required of the structure, the system typology, and the construction material considered, and can be found in prEN 1998-1-2 (2021). Different values are prescribed for concrete, masonry, steel and aluminium structures, but no values of the behaviour factors have been proposed for stainless steel frames yet.

2.7. Concluding remarks

Stainless steel is increasingly used in structural engineering because of its remarkable mechanical properties and excellent corrosion resistance. The stress-strain behaviour of stainless steel is nonlinear and can be accurately predicted using the two-stage Ramberg-Osgood material model, but to achieve safe and more optimised stainless steel structures, the nonlinear response of the material must be taken into account at all levels of design. In recent decades, research has focused on material, cross-section and member performance under predominantly static loads, and alternative approaches, such as the Continuous Strength Method, have been developed to account for the strain hardening and ductility of stainless steels. In addition, studies on the overall behaviour of stainless steels have increased in the last years, but have been based on solely numerical studies, without providing any experimental evidence on the system performance of such structures. Likewise, research on the seismic behaviour of stainless steels is very scarce, preventing designers to take full advantage of the suitable seismic features of these alloys.

As a consequence, stainless steel structural design standards are increasingly effective for static actions, but further research is needed on the performance of systems under static loads (especially experimental studies), to assess the suitability of the expressions recently included in the new European and US codes for stainless steel structures, and also to provide recommendations for the safe and efficient seismic design of stainless steel structures.

PART I

Performance of stainless steel structures under static loads

CHAPTER 3

Experimental programme on stainless steel frames

3.1. Introduction

Advances in the research of more complex stainless steel structural systems are still scarce and generally limited to numerical studies (Arrayago et al. 2017c; Walport et al. 2019b; González-de-León et al. 2021), while only preliminary results are available for experimental results (Arrayago et al. 2019). Alternative, several experimental studies have been already carried out on carbon steel frames (Wilkinson and Hancock 1999; Avery and Mahendran 2000; Zhang et al. 2016b; Blum and Rasmussen 2018). Recent studies demonstrated that the degradation of stiffness due to the nonlinear material response of stainless steel alloys causes greater deformations and increases second order effects (Walport et al. 2019b) and the lack of guidance on plastic design represents an obstacle to the optimal design of stainless steel structures since their high ductility and strain hardening are not taken into account in design (Arrayago et al. 2017c). Although these studies lead to importance modifications of the future European standard (prEN 1993-1-4 2021; prEN 1993-1-14 2021), they were limited to numerical results. With the aim of investigating experimentally the behaviour of austenitic stainless

steel frames when subjected to static loading, a comprehensive experimental programme on sway and non-sway stainless steel frames with slender and stocky rectangular hollow sections (RHS) was carried out at the Laboratory of Technology of Structures and Materials at the Universitat Politècnica de Catalunya. This chapter presents the experimental results obtained from previous tests in which the performance of stainless steel at different levels – material characterisation, cross-sections and members – was studied, a detailed description of test specimens and the adopted experimental set-up for the frame tests. Experimental results of the frame tests are provided in Chapter 4.

3.2. Preliminary tests on material and members

The preliminary experimental programme encompassed a study at material, cross-section and member levels on EN 1.4301 austenitic stainless steel RHS: (i) a set of tensile tests on flat and corner coupons for each cross-section to characterise the stress-strain behaviour of the material, (ii) stub column tests (SC) from which cross-sectional compression resistances were obtained, (iii) four-point bending moment tests (B) to determine the bending moment capacities and (iv) flexural buckling tests from which the column resistances in major and minor axes were determined under pin-ended conditions (C1 and C2).

Four different cross-section geometries, ranging from stocky to slender, were investigated. Cross-sections follow the notation CS1-120×80×6, CS2-100×80×4, CS3-120×40×4 and CS4-200×100 3, while the labelling of the different specimens includes the reference numbering for the cross-section followed by the identification of the test type (SC for stub columns, B for beams, and C1 and C2 for columns investigated in major and minor axes, respectively). Table 3.1 summarises the geometric properties of the specimens measured before tested, in which H is the total height, B is the total width and t is the wall thickness of the cross-sections. In addition, R_{ext} represents the external corner radius, L is the total specimen length and w corresponds to the relevant local (w_0) or member (w_g) measured imperfection amplitude. Local imperfections are important for members in compression governed by cross-section behaviour, while member imperfections become more relevant when the response is controlled by flexural buckling. For beams, which are loaded transversally to the specimens, local and member imperfections have negligible effect for the magnitudes reported in Table 3.1. Detailed descriptions of the preliminary tests, including measurement of imperfections and assessment of the results, can be found in (Arrayago et al. 2020b).

Table 3.1. Measured geometric properties of the tested specimens.

Specimen	H [mm]	B [mm]	t [mm]	R_{ext} [mm]	L [mm]	w_0 [mm]	w_g [mm]
CS1-SC	119.8	80.0	6.0	19.5	360.0	0.046	--
CS2-SC	100.2	80.6	3.9	12.7	299.8	0.048	--
CS3-SC	120.0	41.5	3.9	12.6	360.3	0.041	--
CS4-SC	199.1	103.3	2.8	8.1	600.0	0.241	--
CS1-B	120.0	80.0	6.0	21.1	1700.5	--	--
CS2-B	99.8	79.8	3.9	12.9	1700.0	--	--
CS3-B	120.0	41.1	3.9	12.2	1700.5	--	--
CS4-B	199.0	103.0	2.8	10.5	1702.0	--	--
CS1-C1	120.2	80.1	6.0	20.3	1500.0	--	1.08
CS1-C2	119.9	80.0	6.0	19.5	1502.0	--	0.55
CS2-C1	99.5	80.0	3.9	11.4	1500.0	--	1.04
CS2-C2	99.5	80.3	3.8	13.3	1500.0	--	0.69
CS3-C1	120.2	41.0	3.9	11.8	1500.0	--	1.13
CS3-C2	120.0	40.9	3.8	11.7	1500.0	--	0.77
CS4-C1	199.0	102.0	2.8	10.7	1500.5	--	1.82
CS4-C2	199.0	103.0	2.8	12.2	1500.0	--	1.33

The key results from each campaign tests are reported below. Detailed descriptions of the preliminary tests, including measurement of imperfections and assessment of the results, can be found in (Arrayago et al. 2020b).

3.2.1. Tensile coupon tests

The stress-strain behaviour of the tested specimens was determined by means of a set of tensile coupon tests. Two coupons were cut from each of the four cross-sections investigated. In order to correctly characterise the effect of the cold-forming process, coupons were extracted from both flat (F) and corner (Co) regions of the different cross-sections. Table 3.2 reports a summary of the most relevant material parameters for the different coupons, while Figure 3.1 presents the stress-strain curves measured from the conducted tensile tests.

Table 3.2. Key material characterisation parameters from tensile coupon tests.

Specimen	E [MPa]	$\sigma_{0.05}$ [MPa]	f_y [MPa]	f_u [MPa]	ε_u [mm/mm]	n	m
CS1-F	185778	396	479	679	0.39	7.05	2.55
CS2-F	183098	332	398	622	0.36	7.11	2.33
CS3-F	197066	526	563	721	0.26	7.02	3.82
CS4-F	188239	331	399	631	0.41	7.09	2.49
CS1-Co	185360	374	635	840	0.34	5.40	7.89
CS2-Co	181345	384	539	746	0.45	5.55	7.02
CS3-Co	172619	454	652	856	0.32	5.52	7.74
CS4-Co	189123	414	561	757	0.28	5.57	6.88

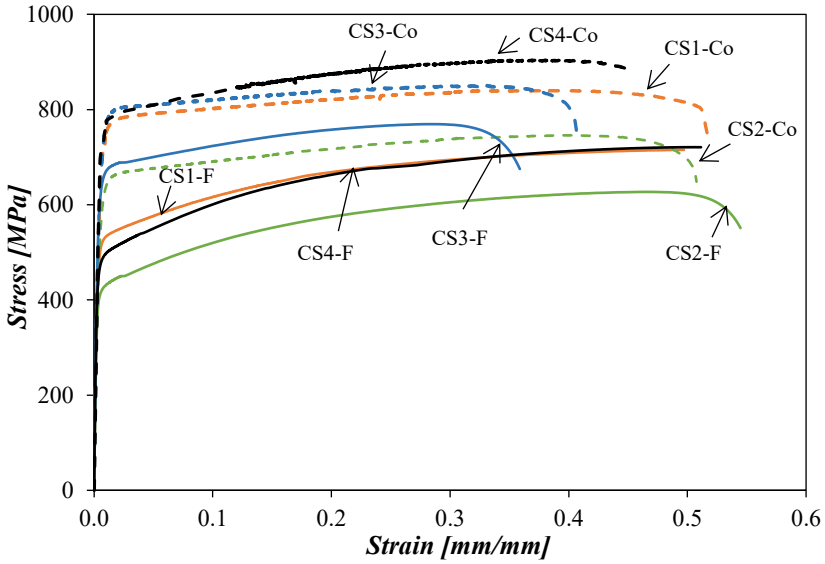

Figure 3.1. Measured stress-strain curves for flat and corner coupons.

3.2.2. Stub column tests

The cross-sectional compression resistance of the analysed cross-sections was determined by conducting four stub column (SC) tests under pure compression. Key experimental results are summarised in Table 3.3, where $N_{c,u}$ is the ultimate axial compression load and $\delta_{c,u}$ is the corresponding end shortening. Table 3.3 also reports the cross-sectional classification in compression according to EN 1993-1-4 (2015) and the calculated $N_{c,u}/N_{pl}$ ratios, where N_{pl} is the cross-sectional squash load calculated based on the weighted average yield stress values calculated from the flat and corner regions of the cross-sections, as indicated in the Design Manual (SCI 2017). Local slenderness calculated as reported in Section 2.4.2 are also reported.

Table 3.3. Key experimental results for stub column tests.

Specimen	Cross-section class in compression	Local slenderness $\bar{\lambda}_p$ in compression	$N_{c,u}$ [kN]	$\delta_{c,u}$ [mm]	$N_{c,u}/N_{pl}$
CS1-SC	1	0.50	1197.6	1.6	1.01
CS2-SC	3	0.60	673.8	2.1	1.16
CS3-SC	4	0.77	552.3	2.0	0.81
CS4-SC	4	1.64	440.6	2.1	0.63

3.2.3. Four-point bending tests

The bending moment capacity of the studied cross-sections was investigated by conducting four-point bending tests (B). The key experimental results are reported in Table 3.4, where F_u is the ultimate total load, and d_u and M_u are the corresponding midspan deflection and bending moment. According to the results shown in Table 3.4, the EN 1993-1-4 (2015) classification of the different cross-sections coincides with experimental results, as the M_u/M_{el} and M_u/M_{pl} ratios attest, where M_{el} and M_{pl} are

the elastic and plastic bending moment capacities, respectively, based on the weighted average material properties.

Table 3.4. Key experimental results for four-point bending tests.

Specimen	Cross-section class in bending	Local slenderness $\bar{\lambda}_p$ in bending	F_u [kN]	d_u [mm]	M_u [kNm]	M_u/M_{el}	M_u/M_{pl}
CS1-B	1	0.27	232.6	44.8	59.3	2.02	1.32
CS2-B	1	0.42	92.4	56.4	23.6	1.60	1.22
CS3-B	1	0.32	105.6	46.8	26.9	1.68	1.15
CS4-B	4	0.78	114.3	14.1	29.1	0.81	0.65

3.2.4. Column tests

The preliminary experimental programme was finished by testing eight austenitic stainless steel columns under pure compression around major and minor axis and pin-ended boundary conditions (C1, C2). Table 3.5 reports the key experimental results for the conducted flexural buckling tests on austenitic stainless steel columns, where $N_{b,u}$ is the ultimate flexural buckling axial compression load and $d_{b,u}$, $\delta_{b,u}$, and $\theta_{b,u}$ are the mid-height lateral deflection, end shortening and end rotation corresponding to $N_{b,u}$, respectively. The actual load eccentricities e_m, calculated as explained in (Arrayago et al. 2020b) are also reported.

Table 3.5. Key experimental results for column tests.

Specimen	Flexural buckling axis	$N_{b,u}$ [kN]	$d_{b,u}$ [mm]	$\delta_{b,u}$ [mm]	$\theta_{b,u}$ [deg]	e_m [mm]
CS1-C1	Major	--	--	--	--	2.65
CS1-C2	Minor	--	--	--	--	2.97
CS2-C1	Major	491.9	14.4	7.22	3.11	2.97
CS2-C2	Minor	454.4	11.2	10.82	2.42	1.13
CS3-C1	Minor	194.8	13.5	4.83	3.06	1.18
CS3-C2	Minor	202.5	12.5	5.40	2.83	1.17
CS4-C1	Major	407.6	0.9	14.17	0.50	4.21
CS4-C2	Minor	440.1	6.4	8.06	0.54	3.75

3.3. Stainless steel frame specimens

3.3.1. General description

The experimental programme on frames was comprised of four single-storey and single-bay austenitic stainless steel portal frames. All frames showed the same nominal height (h) of 2.0 m and a nominal span between columns (L) equal to 4.0 m, and were fabricated upon the four RHS cross-sections reported in Section 3.2. Frame 1 to Frame 4 were fabricated from cold-formed RHS specimens with cross-sections CS1 to CS4, respectively, with a constant cross-section for both columns and beams for each frame. The connections between the beams and the columns were performed by welding auxiliary 16 mm-thick steel plates with an inclination of 45º, based on the stiffened knee joint provided in the

CIDECT design guide (Parker et al. 1992) for RHS portal frames. These stiffened welded connections were proved to be capable of achieving plastic bending moment capacities in cold-formed RHS frames by Wilkinson and Hancock (2000). Likewise, for the connections at supports additional 16 mm-thick steel plates were welded at the bottom edges of the columns, which were provided with different perforations. These allowed having boundary conditions representing both fixed- and pin-ended supports with the same general configuration by simply changing the number and location of bolts.

Table 3.6 summarises the general definition of frame specimens, in which the overall geometries, cross-section dimensions and boundary conditions (BC's) are reported. In this table, the $\alpha_{cr,sw}$ and $\alpha_{cr,sw,ss}$ parameters, which indicates the susceptibility of the frames to second order effects and were calculated as given in Eq. 2.9 and Eq. 2.11, respectively, are also reported. Noted that for the specific case of austenitic stainless steel single-storey frames, Y factor is equal to 0.8. As shown, according to EN 1993-1-1 (2005), Frame 1 and Frame 2 can be considered as non-sway frames (being $\alpha_{cr,sw} > 10$, with second order effects being expected to be negligible), while Frames 3 and 4 are classified as sway frames (with $\alpha_{cr,sw} < 10$, in which second order effects are expected to be relevant). As it can be observed by comparing $\alpha_{cr,sw}$ and $\alpha_{cr,sw,ss}$, the nonlinear material response has a noticeable influence on the expected susceptibility of the studied frames to second order effects.

Table 3.6. General definition of frame specimens (based on nominal properties).

Specimen	Cross-section	h [m]	L [m]	BC's (supports)	$\alpha_{cr,sw}$	$\alpha_{cr,sw,ss}$	Column slenderness $\bar{\lambda}_c$	Local slenderness $\bar{\lambda}_p$
Frame 1	CS1	2.0	4.0	Fixed-end	11.7	8.8	0.60	0.50
Frame 2	CS2	2.0	4.0	Fixed-end	11.8	9.7	0.60	0.60
Frame 3	CS3	2.0	4.0	Pin-end	3.4	2.6	2.53	0.77
Frame 4	CS4	2.0	4.0	Pin-end	7.6	6.5	1.15	1.64

Table 3.6 also reports the calculated column slenderness values $\bar{\lambda}_c$, based on the effective length calculations for sway and non-sway frames, as well as the local slenderness values of the cross-sections in compression $\bar{\lambda}_p$. Note that according to EN 1993-1-4 (2015) local buckling effects appear beyond a local slenderness value of $\bar{\lambda}_p$= 0.65, hence the cross-sections used in the fabrication of Frames 1 and 2 correspond to stocky cross-sections in pure compression, while Frames 3 and 4 correspond to slender cross-sections, in line with the results reported in Table 3.3. Alternatively, these cross-sections are classified as class 1 in bending for Frames 1 to 3, and as class 4 for Frame 4, as indicated in Table 3.4.

3.3.2. Initial imperfections

Characterising the actual initial imperfections of the frames by measuring the initial geometry was one of the key aspects in frame tests, as they might have considerable influence on the response and ultimate capacity of such structures. In addition, the collected data contributed to the available database on frame

imperfection measurements, which is considerably scarce. The initial geometry of each frame was carefully measured prior to testing once it was put in place by means of a precision theodolite, as shown in Figure 3.2. The actual geometry of the columns was characterised by monitoring five different points along their height, while the position of five additional points along the beam length was also measured. This allowed introducing accurate initial imperfections into subsequent numerical studies, as well as evaluating the influence of member and global initial imperfections on the overall response of the frames. In addition, several points of the frames were monitored during the tests and their movements were recorded using a Lidar system (see Figure 3.2). Preliminary results corresponding to this analysis are available in (Chacón et al. 2021).

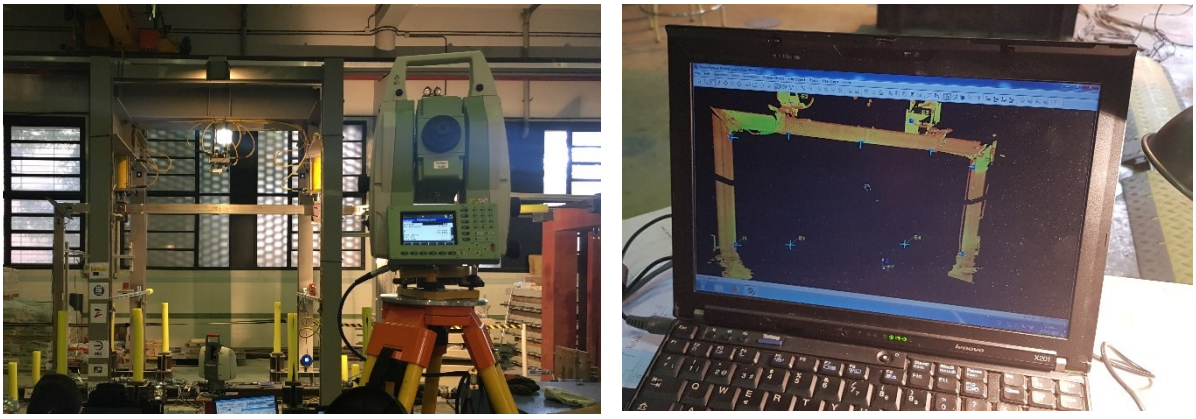

Figure 3.2. General view of the theodolite and Lidar system.

Figure 3.3 and Figure 3.4 show the measured initial geometry for the four stainless steel frames, together with the perfect geometry of the analysed frames. While Figure 3.3 presents the measured in-plane (X-Z) deviations, Figure 3.4 shows the out-of-plane (Y-Z) deviations measured from the columns. Since the measured imperfections were considerably low, they have been amplified by a factor 40 in Figure 3.3, and by a factor 5 in Figure 3.4, in order to make the imperfection patterns visible, and maximum deviation values are reported for each frame. Results in Figure 3.3 indicate that Frames 1 and 2 showed sway-shaped initial imperfections, while for Frames 3 and 4 the imperfection shapes were assimilable to non-sway modes. According to EN 1993-1-1 (2005), the equivalent sway imperfection to include in the frame analysis can be estimated through the expression given in clause §5.3.2(3). For the analysed frames, this expression provides a maximum drift of 8.6 mm at the top of the columns, which is similar to the imperfection measured for Frame 2, but much higher than the values recorded for Frames 1, 3 and 4. In a similar way, the maximum deviation due to the inclination of columns in portal frames according to the erection tolerances given in EN 1090-2 (2018) is equal to 4 mm and therefore, all measured imperfections except for Frame 2 were built in accordance with this standard. Alternatively, all four frames showed considerable out-of-plane deviations, as illustrated in Figure 3.4, which were above the tolerances given in EN 1090-2 (2018). However, and since the frames were laterally restrained in several points throughout the duration of the tests, these imperfections were not expected to influence the behaviour of the tested stainless steel frames.

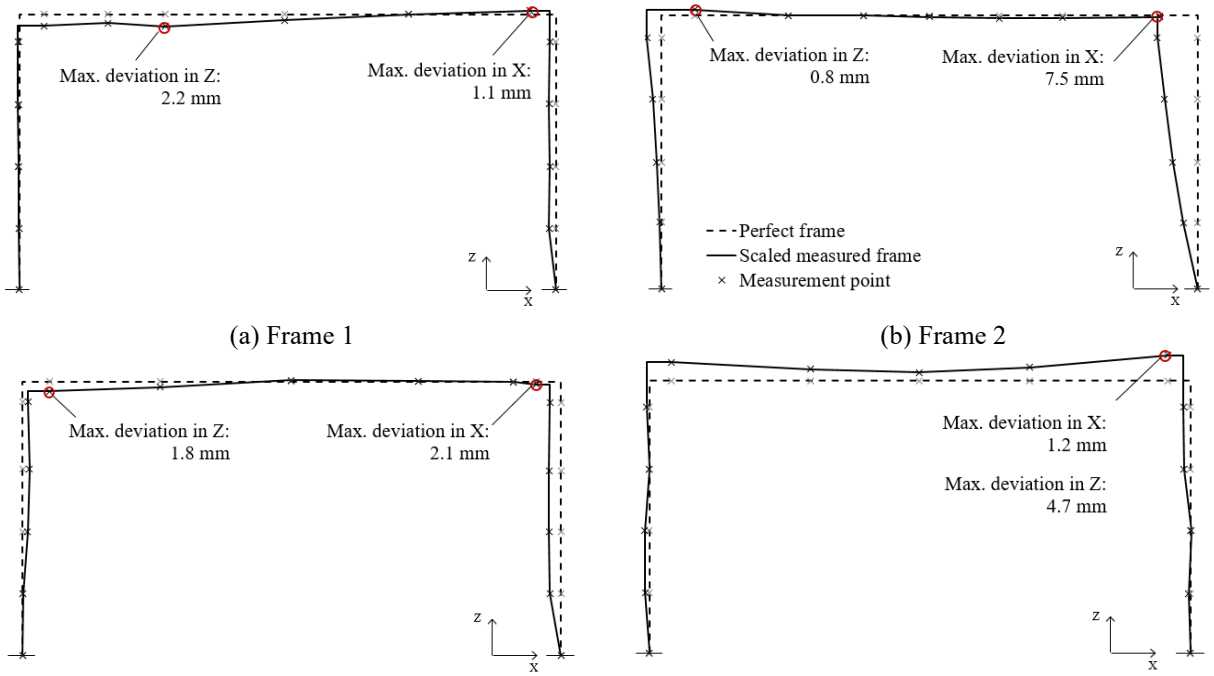

(a) Frame 1 (b) Frame 2

(c) Frame 3 (d) Frame 4

Figure 3.3. Measured in-plane initial imperfections in stainless steel frames.

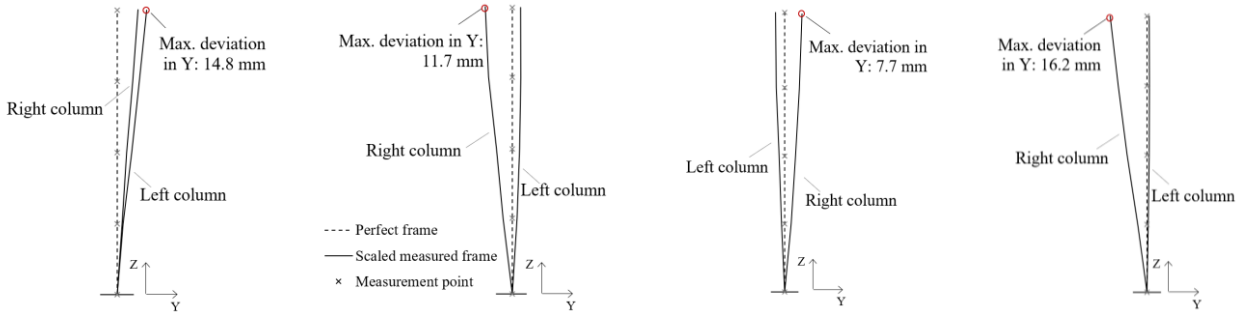

(a) Frame 1 (b) Frame 2 (c) Frame 3 (d) Frame 4

Figure 3.4. Measured out-of-plane initial imperfections in stainless steel frames.

3.4. Frame test set-up and instrumentation

The experimental set-up adopted in stainless steel frame tests, including the definition of the loading scheme and protocols, the description of auxiliary arrangements – at loading sections, supports and lateral restraint points – and the design and validation of load cells are described herein. The layout of the general test set-up can be seen in Figure 3.5, in which the most relevant parts are highlighted and described extensively in the following sub-sections.

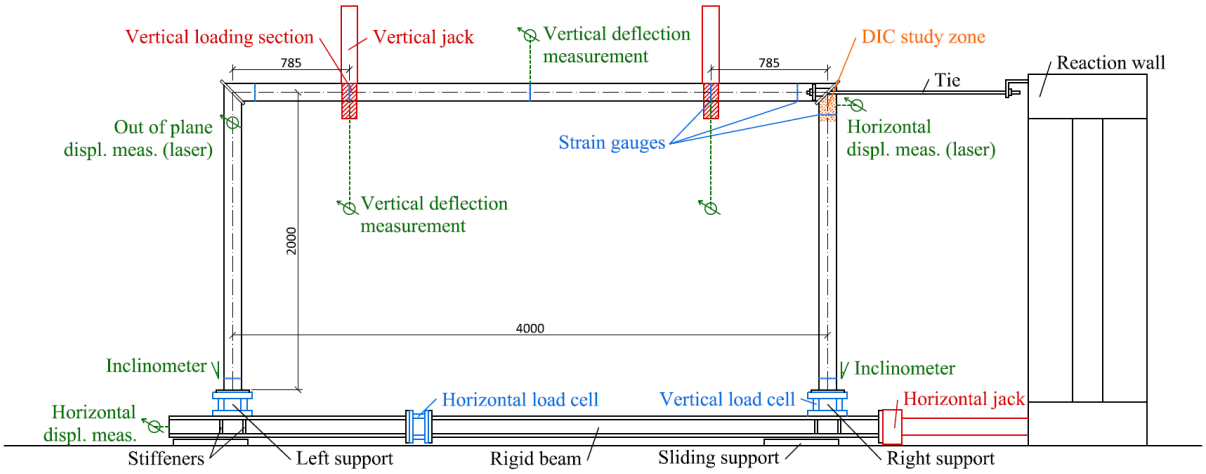

Figure 3.5. General set-up of stainless steel frame tests.

3.4.1. Loading scheme and protocol

The aim of this experimental programme was to investigate the performance of stainless steel frames subjected to static vertical and horizontal loading. Typical gravity and wind loads, transferred to frames via purlins and girts, are similar to distributed loads. Since it is difficult to reproduce this in a laboratory, point loads are usually applied. Another key aspect in frame tests are the large in-plane sway displacements, which difficult downwards loads to remain vertical, and applying these loads as gravity loads is usually not feasible due to load magnitude requirements. These issues have already been reported in the literature by several authors testing steel frames (Wilkinson and Hancock 1999; Avery and Mahendran 2000; Zhang et al. 2016c; Blum et al. 2018). One of the solutions adopted by some of these authors was the adoption of gravity load simulators (Wilkinson and Hancock 1999), the movement of the vertical actuator to eliminate the relative horizontal displacement between the strong floor and the loading sections (Zhang et al. 2016c; Blum et al. 2018) or the adoption of slightly different but equivalent loading schemes in which the horizontal displacement of column supports was imposed (Avery and Mahendran 2000). Based on the equipment available at the laboratory and the estimated values of the applied loads, this last option was considered the most suitable for this experimental programme on stainless steel frames.

Preliminary numerical simulations were developed for the two loading schemes shown in Figure 3.6 to assess the accuracy of the selected solution. For this, the loading scheme at which column supports were move away from the fixed point (i.e., loading scheme 2) was studied and compared to the frame subjected to a horizontal load acting at the right knee connection column (i.e., loading scheme 1).

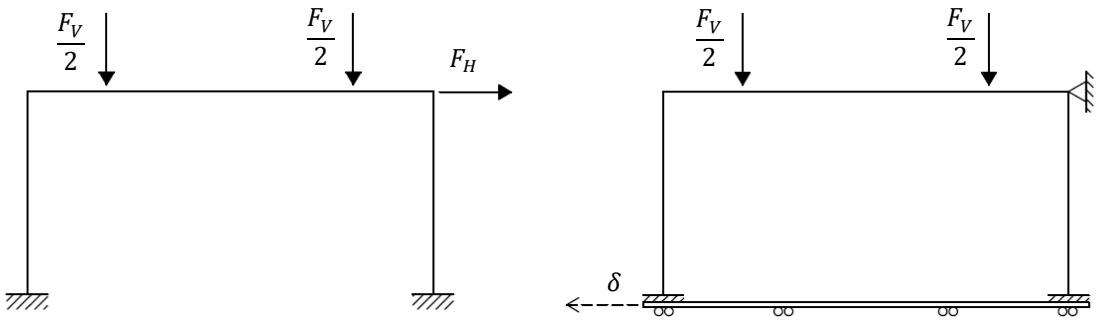

Loading scheme 1 Loading scheme 2

Figure 3.6. Loading schemes.

Figure 3.7 presents the horizontal load-lateral drift paths predicted from finite element models for Frame 1 for these two loading schemes, showing an equivalent behaviour. Although the most straightforward loading scheme case for a frame subjected to vertical and horizontal loading would be loading scheme 1, the limitations regarding vertical load simulators and reaction walls at the laboratory made loading scheme 2 the most suitable option to be adopted for the frame tests.

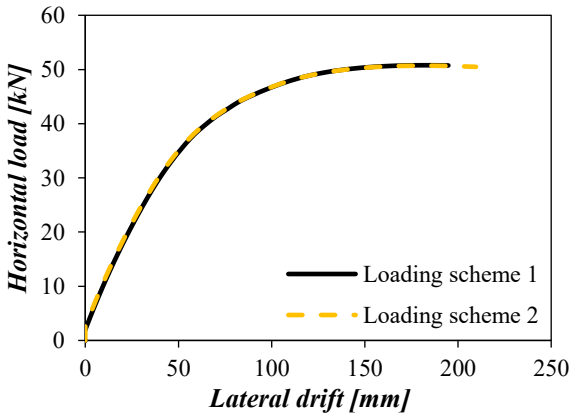

Figure 3.7. Comparison of the responses for the loading cases considered for Frame 1.

The adopted loading scheme consisted of two steps: first, the two vertical point loads were introduced by means of two jacks up to a reference load value $F_{v,ref}$ corresponding to a certain percentage of the maximum vertical resistance of the frames $F_{v,max}$ (see Table 3.7). These maximum vertical resistances $F_{v,max}$ were obtained from preliminary geometric and material nonlinear analysis with initial imperfections (GMNIA) conducted by means of the advanced finite element software ABAQUS (2016), based on the nominal geometric dimensions and the weighted average material properties calculated from the values reported in Section 3.2.1. Then, these vertical loads were kept constant and the horizontal load was introduced in a second step by imposing a horizontal displacement to the column supports through a third jack until the frames collapsed. The vertical loads were introduced by means of two different jacks, at a distance of 785 mm from each column, as shown in Figure 3.5, although both jacks were connected to guarantee that the applied loads were equal at both loading points. For the definition of the position of these point loads, different aspects were considered: (i) second order effects

are higher when vertical loads are applied near the columns; (ii) the development of plastic hinges in the beams is favoured when the vertical loads are applied away from the columns; (iii) if the position of the supports overtakes the position of the applied load when supports are pushed, a change in the frame behaviour can occur and the deformation of the frame starts to revert.

Considering all this, and the facts that the aim of the experimental programme was to study second order effects for the sway frames and the plastic behaviour for the non-sway frames, and that the maximum expected displacement at the supports was 500 mm, vertical loads were defined to act at a distance of 785 mm away from the columns. The decision of having two different jacks instead of a single jack with a spreading beam was based on the deformed shape of the frames once the horizontal loading was applied: when vertical loads are kept constant and the horizontal effect is introduced, deflections at both loading points are not equal and thus it is necessary to have two different jacks applying vertical loads for this second step, as the spreading beam might not be able to follow these deformations, and vertical loads could be unequally applied. Different vertical and horizontal loading rates were defined for each of the frames to ensure safety and reasonable duration of the tests, which were set to an approximate duration of 90 minutes. The vertical load introduction during the first loading step was performed under displacement control until the reference loads were reached. During the second loading step, horizontal loads were also introduced with displacement control, although the hold of the reference vertical loads was load-controlled. Table 3.7 reports the rates adopted for the four frame tests.

Table 3.7. Adopted test rates for vertical and horizontal loading steps in frame tests.

Specimen	Step 1: Vertical loading (Duration: 30 min approx.)			Step 2: Horizontal loading (Duration: 60 min approx.)
	Test rate [mm/min]	$F_{v,ref}$ [kN]	Proportion of $F_{v,max}$	Test rate [mm/min]
Frame 1	2.00	157.3	65%	3.30
Frame 2	2.80	85.0	80%	3.30
Frame 3	1.27	44.6	35%	2.50
Frame 4	0.67	126.7	40%	0.83

3.4.2. Auxiliary elements

3.4.2.1. Vertical loading

With the aim of avoiding local web failure (i.e., web crippling), the auxiliary elements shown in Figure 3.8 were designed for the vertical loading sections, inspired in the arrangements described in Li and Young (2018). These elements also contributed to the lateral stability of the frames and were composed of three steel plates, welded in a U-shape. The horizontal parts had a small hole in the middle to connect them to the vertical loading jacks. Likewise, the side plates had two holes to allow inserting supplementary T-shaped elements (composed by a steel bar welded to a small steel plate) with Teflon

plates, which could be adjusted to fit the different sizes of each cross-section. The correct distribution of the loads was favoured through 10 mm-thick neoprene pads.

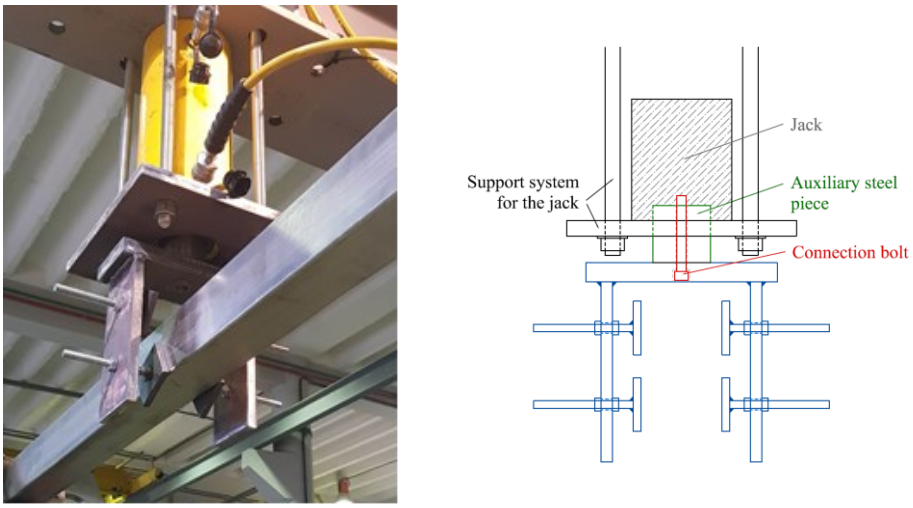

Figure 3.8. General view and details of the vertical loading section auxiliary elements and their connection to the jacks.

3.4.2.2. Horizontal loading

Horizontal loading was introduced by imposing a displacement at the column supports through a horizontal jack once the vertical loading had been applied. In order to guarantee the same imposed horizontal displacement at both supports, a rigid support beam was prepared (see Figure 3.5 and Figure 3.9). This beam was fabricated from two European HEM 120 beams, placed side by side, and connected at certain locations by welding steel plates. An especially fabricated load cell was placed in the beam to measure the horizontal reactions at the left support, as shown in Figure 3.12(b), which is further described in Section 3.4.3. The beam was thus discontinuous at the location at which the horizontal load cell was placed, and the load cell was bolted to two end plates welded to the end parts of the rigid beam. The location of the horizontal load cell was carefully chosen after studying the deflections at the rigid beam when subjected to the maximum expected loads and bending moments, making sure that neither the rigid beam nor the load cell showed excessive vertical deflections. In addition, the webs of the HEM 120 sections were reinforced by adding stiffeners at the column connection areas as shown in Figure 3.9.

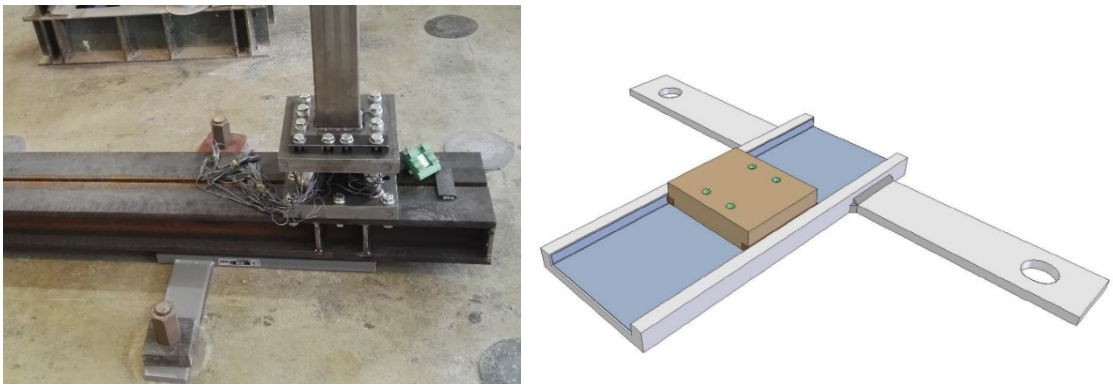

Figure 3.9. Details of the designed sliding supports and connection elements.

The rigid beam was supported on two sliding supports, which allowed a smooth and frictionless movement of the frames (see Figure 3.9). These supports were especially fabricated by MeKano4 S.A, a company specialized in bridge construction solutions. These elements consisted of steel plates with one of their surfaces covered with a Teflon plate sliding on a polished stainless steel surface, bolted to the rigid beam by means of four bolts, and connected to the strong floor through tensioned high strength bars. The length of these elements was equal to 500 mm, which was the maximum expected horizontal displacement according to the conducted preliminary finite element analyses.

3.4.2.3. Column supports

The experimental programme consisted of two stainless steel frames with fixed-ended support conditions, representing non-sway frames, and two additional sway frames with pin-ended supports. In order to guarantee these boundary conditions and to simplify the process of switching frames once they were tested, steel plates were welded at the end faces of each column. The connection of the specimens to the rigid beam was performed by means of two additional load cells similar to that shown in Figure 3.12(a), which were also especially fabricated and which are described in Section 3.4.3. These load cells were bolted to the plates welded to the column ends, as well as to the rigid beam. Fixed-ended boundary conditions were achieved by using twelve bolts between the steel plate and the load cell (see Figure 3.10(a), while for pin-ended conditions only four bolts were used (see Figure 3.10(b)). As these figures show, support sections, as well as beam-column connections, were further strengthened against localized effects by welding additional stiffeners, as shown in Figure 3.10.

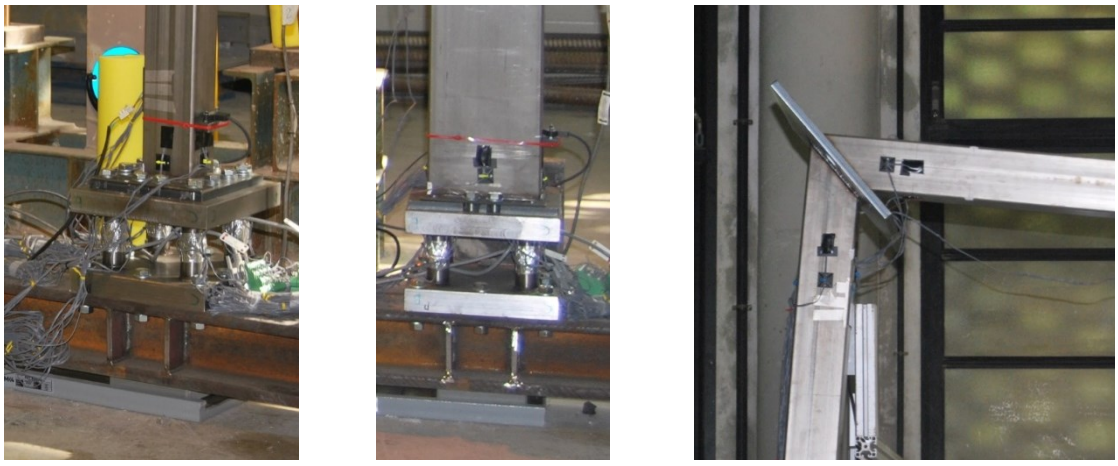

(a) (b) (c)

Figure 3.10. (a) Fixed-ended support (Frame 2); (b) Pin-ended support (Frame 4); (c) beam-column connection.

3.4.2.4. Horizontal displacement restraint point

As described in the previous section, the loading scheme considered in this experimental programme was based on the fact that the beams of the tested stainless steel frames had restrained horizontal displacements. For this, steel plates used in the beam-column connections were prepared with two additional holes and the top parts of the right columns were tied to a reaction wall by means of high

strength bars, as shown in Figure 3.11. In addition to restraining in-plane horizontal displacements, this configuration contributed to the lateral out-of-plane stability of the frames.

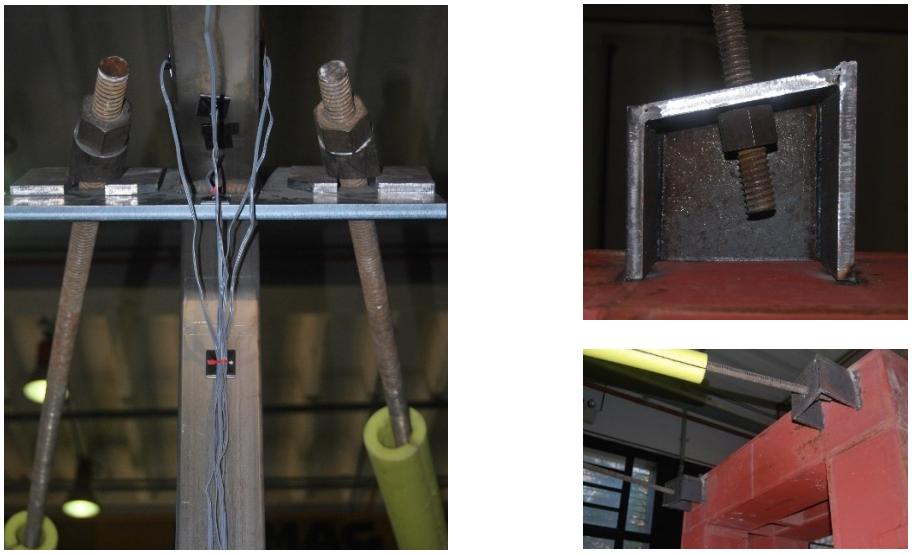

Figure 3.11. General view and details of the horizontal displacement restraint point on the top of right columns and connection to reaction wall.

3.4.3. Load cells

The accurate measurement of support reactions was another key aspect of frame tests, as they provided essential information for the calculation of the bending moments at any particular cross-section. Recording total vertical and horizontal applied loads during tests was simple as they could be directly obtained from the actuators. However, this was not enough since the distribution of these loads in both supports was required. This meant that during the tests vertical and horizontal reactions at both supports needed to be measured, as well as moment reactions for the fixed-ended frames. With the aim of capturing these reactions, three "bespoke" load cells, similar to those used by Young and Rasmussen (2003), were fabricated. Two different types of load cells were considered: two load cells for vertical supports – measuring vertical reactions and moment reactions – and one load cell for the rigid beam –measuring horizontal reactions at the left support. Each load cell consisted of two thick steel plates connected by means of four welded solid steel studs, as shown in Figure 3.12. Four strain gauges were attached to each of the steel studs, which provided the necessary information for the calculation of the reaction forces and moments acting on each load cell.

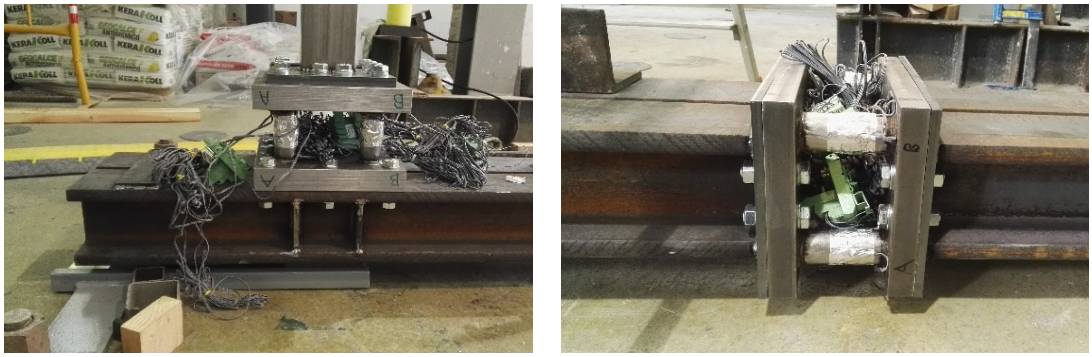

(a) (b)

Figure 3.12. General view of the designed (a) vertical and (b) horizontal load cells.

Once load cells were fabricated, they were calibrated on an 8805 INSTRON hydraulic machine (see Figure 3.13). The aim of this calibration was to assess the capability of the fabricated load cells to measure applied loads and moments accurately by comparing them with the reference values introduced by the actuator. For this, different tests were performed on each of the three load cells, including concentric and eccentric load cases, with loading protocols at which the load was applied in 20 kN increments up to a total load of 80 kN, taking 180 second to reach 20 kN and with 5 second holds after each increment, reaching the maximum load after 740 seconds. From the recorded strains, measured loads N_{meas} and moments M_{meas} were calculated and compared with the external axial loads $N_{applied}$ and moments $M = N_{meas} \cdot e$, where e is the load eccentricity, as shown in Figure 3.13.

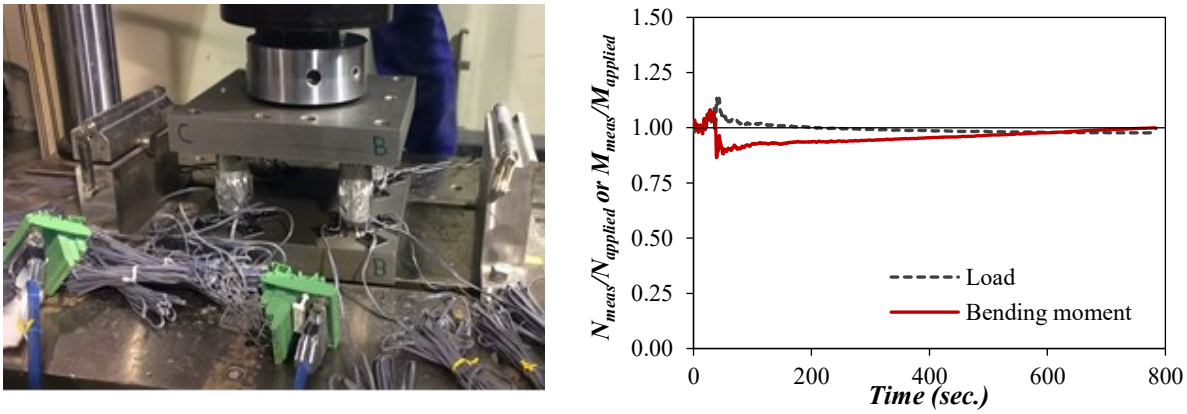

Figure 3.13. Calibration process of the load cells.

3.4.4. Instrumentation

In addition to the measurement of support reactions, further magnitudes needed to be recorded during the tests for an accurate characterisation of the performance of stainless steel frames. Figure 3.5 shows all measurement devices and magnitudes considered during the tests. Deflections were measured at the loading sections and midspan sections of the beams by means of string potentiometers, and the horizontal displacement of the rigid beam was recorded at the left support in addition to the measurement provided by the horizontal jack to check the uniformity of the movement. The vertical settlement displacements at supports were also recorded by means of LVDT transducers, measuring the relative displacements between the steel plates welded to the column ends and an external fixed reference point (i.e., the strong floor of the laboratory). One laser device was placed on the top of the right column, in the section at which the horizontal displacement of the frame was restrained, as a safety measurement of possible horizontal movements or elongations at the ties. A second laser device recorded the out-of-plane displacement of the top left column to monitor the deviation of the frames from the purely in-plane response. In addition, two inclinometers were placed close to the support sections to measure column rotations in the in-plane and out-of-plane directions.

Moreover, strains at the four faces of the rectangular hollow sections were recorded by means of strain gauges to estimate stress distributions and bending moments at certain locations. For this, column sections located at supports and at heights around 1900 mm from the supports were chosen. In the beams, vertical loading sections were instrumented, as well as the midspan section and additional sections adjacent to the beam-to-column connections. From the loading scheme defined for the frame tests, the critical cross-section – that subjected to the most unfavourable combination of bending moment and axial load – was the upper point of the right column at which the horizontal displacement was restrained. Finally, in order to accurately capture the response of these areas, a Digital Image Correlation (DIC) system was implemented, contributing to the better understanding of the response of these sections.

3.5. Concluding remarks

This chapter presents an extensive experimental programme conducted on austenitic stainless steel frames at the Universitat Politècnica de Catalunya. The experimental programme comprised previous tests at different levels – material characterisation, cross-sections and members – on EN 1.4301 austenitic stainless steel specimens with rectangular hollow section to allow a comprehensive analysis of the frame test results, which results are summarised in this chapter. In addition, an extensively description of the experimental set-up for the stainless steel frame tests is provided, including the measurement of initial global imperfections and the adopted loading schemes, auxiliary elements and instrumentation, through a detailed explanation of the different issues encountered in the process of their definition. These include strategies to guarantee the verticality of the loads representing gravitational loads during sway deflections, to define the optimal location of the point vertical loads and to measure all necessary support reactions. It should be noted that the experience gained in the preparation and execution of these complex frame tests has already helped researchers to plan efficiently future experimental programmes on structural systems (Juza and Jandera 2022; Yun et al. 2022).

Corresponding publication: Arrayago I., González-de-León I., Real E. and Mirambell E. (2020). Tests on stainless steel frames. Part I: Preliminary tests and experimental set-up. *Thin-Walled Structures*, 157, 107005. https://doi.org/10.1016/j.tws.2020.107005

CHAPTER 4

Analysis and assessment of experimental tests. Second order effects according prEN 1993-1-4

4.1. Introduction

Based on recent numerical studies, European standards prEN 1993-1-4 (2021) and prEN 1993-1-14 (2021) will include rules for the global designing of stainless steel structures considering the interaction of material and geometric nonlinearities and will give guidance on plastic design, respectively. However, experimental results are fundamental to assess the accuracy of the new design expressions accounting for the material nonlinearity on the sensitivity of stainless steel frames to second order effects and to investigate the applicability of global plastic design methods to stainless steel structures. With this purpose, a comprehensive experimental programme on sway and non-sway stainless steel frames with slender and stocky rectangular hollow sections (RHS) was carried out at the Laboratory of Technology of Structures and Materials at the Universitat Politècnica de Catalunya. This chapter presents the results from the experimental campaign and studies the interaction of material and geometric nonlinearities and the influence of the second order effects in the amplification of internal forces. Details of the experimental set-up and the results from tensile coupon tests and structural member tests that are relevant to the understanding of this chapter are given in Chapter 3.

4.2. Experimental response of stainless steel frames

This section presents the experimental results measured during the tests on austenitic stainless steel frames, showing results corresponding to the vertical and horizontal response of the frames separately. Table 4.1 reports the absolute maximum vertical loads $F_{v,max}$ introduced during the first steps of the loading process and the corresponding vertical displacements at the beam midspan section d_v for each frame. As described in Section 3.4.1, these vertical loads were maintained constant during the second loading steps, at which the absolute maximum horizontal loads $F_{h,max}$ and the corresponding horizontal displacements at the column supports d_h shown in Table 4.1 were recorded. Tests were stopped before the collapse of the frames was reached due to safety reasons, and thus results presented in this chapter correspond to the maximum loads recorded during the tests. An overall view of Frame 2 deformed under the combination of vertical and horizontal loads can be seen in Figure 4.1, while Figure 4.2 shows a detail of the local buckling failure of the upper right column section for Frame 4 and the deformed left column for Frame 1.

Table 4.1. Measured maximum loads and displacements.

Specimen	Vertical loading step		Horizontal loading step	
	$F_{v,max}$ [kN]	d_v [mm]	$F_{h,max}$ [kN]	d_h [mm]
Frame 1	157.3	68.5	42.1	82.7
Frame 2	85.0	93.5	20.8	106.2
Frame 3	44.6	39.6	18.7	82.2
Frame 4	126.7	25.6	24.4	26.2

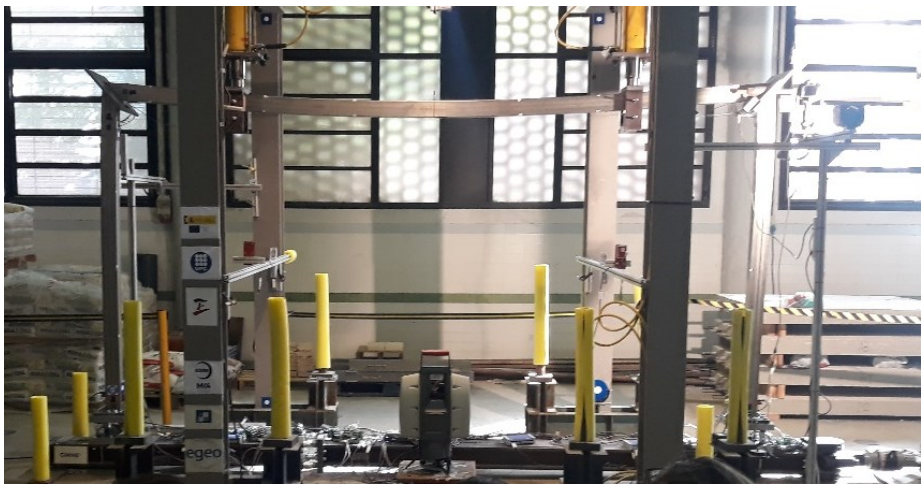

Figure 4.1. View of the deformed shape of Frame 2 during the test.

(a) (b)

Figure 4.2. Details of: (a) the local buckling failure in Frame 4 and (b) the deformed left column in Frame 1.

The out-of-plane response of the frames was controlled during the tests through the measurement of the out-of-plane displacement of the left column-to-beam connection, which is presented in Figure 4.3. Note that positive displacements in Figure 4.3 represent backwards displacements if Figure 4.1 is taken as reference. All four frames showed a similar response: during the vertical loading step, the out-of-plane displacement of the frames gradually increased until the moment at which horizontal loads were introduced (marked with vertical lines for each frame in Figure 4.3). As the horizontal loading increased, tension forces at the beams became more relevant and contributed to the lateral stability of the frames, and the out-of-plane displacements were gradually reverted, as shown in Figure 4.3. However, the magnitudes of the measured out-of-plane displacements were small for all specimens and it can be assumed that the lateral restraint was adequate, ensuring the in-plane behaviour of the frames.

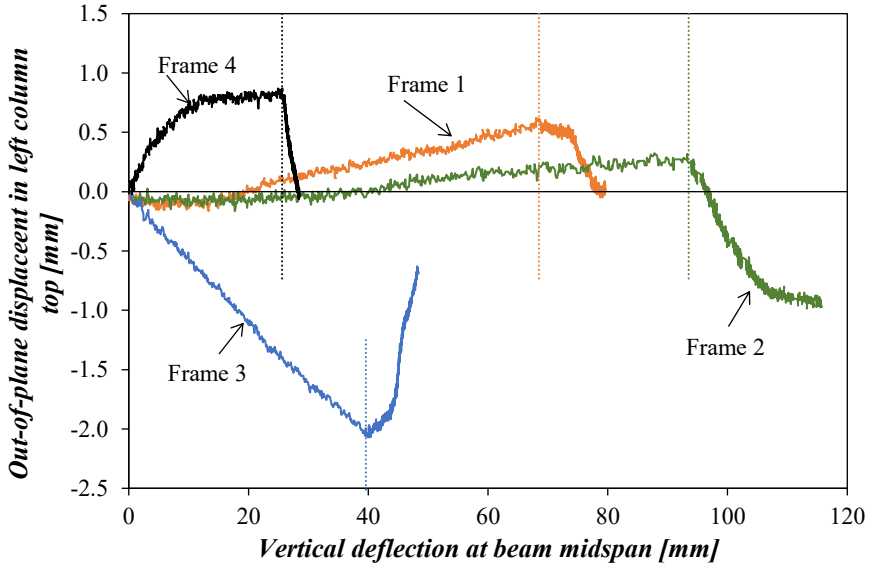

Figure 4.3. Measured out-of-plane displacements for stainless steel frame tests.

The vertical and horizontal responses of the tested stainless steel frames are presented in the following sub-sections, followed by a detailed analysis of the structural behaviour of the column supports and the local buckling failure analysis of the critical cross-section for Frame 4. The sign criteria adopted in the

analysis and throughout the chapter are summarised as follows: vertical and horizontal reactions are considered positive when directed upwards and to the left, respectively (taking Figure 4.1 as reference), while counter-clockwise moments are defined positive.

4.2.1. Vertical response of stainless steel frames

Measured vertical load-vertical deflection curves for stainless steel frame tests are presented in Figure 4.4. These figures show the relationship between the total vertical loads applied, measured directly from the jacks, and the corresponding vertical deflections at the midspan sections of the beams for the full tests, including the vertical and horizontal loading steps. In addition, vertical reactions measured from the left and right column load cells and the sum of reactions are also plotted.

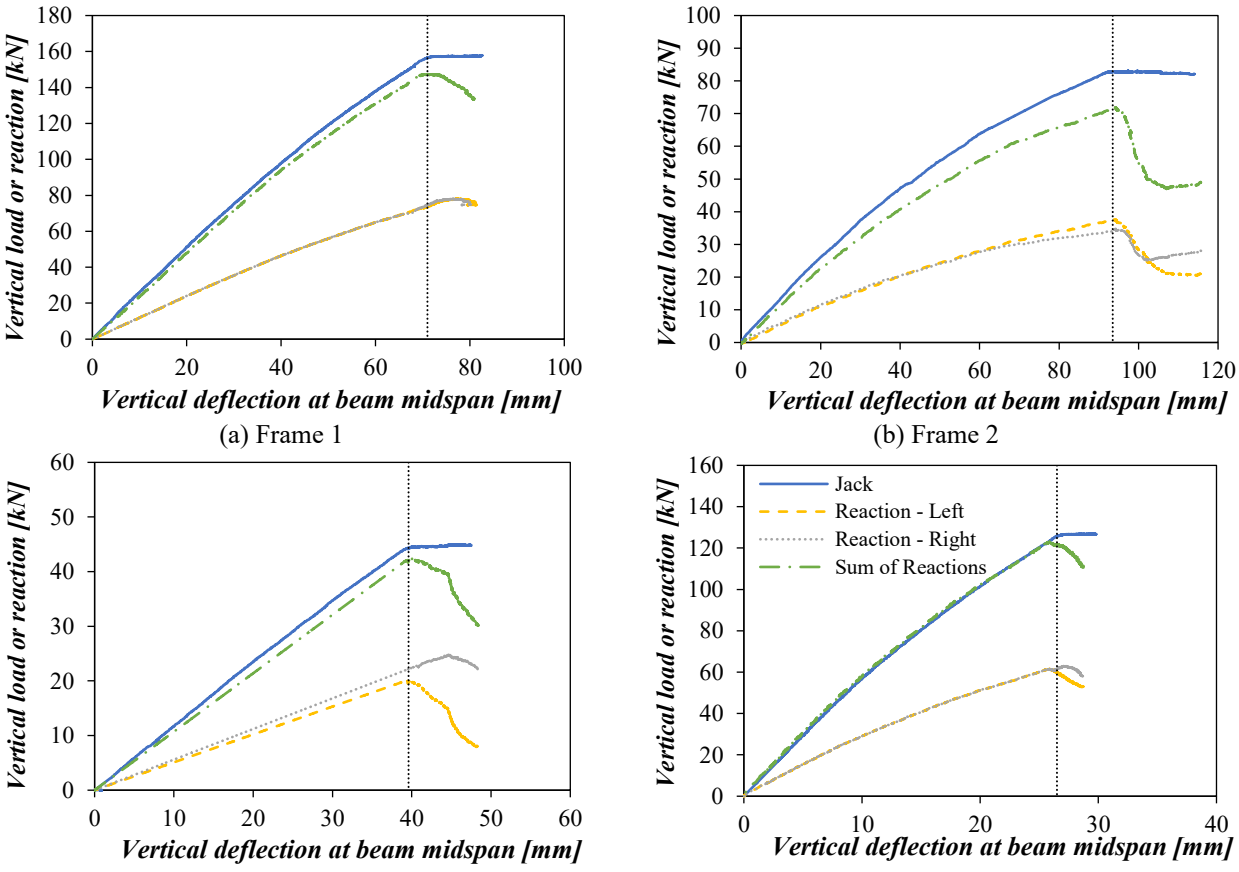

Figure 4.4. Measured vertical load-vertical deflection curves for stainless steel frame tests.

Results in Figure 4.4 indicate that while the total applied load could be considered equivalent to the sum of support reactions during the vertical loading steps, part of this vertical load was no longer resisted by the supports when the horizontal loads were introduced (marked with vertical lines as in Figure 4.3). The differences between the total vertical loads measured from the jacks and the sum of support reactions were attributed to the partial restriction to vertical displacements existing at the restraining ties, which was later confirmed by numerical simulations. The highest discrepancies between the total vertical load measured from the jacks and the sum of reaction were observed for

Frame 2, the first frame being tested, and so it is likely that partial settlements occurred in the load cells during this test. In general, it can be observed that the highest the total vertical load applied, the more similar the load measurements from the jacks and from the load cells are (i.e., Frames 1 and 4). Note that the maximum axial force values measured in the columns for the different frames only represent 5-15% of the cross-section compression capacities $N_{c,u}$ reported in Table 3.3, which suggests that the behaviour of the frames was governed by bending.

4.2.2. Horizontal response of stainless steel frames

This sub-section presents the horizontal experimental response of stainless steel frames. Figure 4.5 illustrates the horizontal response of the frames during the second loading step at which horizontal loads were introduced while maintaining the vertical loads constant, showing the measured total horizontal load-horizontal displacement at supports curves for each frame. It should be noted that due to the loading set-up chosen, minor horizontal loads were introduced in the frames during the initial vertical loading steps in the form of reaction forces at the ties, which can be observed in Figure 4.5 for a horizontal displacement equal to zero.

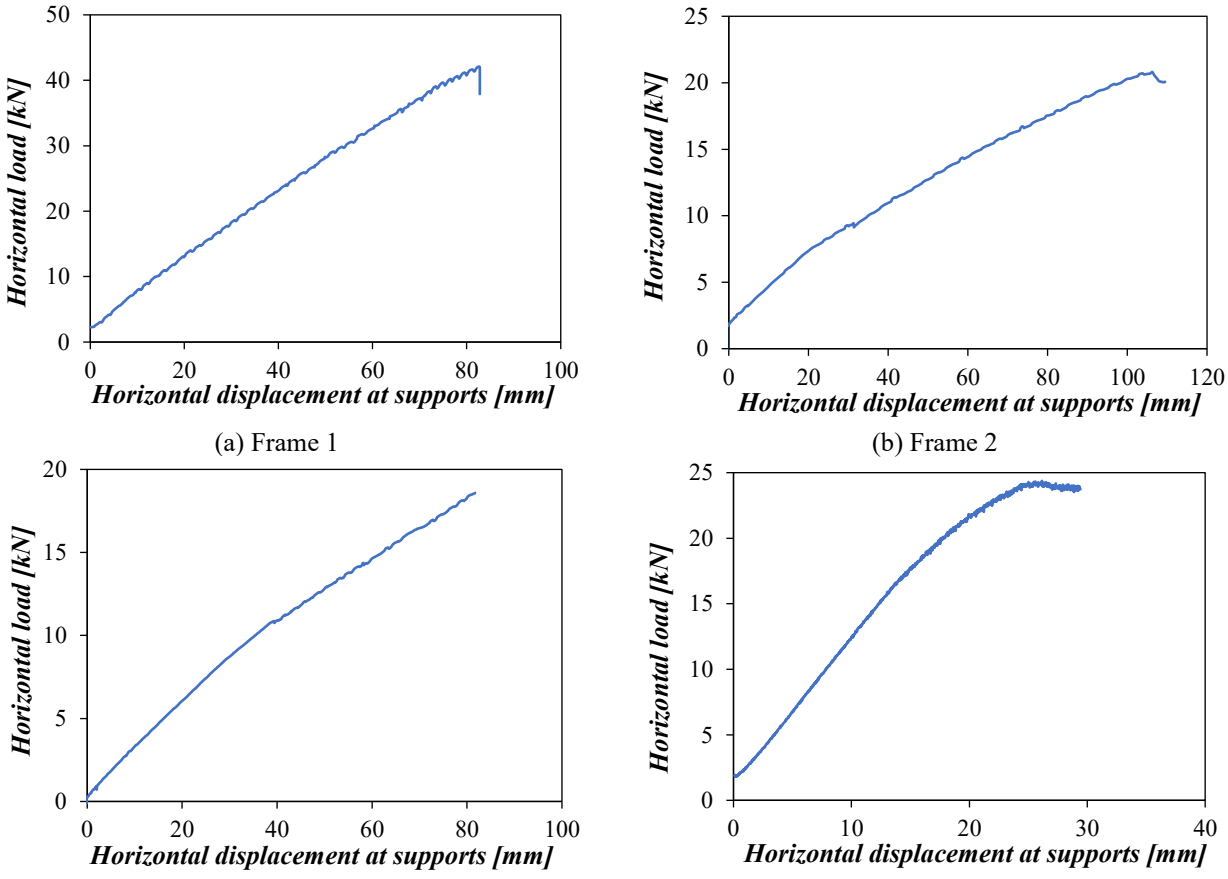

(a) Frame 1 (b) Frame 2

(c) Frame 3 (d) Frame 4

Figure 4.5. Measured horizontal load-horizontal displacement curves for stainless steel frame tests.

The evolution of the measured horizontal reactions is shown in Figure 4.6 for the four stainless steel frames. The vertical deflection at the beam midspan is used as reference magnitude in this figure and

throughout the chapter because this was the only measured magnitude showing continuously increasing values during the full tests and thus allowed representing the evolution of different measurements over the vertical and horizontal loading steps, as shown in Figure 4.3 and Figure 4.6. While the left support reactions H_L were obtained from the strains recorded from the load cell located at the rigid loading beam, right support reactions H_R were calculated as the difference between the total applied horizontal load H_{tot} as per the horizontal jack and the measured left support reactions H_L, H_R=$H_{tot} - H_L$. As shown in Figure 4.6, during the vertical loading steps, horizontal reactions were equal in value at both supports but showed opposite directions. However, due to the introduction of the horizontal loads in the second loading steps, reactions at the right supports increased while changing the direction of the reaction at the left supports.

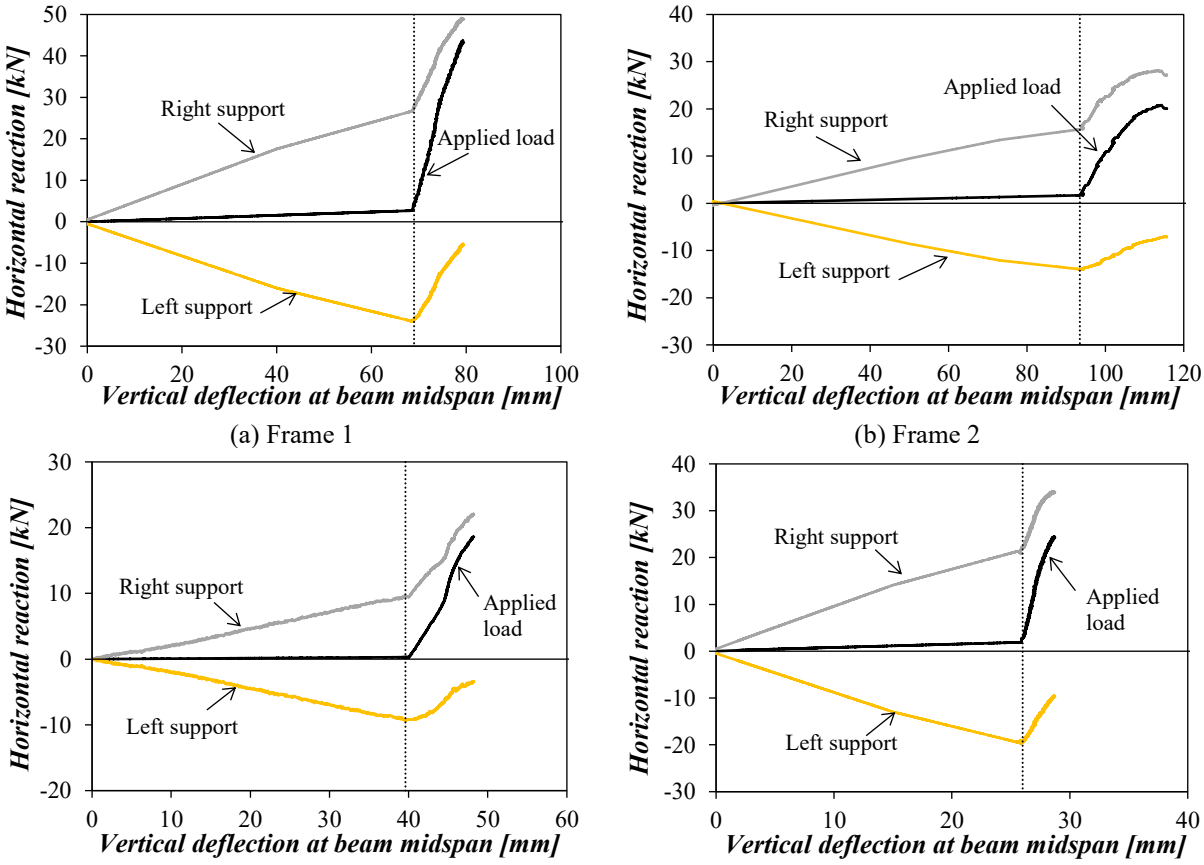

(a) Frame 1 (b) Frame 2

(c) Frame 3 (d) Frame 4

Figure 4.6. Measured horizontal reactions throughout stainless steel frame tests.

4.2.3. Response of frame supports

4.2.3.1. General

Support conditions at stainless steel frame columns were designed to represent both pin-ended and fixed-ended boundary conditions, as described in Section 3.4.2.3. Frames were connected to the load cells by means of welded steel plates and bolts, and required boundary conditions were achieved by assigning a different number of bolts to each frame. While fixed-ended frames were connected through

a total of twelve perimeter bolts at each column support, pin-ended frames had only four bolts per support, located close to the cross-section centroid (see Figure 4.7). Although the support connections shown in Figure 4.7 ideally represented pin-ended and fixed-ended boundary conditions, connections showed a semi-rigid response that slightly differed from their theoretical response: "pin-ended" connections partially transmitted moments to the supports, while "fixed-ended" connections showed non-negligible in-plane rotations, and measured moment reactions were lower than those expected for pure fixed-ended conditions. This is further investigated in the following sub-section. Figure 4.8 presents the evolution of the moment reactions at the left and right supports in terms of the vertical deflection at the beam midspans for the four frame tests and correspond to both the vertical and horizontal loading steps. These moments were calculated from the strain measurements at the load cells by using Eq. 4.1, in which the equivalent loads at each steel stud $F_{stud,i}$ are multiplied by half of the distance between studs $s/2$. The equivalent loads $F_{stud,i}$ can be obtained from Eq. 4.2, in which $\varepsilon_{av,i}$ is the averaged strain for the four strain gauges attached to each of the steel studs conforming the load cells, and A and E are the cross-section area and the Young's modulus of the studs. The ultimate bending moment resistances $M_{c,u}$ obtained from the four-point bending tests reported in Table 3.4 are also included in Figure 4.8 for comparison purposes.

$$M_{load,cell} = \frac{s}{2}\left(F_{stud,1} + F_{stud,2} - F_{stud,3} - F_{stud,4}\right) \quad \text{Eq. 4.1}$$

$$F_{stud,i} = AE\varepsilon_{av,i} \quad \text{Eq. 4.2}$$

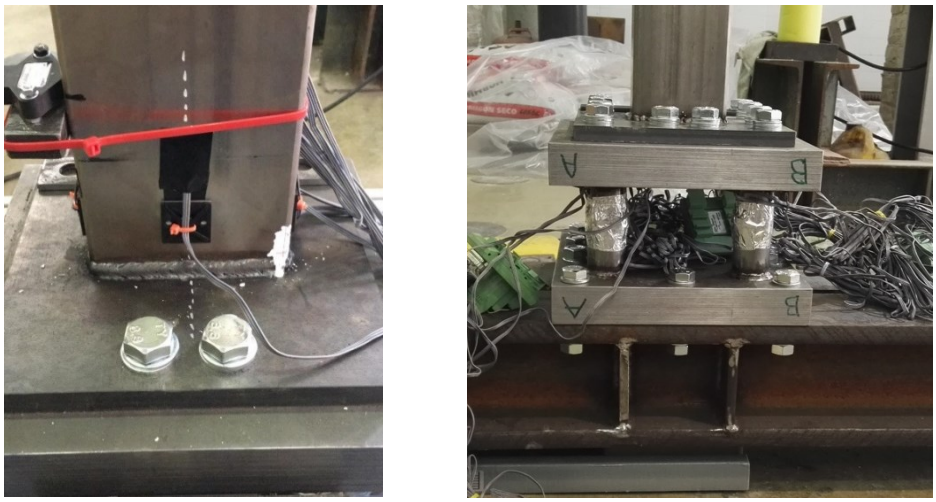

(a) (b)

Figure 4.7. (a) Pin-ended and (b) fixed-ended support connections adopted in stainless steel frame tests.

In these figures, the instant at which the horizontal load was introduced can be clearly identified for the different frames, as it corresponds to a change in the evolution of moment reactions, and which has also been indicated by vertical reference lines. After that, moment reactions at the right supports increased more pronouncedly and a moment reversal was observed for the left supports, since the horizontal load

introduced moments with opposite sign. According to the results shown in Figure 4.8, the recorded moment reaction at the right support was significantly close to the flexural capacity of the cross-section for Frame 2, while for the rest lower proportions of the corresponding bending resistances were reached. It should be noted that Frame 2 was tested with the largest proportion of the ultimate vertical load introduced during the vertical loading step (see Table 3.7). From the comparison of the bending moments measured for the right and left supports for each of the frames in Figure 4.8, it is appreciable that bending moments corresponding to the left supports are lower, especially for Frame 4. This can be explained by the different rotational stiffness of the left and right supports, which is further discussed in Section 4.2.3.2.

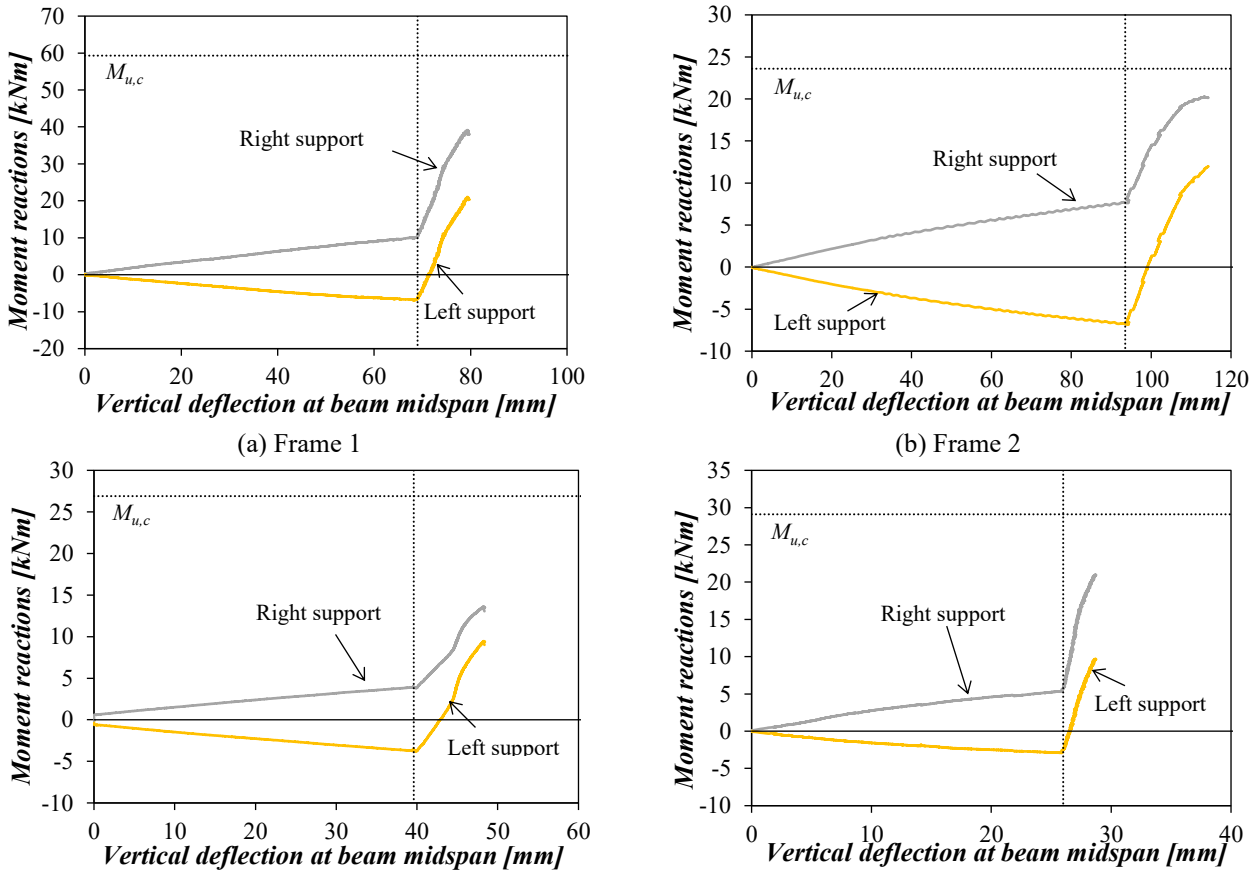

Figure 4.8. Measured moment reactions at supports throughout stainless steel frame tests.

Figure 4.9 presents the measured in-plane and out-of-plane rotations at the sections adjacent to the supports for the four stainless steel frames, in which clockwise in-plane rotations were defined as positive and counter-clockwise rotations as negative. Rotations were measured in both columns at a distance equal to 140 mm from the supports for Frame 1 and 115 mm for the rest, for space requirements. Note that the inclinometer corresponding to the right column stopped measuring rotations when the horizontal loading was introduced in Frame 2, and thus only results corresponding to the vertical loading step are provided for this specimen. According to the rotation measurements presented in Figure 4.9, in-plane rotations for Frames 1 and 2 are very similar yet not negligible, since the adopted boundary conditions showed a semi-rigid behaviour not

directly assimilable to the ideal fixed-ended conditions. Similarly, measured rotations for Frames 3 and 4 were lower than those expected for pure pin-ended boundary conditions. The characterisation of the actual response of these semi-rigid support conditions is necessary in order to provide the required input information for the validation of Finite Element (FE) models by assigning the appropriate stiffness to each support. This is addressed in the following sub-section.

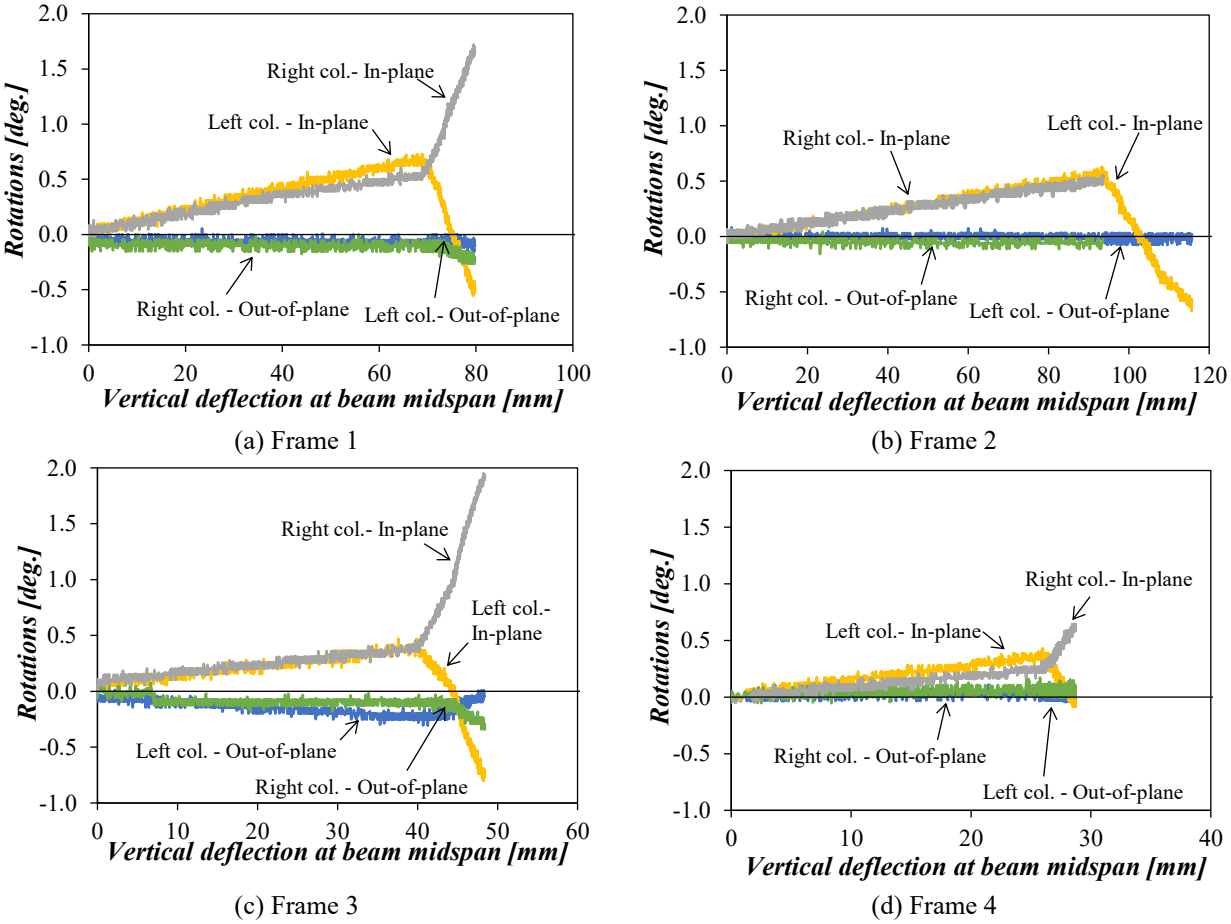

(a) Frame 1 (b) Frame 2

(c) Frame 3 (d) Frame 4

Figure 4.9. Measured rotations near supports throughout stainless steel frame tests.

4.2.3.2. Rotational stiffness of the supports

The measurements of moment reactions and rotations at the supports reported in the previous section indicated that actual boundary conditions were different from the ideal "pin-ended" or "fixed-ended" conditions, since significant rotations were recorded for Frames 1 and 2 (with theoretical "fixed-ended" conditions) while substantial moment reactions were observed for Frames 3 and 4 (with theoretical "pin-ended" conditions). This indicated that a deeper analysis of the rotational stiffness of the supports was required. The experimental in-plane bending moment stiffness of each support was estimated for the different frames from the moment-rotation relationships measured from load-cells and inclinometers, respectively. Figure 4.10 shows the experimental moment-rotation relationships for the vertical loading steps, before the moment reversal occurred for left supports when the horizontal loading was introduced. Note that while the signs of the moment reactions correspond to the sign criteria adopted in the study, these moments are plotted against the absolute values of the rotations to make comparisons simpler with Figure 4.8.

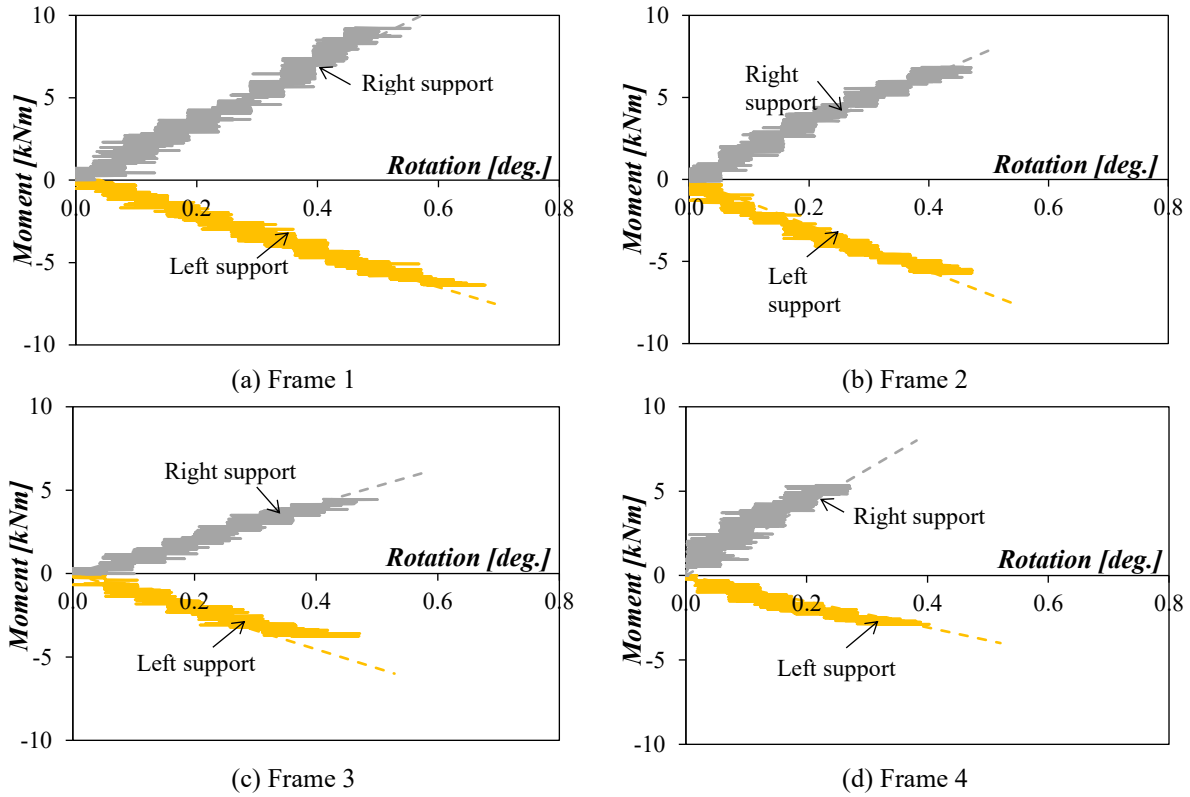

(a) Frame 1 (b) Frame 2

(c) Frame 3 (d) Frame 4

Figure 4.10. Estimation of rotational stiffness at supports from experimental moment-rotation curves.

The estimated stiffness values are reported in Table 4.2, which were also validated by means of the developed FE models (see Section 4.3.1). Results shown in Figure 4.10 and Table 4.2 suggest that the rotational stiffness of the supports was affected by different factors, including the number of bolts, the dimensions of the cross-sections comprising the columns, the existence of the ties at the right knee connection and the "pre-tensioning load" used when fastening the ties.

Table 4.2. Estimated support rotational stiffness for stainless steel frame tests.

Specimen	Left support [kNm/rad]	Right support [kNm/rad]	EN 1993-1-8 limit for rigid connection [kNm/rad]
Frame 1	1.0×10^3	1.2×10^3	8.88×10^3
Frame 2	6.4×10^2	1.2×10^3	4.46×10^3
Frame 3	4.1×10^2	4.4×10^2	4.41×10^3
Frame 4	4.4×10^2	1.2×10^3	22.23×10^3

It is worth mentioning that the initial rotational stiffness boundaries provided in clause §5.2.2 of EN 1998-1-8 (2005) "Classification by stiffness" depend on the member stiffness factors EI, where I is the second moment of area of the member. In general, the left supports showed lower stiffness than the equivalent right supports, probably caused by the presence of the ties at the right knee connections. According to clause §5.2.2.5(2) in EN 1993-1-8 (2005), column bases may be classified as rigid provided the condition $S_{j,ini} \geq 30EI_c/L_c$ is satisfied for frames without bracing system that reduces the horizontal displacement, where $S_{j,ini}$ is the initial rotational stiffness, I_c is the second moment of area of the column and L_c is the storey height of the column. Calculated limiting values for the initial

rotational stiffness for each frame are provided in Table 4.2. From these values, and considering that moment reactions were recorded for the four frames, it can be concluded that all frames presented semi-rigid column base connections.

4.2.4. Local buckling in Frame 4

Frame 4 was made from stainless steel RHS members with considerably high local slenderness values ($\bar{\lambda}_p$ =1.64, as per Table 3.6) and thus the frame failed showing a combination of local and overall instability modes. Local buckling failure at the critical upper right column section was evident at the final deformed stage of the frame (see Figure 4.2), but the moment at which local buckling started can be analytically estimated and identified from the measurements of the strain gauges attached at this critical section. From the width and thickness of the most compressed panel comprising the cross-section, the elastic critical local buckling stress $\sigma_{cr,l}$ can be calculated. From this value, the stress corresponding to the initiation of the local buckling can be calculated for the limiting slenderness between class 3 and class 4 cross-sections given in EN 1993-1-4 (2015), $\bar{\lambda}_p$= 0.65. Assuming linear elastic behaviour, the load corresponding to the initiation of local buckling at the critical cross-section located at the internal upper side of the right column is calculated, which correspond to a total vertical load value equal to 85.3 kN Frame 4 included several strain gauges at the right knee connection, at both the section corresponding to the beam (labelled as section S2) and corresponding to the column (labelled as section S6), as shown in Figure 4.2, which also permitted identifying the approximate load at which local buckling initiated. Measured strain values are shown in Figure 4.11 against the applied total vertical load for the strain gauges attached at the most compressed parts of these sections. From the curves shown in Figure 4.11 it can be appreciated that strain gauges located at the centres of the RHS faces (strain gauges S2.4 and S6.3 for the beam and column, respectively) recorded different strain values for a total vertical load level of approximately 80-90 kN, in line with the analytical estimation of the local buckling load.

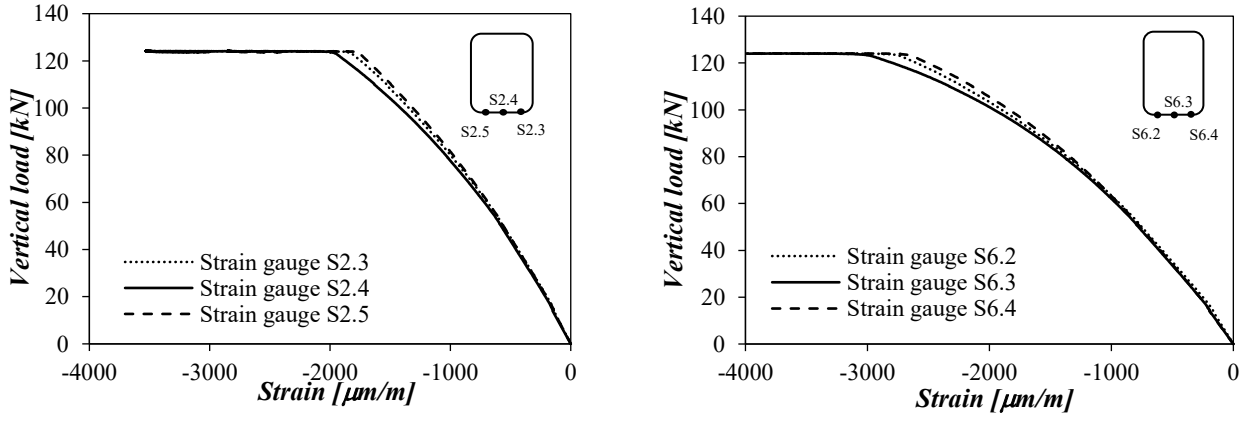

(a) (b)

Figure 4.11. Local buckling initiation at the critical cross-section for Frame 4 at (a) section S2 and (b) section S6.

4.3. Analysis and assessment of second order effects

A deeper analysis of the experimental results on stainless steel frames required the development of advanced Finite Element (FE) models due to the loading sequence adopted and the actual boundary conditions, for which no direct analytical solution was available. This section describes the FE model developed and its validation against the experimental results reported. These FE models were used to model the behaviour of the frames under different conditions to evaluate the influence of the material nonlinearity on the amplification of internal forces due to second order effects, as well as to investigate the interaction between geometric and material nonlinearities.

4.3.1. Finite element model

In order to numerically simulate the behaviour of the four stainless steel frames tested in the laboratory, FE models were developed using the general-purpose software ABAQUS (2016) and validated against the experimental results presented in this chapter. The S4R element type was chosen from the ABAQUS library (2016) to model the mid-surfaces of the cross-sections, which has been widely used in the simulation of cold-formed stainless steel members (Huang and Young 2013; Arrayago et al. 2015), with a mesh size of approximately 10 mm×10 mm. Different material properties were defined for the flat and corner regions (see Figure 2.2) of the members comprising the frames, as per the corresponding stress-strain curves measured from the tensile coupon tests reported in Table 3.2. Figure 4.12 presents a schematic summary of the details adopted in the developed FE models, including boundary conditions at supports and at the right knee connection, lateral restrains at loading sections, the application of vertical and horizontal loads and the definition of rotational and translational springs. The geometrically and materially nonlinear FE analyses were solved using the General Static method for the steps corresponding to the vertical loads, up to the maximum load values recorded during the test (see values reported in Table 4.1), and the Static Riks method for the horizontal loading steps. Surfaces at the lowest faces of the beams corresponding to the vertical loading points were connected to two reference points through kinematic couplings and two vertical point loads were introduced in these reference points (see Figure 4.12) to simulate the web crippling prevention system used in the tests. Horizontal loading was introduced by imposing a prescribed displacement at the column supports. Initial imperfections with the shape of global buckle modes were introduced in the models, which were obtained from prior linear buckling analyses and amplified according to the measured imperfection values reported in Figure 3.3. Following the experimental set-up, the response of the simulated frames was limited to the in-plane behaviour through lateral restrains assigned at the loading sections, as shown in Figure 4.12, and the beam-to-column connections were modelled through 16 mm-thick steel plates equivalent to those used in the tests.

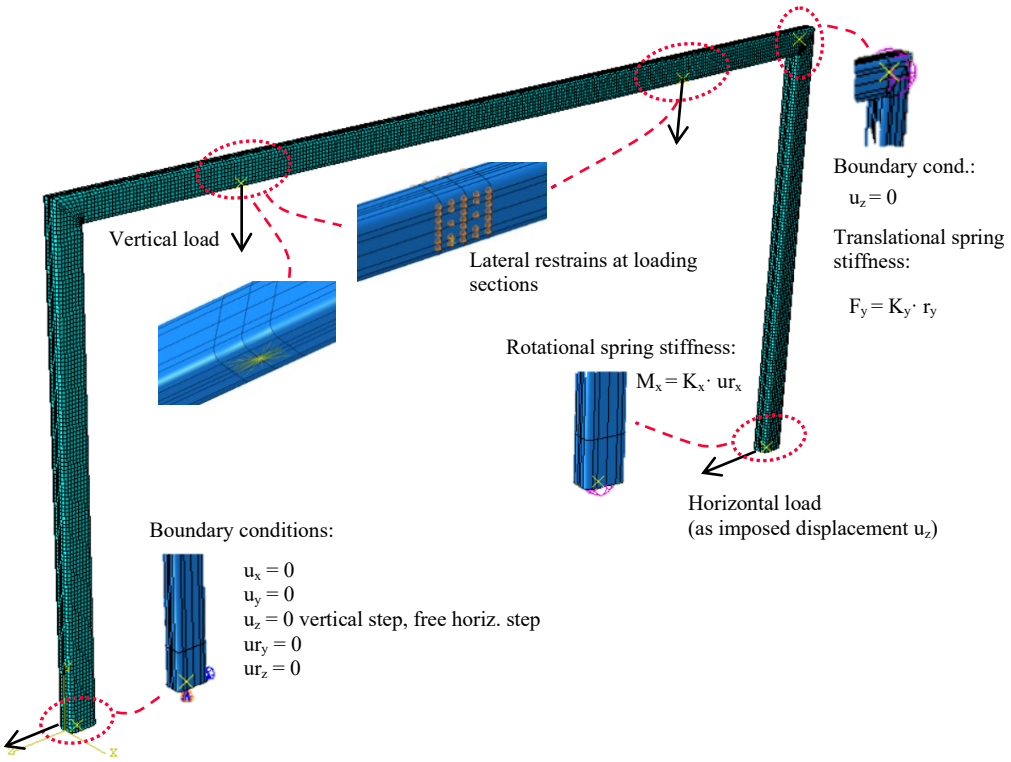

Figure 4.12. Details of the developed FE models.

From the results shown in Figure 4.8 and Figure 4.9, it was necessary to replicate the actual boundary conditions occurring during the test, which were considerably different from the theoretical conditions shown in Table 3.6. Nodes at the bottom ends of the columns were kinematically coupled and connected to two reference points, to which relevant boundary conditions were applied (see Figure 4.12). All degrees of freedom except rotations corresponding to major axis bending were restrained at support sections during the vertical loading steps, after which the horizontal in-plane displacements were released for the horizontal loading steps. The degrees of freedom corresponding to major axis bending rotations were modelled by means of elastic rotational springs, using the *Spring1 elements available in the ABAQUS library (2016) and assigning the stiffness values reported in Table 4.2. Finally, the effect of the tie connecting the frames to the reaction wall and restraining their horizontal displacement was also modelled by means of kinematical couplings between the steel plates connecting the beams and the right columns and reference points located at the centre of the steel plates. These points had the horizontal in-plane displacements restrained, and *Spring1 type elastic springs were assigned for the vertical displacement, with a stiffness equal to 5.0×10^3 kN/m for all the frames. This value was iteratively obtained from numerical simulations comparing the predicted vertical reactions to the measured experimental values, since no direct measurement of the load-displacement relationship of these points was available from the tests.

Table 4.3 presents the results of the comparison between the developed finite element models with the corresponding measurements from the frame tests presented in this chapter. Numerical-to-experimental ratios of the maximum vertical and horizontal loads F_v and F_h, and the corresponding vertical deflections and horizontal displacements d_v and d_h are reported. The predicted numerical load-displacement paths are also compared to the experimental curves in Figure 4.13 for the vertical and horizontal loading steps.

Table 4.3. Comparison between experimental and FE results for the austenitic stainless steel frames.

Specimen	$F_{v,FE}/F_{v,exp}$	$d_{v,FE}/d_{v,exp}$	$F_{h,FE}/F_{h,exp}$	$d_{h,FE}/d_{h,exp}$
Frame 1	1.00	1.04	1.00	0.99
Frame 2	1.00	1.00	1.00	0.96
Frame 3	1.00	0.97	1.00	0.98
Frame 4	1.00	1.01	1.00	1.05
Average	1.00	1.01	1.00	1.00
COV	0.000	0.023	0.000	0.034

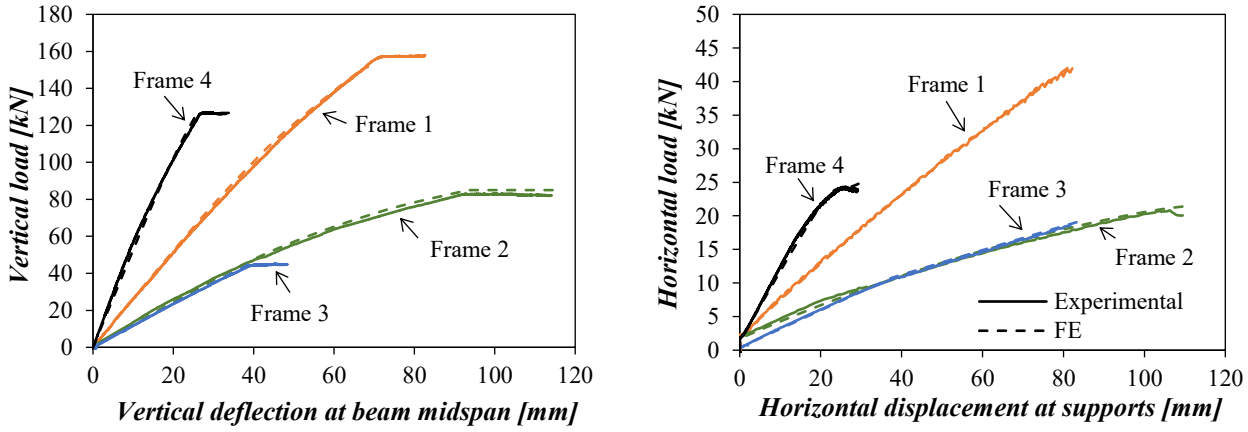

(a) (b)

Figure 4.13. Comparison of experimental and FE load-displacement curves for austenitic stainless steel frames for: (a) vertical loading step and (b) horizontal loading step.

Finally, Figure 4.14 shows the comparison of the failure modes predicted by the developed FE models with those observed from the tests, including the overall failure mode for Frame 1 and a detail of the local buckling failure at the critical section for Frame 4, showing equivalent failure modes. These results showed a good agreement between the developed numerical models and the tests, and thus the FE models were used in the further analysis of the experimental results.

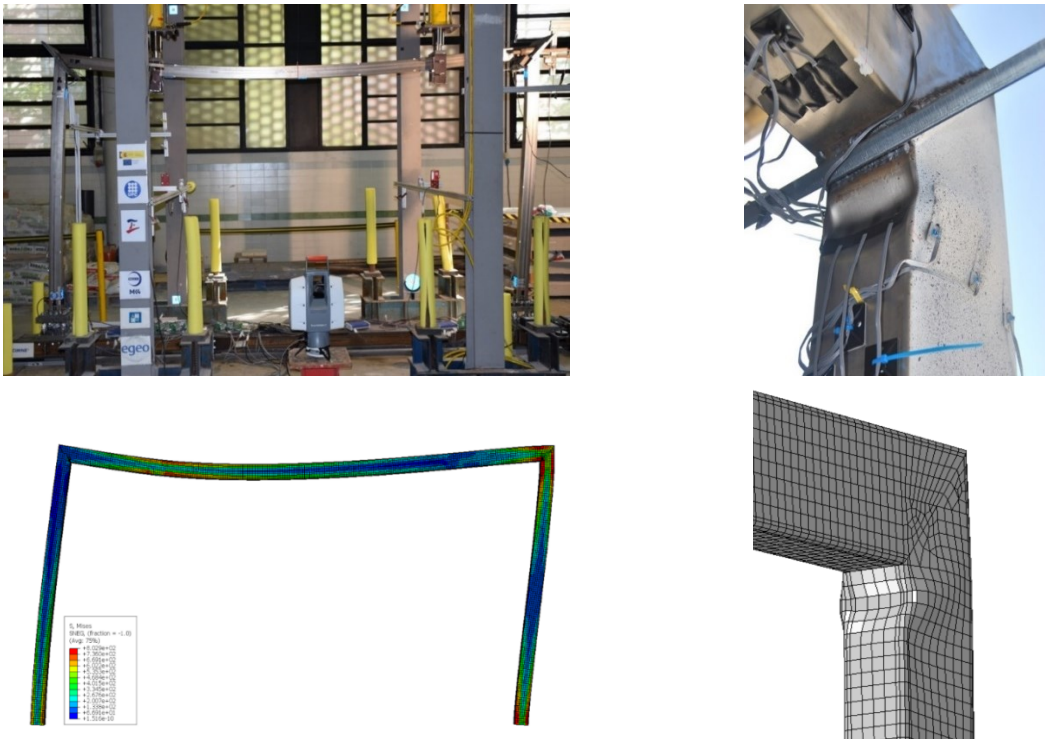

(a) (b)

Figure 4.14. Comparison of experimental failure modes with those predicted by FE models: (a) overall failure for Frame 1 and (b) detail of the local buckling failure at the critical section for Frame 4.

4.3.2. Interaction of geometric and material nonlinearities

The analysis of the interaction between geometric nonlinearities (i.e., second order effects) and material nonlinearities characterising the stress-strain response of stainless steel alloys is presented in this section for the four stainless steel frames tested. The influence of the interaction of material nonlinearities on second order effects can be evaluated by comparing the experimental load-displacement paths with the corresponding theoretical paths considering elastic or plastic material properties and first or second order analyses. Figure 4.15 and Figure 4.16 show the load-vertical deflection and load-horizontal displacement paths for different types of analyses including first order elastic analysis (LA), second order elastic analysis (GNA), first order plastic analysis (MNA) and second order plastic analysis with imperfections (GMNIA), and present the comparison with the corresponding experimental curves for the vertical and horizontal loading steps, respectively. These numerical paths were determined from the FE models described in Section 4.3.1.

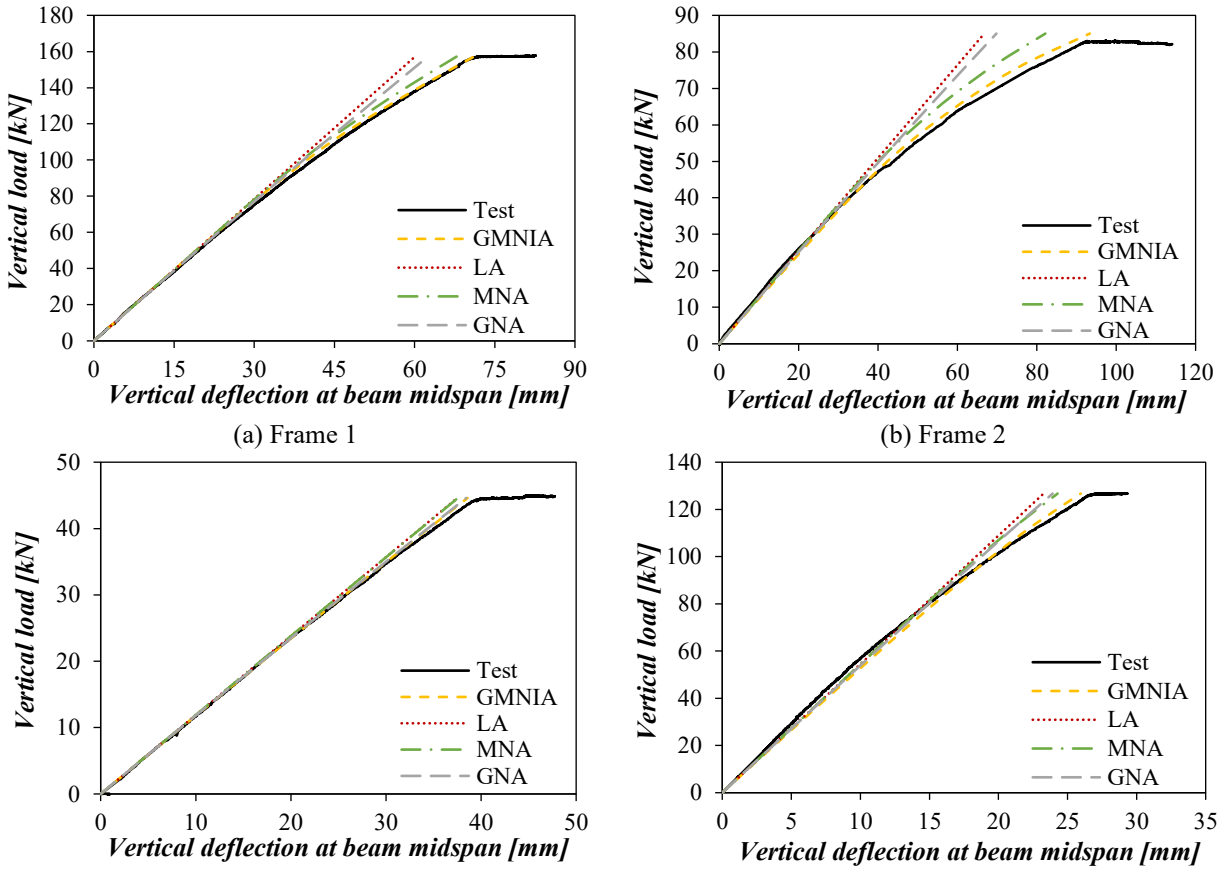

Figure 4.15. Influence of second order effects on stainless steel frame tests throughout the vertical loading step.

The comparison of experimental and different theoretical vertical load-deflection paths in Figure 4.15 indicate that the response of Frame 3 was elastic during the vertical loading step, but remarkable nonlinearities occurred for Frames 1 and 2. The comparison of the experimental (or GMNIA) and MNA load-deflection curves indicate that while in Frame 1 this nonlinearity could be attributed almost entirely to the nonlinear material response of the stainless steel alloy, the interaction between geometric and material nonlinearities occurred in Frame 2. Alternatively, the nonlinearity observed for Frame 4 at the vertical loading step can be attributed to initial imperfections, since the calculated paths for MNA, GNA and LA are practically the same. Note that Frame 4 showed the highest cross-section slenderness among the four frames, and thus the highest sensitivity to initial imperfections. The analysis of the horizontal load-displacement paths presented in Figure 4.16 shows that an interaction between material and geometrically nonlinearities occurred for Frames 1 and 2 during the horizontal loading step, with a higher proportion of the material nonlinearity. Finally, results for Frames 3 and 4 suggest that the response of these frames was more significantly affected by existing imperfections, although material and geometric nonlinearities were more pronounced during the horizontal loading step than for the vertical loading step.

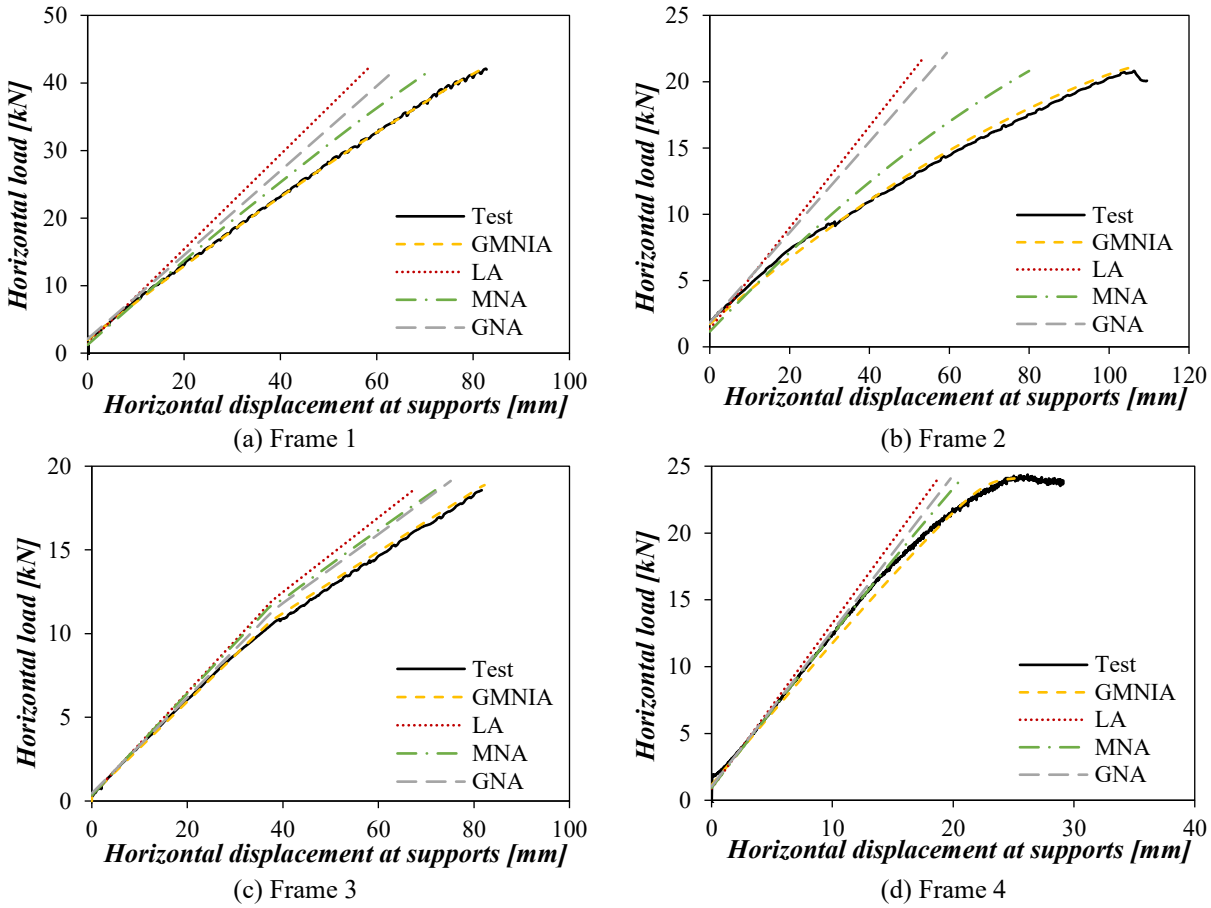

(a) Frame 1 (b) Frame 2

(c) Frame 3 (d) Frame 4

Figure 4.16. Influence of second order effects on stainless steel frame tests throughout the horizontal loading step.

4.3.3. Influence of material nonlinearity on second order effects

This last Section presents a preliminary assessment of the influence of the material nonlinearity on second order effects through the analysis of stainless steel frame tests. As mentioned in Section 2.5, recent research on stainless steel frames concluded that the degradation of stiffness due to the nonlinear material response of stainless steel alloys significantly affects the distribution of internal forces (Walport et al. 2019b). According to EN 1993-1-1 (2005), second order sway effects can be estimated from a first order analysis through the amplification of horizontal loads by the factor k_{sw} given by Eq. 2.10 for single storey frames designed on the basis of elastic global analysis (LA). Walport et al. (2019b) adapt this method for stainless steel structures, by replacing the k_{sw} for $k_{sw,ss}$ given in Eq. 2.12, and the elastic analysis by a first order plastic analysis (MNA). According to Walport et al. (2019a), the use of this MNA+$k_{sw,ss}$ approach is only adequate for those cases where sway effects are dominant.

Alternatively, Walport et al. (2019a) demonstrated that the amplification concept proposed by Lim et al. (2005) to relate loads for first order and second order analyses for a given level of deflection (given by Eq. 4.3) is more adequate for structures designed plastically, since this method is capable of capturing both sway and non-sway effects, provided that the modified elastic buckling load factor $\alpha_{cr,sw,ss}$ is

considered to account for the stiffness degradation due to plastification, as per Eq. 4.4. In these equations α_{p1} represents the first order plastic analysis load, while α_{p2} represents the second order plastic analysis load, which was taken as the experimental load in this analysis (i.e., $\alpha_{p2} = \alpha_{p,exp}$).

$$\frac{\alpha_{p2}}{\alpha_{p1}} = \frac{\alpha_{cr} - 1}{\alpha_{cr}} \quad \text{Eq. 4.3}$$

$$\frac{\alpha_{p2}}{\alpha_{p1}} = \frac{\alpha_{cr,sw,ss} - 1}{\alpha_{cr,sw,ss}} \quad \text{Eq. 4.4}$$

Frames considered in this study were tested following a two-step loading scheme and the proportion of the horizontal-to-vertical loading was not constant. Thus, the elastic buckling load factor changed during the tests. Under idealistic conditions in which the frames were free to deform following the required sway modes, the lowest (i.e., most critical) elastic buckling load factors would occur during the first vertical loading steps, when the frames would be more susceptible to second order effects. As the horizontal loading was introduced, elastic buckling load factors would increase, showing different values since the ratio of vertical-to-horizontal loads would vary for every horizontal loading increment. Therefore, different test stages need to be considered for the analysis of the experimental results. However, the adopted test configuration restrained the in-plane movement of the column supports during the vertical loading steps and thus frames were prevented from adopting the sway-mode deformed shape. In fact, during these vertical loading steps the behaviour of the frames could be considered equivalent to isolated beam or column behaviour, without sway effects being able to develop. Thus, the analysis presented in this sub-section is limited to the horizontal loading steps, which included constant vertical loads and increasing horizontal loads.

Table 4.4 reports the calculated elastic buckling load factors corresponding to two different loading stages, including the maximum vertical load $F_{v,max}$ combined with two different levels of horizontal load, $F_h/F_{h,max}$ ratios of 0.5 and 1.0 (i.e., $F_{v,max}$+0.5$F_{h,max}$ and $F_{v,max}$+$F_{h,max}$). Elastic buckling load factors α_{cr} were obtained as the lowest sway buckling modes from buckle analyses carried out from the FE models described in Section 4.3.1, assigning the appropriate vertical-to-horizontal load proportions, $F_{v,max}$+0.5$F_{h,max}$ and $F_{v,max}$+$F_{h,max}$. For Frame 1, Frame 2 and Frame 3 FE models with shell elements were used, while for Frame 4, made from a considerably slender cross-section, beam-element based FE models were adopted to obtain the sway buckle modes. Alternatively, modified elastic buckling load factors $\alpha_{cr,sw,ss}$ were calculated from Eq. 2.11, in which the K_s/K ratios were estimated from the first order plastic (MNA) and first order elastic (LA) load-lateral deflection curves at $F_h/F_{h,max}$ = 0.5 and $F_h/F_{h,max}$ = 1.0 load levels, and are reported in Table 4.4. The analysis of these results showed that $\alpha_{cr,sw}$ values increased as the proportion of the horizontal load increased for the

four frames, as they became more stable, although differences were small for the considered load levels. On the contrary, $\alpha_{cr,sw,ss}$ values decrease when the proportion of the horizontal load is increased. This can be attributed to the fact that while for the calculation of the $\alpha_{cr,sw}$ values a proportional horizontal-vertical loading was considered in the buckle analyses, the calculation of the $\alpha_{cr,sw,ss}$ factors for the specific case of the tested frames considers both proportional and two-step loading in their calculation through the $\alpha_{cr,sw}$ and K_s/K factors, respectively. In an ideal case of simultaneous vertical and horizontal loading, i.e., loading scheme usually considered in design, $\alpha_{cr,sw}$ and $\alpha_{cr,sw,ss}$ values would show the same trend for increasing horizontal load proportions. It should also be noted that the $\alpha_{cr,sw}$ and $\alpha_{cr,sw,ss}$ values reported in Table 3.6 and Table 4.4 are considerably different because the preliminary values included in Table 3.6 corresponded to the ideal boundary conditions (perfect fixed-ended and pin-ended conditions), while the values in Table 4.4 were obtained for the actual rotation restraints occurring during the tests, thus making Frames 1 and 2 more flexible and Frames 3 and 4 stiffer than in the preliminary models.

Table 4.4. Key parameters for the analysis of the influence of material nonlinearity on second order effects at different horizontal load levels.

Specimen	Horizontal load level $F_h/F_{h,max}$ = 0.5					Horizontal load level $F_h/F_{h,max}$ = 1.0				
	$\alpha_{cr,sw}$	K_s/K	$\alpha_{cr,sw,ss}$	$k_{sw,req}$	α_{p2}/α_{p1}	$\alpha_{cr,sw}$	K_s/K	$\alpha_{cr,sw,ss}$	$k_{sw,req}$	α_{p2}/α_{p1}
Frame 1	8.74	0.86	6.04	1.23	0.93	8.76	0.81	5.70	1.24	0.89
Frame 2	8.42	0.74	4.98	1.16	0.89	8.48	0.64	4.32	1.21	0.84
Frame 3	13.13	0.98	10.33	1.21	0.91	13.46	0.94	10.07	1.10	0.91
Frame 4	19.57	0.93	14.61	1.00	1.00	19.69	0.91	14.26	1.54	0.82

The accuracy of the expression for the amplification factors due to second order effects given in Eq. 2.10 and Eq. 2.12 is assessed in Figure 4.17 for the stainless steel frame test results. Required amplification factors $k_{sw,req}$, shown in Table 4.4, have been calculated from first order plastic analyses to align the sway deflections from the experimental load-lateral displacement curves for the two loading stages considered in Table 4.4, following the MNA+$k_{sw,ss}$ approach given in (Walport et al. 2019b). Calculated amplification factors $k_{sw,req}$, are plotted against the two elastic buckling load factors considered in Figure 4.17, $\alpha_{cr,sw}$ and $\alpha_{cr,sw,ss}$, along with the predicting expressions given in Eq. 2.10 and Eq. 2.12. According to the results presented in Figure 4.17, the $\alpha_{cr,sw,ss}$ factor proposed by Walport et al. (2019b) to account for the influence of material nonlinearity on the global analysis of austenitic stainless steel frames can be considered to be in good agreement with the amplification factors calculated for the tests. Note that this expression only captures amplifications due to sway effects, and thus further reductions would be necessary for Frame 4, which failed due to a combination of local buckling and sway effects.

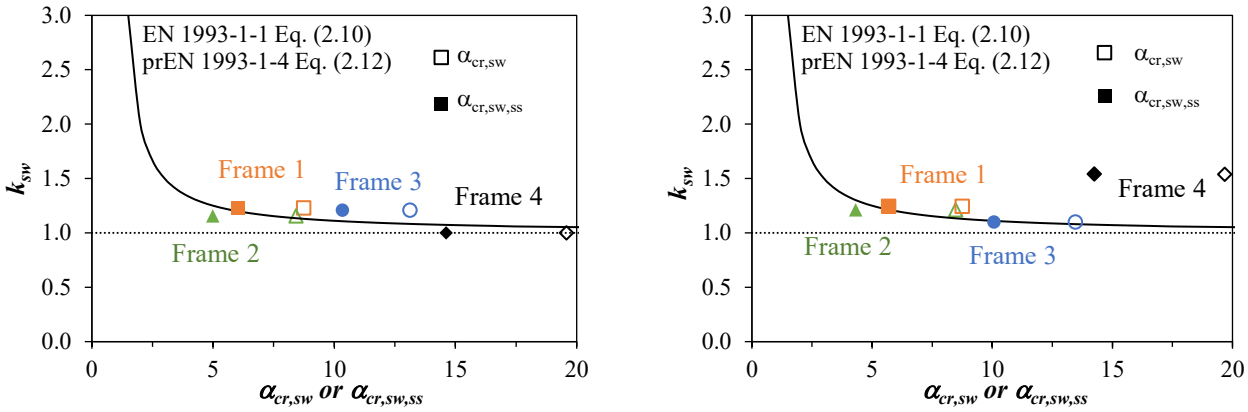

Figure 4.17. Bending moment amplification due to second order effects in stainless steel frames (a) for $F_h/F_{h,max}$ = 0.5 and (b) $F_h/F_{h,max}$ = 1.0.

Finally, Figure 4.18 plots the reduction factors for loads for first order analyses relative to the experimental loads α_{p2}/α_{p1} for the tested stainless steel frames against the corresponding $\alpha_{cr,sw}$ and $\alpha_{cr,sw,ss}$ factors. Results indicate that the $\alpha_{cr,sw,ss}$ factor is capable of capturing the stiffness reduction of the frames due to material nonlinearity and the agreement of the experimental results with the load factor reduction expression given in Eq. 4.4 is good. As for Figure 4.17, the anomalous results for Frame 4 can be explained by the local buckling interaction in the frame collapse.

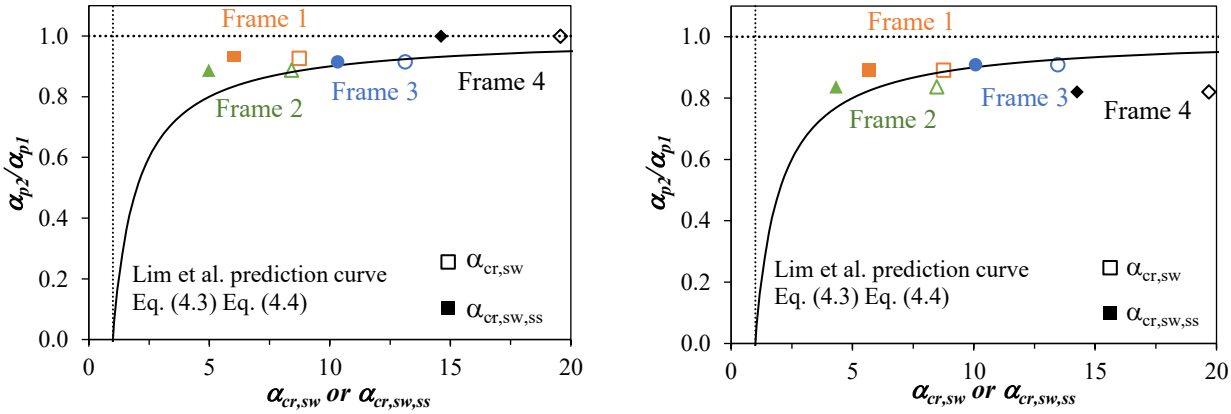

Figure 4.18. Reduction factors from first order analysis to experimental loads in stainless steel frames (a) for $F_h/F_{h,max}$ = 0.5 and (b) $F_h/F_{h,max}$ = 1.0.

4.4. Concluding remarks

This chapter presents the results of an experimental programme carried out on austenitic stainless steel frames at the Universitat Politècnica de Catalunya. The results include the evolution of total vertical and horizontal loads and reactions, moment reactions in support sections and local buckling failure in class 4 cross-sections. Advanced finite element models of the frame tests were used in conjunction with experimental results to assess the applicability of the approaches to estimate the amplification factors

due to second order effects and the reduction of loads from first order to second order analysis to stainless steel frames, characterised by a significantly nonlinear stress-strain response. Finite element models allowed to investigate the influence of geometric and material nonlinearities, and the analysis of experimental results allowed the validation of the modified $\alpha_{cr,sw,ss}$ factor proposed by Walport et al. (2019b), which was developed on the basis of numerical results. These experimental results can be used in future studies as benchmark for the validation of numerical models for subsequent analysis of the response of structural systems.

Corresponding publication: Arrayago I., González-de-León I., Real E. and Mirambell E. (2020). Tests on stainless steel frames. Part II: Results and analysis. *Thin-Walled Structures*, 157, 107006. https://doi.org/10.1016/j.tws.2020.107006

CHAPTER 5

A stiffness reduction method for the in-plane design of stainless steel frames according to prEN 1993-1-4

5.1. Introduction

The simplicity and accuracy of Stiffness Reduction Methods (SRM), among which the Direct Analysis Method (DM) proposed in AISC 360 (2022) and AISC 370 (2021) is included – see Section 2.5.2 – have driven their adaptation into the European framework (Landesmann and Batista 2005; Barszcz and Gizejowski 2007). Thus, it should be highlighted the SRM proposed by Kucukler et al. (2014, 2016) for the in-plane design of carbon steel structures and members, where the global imperfections must be included and cross-section capacities must be checked, as in the DM, but no member checks are required since the proposed stiffness reduction factors are derived from the European buckling curves given in EN 1993-1-1 (2005) and are thus implicitly present in the calibrated reduction factors.

This chapter presents an adaptation of the SRM proposed by Kucukler et al. (2014, 2016) to stainless steel members and planar structures with stocky sections considering the provisions given in the upcoming version of European standard prEN 1993-1-4 (2021). The proposed approach was developed

considering stocky Rectangular Hollow Section (RHS) members made of austenitic, ferritic and duplex stainless steel alloys, and predicts the ultimate capacity and internal forces in stainless steel structures by performing a second order elastic analysis in which the stiffnesses of the members are reduced by a set of factors to account for the effect of the spread of plasticity, residual stresses and member imperfections.

5.2. Finite element modelling

5.2.1. General

In this section, the Finite Element (FE) models used for the assessment and validation of the proposed Stiffness Reduction Method (SRM) are described. The assessment and validation required different types of analysis:

- second order plastic analysis with imperfections (GMNIA) to recreate the actual behaviour of the structural members and to obtain the target strength values (to be compared with the SRM),

- first order elastic analysis (LA) and second order elastic analysis with stiffness reduction (GNA-SR) (to implement the SRM).

The assessment was made on stainless steel columns, beams, beam-columns, and frames, and two types of numerical models were developed with the general-purpose software ABAQUS (2016). GMNIA analyses of structural members were performed on shell-type FE models capable of realistically reproducing local buckling effects, while GNA-SR and LA analyses were conducted on beam-type FE models. For computational efficiency reasons, beam-type FE models were chosen for GMNIA, LA and GNA-SR analyses of portal frames. The modified Riks method available in ABAQUS (2016) was used to solve all the FE analyses.

5.2.1.1. Benchmark models for stainless steel members

Shell FE models of stainless steel columns, beams and beam-columns were developed using four-noded shell elements, denoted as S4R (ABAQUS 2016), and used in conjunction with GMNIA analyses to estimate the actual capacity of the investigated members. The use of S4R elements together with a GMNIA analysis is widely accepted to reproduce accurately the behaviour of cold-formed steel (Li and Young 2018) and stainless steel (Theofanous and Gardner 2009; Arrayago et al. 2015b) members. After a mesh convergence study, flat regions were discretised following a uniform mesh size of 10 mm, while the curved corner regions were divided into a four-element mesh. Local imperfections were included in the form of the local buckling mode obtained from prior linear elastic eigenvalue buckling analyses with the amplitudes proposed by Gardner and Nethercot (2004b).

In the case of columns and beam-columns, initial member imperfections were also incorporated following a half sinusoidal shape using the corresponding buckling mode with an amplitude equal to $L_c/1000$, where L_c is the length of the member. Pin-ended boundary conditions were defined by means of kinematic coupling constraints between the end sections of the members and reference points contained in the plane of the cross-sections, to which boundary conditions and loading arrangements were assigned. All degrees of freedom, except the rotation around the minor axis, were constrained at the lower reference point. Similar boundary conditions were assigned to the upper reference point, but the longitudinal displacement was also allowed, and the load was applied as an imposed vertical displacement. While the reference points were located at the centroid of the cross-sections in the models for columns, in the beam-column models both reference points were shifted horizontally to simulate eccentric loads.

Beams were modelled following the four-point bending test configuration (4PB). The loading and support sections were defined as regions forced to move as rigid bodies, placed at the bottom flange of the beams and connected to reference points located at the centre of each region. A more detailed description of these regions is provided in (Arrayago et al. 2017a, 2017b). The support reference points were placed 1500 mm apart, according to the loading scheme described in (Arrayago et al. 2020b), while the loading reference points were placed at a distance of 510 mm from the ends of the members. The loads were applied as imposed vertical displacements at the loading reference points. The longitudinal and out-of-plane displacements were restrained at the midspan cross-sections, while only the vertical displacement was constrained at the support reference points.

5.2.1.2. Benchmark models for stainless steel frames

Numerical models of the frames used as benchmarks in Section 5.6 were analysed by performing a GMNIA analysis and were developed by using Timoshenko linear B21 elements (ABAQUS 2016), since S4R elements are too computationally expensive for a parametric study (Walport et al. 2019b, 2021c; González-de-León et al. 2021). Each member of the frame was divided into 100 finite elements and cross-sections were defined using the default box-section option in ABAQUS (2016). It is worth mentioning that, in practice, a much smaller number of finite elements than the 100 elements adopted in this study can be used to model individual structural elements. As suggested by Kucukler et al. (2016), four elements may be sufficient for sway structures, while sixteen elements may be required for non-sway structures. Initial global imperfections were included through notional horizontal loads assuming an out-of-plumb angle of 1/200 according to EN 1993-1-1 (2005), while the member imperfections of the columns were introduced by directly modifying the position of the nodes following a half-sine wave shape with an amplitude of $L_c/1000$ in the most detrimental direction. Finally, both fixed- and pin-ended boundary conditions were adopted at the supports of the columns, while vertical and horizontal concentrated loads were applied simultaneously at the top of the columns (see Figure 5.9).

5.2.1.3. Models for stainless steel members and frames using the Stiffness Reduction Method

For all the FE models carried out using the Stiffness Reduction Method (including columns, beams, beam-columns, and frames), LA and GNA-SR analyses were performed on models using Timoshenko linear in-plane beam elements B21 (ABAQUS 2016). In the case of GNA-SR analyses, the cross-section geometry was defined using the generalized-section available in ABAQUS (2016). Generalized-sections allow reducing the moment of inertia (I) without modifying the nominal cross-section area (A) and the material properties, i.e., the Young's modulus (E), so that the flexural stiffness (EI) is modified while the axial stiffness of the members (EA) remains constant (Kucukler et al. 2016). Members were divided into 100 elements. Although the proposed stiffness reduction factor for columns already incorporates the effect of member imperfections, to ensure that the geometrical nonlinearities were triggered in the column models, an imperfection amplitude of 0.001% L_c was incorporated following a half sinusoidal shape (Shen and Chacón 2020). In the case of frames, notional horizontal loads were applied assuming a drift angle of 1/200, as recommended in EN 1993-1-1 (2005), in both LA and GNA-SR analyses. The loads were applied as imposed displacements and the boundary conditions were defined following the configurations described above.

5.2.2. Material model

In both shell and beam FE models, nonlinear material properties were defined by assigning user-defined true stress-plastic strain curves according to the two-stage Ramberg-Osgood material model shown in Eq. 2.1 and Eq. 2.2.

The study covered austenitic, ferritic and duplex stainless steel RHS members. Table 5.1 summarises the key weighted average material properties considered, which were calculated as given in Section 2.3 from the material properties reported in Table 3.2 for the flat and corner regions of stainless steel RHS sections. Weighted average material properties were assigned to all the FE models to facilitate the comparison between GMNIA and GNA-SR analyses.

Table 5.1. Key material characterisation parameters for parametric studies.

Stainless steel	E [GPa]	f_y [MPa]	f_u [MPa]	ε_u [mm/mm]	n	m
Austenitic	198	428	650	0.39	5.5	3.7
Ferritic	185	498	520	0.06	11.4	3.1
Duplex	201	707	874	0.36	5.6	4.9

5.2.3. Validation of FE models

Numerical models for structural members (columns, beams and beam-columns) were validated using shell-type FE models, while the numerical models for portal frames were validated using both shell-type and beam-type FE models, as described in this section.

The FE models of stainless steel members used in the present study were validated against the experimental results on cold-formed EN 1.4301 austenitic beams and columns with RHS cross-sections reported in (Arrayago et al. 2020b) and summarised in Table 3.4 and Table 3.5, respectively. The accuracy of the FE model for columns was assessed by comparing the results of the GMNIA analysis with those of columns subjected to pure compression under pin-ended boundary conditions. The cross-sections were modelled using S4R elements and divided into corner regions and flat regions (see Figure 2.2); the measured material properties given in Table 3.2, using the model given in Eq. 2.1 and Eq. 2.2, were assigned to each region. For this particular validation, the reference points connected to the end cross-sections were placed at a distance of 50 mm, following the experimental set-up (Arrayago et al. 2020b). Local and global imperfections were included by using the corresponding buckling modes and the measured amplitudes reported in Table 3.1. To validate the numerical models of the beams, experimental results from four-point bending tests, with the stainless steel RHS sections bent around their major axis, were used. The same type of S4R elements and material models used for columns were also employed for beams. The test set-up coincided with that described above for the numerical models of beams, whereby the distance between the support reference points was 1500 mm and between the load reference points, 510 mm. Local imperfections were included using the pattern given by the relevant buckling modes and with the amplitudes measured from the test specimens, as given in Table 3.1. Figure 5.1 presents the experimental load-lateral deflection curves of columns under pure compression around major (S2) and minor (S3) axis and the experimental load-midspan deflection curves for beams subjected to major axis bending, compared to the corresponding FE curves. The results demonstrate that the numerical analysis approach used in the present study can accurately simulate the actual behaviour of stainless steel members. It was observed that the failure modes also concurred. Therefore, the use of the numerical analysis approach presented herein is appropriate to obtain reference data to be compared with the results predicted from the proposed Stiffness Reduction Method.

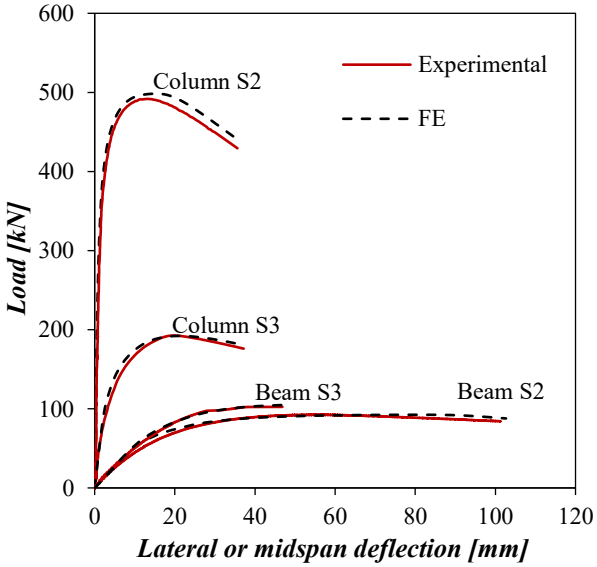

Figure 5.1. Comparison of FE load-deflection curves for S2 (RHS 120×100×4) and S3 (RHS 120×40×4) austenitic stainless steel columns and four-point bending beams with the experimental results reported in (Arrayago et al. 2020b).

The accuracy of the shell-type - (Section 5.2.1.2) and beam-type (Section 5.2.1.3) FE models of stainless steel frames was assessed by comparing the results obtained from a geometrically and materially nonlinear analysis with imperfections (GMNIA) to the experimental ultimate loads, deflections and displacements shown by the Frame 1 and reported in Chapter 4. For this purpose, the position of the vertical loads shown by the frames of this study (see Figure 5.9) was slightly modified to be equivalent to the experimental one (see Figure 3.6(a). Likewise, only for the validation purposes, the loading scheme was divided into two steps (as explained in Section 3.4.1). The characteristics of these steps are given in Section 4.3.1. In order to reproduce the stiffness of the actual experimental boundary conditions, boundary conditions for both shell- and beam-type models where defined by means of springs elements. The values of stiffness assigned to the spring elements are reported in Section 4.2.3.2. In the case of shell-type FE model, the flat and corner material properties defined in Table 3.2 for CS1 were assigned to the corresponding areas, while in the case of beam-type FE model, the weighted average material computed as given in Figure 2.2 was assigned to the whole cross-section. In-plane initial geometric imperfections were defined by means of the first sway buckling mode obtained from prior buckle analyses, which was dominant, with an amplitude according to EN1993-1-1 (2005) and equal to 8.6 mm, since the measured initial imperfection resulted to be too small. Note that the shell-type FE model corresponds to the numerical model given in Section 4.3.1.

Figure 5.2(a) shows the total vertical load-midspan deflection responses for the beam-type FE model, the shell-type FE model and the tested frame. Note that the total vertical load-midspan deflection curve for the shell FE model is closer to the experimental curve than the response of the beam FE model. This is attributed to the more accurate geometric definition of the cross-sections allowed in the shell element models, since box-section beam type sections available in the ABAQUS (2016) do not account for the rounded corner areas. The horizontal load-horizontal displacement at column support curves are represented in Figure 5.2(b). From Figure 5.2, it can be concluded that both FE models are capable of accurately reproducing the experimental behaviour for frame S1.

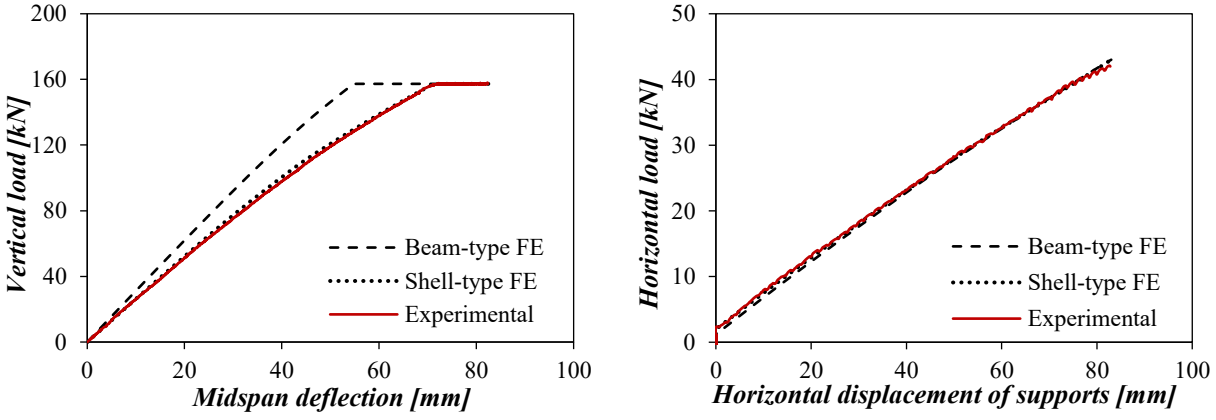

(a) (b)

Figure 5.2. Comparison of experimental and numerical (a) vertical load-midspan deflection and (b) horizontal load-horizontal displacement curves.

5.3. Stiffness reduction under axial loading

In this section, the development of the stiffness reduction factor τ_N accounting for the loss of stiffness due to geometrical imperfections, residual stresses and the spread of plasticity in stainless steel columns under axial loading is presented, as well as its validation by the comparison of GNA-SR and GMNIA results.

5.3.1. Derivation of stiffness reduction factor τ_N

The stiffness reduction factor τ_N of a column subjected to axial loading was derived from the European buckling curves specified in the next version of the prEN 1993-1-4 (2021) standard and following the methodology proposed by Kucukler et al. (2014) for carbon steel columns. The stiffness reduction factor τ_N is the ratio between the inelastic and the elastic critical buckling loads of the member, $N_{cr,i}$ and N_{cr} respectively, and can be expressed in terms of the flexural buckling reduction factor χ and the member slenderness $\bar{\lambda}$, as shown in Eq. 5.1.

$$\tau_N = \frac{N_{cr,i}}{N_{cr}} = \chi\bar{\lambda}^2 \qquad \text{Eq. 5.1}$$

The buckling curves to calculate the flexural buckling reduction factor χ prescribed in the latest edition of the Structural Design Manual (SCI 2017) and in the upcoming version of prEN 1993-1-4 (2021) are based on the Ayrton-Perry approach (Maquoi and Rondal 1978). The buckling reduction factor is given by Eq. 5.2, where the effects of the residual stresses and member imperfections are included in the auxiliary parameter ϕ defined in Eq. 5.3. The values of the imperfection factor α and the limiting slenderness $\bar{\lambda}_0$ depend on the type of cross-section, stainless steel family and the buckling axis considered. For the specific case of cold-formed stainless steel RHS columns, the imperfection factor adopts a value of α=0.49 (prEN 1993-1-4 2021; SCI 2017), while the limiting slenderness is $\bar{\lambda}_0$=0.3 for austenitic and duplex stainless steels, and $\bar{\lambda}_0$=0.2 for ferritic alloys.

$$\chi = \frac{1}{\phi + \sqrt{\phi^2 - \bar{\lambda}^2}} \qquad \text{but } \chi \leq 1.0 \qquad \text{Eq. 5.2}$$

$$\text{where } \phi = 0.5\left[1 + \alpha\left(\bar{\lambda} - \bar{\lambda}_0\right) + \bar{\lambda}^2\right] \qquad \text{Eq. 5.3}$$

The reduction function τ_N proposed herein and given in Eq. 5.4 and Eq. 5.5 is adopted from Kucukler et al. (2014), which in turn comes from the European buckling curves for carbon steel, but assumes the imperfection factor and limiting slenderness values calibrated for stainless steel alloys (prEN 1993-1-4 2021). It is noteworthy that the strength prediction resulting from applying the proposed reduction factor τ_N and performing a GNA-SR analysis up to failure is identical to that estimated from the European buckling curve $N_{b,Rk}$. Hence, the maximum column resistance estimated by the proposed SRM is the

squash load of the gross cross-section N_{pl}, and the applied axial load N_{Ed} in Eq. 5.4 and Eq. 5.5 should not be greater than the characteristic column strength $N_{b,Rk}$.

$$\tau_N = \frac{4\psi^2}{\alpha^2 \frac{N_{Ed}}{N_{pl}}\left[1+\sqrt{1-4\psi\frac{(N_{Ed}/N_{pl}-1)}{\alpha^2\, N_{Ed}/N_{pl}}}\right]^2} \quad \text{but} \quad \tau_N \leq 1.0 \qquad \text{Eq. 5.4}$$

$$\text{where} \quad \psi = 1 + \bar{\lambda}_0 \alpha \frac{N_{Ed}}{N_{pl}} - \frac{N_{Ed}}{N_{pl}} \qquad \text{Eq. 5.5}$$

From the relationship presented in Eq. 5.1, it is possible to derive stiffness reduction functions that consider imperfections and residual stresses based on any buckling curve. For assessment purposes, the stiffness reduction factors derived from the buckling curves proposed in AISC 370 (2021) for RHS stainless steel columns were also calculated. Figure 5.3 shows the comparison of the stiffness reduction functions specifically obtained herein for austenitic and duplex RHS columns from the buckling curves in prEN 1993-1-4 (2021) and AISC 370 (2021). As shown in Figure 5.3, both stiffness reduction functions are very similar, as the flexural buckling curves prescribed in AISC 370 (2021) have been recently revised to provide strength predictions comparable to those predicted with the European curves (Meza and Baddoo 2021). These new buckling curves provide similar or slightly higher strength predictions than the equivalent European curves and show a larger yield plateau due to the less strict reliability requirements stipulated for the AISC 370 specification. The new expression for the AISC 370 buckling curves is defined in three stages depending on the slenderness or stress ratios. For high slenderness ratios, i.e., low N_{Ed}/N_{pl} ratios, the AISC 370 design buckling stress is a constant proportion of the elastic buckling stress, resulting in the plateau shown in Figure 5.3 and which adopts a value of 0.82 for austenitic and duplex RHS members.

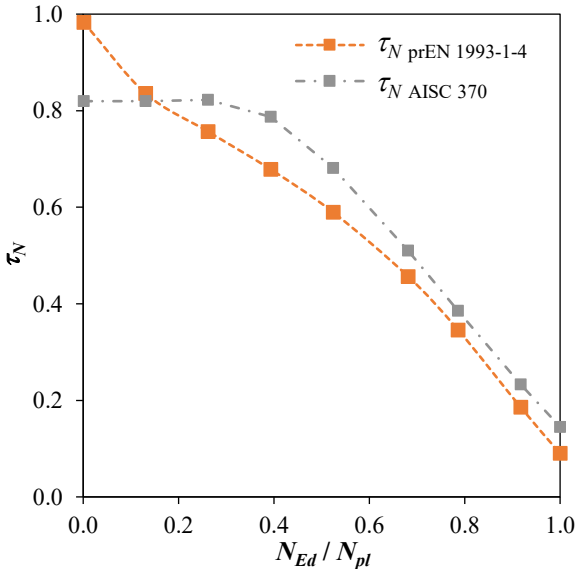

Figure 5.3. Comparison between the proposed stiffness reduction factor τ_N and the stiffness reduction factor derived from AISC 370 (2021) buckling curves for an austenitic stainless steel column.

5.3.2. Application of the proposed stiffness reduction factor τ_N

The ability of the proposed stiffness reduction factor τ_N based on the European buckling curves for stainless steel RHS columns to consider the effects of material nonlinearities, initial imperfections and residual stresses was evaluated by numerical FE analyses. For this, a range of simply supported columns made of the austenitic, ferritic and duplex materials reported in Table 5.1 were studied. The geometry of the cross-section considered in the assessment corresponds to the section RHS1 shown in Table 5.2, where H is the total height of the cross-section, B is the total width, t is the wall thickness and R_{ext} is the external corner radius. Local slenderness values under pure compression $\bar{\lambda}_{p,c}$ are also reported. Table 5.2 also includes the geometric characteristics of the other cross-sections used in this study (RHS2 and RHS3), and the local slenderness values under major axis bending $\bar{\lambda}_{b,y}$ and minor axis bending $\bar{\lambda}_{b,z}$ for the three cross-sections. All local slenderness $\bar{\lambda}_{p,i}$ values reported in Table 5.2 were calculated as reported in Section 2.4.2. Finally, the assessment presented in this section considered different stainless steel columns with varying member lengths, which corresponded to member slenderness $\bar{\lambda}$ values that ranged from 0.25 to 2.00. In total, 8 columns were analysed for each stainless steel family.

Table 5.2. Cross-section geometric properties and local slenderness values under different load cases.

Cross-section	H [mm]	B [mm]	t [mm]	R_{ext} [mm]	Stainless steel	$\bar{\lambda}_{p,c}$	$\bar{\lambda}_{p,by}$	$\bar{\lambda}_{p,bz}$
RHS1	90.0	76.0	6.0	9.5	Austenitic	0.32	0.25	0.29
					Ferritic	0.36	0.28	0.33
					Duplex	0.41	0.32	0.37
RHS2	125.0	76.0	6.0	9.5	Austenitic	0.43	0.25	0.41
					Ferritic	0.48	0.28	0.46
					Duplex	0.55	0.32	0.52
RHS3	146.0	76.0	6.0	9.5	Austenitic	0.50	0.26	0.48
					Ferritic	0.56	0.29	0.54
					Duplex	0.64	0.33	0.61

The proposed reduction factor τ_N was used to estimate the ultimate strength of the investigated columns by conducting a GNA-SR analysis and its accuracy was assessed by comparing these estimations with the ultimate capacities of the same columns predicted from a GMNIA analysis. The ultimate strength of the columns was estimated as the applied load when the most loaded cross-section reached its cross-section capacity in the GNA-SR analyses proposed in the present study. The ultimate cross-section capacity was determined using the Continuous Strength Method (CSM) interaction equation for RHS cross-sections under combined axial load plus uniaxial bending provided in prEN 1993-1-4 (2021), but slightly modified to limit the axial forces up to the squash load of the gross cross-section N_{pl}, since the buckling curves from which the factor τ_N was derived are limited to N_{pl}. Since RHS1 is a stocky cross-section, the ultimate cross-section resistance of the columns analysed through the GNA-SR proposed herein is that shown in Eq. 5.6 (prEN 1993-1-4 2021). The parameter a in Eq. 5.6 depends on the axis

of bending and it corresponds to $a = a_w = (A - 2bt)/A$ when calculating the major axis strength and $a = a_f = (A - 2ht)/A$ for minor axis bending, where b and h are the internal width and height of the cross-section, respectively, and A is the cross-sectional area. In the case of RHS sections with local slenderness values $\bar{\lambda}_p$>0.60, the linear interaction equation given in Eq. 5.7 might be used. Note that, for comparison purposes, partial safety factors for cross-section γ_{M0} and member γ_{M1} resistances are equal to unity in this study.

$$M_{Ed} \leq M_{N,csm} = M_{csm} \frac{1 - \left(N_{Ed}/N_{pl}\right)}{1 - 0.5a} \leq M_{csm} \qquad \text{for } \bar{\lambda}_p \leq 0.60 \qquad \text{Eq. 5.6}$$

$$\frac{N_{Ed}}{N_{pl}} + \frac{M_{Ed}}{M_{csm}} \leq 1 \qquad \text{for } \bar{\lambda}_p > 0.60 \qquad \text{Eq. 5.7}$$

The results obtained using the proposed stiffness reduction factor τ_N for stainless steel columns are plotted in Figure 5.4 along with those corresponding to the stiffness reduction factors derived from the buckling curves proposed in AISC 370 (2021), as discussed in Section 5.3.1. The discrepancies observed between the GNA-SR and GMNIA results are associated with the accuracy or adjustment of the buckling curves considered to the specific stainless steel materials considered in the present study. Both AISC 370 (2021) and prEN 1993-1-4 (2021) buckling curves were calibrated using a large number of data and provide accurate predictions of the ultimate buckling strengths. Since the proposed τ_N factor was directly obtained from the European buckling curves, the GNA-SR$\tau_{N\,\text{prEN 1993-1-4}}$ curves shown in Figure 5.4 overlap the prEN 1993-1-4 (2021) buckling curves. Hence, the accuracy of the proposed τ_N factor will depend on the fit of the flexural buckling curves to the ultimate member resistance of stainless steel columns. Based on the results shown in Figure 5.4, it can be concluded that the austenitic buckling curve prescribed in prEN 1993-1-4 (2021) was in good correlation with the studied austenitic cases, while less accurate fits were found for the ferritic and duplex materials studied.

For the cases considered in this section, i.e., members under pure compression, it is possible to approximate the inelastic buckling strength of the column by reducing the elastic critical buckling load N_{cr} by τ_N. Furthermore, equivalent results may be obtained when a Linear Buckling Analysis with Reduced Stiffness (LBA-SR) is carried out. The latter approach is especially recommended for columns subjected to non-uniform axial forces, with non-uniform cross-section or various boundary conditions (Kucukler et al. 2014).

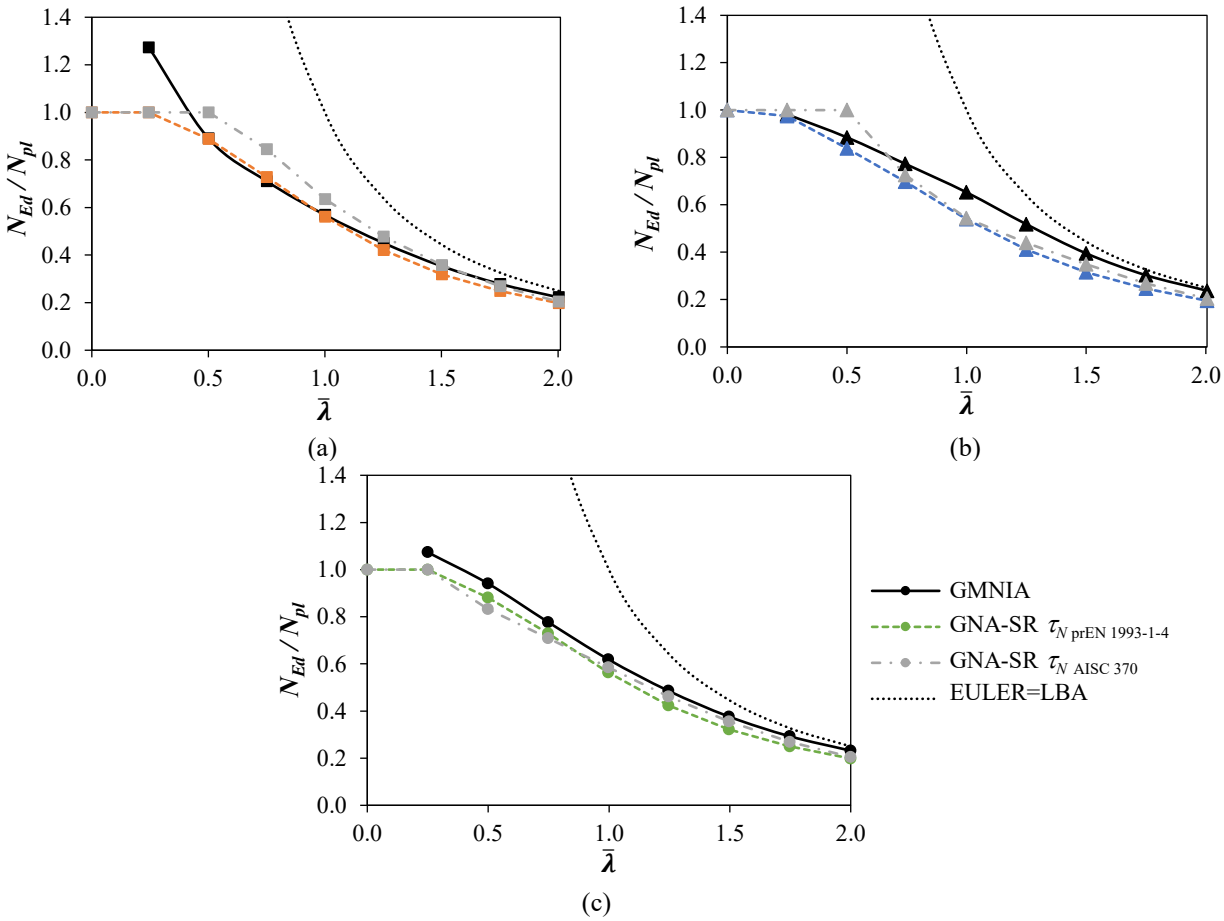

Figure 5.4. Comparison of the results obtained from different GNA-SR analyses with GMNIA predictions on (a) austenitic, (b) ferritic and (c) duplex stainless steel simply supported columns.

5.4. Stiffness reduction under bending

In this section, the derivation of the stiffness reduction function τ_M for estimating the yield distribution effects on the structural behaviour of beams under pure bending through a GNA-SR analysis is presented. Application of the derived τ_M factor and the assessment of the results are also provided.

5.4.1. Derivation of stiffness reduction factor τ_M

In out-of-plane restrained beams subjected to constant bending moment, the stiffness reduction function τ_M estimates the spread of plasticity in the cross-section and, therefore, it depends on the cross-sectional geometry, material response and residual stresses, but not on the initial geometrical imperfections (Kucukler et al. 2014). The reduction factor τ_M corresponding to a certain bending moment M_{Ed} can be expressed as the ratio between the tangent flexural stiffness at a particular bending moment value EI_t, and the initial flexural stiffness EI. As shown in Eq. 5.8, the tangent flexural stiffness of a member at any given bending moment value EI_t corresponds to the derivation of $dM_{Ed}/d\kappa$, where κ is the curvature; in other words, to the slope of the moment-curvature curve at M_{Ed}.

$$\tau_M = \frac{EI_t}{EI} = \frac{\frac{dM_{Ed}}{d\kappa}}{EI} \quad \text{Eq. 5.8}$$

Real and Mirambell (2005) proposed an analytical expression to describe the bending moment-curvature relationship of stainless steel beams subjected to bending moment up to a moment M_{02}, which corresponds to the moment at which the maximum normal tensile stress is equal to the yield stress f_y. Note that for materials showing nonlinear stress-strain responses such as stainless steels, M_{02} is different from the elastic bending moment of the section and can be estimated by integrating the nonlinear stress distribution of the cross-section (Real and Mirambell 2005). The expression approximates the cross-sectional curvature as a combination of elastic and plastic components. While the elastic component corresponds to the ratio of the applied moment M_{Ed} and the initial flexural stiffness EI, the plastic component is governed by the definition of the plastic curvature $\kappa_{p,02}$ for M_{02}. Recently, Shen and Chacón (2020) proposed a stiffness reduction function for stainless steel RHS beams based on Real and Mirambell's approximation. However, the proposed function was only valid up to a moment equal to the elastic moment M_{el}, so a second stage was added to the τ_M formula to consider nonlinear stress distributions up to the plastic moment M_{pl} (Shen and Chacón 2020).

In an effort to simplify this approach, the alternative expression for the calculation of the curvature up to M_{pl} given in Eq. 5.9 is proposed in this study. Eq. 5.9 is based on Real and Mirambell's expression but, while the elastic component is the same, the plastic component uses the plastic moment M_{pl} instead of M_{02}, and the plastic curvature κ_p corresponding to M_{pl} is adopted (instead of the $\kappa_{p,02}$ curvature). The plastic curvature κ_p, defined in Eq. 5.10, can be determined as the difference between the curvatures corresponding to the plastic M_{pl} and elastic M_{el} bending moments. These curvatures are calculated based on the strains and the cross-section half-heights, i.e., $\kappa = \varepsilon/(H/2)$. While the strain for M_{el} is straightforward, that for M_{pl} can be accurately estimated as $3\varepsilon_y$ for RHS, following the recommendations in (Arrayago et al. 2017a; Arrayago and Rasmussen 2021a).

$$\kappa = \frac{M_{Ed}}{EI} + \kappa_p \left(\frac{M_{Ed}}{M_{pl}}\right)^{n-1} \quad \text{Eq. 5.9}$$

$$\kappa_p = \frac{2}{H}\left(3\varepsilon_y - \varepsilon_y\right) \quad \text{Eq. 5.10}$$

By deriving Eq. 5.9 with respect to κ, substituting the resulting expression into Eq. 5.8 and assuming $2\varepsilon_y EI/H = M_{el}$, the stiffness reduction factor τ_M shown in Eq. 5.11 is obtained.

$$\tau_M = \left[1 + (n-1)\frac{2M_{el}}{M_{pl}}\left(\frac{M_{Ed}}{M_{pl}}\right)^{n-2}\right]^{-1} \quad \text{Eq. 5.11}$$

The τ_M factor estimated by Eq. 5.11 has been assessed against the τ_M value derived from the numerical moment-curvature relationship obtained through a GMNIA analysis. Simply supported beams subjected to four-point loading conditions and bending around minor axis, as described in Section 5.2, were considered, and corresponded to the three stainless steel alloys shown in Table 6.1 and the cross-sections RHS1, RHS2 and RHS3 presented in Table 5.2. Bending moment-curvature relationships were determined at the midspan sections from the FE models, where the bending moment distribution is constant, and curvatures were calculated from Eq. 5.12, where u_{av} is the average value of the deflections at the loading sections, u_2 is the deflection at the midspan section and L_p is the distance between applied loads (Rasmussen and Hancock 1993b).

$$\kappa = \frac{8(u_2 - u_{av})}{4(u_2 - u_{av})^2 + {L_p}^2} \quad \text{Eq. 5.12}$$

Figure 5.5 shows the comparison between the stiffness reduction factor τ_M given in Eq. 5.11 for a RHS2 austenitic beam against the flexural stiffness reduction factor derived from GMNIA results. Suggested by Shen and Chacón (2020), and as demonstrated in Figure 5.5, substituting the term $(n-1)$ in Eq. 5.11 by $(n-1)/2$ provides a better fit of the analytical expression of τ_M. Consequently, the proposed stiffness reduction function τ_M is given in Eq. 5.13. As shown in Figure 5.5, the fit obtained with Eq. 5.13 is excellent up to M_{el}, and becomes poorer beyond this value due to the strain hardening of the material.

$$\tau_M = \left[1 + (n-1)\frac{M_{el}}{M_{pl}}\left(\frac{M_{Ed}}{M_{pl}}\right)^{n-2}\right]^{-1} \quad \text{Eq. 5.13}$$

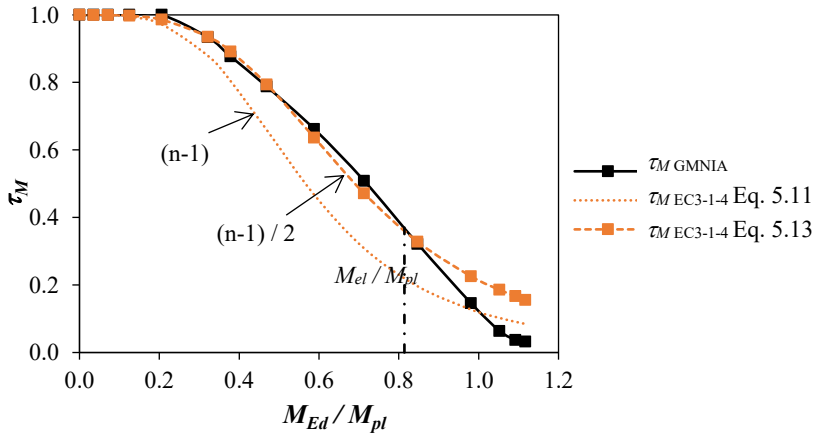

Figure 5.5. Assessment of the proposed stiffness reduction factor τ_M for austenitic stainless steel beams under constant bending moment (RHS2 cross-section).

5.4.2. Application of the proposed stiffness reduction factor τ_M

The accuracy of the proposed stiffness reduction function given in Eq. 5.13 was verified by means of FE analyses. A parametric analysis of simply supported beams following the four-point bending test configuration (4PB) was carried out. Beams bent about their minor axes, were 1500 mm long and vertical loads were applied at a distance of 510 mm away from the supports. Different materials corresponding to the three stainless steel families defined in Table 6.1 were analysed, considering three cross-sections (RHS1, RHS2 and RHS3 sections presented in Table 5.2) with varying local slenderness values for each material. Moment-curvature relationships were determined at the midspan sections as explained above. Figure 5.6 shows the comparison of the proposed stiffness reduction factor τ_M given in Eq. 5.13 against the corresponding GMNIA results for austenitic, ferritic and duplex simply supported beams with RHS1 cross-section. The largest differences observed between the GMNIA and GNA-SR curves are in the cases of austenitic and duplex alloys. These discrepancies can be explained by the existing resistance reserve after M_{el} due to the strain hardening of the material, which the proposed stiffness reduction function τ_M does not take into account.

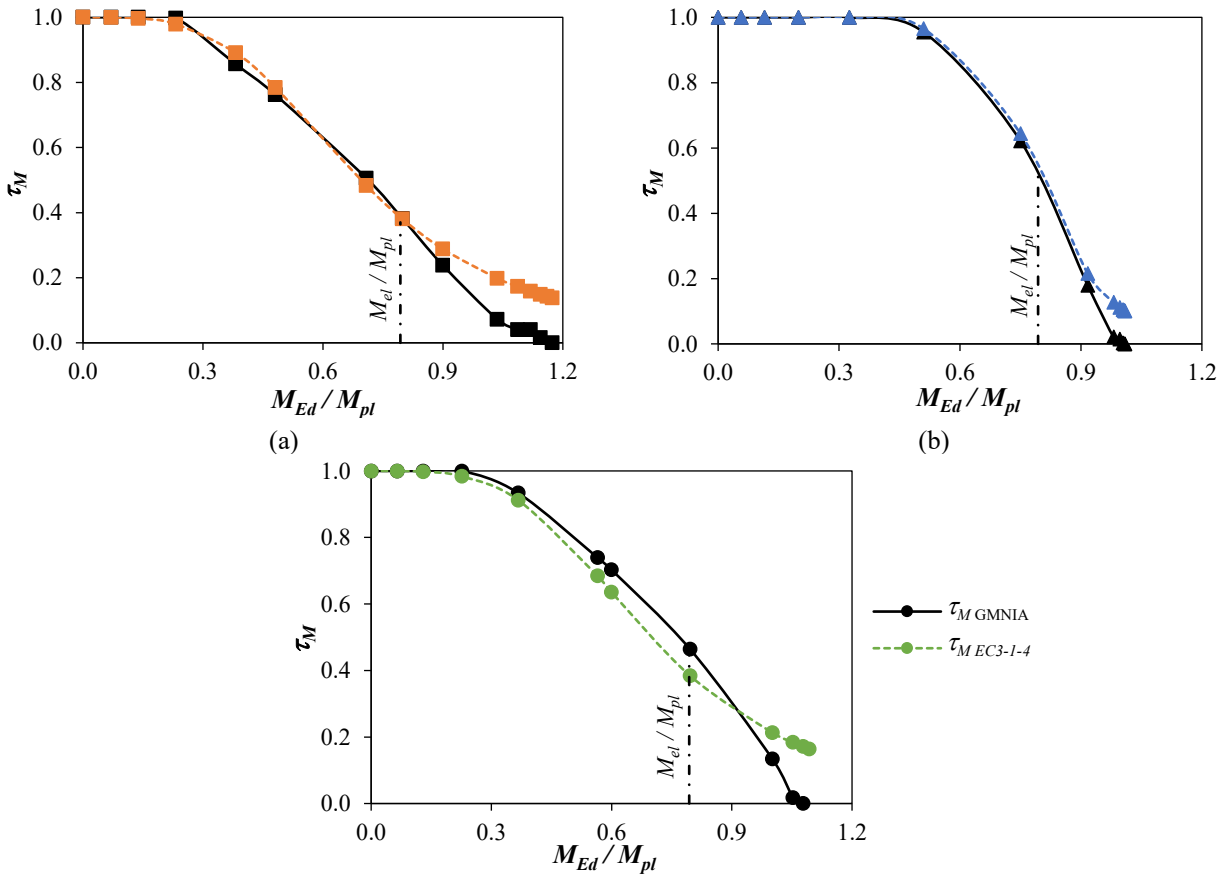

Figure 5.6. Evaluation of the proposed reduction function τ_M for (a) austenitic, (b) ferritic and (c) duplex stainless steel simply supported beams under minor axis bending (RHS1 cross-section).

5.5. Stiffness reduction under combined axial load and bending

In this section, a stiffness reduction function τ_{NM} that considers the detrimental effects of material nonlinearities, residual stresses and initial imperfections in stainless steel members under combined loading is presented. Results for a variety of beam-columns analysed according to the Stiffness Reduction Method (SRM) using the proposed τ_{NM} factor are also shown and assessed against the capacity of stainless steel benchmark members subjected to a combination of axial load and uniform bending. Finally, the consideration of different lineal moment distributions along the member length is addressed.

5.5.1. Proposal of stiffness reduction factor τ_{NM}

Kucukler et al. (2014) proposed a stiffness reduction factor τ_{NM} to take into account the effect of yielding in I-section (IPE and HE) carbon steel beams-columns subjected to a combination of axial load and uniform bending. The τ_{NM} expression proposed by Kucukler et al. (2014) depends on two factors, which in turn depend on the cross-sectional aspect ratio H/B ($H/B \leq 1.2$ or >1.2) and the axis of buckling and bending. The cross-sections studied in this research are stainless steel rectangular hollow cross-sections (RHS) with $H/B>1.2$. Since RHS cross-sections subjected to combined axial and uniaxial bending moment for both major and minor axes behave similarly to I-sections under axial load plus strong axis bending, the τ_{NM} factor proposed by Kucukler et al. (2014) for carbon steel I-section beam-columns with $H/B>1.2$ for combined axial load and major axis bending is adopted herein. Thus, the interaction stiffness reduction function τ_{NM} used in this study is given in Eq. 5.14, in which τ_N and τ_M correspond to the reduction factors determined from Eq. 5.4 and Eq. 5.13, respectively.

$$\tau_{NM} = \tau_N \tau_M \left\{1 - \left(\frac{N_{Ed}}{N_{pl}}\right)^{0.8} \left(\frac{M_{Ed}}{M_{pl}}\right)\right\} \quad \text{Eq. 5.14}$$

5.5.2. Application of the proposed stiffness reduction factor τ_{NM}

A comprehensive parametric analysis on simply supported austenitic, ferritic and duplex stainless steel beam-columns subjected to axial load and uniform minor axis bending moment was conducted to assess the accuracy of the proposed τ_{NM} factor. Material properties considered in the FE models are shown in Table 5.1, and the details of the models have been discussed in Section 5.2. The member slenderness $\bar{\lambda}$ values considered were 0.5, 1.0 and 1.5, and the cross-sections analysed corresponded to the sections RHS1 and RHS2 defined in Table 5.2. Investigated bending moment-axial load ratios varied from pure compression to pure bending moment. Generally, constant bending moments were introduced by means of eccentric axial loads, with load eccentricity values equal to e_0=0.1B, 0.3B, 0.75B, 1.5B, 3.0B and 9.0B, where B is the total cross-section width. Only in the cases with null axial loading (i.e., pure bending moment loading), members were subjected to equal bending moments applied at the endpoints.

The ultimate load and bending moment resistances of the beam-columns were obtained from a GNA-SR analysis using the τ_{NM} function proposed in Eq. 5.14 and following the procedure explained in Section 5.3.2. Since the local slenderness values of RHS1 and RHS2 are lower than 0.60, the ultimate applied loads N_{Ed} and corresponding bending moments M_{Ed} were determined from the GNA-SR analyses by applying the interaction equation given in Eq. 5.6 at the critical cross-sections. These values are compared with the ultimate strengths predicted from the GMNIA analyses in Figure 5.7, which shows the nondimensional ultimate loads N_{Ed}/N_{pl} and bending moments M_{Ed}/M_{pl} predicted from the GNA-SR analyses using the proposed reduction factor τ_{NM} for simply supported beams-columns under uniform uniaxial bending for the cross-section RHS2, the three stainless steel families and the three member slenderness $\bar{\lambda}$ values considered. Ultimate capacities of restrained beam-columns predicted from the GMNIA analyses are also provided as benchmark. As mentioned in Section 5.3.1, the compression resistances in members are limited to the flexural buckling resistance values $N_{b,Rk}$, which are represented by dashed horizontal lines in Figure 5.7, while the ultimate bending capacities are limited by the CSM bending resistance as Eq. 5.6 assumes M_{csm} as endpoint.

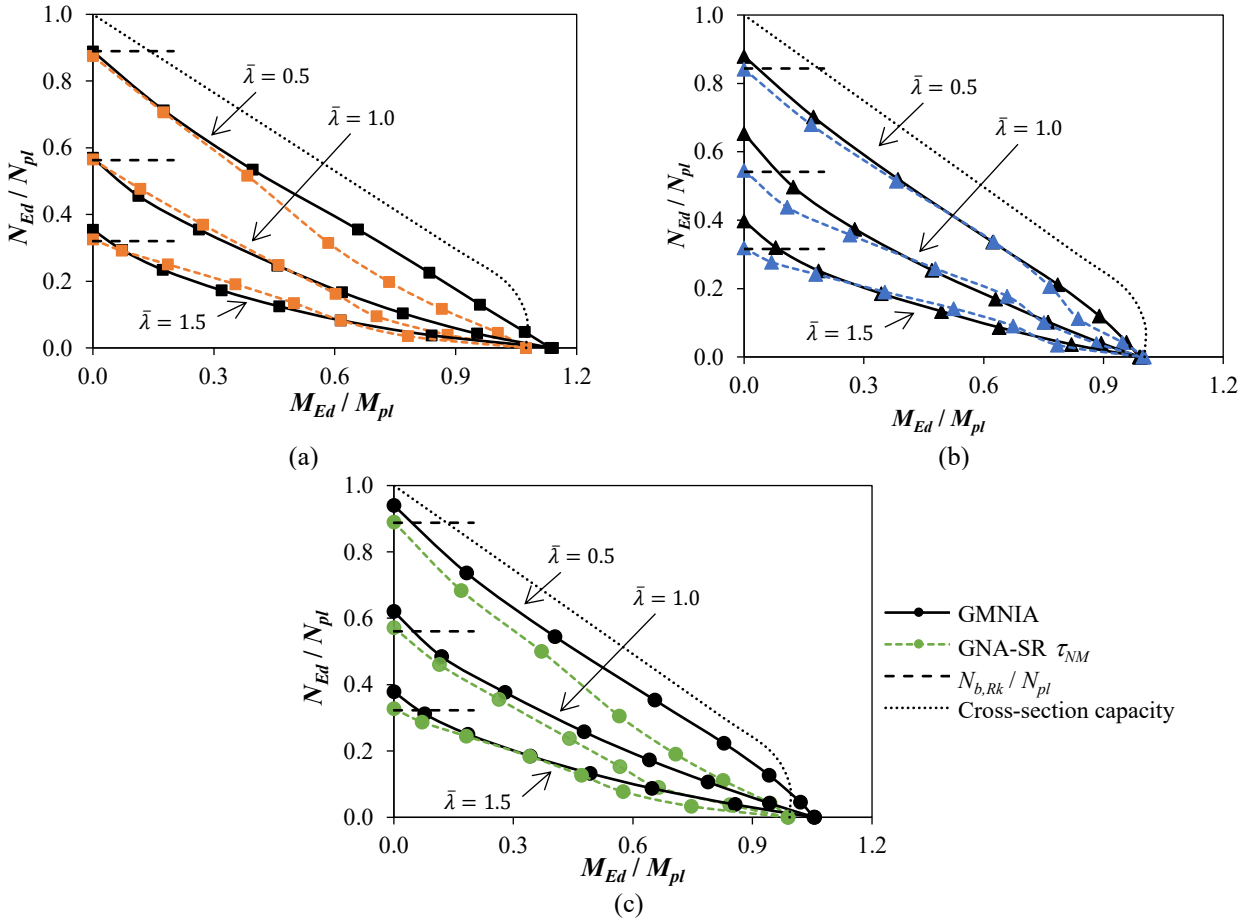

Figure 5.7. Evaluation of GNA-SR results for (a) austenitic, (b) ferritic and (c) duplex stainless steel beam-columns under combined axial loading and uniform minor axis bending (RHS2 cross-section).

Accurate and generally safe predictions are obtained for all materials and member slendernesses, since the GNA-SR predicted member strengths tend to lay below the GMNIA-predicted capacities. The most

conservative estimations are obtained for stocky (i.e., short) specimens, since their structural behaviour is similar to that exhibited by the cross-section, without showing instability. In addition, when loading is governed by compressive loads, results seem to be more precise for austenitic alloys since, as discussed in Section 5.3.2, the austenitic buckling curve specified in the upcoming prEN 1993-1-4 (2021) standard is in good agreement with the austenitic material used in the present study, while the buckling curves are worse fitted for the studied ferritic and duplex materials, as it was shown in Figure 5.4.

It is worth emphasizing that the GNA-SR curves shown in Figure 5.7 are very close to the GMNIA curves in those loading cases governed by bending moment, even if the proposed τ_M function gradually loses accuracy when $M_{Ed}>M_{el}$, as discussed in Section 5.4.1. Based on these results, it can be concluded that the τ_M factor defined by Eq. 5.13 accurately captures the stiffness loss of stainless steel beams subjected to constant bending up to a value of M_{csm}, and consequently a second stage of the formulation for τ_M is not necessary. This fact is especially valuable considering the simplicity of the proposed τ_M formula compared to those available in the literature (Kucukler et al. 2014; Shen and Chacón 2020).

In addition, the accuracy of the stiffness reduction function was assessed through the ratio ζ defined in Eq. 5.15, following the approach adopted in (Kucukler et al. 2016), which is the ratio between the radial distances measured from the origin to the normalised interaction GNA-SR (ζ_i) and GMNIA (ζ_{GMNIA}) curves.

$$\zeta = \frac{\zeta_i}{\zeta_{GMNIA}} = \frac{\sqrt{\left(N_{Ed,i}/N_{pl}\right)^2 + \left(M_{Ed,i}/M_{pl}\right)^2}}{\sqrt{\left(N_{Ed,GMNIA}/N_{pl}\right)^2 + \left(M_{Ed,GMNIA}/M_{pl}\right)^2}} \qquad \text{Eq. 5.15}$$

Table 5.3 summarises the comparison of the ultimate capacities of GNA-SR with those of GMNIA, where ζ_{av} and ζ_{cov} are the average value and the coefficient of variation (COV) of the calculated ζ ratios for the different beam-columns investigated and the member slenderness considered, and ζ_{max} and ζ_{min} are the maximum and minimum ζ values. ζ values lower than 1.0 correspond to conservative predictions. As reported in Table 5.3, the GNA-SR method provides accurate ultimate strength predictions, with ζ_{av} values close to 1.0 and considerably small coefficients of variation (COV), especially in the cases of austenitic and ferritic beam-columns. However, the COV values tend to increase for increasing member slenderness $\bar{\lambda}$ values. It should be noted that the errors in the unconservative side (i.e., ζ values higher than 1.0) are usually not greater than 10% ($\zeta \leq 1.10$), and that only in the case of slender austenitic members subjected to similar proportions of bending moment and axial compression forces (see Figure 5.7), the SRM exceeds considerably the ultimate GMNIA strength (showing ζ_{max} values of 1.16 and 1.10). In contrast, the most conservative predictions are obtained for duplex members, with ζ_{max} values reported in Table 5.3 being always ≤1.0, and ζ_{min} values ≤0.85. For ferritic and duplex stainless steel members, the minimum ζ values are usually obtained under pure compression (i.e., for columns) because, as discussed in Section 5.3.2, the

European buckling curves (and consequently τ_N) provide reasonable, but not perfect, ultimate member resistances for these materials.

Table 5.3. Comparison of the ultimate capacities obtained through GNAR-SR and GMNIA analyses for simply supported beam-columns subjected to axial compression and uniform bending moment.

Stainless steel	Cross-section	$\bar{\lambda}$	ζ_{av}	ζ_{cov}	ζ_{max}	ζ_{min}
Austenitic	RHS1	0.5	0.99	0.022	1.02	0.95
		1.0	1.03	0.038	1.08	0.97
		1.5	1.05	0.073	1.16	0.90
	RHS2	0.5	0.94	0.043	0.99	0.88
		1.0	0.98	0.048	1.05	0.92
		1.5	1.00	0.068	1.11	0.92
Ferritic	RHS1	0.5	0.99	0.022	1.02	0.95
		1.0	0.97	0.080	1.07	0.83
		1.5	0.98	0.098	1.08	0.80
	RHS2	0.5	0.98	0.023	1.01	0.94
		1.0	0.96	0.070	1.05	0.84
		1.5	0.97	0.089	1.06	0.80
Duplex	RHS1	0.5	0.94	0.033	0.98	0.89
		1.0	0.95	0.039	1.00	0.89
		1.5	0.95	0.054	1.03	0.86
	RHS2	0.5	0.91	0.037	0.95	0.85
		1.0	0.91	0.037	0.95	0.84
		1.5	0.93	0.049	1.00	0.87

5.5.3. Moment gradient effect

Consideration of the effects derived from bending moment gradients along the member length is assessed herein. To account for linear moment gradient variations, the proposed τ_{NM} function was modified applying an equivalent uniform moment factor C_m to the maximum bending moment along the member length M_{Ed}. Since the present work focuses on members with linear moment gradients, the expression for C_m developed by Austin (1961) and shown in Eq. 5.16 is used, where μ is the ratio between the smaller and larger applied end moments. The effectiveness of this expression has been widely validated and it is the equivalent uniform moment factor adopted in EN 1993-1-1 (2005).

$$C_m = 0.6 + 0.4\mu \qquad \text{but } C_m \geq 0.4 \qquad \text{Eq. 5.16}$$

Therefore, Eq. 5.17 and Eq. 5.18 should be used in the calculation of τ_M and τ_{NM} instead of Eq. 5.13 and Eq. 5.14 to include the variation of bending moment in beam-columns.

$$\tau_M = \left[1 + (n-1)\frac{M_{el}}{M_{pl}}\left(\frac{C_m M_{Ed}}{M_{pl}}\right)^{n-2}\right]^{-1} \qquad \text{Eq. 5.17}$$

$$\tau_{NM} = \tau_N \tau_M \left\{1 - \left(\frac{N_{Ed}}{N_{pl}}\right)^{0.8}\left(\frac{C_m M_{Ed}}{M_{pl}}\right)\right\} \qquad \text{Eq. 5.18}$$

Figure 5.8 shows the comparison between the GNA-SR and GMNIA results for two typical austenitic and duplex cases of simply supported beam-columns under axial load and varying minor axis bending along the length for cross-section RHS1. Linear bending moment distributions were obtained by applying an eccentricity only at one of the supports for the bending moment distribution corresponding to μ=0, and by applying load eccentricities with different signs at the two ends of the beam-columns for μ=-0.5. GNA-SR predictions were limited by the cross-section interaction equation given in Eq. 5.6, as in the previous sections.

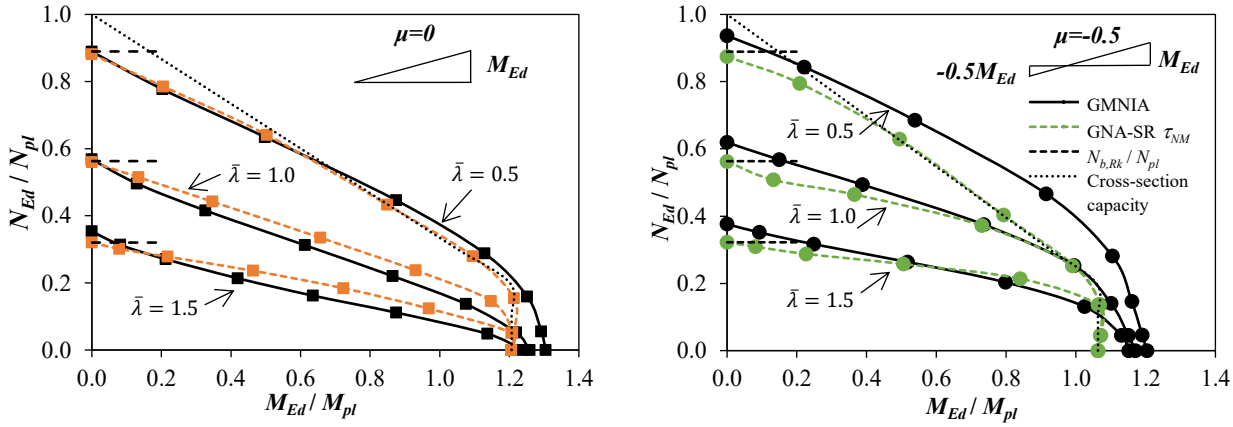

Figure 5.8. Comparison of GNA-SR results for the proposed reduction factor for (a) austenitic and (b) duplex stainless steel beam-columns under combined axial loading and varying minor axis bending (RHS1 cross-section).

Similarly to the results reported in Table 5.3 for beam-columns under uniform bending moment, Table 5.4 summarises the ζ_{av}, ζ_{cov}, ζ_{max} and ζ_{min} values obtained from the comparison of the ultimate capacities predicted by the proposed GNA-SR approach with those of GMNIA for austenitic, ferritic and duplex beam-columns subjected to axial compression and bending moment gradients. It is worth noting that a number of the results shown in Figure 5.8 and Table 5.4 for austenitic slender members, particularly under high bending and for the μ=-0.5 distribution, are on the unsafe side, although deviations lie within the 10-18% range. This is because (1) the equivalent moment factor C_m neglects the influence of the member length and the level of axial load, as previously highlighted in (Zhao et al. 2016b), which may lead to an overestimation of the beneficial effect of moment gradients on the beam-column stability, and (2) the proposed τ_M factor does not accurately capture the loss of stiffness due to material nonlinearity after M_{pl}, as discussed in Section 5.4, which is of particular relevance for austenitic beam-columns under the μ=-0.5 distribution. Nevertheless, the analysis presented in Section 5.6 for austenitic portal frames indicates that good predictions of the ultimate frame strengths are obtained when the C_m factor is used in the analysis of structural systems, which is the relevant situation in design. The frames investigated covered the same ranges of member slenderness $\bar{\lambda}$ and μ factors considered in this section. Besides, results in Table 5.4 indicate that, on average, GNA-SR results are in good agreement with those predicted by GMNIA for the bending moment distributions considered (i.e., ζ_{av} values are close to 1.0).

Table 5.4. Comparison of the ultimate capacities obtained through GNAR-SR and GMNIA analyses for simply supported beam-columns subjected to axial compression and gradient bending moment.

Specimen	Bending moment distribution μ	$\bar{\lambda}$	ζ_{av}	ζ_{cov}	ζ_{max}	ζ_{min}
Austenitic RHS1	0	0.5	0.97	0.030	1.01	0.92
		1.0	1.03	0.042	1.08	0.96
		1.5	1.03	0.074	1.14	0.91
	-0.5	0.5	0.94	0.042	1.00	0.89
		1.0	1.02	0.054	1.10	0.94
		1.5	1.02	0.097	1.18	0.91
Ferritic RHS1	0	0.5	0.97	0.021	0.99	0.94
		1.0	0.96	0.089	1.07	0.83
		1.5	0.96	0.103	1.09	0.80
	-0.5	0.5	0.95	0.018	0.98	0.92
		1.0	0.94	0.082	1.03	0.83
		1.5	0.94	0.104	1.06	0.80
Duplex RHS1	0	0.5	0.92	0.015	0.94	0.90
		1.0	0.95	0.030	1.00	0.91
		1.5	0.95	0.054	1.01	0.86
	-0.5	0.5	0.91	0.027	0.94	0.87
		1.0	0.94	0.039	1.00	0.89
		1.5	0.95	0.070	1.05	0.86

5.6. Stiffness reduction factors applied to portal frame design

In this section, the proposed stiffness reduction factor τ_{NM} is applied to the in-plane design of stainless steel portal frames. The assessment of the Stiffness Reduction Method was carried out through the comparison of the ultimate loads obtained for the τ_{NM} factor proposed herein with those determined using the Direct Analysis Method prescribed in the AISC 370 (2021) specification and the ultimate strengths predicted from GMNIA analyses.

5.6.1. Application of the proposed method for in-plane global design

The accuracy of the proposed Stiffness Reduction Method (SRM) to predict the global behaviour of stainless steel structures was assessed through a parametric study comprising austenitic RHS portal frames. A total of 20 single-span in-plane frames were studied: the height (L_c) of all columns was 2 m, while the span lengths (L_b) varied from 2 m to 4 m. All members featured the austenitic stainless steel material properties reported in Table 3.2 and the RHS1 cross-section given in Table 5.2, oriented in such a way that all members bent about their major axes. The loading scheme, shown in Figure 5.9, ensured that the most loaded cross-sections were located at the columns in all frames. Both fixed- and pin-ended support conditions were analysed and vertical (V_{Ed}) and horizontal (H_{Ed}) loads were applied simultaneously in different proportions at the top of the columns.

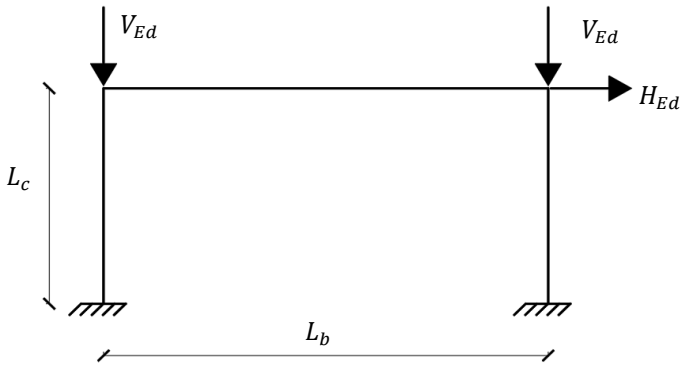

Figure 5.9. Loading scheme for austenitic stainless steel portal frames.

Table 5.5 summarises the horizontal load H_{Ed} values studied as a function of the applied vertical load V_{Ed}. Note that H_{Ed}=0 and V_{Ed}=0 imply that the portal frame was loaded only vertically or horizontally, respectively. Member slenderness $\bar{\lambda}$ values ranged from 1.01 to 2.29, while bending moment distribution factors were μ=-1 for beams, and μ=[-0.59,-0.74] and μ=0 for fixed- and pin-ended columns, respectively, which are in line with the beam-column cases analysed in Section 5.5.3.

Table 5.5. Frame cases analysed.

Frame case No.	Boundary conditions	L_c x L_b	Horizontal loading H_{Ed}
1-12	Fixed-ended	2 x 4 m 2 x 2 m	H_{Ed}=0, 0.03V_{Ed}, 0.01V_{Ed}, 0.25V_{Ed}, 1.0V_{Ed}, V_{Ed}=0
13-20	Pin-ended	2 x 4 m 2 x 2 m	H_{Ed}=0, 0.01V_{Ed}, 1.0V_{Ed}, V_{Ed}=0

The frames described above were analysed using the SRM proposed herein, i.e., by performing GNA-SR analyses on the numerical models described in Section 5.2.1.3, and the predicted ultimate capacities and internal forces were compared to those estimated from GMNIA. The application of the SRM to obtain the ultimate load of a structure is an iterative process, as stiffness reduction factors should be calculated for the load levels at which cross-section capacities are checked, and re-run until the capacity of the cross-sections is fully utilised (Kucukler et al. 2016; Walport et al. 2021b). In the GNA-SR analysis, the flexural stiffness of each member was reduced by the corresponding τ_{NM} factor determined from Eq. 5.18, where the factors τ_N and τ_M were obtained from Eq. 5.4 and Eq. 5.17. The GNA-SR analysis was conducted until the most loaded section of the frame reached its resistance capacity, evaluated from the cross-section interaction equation Eq. 5.6, since RHS1 exhibits a local slenderness lower than 0.60. For the studied pin-ended frames, the critical sections were located at the beam-to-column joints, while for the fixed-ended frames the critical sections were those at the supports of the columns. Note that since the GMNIA analyses were carried out on beam-type FE models (as explained in Section 5.2.1.2), the frame strengths and target internal forces were also obtained by checking the resistances of the critical cross-sections through the same Eq. 5.6 used for SRM analyses.

For assessment purposes, the 20 single-span in-plane frames were also analysed following the Direct Analysis Method (DM) prescribed in AISC 370 (2021) for the design of stainless steel structures, in which the flexural stiffness of the members is adjusted by two different factors, τ_g and τ_b. The first factor τ_g corresponds to a general stiffness reduction, which is applied to all members and accounts for the reduction in member stiffness due to the development and spread of plasticity. A constant value of τ_g=0.7 is adopted for all stainless steel members, as proposed by Walport et al. (2021b). The second factor τ_b is an additional factor that is applied to the stiffness of those members that contribute to the stability of the structure. τ_b is given by Eq. 5.19 when considering the Load and Resistance Factor Design (LRFD) approach and was derived from the Ramberg-Osgood expression, so it considers the further loss in stiffness due to material nonlinearities, and it also takes into account the detrimental effect of residual stresses by means of the effective strain hardening exponent n_{eff}. The value of n_{eff} depends on the strain hardening coefficient n, the cross-section type and the buckling axis, and was proposed by Walport et al. (2021b) and is tabulated in AISC 370 (2021). For the case of rectangular hollow sections studied herein, n_{eff} assumes a value equal to the strain hardening coefficient n, as the effects of residual stresses is negligible (Walport et al. 2021b).

$$\tau_b = \frac{1.0}{1.0 + 0.002 n_{eff} \frac{E}{f_y} \left(\frac{N_{Ed}}{N_{pl}}\right)^{n_{eff}-1}} \qquad \text{Eq. 5.19}$$

There are three potential design options in AISC 370 (2021) when the DM is adopted: (1) not including member imperfections explicitly in the structural analysis and verifying the structure by checking member capacities, (2) including member imperfections in the analysis and verifying the capacity of the structure through cross-section strength equations that use the plastic section capacities N_{pl} and M_{pl}, and (3) including member imperfections in the analysis and verifying the capacity of the structure through cross-section checks that are anchored to the more accurate CSM end-points. Both member and cross-section checks should follow the corresponding design provisions prescribed in AISC 370 (2021). In the comparisons carried out in this study, the latter approach is adopted because it is the option that is most similar to the GNA-SR proposal presented. Notional loads were used to include initial global imperfections with a value equal to $0.002N_{Ed}$, which is based on a nominal initial storey out-of-plumbness ratio of 1/500 according to AISC 370 (2021), while member imperfections were included in the beam-type FE models by directly modifying the position of the nodes following a half-sine wave shape with an amplitude of L_c/1000 in the most detrimental direction, as for the GMNIA models described in Section 5.2.1.2. Note that although the nominal out-of-plumbness ratio adopted for the DM is slightly lower than the corresponding value used in the GNA-SR analyses, the member imperfection amplitudes are equivalent, since the imperfection amplitude used in the calibration of the European buckling curves was L_c/1000. Since member instability is directly accounted for in the analysis, the

capacity of the structure is verified by means of cross-section checks. Eq. 5.20 and Eq. 5.21 show the CSM cross-section interaction equations provided in AISC 370 (2021), where N_{Ed} and M_{Ed} are the second order internal axial force and bending moment obtained from the DM at the critical sections, and $P_{n,csm}$ and $M_{n,csm}$ are the CSM cross-section resistances in compression and bending, respectively. Note that the AISC 370 $P_{n,csm}$ and $M_{n,csm}$ capacities are based on the same CSM base curve given in Eq. 2.4, but adopt a lower value of 5 for the Ω parameter (Walport et al. 2021b; AISC 370 2021). Formulae to calculate $P_{n,csm}$ and $M_{n,csm}$ are provided in (Walport et al. 2021b; AISC 370 2021). In the present study partial safety and resistance factors proposed in prEN 1993-1-4 (2021) and AISC 370 (2021) assume values equal to unity.

$$\frac{N_{Ed}}{P_{n,csm}} + \frac{8}{9}\frac{M_{Ed}}{M_{n,csm}} \leq 1.0 \qquad \text{for } N_{Ed} \geq 0.2\, P_{n,csm} \qquad \text{Eq. 5.20}$$

$$\frac{N_{Ed}}{2P_{n,csm}} + \frac{M_{Ed}}{M_{n,csm}} \leq 1.0 \qquad \text{for } N_{Ed} < 0.2\, P_{n,csm} \qquad \text{Eq. 5.21}$$

5.6.2. Assessment of the results

The ultimate load predictions obtained with the proposed SRM for stainless steel frames subjected to combined vertical and horizontal loads are summarised in Figure 5.10, where the results plotted in Figure 5.10(a) correspond to large span frames and in Figure 5.10(b) to short span frames. Both figures show the SRM predictions for fixed- and pin-ended boundary conditions, as well as the AISC 370-DM (2021) predictions and the GMNIA results for reference.

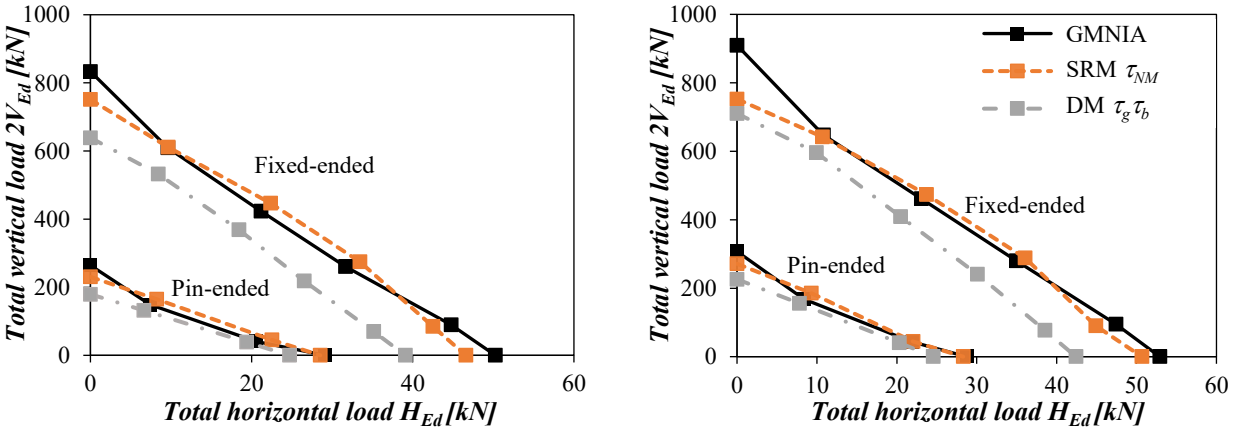

Figure 5.10. Assessment of the results for the proposed stiffness reduction factors against GMNIA results and the AISC 370-DM (2021) for austenitic stainless steel in-plane portal frames with (a) L_b=4 m and (b) L_b=2 m under vertical and horizontal loading (RHS1 cross-section).

In addition, Table 5.6 reports the values of the stiffness reduction factors for each member of the studied frames, according to the proposed SRM ($\tau_{NM,i}$) and the AISC 370-DM ($\tau_g \tau_{b,i}$) approaches, where the subscripts l, r and b refer to the left column, the right column and the beam, respectively. Note that for all the cases analysed in this research, the AISC 370-DM stiffness reduction factor for the beams is

equal to $\tau_g \tau_{b,b} = \tau_g$ =0.70. Similar stiffness reduction factors and ultimate capacities were estimated for large span frames and short span frames, and the differences were associated with the type of boundary condition and load combinations. Following the approach given in (Kucukler et al. 2016), Table 5.6 also provides the parameter ζ, which refers to the accuracy of the considered method for the prediction of the ultimate frame strengths. The factor ζ is determined using Eq. 5.15, where M_{Ed} refers to the bending moment in the column and the subscript i refers to the assessed method (i.e., the proposed SRM or the AISC 370-DM approach). Recall that ζ values lower than 1.0 correspond to conservative predictions.

Table 5.6. Assessment of the accuracy of the proposed stiffness reduction method SRM and the AISC 370-DM for the prediction of ultimate strengths in austenitic stainless steel portal frames.

Frame case	Horizontal loading H_{Ed}	SRM				AISC 370-DM			
		$\tau_{NM,l}$	$\tau_{NM,r}$	$\tau_{NM,b}$	ζ	$\tau_g\tau_{b,l}$	$\tau_g\tau_{b,r}$	$\tau_g\tau_{b,b}$	ζ
2 x 4 m Fixed-ended	H_{Ed}=0	0.61	0.61	1.00	0.91	0.59	0.59	0.70	0.77
	$0.03V_{Ed}$	0.66	0.66	0.96	1.00	0.68	0.68	0.70	0.87
	$0.01V_{Ed}$	0.70	0.69	0.92	1.05	0.70	0.70	0.70	0.87
	$0.25V_{Ed}$	0.72	0.70	0.91	1.05	0.70	0.70	0.70	0.84
	$1.0V_{Ed}$	0.70	0.68	0.87	0.94	0.70	0.70	0.70	0.78
	V_{Ed}=0	0.71	0.71	0.84	0.92	0.70	0.70	0.70	0.78
2 x 2 m Fixed-ended	H_{Ed}=0	0.56	0.55	1.00	0.83	0.54	0.54	0.70	0.78
	$0.03V_{Ed}$	0.64	0.63	0.96	0.99	0.67	0.67	0.70	0.92
	$0.01V_{Ed}$	0.69	0.67	0.93	1.02	0.70	0.69	0.70	0.89
	$0.25V_{Ed}$	0.71	0.68	0.89	1.03	0.70	0.70	0.70	0.86
	$1.0V_{Ed}$	0.73	0.67	0.83	0.94	0.70	0.70	0.70	0.81
	V_{Ed}=0	0.71	0.70	0.79	0.95	0.70	0.70	0.70	0.80
2 x 4 m Pin-ended	H_{Ed}=0	0.81	0.81	1.00	0.88	0.70	0.70	0.70	0.68
	$0.01V_{Ed}$	0.81	0.80	0.96	1.10	0.70	0.70	0.70	0.89
	$1.0V_{Ed}$	0.66	0.62	0.86	1.08	0.70	0.70	0.70	0.94
	V_{Ed}=0	0.39	0.39	0.70	0.97	0.70	0.70	0.70	0.85
2 x 2 m Pin-ended	H_{Ed}=0	0.79	0.79	1.00	0.89	0.70	0.70	0.70	0.74
	$0.01V_{Ed}$	0.79	0.77	0.96	1.09	0.70	0.70	0.70	0.93
	$1.0V_{Ed}$	0.65	0.55	0.84	1.00	0.70	0.70	0.70	0.93
	V_{Ed}=0	0.38	0.38	0.71	0.98	0.70	0.70	0.70	0.85

According to the results shown in Figure 5.10 and Table 5.6, the proposed SRM accurately predicts the ultimate capacities of the frames. Only in the case of high vertical loads, in which the structural behaviour of the frames is determined by the buckling of their columns in compression, the SRM slightly underestimates the GMNIA strength predictions. While in the GMNIA analyses the vertical reaction observed in the supports were higher than the flexural buckling resistances $N_{b,Rk}$, in the SRM the column capacities were limited to $N_{b,Rk}$, as discussed in Section 5.3.1. In any case, the predictions obtained by the proposed SRM are adequate and provide a reasonable safety margin. Accurate and safe results are also obtained when using the AISC 370-DM (2021) approach studied herein, although the ultimate capacity of fixed-ended frames is slightly underestimated, as shown in Figure 5.10. The discrepancies between the two approaches are partly due to the use of different strength interaction

equations to limit the GNA-SR analyses, but mainly to the fact that the CSM base curve adopts a different limiting value for Ω in the two approaches (i.e., Ω = 15 in prEN 1993-1-4 (2021) but Ω = 5 in AISC 370-DM (2021)). Regarding the interaction equations, even if the AISC 370-DM equations are anchored to the CSM cross-section resistances, they are more restrictive than the cross-section interaction check used in the proposed SRM (Eq. 5.6) because they adopt a linear interaction function. On the other hand, as the RHS1 cross-section used in this study for the assessment of the design approaches is very stocky, the CSM strain in Eq. 2.4 is limited by the parameter Ω in the two approaches, which adopts different values (i.e., Ω = 5 for the DM as opposed to Ω = 15 for the SRM), and thus the CSM bending moment resistances M_{csm} are significantly different. This can be clearly observed for the cases of fixed-ended portal frames with V_{Ed}= 0, where the frames are almost entirely bending dominated and the differences in interaction equation have almost no consequence, and the results are governed in both cases by the CSM bending moment resistance M_{csm}. Since the SRM approach proposed herein uses a less restrictive ductility limit of Ω = 15, the value of M_{csm}, and thus the predicted capacity of the frames, is higher. Nevertheless, for less stocky cross-sections, where the CSM strain would not be determined by the Ω limit, more similar values of M_{csm} would be obtained for the two approaches and the results obtained from the proposed SRM and the AISC 370-DM would be less different.

The accuracy of the SRM and DM approaches for the prediction of internal forces was also assessed according to the indications given by Kucukler et al. (2016), i.e., through the comparison of the nondimensional internal forces $N_{Ed,i}/N_{pl}$ - $M_{Ed,i}/M_{pl}$ obtained from the considered method (i.e., the proposed SRM or the AISC 370-DM approach) and those obtained from the GMNIA analysis at the critical sections of the columns using Eq. 5.15. Results of the accuracy for the different design methods are summarised in Table 5.7, where ζ_{av} and ζ_{cov} are the average and coefficient of variation (COV) of ζ, and ζ_{max} and ζ_{min} are the maximum and minimum ζ values for the internal forces registered in the columns. As shown in Table 5.7, the internal forces predicted by the proposed SRM approach are in good agreement with those considered as target values (ζ_{av}=1.00 and ζ_{cov}=0.010), while the results obtained for the DM approach are slightly more conservative and more scattered (ζ_{av}=0.85 and ζ_{cov}=0.026). Based on the reported results, it can be concluded that the proposed SRM and the AISC 370-DM (2021) approach analysed herein provide safe predictions of the ultimate in-plane response of stainless steel frames with stocky RHS sections under combined vertical and horizontal loads, but slightly better results are obtained for the proposed SRM approach, especially for fixed-ended frames. In addition, the proposal has the advantage of not requiring the explicit introduction of member imperfections in the numerical models. Finally, it is important to note that the ultimate capacity of the structure obtained by either method will be generally lower than the ultimate load predicted from a GMNIA analysis since both methods are limited to the development of the first plastic hinge without considering any redistribution of internal forces.

Table 5.7. Comparison of the accuracy of the SRM and DM approaches for the prediction of internal forces in the critical column of the frame cases analysed.

Method	ζ_{av}	ζ_{cov}	ζ_{max}	ζ_{min}
SRM	1.00	0.010	1.02	0.98
AISC 370-DM	0.85	0.026	0.88	0.80

5.7. Summary of the proposed Stiffness Reduction Method

The procedure to apply the proposed Stiffness Reduction Method for the in-plane stability design of stainless steel structures with stocky RHS sections is summarised as follows:

(i). Perform a Linear Elastic Analysis (LA) to estimate the maximum internal forces (axial force N_{Ed} and bending moment M_{Ed}) in each member under the design loads.

(ii). Calculate the Stiffness Reduction factors for each member from the proposed formulae:

$$\tau_N = \frac{4\psi^2}{\alpha^2 \frac{N_{Ed}}{N_{pl}}\left[1+\sqrt{1-4\psi\frac{\left(N_{Ed}/N_{pl}-1\right)}{\alpha^2\, N_{Ed}/N_{pl}}}\right]^2} \quad \text{but} \quad \tau_N \leq 1 \qquad \text{Eq. 5.4}$$

$$\text{where} \quad \psi = 1 + \bar{\lambda}_0 \alpha \frac{N_{Ed}}{N_{pl}} - \frac{N_{Ed}}{N_{pl}} \qquad \text{Eq. 5.5}$$

$$\tau_M = \left[1 + (n-1)\frac{M_{el}}{M_{pl}}\left(\frac{C_m M_{Ed}}{M_{pl}}\right)^{n-2}\right]^{-1} \qquad \text{Eq. 5.17}$$

$$\tau_{NM} = \tau_N \tau_M \left\{1 - \left(\frac{N_{Ed}}{N_{pl}}\right)^{0.8}\left(\frac{C_m M_{Ed}}{M_{pl}}\right)\right\} \qquad \text{Eq. 5.18}$$

$$\text{where } C_m = 0.6 + 0.4\mu \quad \text{but } C_m \geq 0.4 \qquad \text{Eq. 5.16}$$

with N_{pl} and M_{pl} being the plastic resistance of the gross cross-section and the plastic moment resistance of the cross-section, respectively; $\bar{\lambda}_0$ and α being the slenderness plateau and imperfection factor given in next version of prEN 1993-1-4 (2021), respectively; and μ being the ratio between the smaller and larger applied end moments.

(iii). Perform a Geometrically Nonlinear Analysis with Stiffness Reduction (GNA-SR) considering initial global imperfections (out-of-plumbness) only. Note that stiffness reduction factors should affect the flexural stiffnesses, but not the axial stiffnesses, of the members.

(iv). Check the cross-section capacity using the internal forces determined from the GNA-SR analysis under the design loads through the following strength interaction expression for stocky sections:

$$M_{Ed} \leq M_{N,csm} = M_{csm}\frac{1-\left(N_{Ed}/N_{pl}\right)}{1-0.5a} \leq M_{csm} \qquad \text{for } \bar{\lambda}_p \leq 0.60 \qquad \text{Eq. 5.6}$$

being $M_{N,csm}$ the plastic moment resistance reduced due to the axial force N_{Ed}, M_{csm} the CSM moment resistance, and $\bar{\lambda}_p$ the local slenderness.

5.8. Concluding remarks

This chapter has presented a Stiffness Reduction Method (SRM) for the in-plane stability design of stainless steel structures with stocky Rectangular Hollow Section (RHS) members based on the provisions included in the upcoming version of the prEN 1993-1-4 (2021) standard. The proposed approach allows predicting the ultimate capacity and internal forces in stainless steel structures by performing a second order elastic analysis in which the stiffness of members is reduced by a set of factors to account for the effect of the spread of plasticity, residual stresses and member imperfections. The method only requires that initial out-of-plumbness imperfections be included, and the verification is limited to checking cross-section capacities. The accuracy of the proposed method is assessed for individual stainless steel structural members (columns, beams, and beam-columns) with different cross-sections and material properties, and for austenitic stainless steel portal frames, against numerical results obtained from GMNIA analyses conducted on finite element models. A comparison between the proposed approach and the Direct Analysis Method prescribed in the AISC 370 (2021) specification is also provided, showing that the results are comparable in the two approaches.

Corresponding publication: González-de-León I., Arrayago I., Real E. and Mirambell E. (2022). A stiffness reduction method for the in-plane design of stainless steel members and frames according with EN 1993-1-4. *Engineering Structures*, 253, 113740. https://doi.org/10.1016/j.engstruct.2021.113740

PART II

Performance of stainless steel structures under cyclic loads

CHAPTER 6

Rotation capacity of cold-formed stainless steel RHS beams under cyclic loading

6.1. Introduction

This chapter presents a study on the rotation capacity and maximum bending moment resistance shown by stainless steel beams subjected to cyclic loading. The correct estimation of the rotation capacity is of paramount importance from an assessment point of view, because it allows establishing the actual capacity of the structure. Likewise, an accurate computation of the maximum bending moment that the dissipative member can withstand allows a precise prediction of the overstrength parameters to be considered in the application of the capacity design principles.

The investigation is based on numerical results on 120 Rectangular and Square Hollow Section beams (RHS and SHS) made of the main structural stainless steel families, i.e., austenitic, ferritic and duplex alloys. Based on the results, analytical expressions to determine plastic rotation capacities are proposed and assessed. Finally, a tri-linear model representing the full moment-rotation curves of stainless steel

beams is developed based on the proposed expressions, which is intended to be adopted in design software as a constitutive law for concentrated plasticity hinges.

6.2. Finite element modelling

In this section, the Finite Element (FE) model used for generating the data required to investigate the behaviour of stainless steel structural members under cyclic bending is described. The validation of the FE model against experimental results reported in the literature is also presented.

6.2.1. General modelling assumptions

Bending moment and rotation capacities of stainless steel beams under cyclic loading were investigated from finite element models developed using the general-purpose software ABAQUS (2016). The mid-surface of the cross-sections was modelled using four-noded shell (S4R) elements, capable of reproducing the actual behaviour of stainless steel structural members when used in conjunction with second order plastic analyses with imperfections (i.e., GMNIA analysis) (Theofanous and Gardner 2009; Arrayago et al. 2015b). After a convergence study to ensure computational efficiency, beams were discretised following a uniform mesh size of 10 mm, except at the curved corner regions, where a four-element mesh was used. This study, focused on stainless steel beams, neglected local imperfections since recent research on the ultimate behaviour of steel structural members subjected to cyclic bending indicated that specimens were not sensitive to these imperfections under these loading conditions when amplitudes showed values lower than 10% of the cross-section thickness (Fang et al. 2018; Zhou et al. 2018), which is the case for typical stainless steel RHS members (Arrayago et al. 2020a). The GMNIA analyses were solved using the modified Riks method available in ABAQUS (2016).

All the analysed beams bent around their major axes and followed the four-point bending test configuration schematized in Figure 6.1, which is based on the experimental campaign reported in (Arrayago et al. 2020b). The span length was 1500 mm, and loads were applied at 510 mm from both supports.

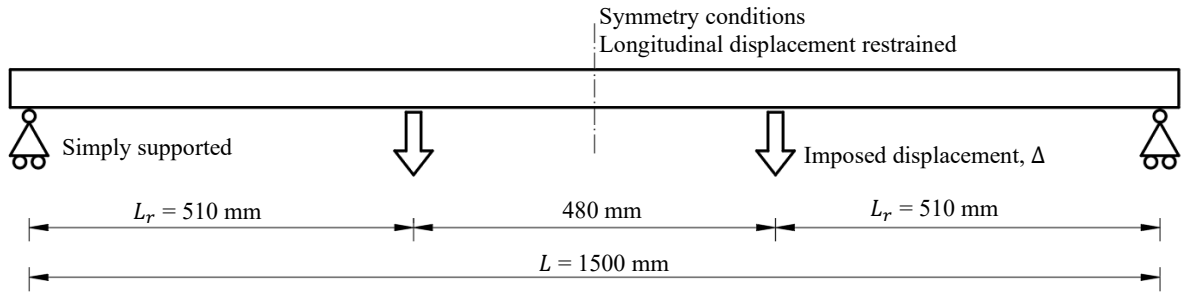

Figure 6.1. Four-point bending test configuration used in this study (based on that reported in (Arrayago et al. 2020b).

Due to the symmetric conditions of the studied specimens, only half-beams were modelled to reduce computational costs. Mid-section nodes were defined as a set of nodes prevented from moving longitudinally and rotating around the minor and major axes. The load and support regions were defined as surfaces at the bottom flange of the beam to avoid web crippling failure (Arrayago et al. 2017b, 2020b; González-de-León et al. 2022). The surfaces were defined as rectangles with the transverse sides equal to the total width minus twice the external radius, i.e., equal to the flat part of the bottom flange, and the longitudinal sides equal to 100 mm (see Figure 6.2). The surfaces were coupled to centroidal reference points and were forced to move as rigid bodies. All degrees of freedom were constrained at the support reference points, except the rotation around the major axis and the displacement in the longitudinal direction. The FE model used in the parametric study is shown in Figure 6.2, where the location of the reference points, coupled surfaces and boundary conditions are clearly indicated.

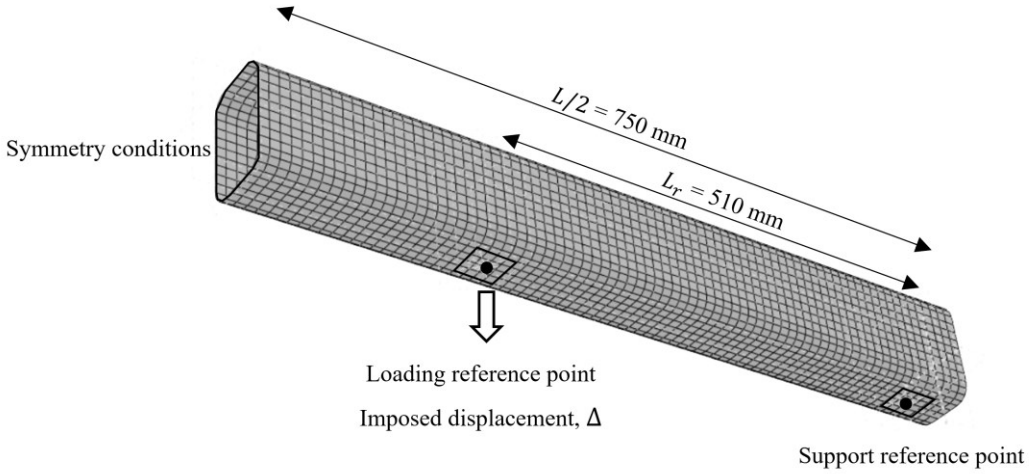

Figure 6.2. Finite element model developed for the parametric study, including loading and boundary conditions.

6.2.2. Cyclic loading

Two point loads were applied as controlled vertical displacements at the loading reference points following the multiple-step loading protocol prescribed in the SAC report (Clark et al. 1997), which was later adopted by the AISC 341 (2016) specification to qualify cyclic tests of beam-to-column moment connections in special and intermediate moment resisting frames. In this loading protocol, the controlling parameter is the drift angle θ, which can be expressed as $\theta = \Delta/L_r$, where Δ is the amplitude of the vertical displacement and L_r is the lever arm, i.e., the distance between the point at which the vertical displacement is imposed and the support (L_r = 510 mm for the four-point test configuration adopted in this study, as shown in Figure 6.1). In this study, the controlling parameter was the amplitude of the imposed displacement Δ, which was incremented as follows: $0.00375L_r$ (6 cycles), $0.005L_r$ (6 cycles), $0.0075L_r$ (6 cycles), $0.01L_r$ (4 cycles), $0.015L_r$ (2 cycles), $0.02L_r$ (2 cycles), with increments of $0.01L_r$ every 2 cycles thereafter. Figure 6.3 shows the cyclic loading protocol used in this study,

adapted from that prescribed in AISC 341 (2016). The cyclic load was applied until, once the ultimate moment (M_u) was reached, the bending moment decreased to a value equal or lower than M_{pl} in the descending branch.

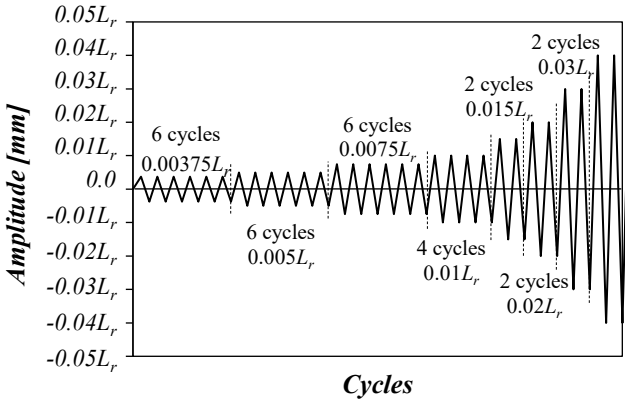

Figure 6.3. Loading protocol adapted from that prescribed in AISC 341 (2016).

6.2.3. Material model

In this study, a nonlinear combined hardening model was assigned to the FE models to simulate the inelastic behaviour of stainless steel under cyclic loading. According to the ABAQUS manual (2016), there are three ways to provide the data for defining the kinematic component: (1) by specifying the material parameters directly, (2) by specifying the test data from a stabilized cycle, or (3) by specifying half-cycle test data. The two first approaches need to be calibrated from cyclic test results (Fang et al. 2018), while in the latter one, which is suitable when specimens are subjected to a limited number of cycles (ABAQUS 2016), the kinematic parameters can be based on the Ramberg-Osgood stress-strain curve derived from a monotonic tensile test. Hence, in the present study, the cyclic behaviour was considered through the kinematic hardening law with half-cycle data option available in ABAQUS (2016) and a backstress = 1. Note that a backstress is the stress coordinate of a point midway between the yield stress in tension and the yield stress in compression (Chancón et al. 2018).

For simplicity, the present parametric study uses the latter approach. It should be noted that the weighted average material properties used herein were obtained from monotonic test results on flat and corner coupons extracted from cold-formed specimens, so residual stresses were implicitly included in the FE models (see Section 2.3). The true stress-strain curves were calculated from the two-stage Ramberg-Osgood material model given in Eq. 2.1 and Eq. 2.2.

6.2.4. FE model validation

The element type, loading protocol and material model used in this study were validated by simulating the tests conducted by Fang et al. (2018). Fang et al. (2018) performed 10 experimental tests on austenitic stainless steel hollow section specimens under constant compression and cyclic bending, following the loading protocol prescribed in AISC 341 (2016), and covered several cross-sections,

compression loads and bending orientations. For validation purposes, the tests referred to as R1 in (Fang et al. 2018), i.e., R1-n0.2-W, R1-n0.4-W, R1-n0.2-S and R1-n0.4-S, were reproduced numerically following the assumptions described in the previous sections. R1 cross-sections tested in (Fang et al. 2018) exhibited an overall width of 61 mm, an overall height of 120.29 mm, 2.72 mm thickness, and 6.80 mm external radii. The n0.2 and n0.4 factors in the specimen IDs correspond to the axial load ratio adopted, n = P/f_yA, being P the applied compression load and A the cross-sectional area, while the last letter refers to the axis of bending: W for minor (weak) axis bending and S for major (strong) axis bending. The nominal total length of the specimens was 660 mm, and the ends of the members were strengthened by means of 80 mm-high stiffeners. The loading scheme adopted in the tests followed two steps. First, an axial compressive load was applied at the top of the column and kept constant. Then, a cyclic bending moment was introduced as an imposed horizontal displacement 785 mm away from the top of the base stiffeners. The amplitude and frequency of each horizontal displacement followed the AISC 341 (2016) recommendations described above, assuming a lever arm length of L_r = 785 mm. The full details of the test arrangements and results can be found in (Fang et al. 2018).

The FE models for the different R1 specimens, including the stiffeners, were developed using S4R elements (ABAQUS 2016) and discretised following the mesh described in Section 6.2.1. Residual stresses were implicitly present in the material properties introduced in the model. As indicated in (Fang et al. 2018), only local imperfections were included in the form of the local buckling mode obtained from a previous linear elastic buckling analysis and with the modified Dawson and Walker amplitude proposed in (Gardner and Nethercot 2004b) to ensure that the geometrical nonlinearities were triggered in the models. It should be recalled that local imperfections were only included in the validation of the numerical model due to the different loading scheme adopted in the models described in (Fang et al. 2018) (i.e., beam-column configuration), but not in the parametric study, as mentioned in Section 6.2.1. Reference points coupled to the end surfaces of the specimens were used to assign boundary conditions: the bottom reference point was located at the centroid of the cross-section, in which all degrees of freedom were constrained, while the upper reference point was located at a distance of 785 mm from the top of the base stiffeners, following the experimental set-up, in which minor and major axis rotations and vertical and horizontal displacements were allowed. The FE model for R1-S specimens is shown in Figure 6.4, where the location of the reference points and boundary conditions are clearly indicated. Loads were applied following two steps: the vertical loading was firstly applied and kept constant, and then the cyclic bending moment was introduced as an imposed horizontal displacement. The amplitude of the horizontal displacement followed the multiple-step loading protocol described in (Fang et al. 2018), which coincides with that prescribed in (AISC 341 2016). True stress-strain curves assigned to the flat and corner parts of the cross-section were obtained using the two-stage Ramberg-Osgood material. Table 6.1 summarises the parameters used to develop the Ramberg-Osgood material curves,

as reported in (Fang et al. 2018). A combined hardening law with half-cycle data and backstress = 1 was assumed.

Table 6.1. Basic material properties for R1 specimens reported in (Fang et al. 2018).

	E [GPa]	f_y [MPa]	f_u [MPa]	ε_u [mm/mm]	n	m
Flat part	189.9	426.2	875.1	0.556	6.1	2.7
Corner part	189.9	741.0	803.8	0.078	6.1	4.2

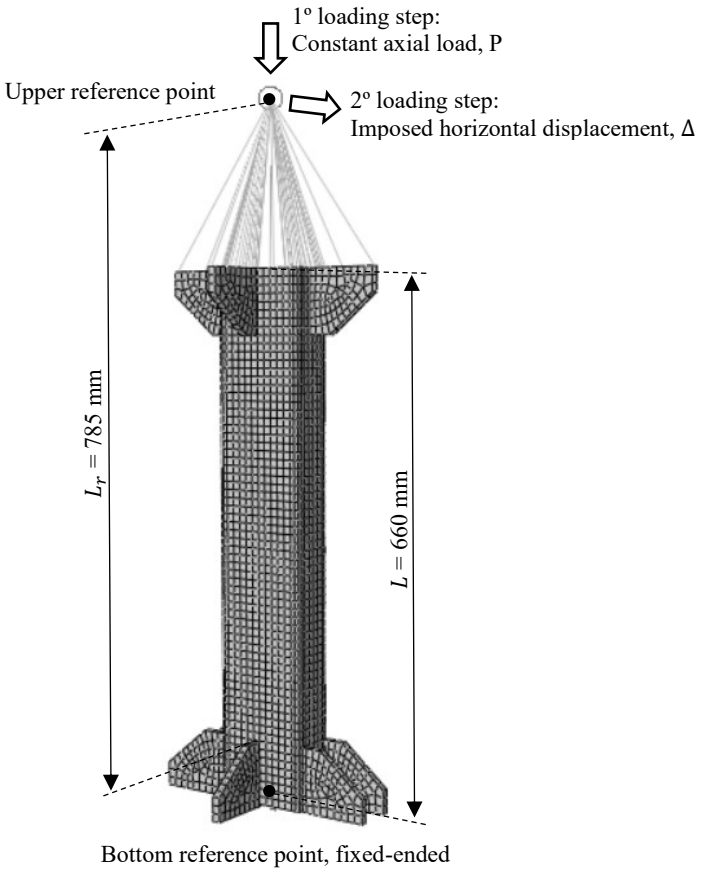

Figure 6.4. Finite element model for the R1-S specimens tested by Fang et al. (2018).

Figure 6.5 shows the experimental moment-drift curves for the (a) R1-n.02-W and (b) R1-n.02-S specimens as provided in (Fang et al. 2018), in which the numerically predicted responses obtained in this study are also plotted. It can be appreciated that the hysteretic loops from the tests and the numerical simulations exhibit a good agreement, with small but reasonable deviations. The numerical simulations responses are influenced by the consideration of the corner regions with enhanced material properties, among other factors. Note that for this study enhanced material properties were assigned to the corner regions plus two adjacent regions, as described above, while the model developed in (Fang et al. 2018) limited the enhanced properties to the corner regions only.

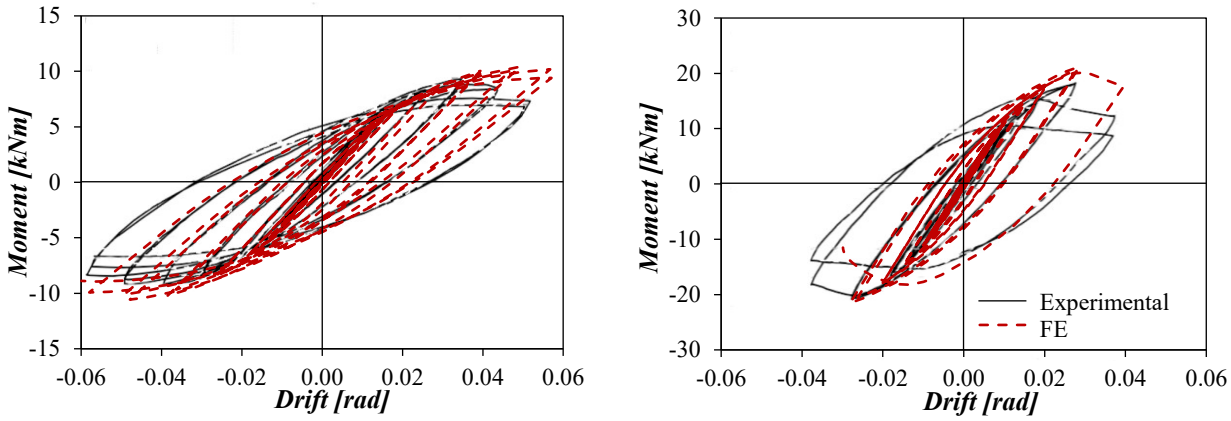

(a) (b)

Figure 6.5. Comparison of experimental and FE moment-drift responses for (a) R1-n0.2-W and (b) R1-n0.2-S specimens reported in (Fang et al. 2018).

The numerical-to-experimental ultimate bending moment M_u and corresponding drift θ_{Mu} ratios are summarised in Table 6.2, including the mean values and the coefficients of variation (COV), with deviations similar to those reported in (Fang et al. 2018). Therefore, it can be concluded that the characteristics of the FE model developed in this study (type of finite elements, boundary conditions, loading protocol, and the material model adopted) are suitable to model the cyclic response of stainless steel members.

Table 6.2. Comparison of FE and test results reported in (Fang et al. 2018) for R1 specimens.

Specimen	$M_{u,FE}$ [kNm]	$\theta_{Mu,FE}$ [rad]	$M_{u,exp}$ [kNm]	$\theta_{Mu,exp}$ [rad]	$M_{u,FE}/M_{u,exp}$	$\theta_{Mu,FE}/\theta_{Mu,exp}$
R1-n0.2-W	10.42	0.049	9.33	0.042	1.12	1.17
R1-n0.4-W	8.35	0.028	7.83	0.028	1.07	0.99
R1-n0.2-S	21.07	0.028	18.38	0.029	1.15	0.97
R1-n0.4-S	16.51	0.020	14.77	0.020	1.12	0.99
Mean					1.11	1.04
COV					0.026	0.090

6.3. Parametric study and results

In this section, the characteristics of the specimens covered in the parametric study are presented. The resulting moment-rotation responses, ultimate moment values and rotation capacities are also provided and discussed.

6.3.1. Description of the parametric study

The parametric study developed in this study investigated the behaviour of 120 stainless steel hollow section beams under cyclic major axis bending. Although the parametric study focused on compact RHS and SHS cross-sections (referred to as class 1 cross-sections in prEN 1993-1-4 (2021), some more slender cross-sections were also included to fully investigate the cyclic hardening and rotation capacity of stainless steel tubular members. The considered cross-sectional total heights ranged from 62 mm to

186 mm, total widths from 62 mm to 156 mm and wall thicknesses between 2 mm and 6 mm. The external corner radius was also modelled and measured $R_{ext} = 2t$ as recommended in (Arrayago et al. 2020a), being t the wall thickness. The parametric study covered austenitic, ferritic and duplex alloys. Table 6.3 summarises the key material parameters for flat and corner regions used to calculate the weighted average material properties assigned to the entire cross-sections. These parameters, which have also been used in previous parametric studies (Arrayago et al. 2017b, 2020d, 2021), were obtained from the monotonic tensile coupon tests reported in (Arrayago and Real 2016) for ferritic stainless steel and published in (Zhao et al. 2016a) for austenitic and duplex stainless steels. Local slenderness $\bar{\lambda}_p$ values ranged from 0.21 to 0.64, and thus corresponded to fully-effective cross-sections since the slenderness limit between slender and fully-effective cross-sections is $\bar{\lambda}_p$ = 0.68 according to the CSM (Afshan and Gardner 2013b; Bock et al. 2015). Local slenderness values were determined as mentioned in Section 2.4.2.

Table 6.3. Key material characterisation parameters for parametric studies.

Stainless steel	Cross-section region	E [GPa]	f_y [MPa]	f_u [MPa]	ε_u [mm/mm]	n	m
Austenitic	Flat	196	355	608	0.45	5.9	3.5
	Corner	201	559	725	0.28	4.8	4.1
Ferritic	Flat	187	485	505	0.07	12.2	2.6
	Corner	178	555	587	0.01	7.9	5.2
Duplex	Flat	198	635	756	0.44	6.0	4.2
	Corner	207	833	1079	0.23	5.0	6.1

6.3.2. Skeleton curves

The results of the parametric study are analysed herein using the skeleton curves of the moment-rotation response of the specimens under cyclic loading obtained by connecting the peak rotation points of the moment-rotation hysteretic loops (Fang et al. 2018). For consistency with the loading protocol, in this study, rotations are defined according to the principles of rigid body mechanism. Hence, rotations (i.e., drift angles) were calculated as the ratios between the deflection measured at the critical section, which for simplicity was assumed to be the loading section, and the distance between the support and the loading sections (i.e., the lever arm L_r= 510 mm). Bending moments were calculated as the product of the vertical reactions obtained at the support and the distance between the support and the loading section (L_r = 510 mm).

The skeleton curve allows the characterisation of the parameters that refer to the ductility of a specimen, such as the ultimate bending moment and the plastic rotation. The ultimate bending moment M_u is the peak moment of the skeleton curve, while the definition of the plastic rotation adopted in this research is based on the prescriptions given in prEN 1998-1-2 (2021), which states that the plastic rotation θ_{pl}

is the difference between the ultimate θ_u and the elastic θ_y rotations of the skeleton curve at a reference bending moment equal to the plastic moment M_{pl}, being M_{pl} the product of the plastic section moduli W_{pl} and the yield stress f_y. As shown in Figure 6.6, the elastic rotation θ_y considered in this study corresponds to the intersection point between the initial tangent stiffness and the plastic bending moment M_{pl}, while the ultimate rotation θ_u corresponds to the rotation when the moment degrades to M_{pl} after reaching M_u. The rotation at the ultimate bending moment is referred to as θ_{Mu} in Figure 6.6.

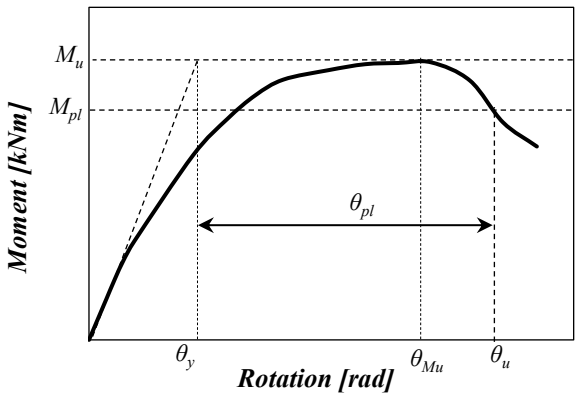

Figure 6.6. Definition of the plastic rotation based on prEN 1998-1-2 (2021).

Figure 6.7 shows the skeleton curves for the (a) austenitic, (b) ferritic and (c) duplex stainless steel beams studied. Note that in Figure 6.7 bending moment values are normalised by the plastic bending moment capacities M_{pl}. A preliminary analysis of the skeleton curve patterns indicated that these depend on the cross-section and material characteristics. To facilitate the analysis of the results, beams have been categorised into four groups according to their local slenderness (beams with local slenderness values $\bar{\lambda}_p > 0.55$ are plotted in green, while black curves correspond to beams with $0.43 \leq \bar{\lambda}_p < 0.55$, blue curves to beams with $0.32 \leq \bar{\lambda}_p < 0.43$, and red curves to beams with $\bar{\lambda}_p < 0.32$). As shown in Figure 6.7, specimens exhibited an elastic deformation until a rotation of 1%-2%, which is consistent with the findings reported in (Fang et al. 2018). Then, the hysteretic loops became higher due to strain hardening and cyclic hardening, i.e., specimens started to exhibit inelastic deformations. Plastic rotation values were found to be related to the local slenderness of the cross-sections, with plastic rotation values increasing as the local slenderness values decreased. Thus, the curves of the stockiest cross-sections (cross-sections with $\bar{\lambda}_p < 0.32$) reached the highest values of plastic rotations and exhibited a more stable hysteretic behaviour with larger dissipated energy. On the other hand, slender sections showed lower values of plastic rotation and only reached moment values higher than M_{pl} for a few cycles. Figure 6.7 also suggests a correlation between the local slenderness and the post-buckling behaviour of the beams. Thus, the difference between the ultimate rotation θ_u and the rotation associated with the ultimate bending moment θ_{Mu} decreases as the value of the local slenderness increases.

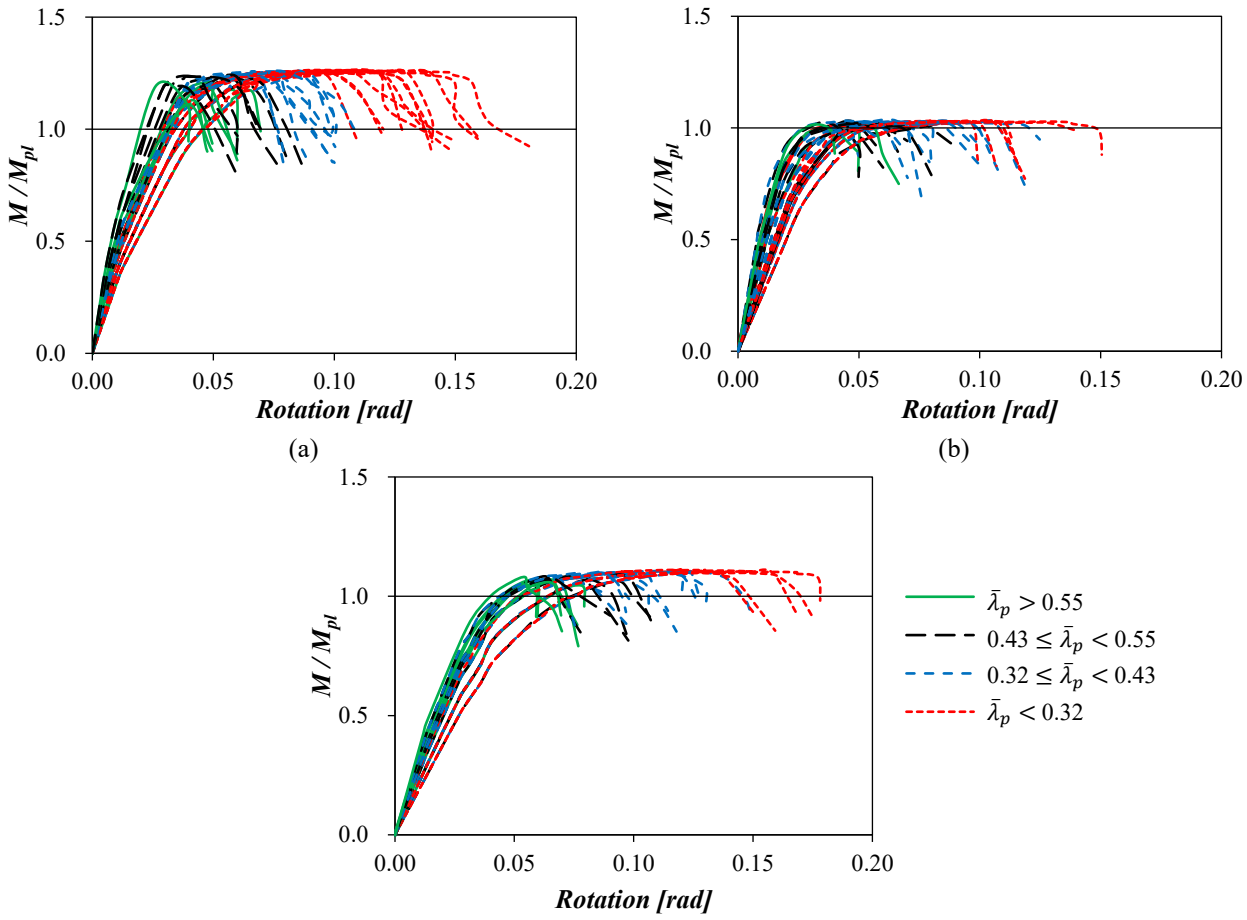

Figure 6.7. Skeleton curves for the studied (a) austenitic, (b) ferritic and (c) duplex stainless steel beams under cyclic loading for different cross-section slenderness ranges.

Regarding the differences observed between the three stainless steel families investigated, the results showed that the austenitic beams started to develop inelastic deformations at the early stages of the loading protocol (i.e., low number of cycles), which is consistent with the typically more rounded stress-strain diagram of austenitic stainless steels (Arrayago and Rasmussen 2021a). As reported in Zhou and Li (2016), austenitic beams exhibited higher values of normalised ultimate bending moment than duplex beams, while the maximum ultimate rotation occurred for a duplex stainless steel beam. On the contrary, ferritic alloys, which typically show less rounded stress-strain curves and lower ductility and strain hardening properties than duplex and austenitic stainless steels, exhibited the lowest plastic rotation and normalised ultimate bending moment values.

6.3.3. Ultimate moment capacities

Numerically predicted ultimate moment values ranged from 4.92 to 99.95 kNm in the case of austenitic beams, from 7.52 to 97.61 kNm for ferritic beams and from 11.37 to 95.93 kNm for duplex beams. Figure 6.8 shows the comparison between the numerical ultimate bending moment resistance M_u and the plastic bending moment capacity M_{pl} as a function of the local slenderness of the cross-section $\bar{\lambda}_p$.

As mentioned in the previous section, the highest M_u/M_{pl} ratios corresponded to austenitic specimens followed by duplex beams, while the M_u/M_{pl} ratios for ferritic beams were close to unity. Even though some of the flanges of the slenderest sections were very close to class 4 according to the prEN 1993-1-4 (2021) cross-section classification limits, all the ultimate bending moment values were higher than M_{pl}. The prEN 1993-1-4 classification is based on the slenderness of the individual plates constituting the cross-sections, and does not account for the contribution of the webs to the local stability of the flanges, tending to be conservative. In fact, if the interaction of the different elements is considered in the calculation of the local slenderness through the elastic local buckling stress of the full cross-section $\sigma_{cr,l}$, as described in Section 2.4.2, all beams investigated are fully-effective ($\bar{\lambda}_p \leq 0.68$). Furthermore, under cyclic loading, higher strengths are to be expected due to hardening effects (Kaufmann et al. 2001; Chacón et al. 2018; Fang et al. 2018). This explains why the numerical M_u values were not only higher than M_{pl}, but also close to the bending moment resistances predicted by the Continuous Strength Method (CSM) M_{csm} (see Eq. 2.6), which considers strain hardening effects.

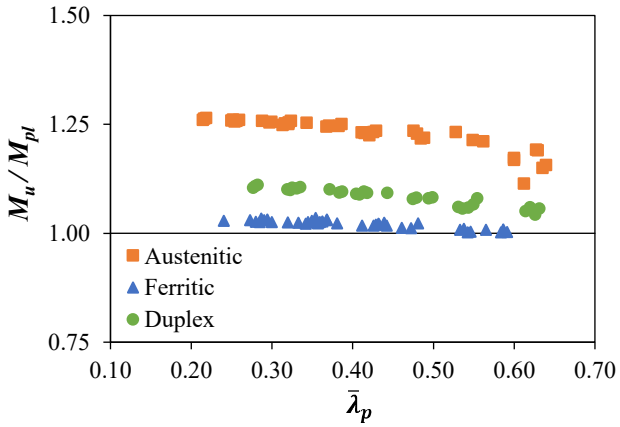

Figure 6.8. Comparison of the ultimate bending moment values M_u with the plastic bending resistance M_{pl} for different stainless steel grades.

Table 6.4 reports the mean values and COV values of the numerical-to-plastic M_u/M_{pl} and numerical-to-CSM M_u/M_{csm} bending moment resistance ratios for the different stainless steel beams investigated. As shown in this Table, assuming that the ultimate bending moment resistance of stainless steel beams subjected to cyclic loading is equal to the plastic bending moment resistance M_{pl} is safe but overconservative, especially in the case of austenitic grades. On the other hand, more accurate and safe predictions of the ultimate bending strengths are obtained when the CSM approach is considered for the different stainless steel families analysed, in line with the conclusions drawn by several previous investigations on stainless steel beams subjected to monotonic loading (Afshan and Gardner 2013b; Bock et al. 2015; Zhao et al. 2017; Arrayago et al. 2017b).

Table 6.4. Assessment of the Eurocode and CSM approaches to predict the ultimate bending resistance of stainless steel RHS beams under cyclic loading.

Stainless steel	M_u/M_{pl}		M_u/M_{csm}	
	Mean	COV	Mean	COV
Austenitic	1.23	0.029	1.12	0.088
Ferritic	1.02	0.009	0.99	0.028
Duplex	1.08	0.018	1.04	0.052

6.3.4. Analysis of rotations and rotation capacities

Ultimate rotation θ_u values ranged from 0.040 to 0.168 rad in the case of austenitic beams, from 0.034 to 0.146 rad for ferritic beams and from 0.059 to 0.178 rad for duplex beams. Similarly, elastic rotation θ_y values, graphically obtained as the intersection point between the initial tangent stiffness and the plastic bending moment M_{pl}, as explained previously, varied from 0.014 to 0.032 rad in the case of austenitic beams, from 0.016 to 0.040 rad in the case of ferritic beams and from 0.028 to 0.053 rad for duplex beams. More detailed mean values of the elastic θ_y, ultimate θ_u and peak moment θ_{Mu} rotations estimated from the parametric study for different stainless steel families and slenderness ranges are reported in Table 6.5, where No. refers to the number of investigated beams for each group. The mean values shown in Table 6.5 correspond to the sub-groups of beams included in the local slenderness ranges indicated. Mean differences between the ultimate θ_u and elastic θ_y rotations, also known as the plastic rotation θ_{pl}, and between the ultimate θ_u and peak moment θ_{Mu} rotations, which are associated to the post-buckling behaviour, are also given in Table 6.5.

Table 6.5. Mean numerical rotation values for stainless steel beams under cyclic loading.

Stainless steel	$\bar{\lambda}_p$	No.	θ_y [rad]	θ_{Mu} [rad]	θ_u [rad]	θ_u-θ_y [rad]	θ_u-θ_{Mu} [rad]
Austenitic	$\bar{\lambda}_p < 0.32$	13	0.027	0.104	0.137	0.111	0.033
	$0.32 \leq \bar{\lambda}_p < 0.43$	11	0.023	0.073	0.092	0.069	0.019
	$0.43 \leq \bar{\lambda}_p < 0.55$	7	0.021	0.054	0.068	0.048	0.015
	$\bar{\lambda}_p > 0.55$	9	0.021	0.044	0.052	0.031	0.007
Ferritic	$\bar{\lambda}_p < 0.32$	9	0.031	0.093	0.111	0.080	0.018
	$0.32 \leq \bar{\lambda}_p < 0.43$	12	0.028	0.074	0.088	0.060	0.014
	$0.43 \leq \bar{\lambda}_p < 0.55$	12	0.026	0.055	0.059	0.033	0.004
	$\bar{\lambda}_p > 0.55$	7	0.025	0.045	0.046	0.021	0.001
Duplex	$\bar{\lambda}_p < 0.32$	7	0.047	0.135	0.161	0.114	0.026
	$0.32 \leq \bar{\lambda}_p < 0.43$	13	0.041	0.105	0.117	0.075	0.012
	$0.43 \leq \bar{\lambda}_p < 0.55$	12	0.039	0.078	0.087	0.048	0.009
	$\bar{\lambda}_p > 0.55$	8	0.036	0.064	0.068	0.032	0.003

Additionally, the plastic rotation capacity of the beams has been calculated following the definitions given in (Mazzolani and Piluso 1997; Nastri and Piluso 2020), which state that the plastic rotation capacity is determined from the normalised moment-rotation curve. Figure 6.9 defines graphically the two measures of plastic rotation capacities established in (Mazzolani and Piluso 1997; Nastri and Piluso 2020).

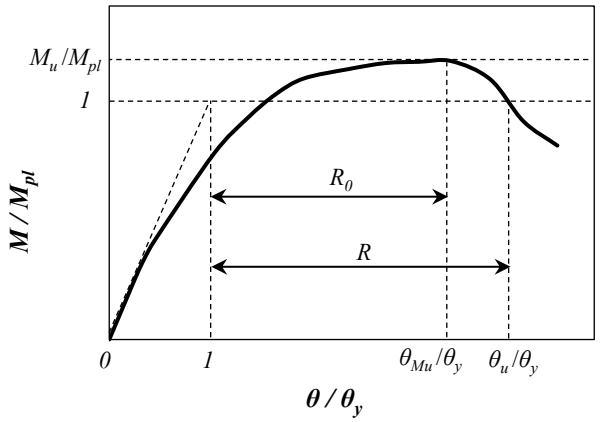

Figure 6.9. Definition of the plastic rotation capacities, R_0 and R.

As shown in Figure 6.9, the plastic rotation capacity disregards the elastic rotation θ_y and can refer either to the stable part of the plastic rotation capacity R_0, which is related to the maximum bending moment, or to the total plastic rotation capacity R, which also includes the post-buckling behaviour. Note that the rotations in Figure 6.9 are normalised by the elastic rotation θ_y. This normalisation allows to implicitly account for the structural configuration (including the length of the beam and boundary conditions) and to derive more generic predictive equations that are independent of these parameters. Equations for determining the stable part R_0 and the total R plastic rotation capacities are given in Eq. 6.1 and Eq. 6.2, respectively.

$$R_0 = \frac{\theta_{Mu}}{\theta_y} - 1 \qquad \text{Eq. 6.1}$$

$$R = \frac{\theta_u}{\theta_y} - 1 \qquad \text{Eq. 6.2}$$

Figure 6.10 shows the (a) stable part R_0 and (b) total R plastic rotation capacities obtained from the parametric study for the different stainless steel alloys and plotted against the corresponding local slenderness values. The plastic rotations have been calculated from Eq. 6.1 and Eq. 6.2 using the elastic rotation θ_y obtained from the skeleton curves to normalise the rotations. From Figure 6.10, the plastic rotation capacities show a clear descending trend for increasing local slenderness values for the three materials, being the results for ferritic and duplex alloys very similar, while the plastic rotation capacities of austenitic beams are slightly higher due to their pronounced ductility. Results in Figure 6.10 suggest that a mathematical function can be proposed, as a function of the local slenderness, to

estimate the stable part and total plastic rotation capacities of stainless steel beams under cyclic loading. This is addressed in the following Section and it is of critical importance in seismic design since the rotation capacity of members affects the capacity of structures, as mentioned in Section 6.1.

6.4. Expressions for the prediction of rotation capacities

In this section, the development of the analytical expressions proposed to estimate the stable part R_0 and the total R plastic rotation capacities of stainless steel RHS cross-sections under cycling loading is presented, as well as a tri-linear model to describe the full moment-rotation curves to use in analysis software for design. The assessment of the accuracy of the proposed expressions and examples of full moment-rotation curves developed with the proposed formulation are also provided.

6.4.1. Analytical expressions for the prediction of plastic rotation capacities

According to the results shown in Figure 6.10, both plastic rotation capacities increase as the local slenderness decreases describing a trend that can be fitted to a power function. Power functions are typically used in the development of design expressions for the estimation of section capacities that depend on the local slenderness under static forces (including strain hardening and local buckling effects), such as the Continuous Strength Method base curve (Afshan and Gardner 2013b) and the different Direct Strength Method strength curves (Becque et al. 2008; Arrayago et al. 2017a).

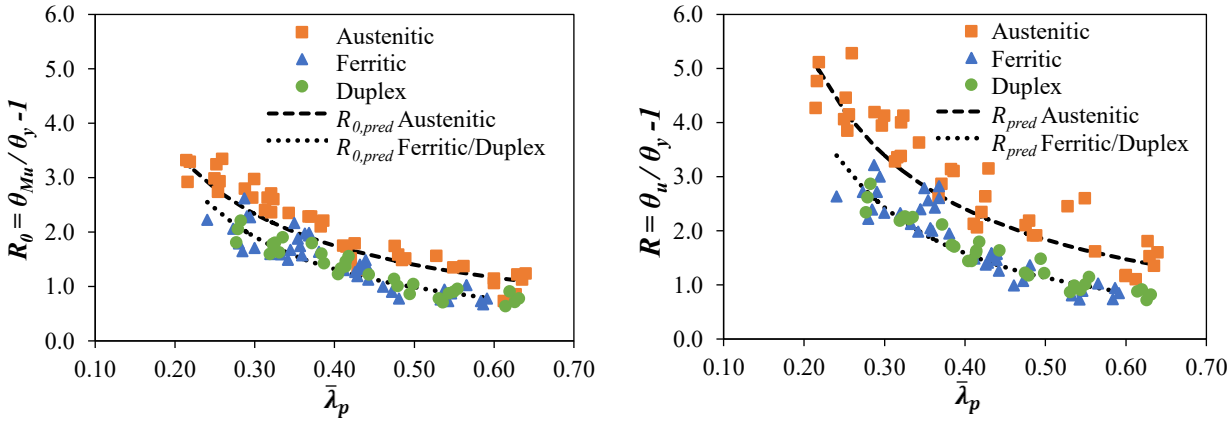

Figure 6.10. Proposal for predicting (a) the stable part of the plastic rotation capacity R_0 and (b) the total plastic rotation capacity R of stainless steel beams under cyclic loading.

Eq. 6.3 shows the proposed power function for estimating the rotation capacities of stainless steel RHS cross-section beams under cyclic loading, where the subscript i refers to the stable part R_0 or the total R plastic rotation capacity, and β and ρ are coefficients to be calibrated from the numerical data generated in this study.

$$R_{i,pred} = \frac{\beta}{\bar{\lambda}_p^{\rho}} \qquad \text{for} \quad \bar{\lambda}_p \leq 0.68 \qquad \text{Eq. 6.3}$$

As highlighted in the previous section, Figure 6.10 shows that austenitic and ferritic/duplex stainless steels behave differently, suggesting that two different functions are necessary for an accurate prediction of the stable part R_0 and the total R plastic rotation capacities of stainless steel RHS beams under cyclic loading with $\bar{\lambda}_p \leq 0.68$. Note that although traditional structural design has considered the behaviour of austenitic and duplex stainless steels to be comparable (prEN 1993-1-4 2021; AISC 370 2021; ASCE 8 2022), recent studies have also demonstrated that duplex stainless steels can be safely grouped with ferritic grades (Arrayago and Rasmussen 2021a). The values of the calibrated β and ρ coefficients, particularised for each stainless steel family (or group of families), are reported in Table 6.6, and the resulting expressions are plotted as dashed (austenitic) and dotted lines (ferritic/duplex) in Figure 6.10. As mentioned earlier, by normalising the rotation values with the elastic rotation it is possible to eliminate the effects of the member length L and the boundary conditions, which are assumed to be implicit in θ_y.

Table 6.6. Coefficients for the proposed expressions to predict the stable part and total plastic rotation capacities of stainless steel beams under cyclic loading.

Stainless steel	Stable part of the rotation capacity $R_{0,pred}$		Total rotation capacity R_{pred}	
	β	ρ	β	ρ
Austenitic	0.7	1.0	0.8	1.2
Ferritic/Duplex	0.4	1.3	0.4	1.5

6.4.2. Assessment of the proposed rotation capacity expressions

The assessment of the proposed expressions for the prediction of the stable part R_0 and the total R plastic rotation capacities is presented in this section by comparing the predicted rotation capacities, calculated with Eq. 6.3 and the β and ρ coefficients reported in Table 6.6, to the corresponding numerical rotation capacities. As shown in Figure 6.10(a), the proposed expressions for the prediction of R_0 are in good agreement with the FE data for all materials. Similar conclusions can be drawn from Table 6.7, where the mean and COV values of the predicted-to-numerical plastic rotation capacity ratios $R_{0,pred}/R_{0,FE}$ for the different stainless steel alloys are reported. As shown, the mean values of the $R_{0,pred}/R_{0,FE}$ ratios are close to unity, with a relatively low scatter in the results for all stainless steel grades, especially for duplex grades. Note that since values higher than 1.0 are considered to be on the unsafe side, the proposed expressions provide a reasonable margin of safety. On the other hand, as shown in Figure 6.10(b), the prediction of the total rotation capacity is also accurate for all stainless steel grades, especially for duplex beams. Analogous results to those obtained for the stable part of the rotation capacity are observed from the R_{pred}/R_{FE} ratios reported in Table 6.7, i.e., total rotation capacity predictions for all stainless steel grades are close to, but lower than, unity, while the scatter of the results is reasonable for all materials. In addition, it is worth noting that the β and ρ coefficients reported in Table 6.6 are also valid when the local slenderness value is computed following the prEN

1993-1-4 (2021) procedure. The resulting local slenderness values were slightly higher than those obtained from the CUFSM software (Li and Schafer 2010), because the interaction between plates is not taken into account. For the cross-sections considered in this study, the values of the local slenderness computed according to the prEN 1993-1-4 (2021) were between 0 and 9% higher than those obtained numerically. As a result, the prediction of the rotation capacities using the proposed expressions with the plate slenderness was found to be almost identical and safe-sided, obtaining slightly lower rotation capacities when using the analytical value of the local slenderness.

Table 6.7. Assessment of the proposed expressions for the prediction of rotation capacities of stainless steel beams under cyclic loading.

Stainless steel	$R_{0,pred}/R_{0,FE}$		R_{pred}/R_{FE}	
	Mean	COV	Mean	COV
Austenitic	0.95	0.156	0.94	0.165
Ferritic	0.98	0.162	0.98	0.176
Duplex	0.99	0.119	0.97	0.102
All grades	0.97	0.146	0.96	0.147

6.4.3. Estimation of moment-rotation curves for stainless steel beams under cyclic loading

The equations proposed in the previous section for the estimation of the stable part and the total rotation capacities can be used to characterise the behaviour of stainless steel beams under cyclic loading in a simplified way and to propose a model that describes the full moment-rotation curves. The proposed moment-rotation curves can be directly implemented in the definition of the concentrated plasticity hinge behaviour of stainless steel structures in analysis software, allowing a more accurate and safer design under seismic forces. To estimate the actual moment-rotation relationship, a tri-linear model is proposed. Figure 6.11 illustrates the proposed tri-linear moment-rotation model, in which the different branches are clearly indicated: (1) a first upward elastic branch from the origin to (θ_y, M_{pl}); (2) a second upward branch from (θ_y, M_{pl}) to (θ_{Mu}, M_{csm}); and (3) a downward linear branch from (θ_{Mu}, M_{csm}) to (θ_u, M_{pl}). The procedure for plotting this tri-linear model is described below.

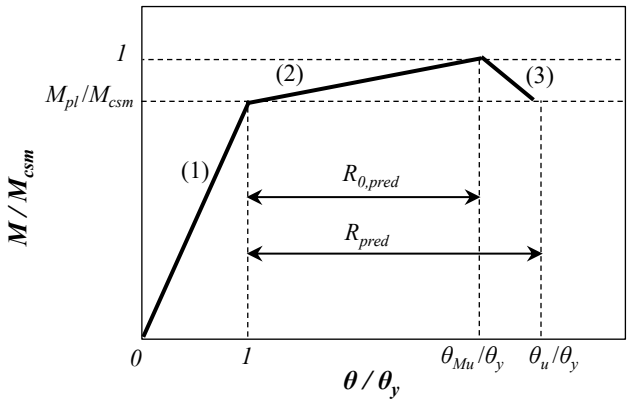

Figure 6.11. Proposed tri-linear moment-rotation curve for a typical RHS stainless steel beam under cyclic loading based on the proposed $R_{0,pred}$ and R_{pred} functions.

The plastic bending moment capacity is calculated from the well-known expression $M_{pl} = f_y \cdot W_{pl}$, while the ultimate moment according to the CSM (i.e., $M_u = M_{csm}$) is given in Eq. 2.6. Regarding the rotation values, once the local slenderness and the stainless steel family of the specimen are known, the stable part $R_{0,pred}$ and total R_{pred} rotation capacities can be estimated from Eq. 6.3 using the suitable β and ρ coefficients. Next, the resulting rotation capacities $R_{0,pred}$ and R_{pred} can be substituted into Eq. 6.1 and Eq. 6.2, respectively, from which the values of the rotation associated with the ultimate bending moment θ_{Mu} and the ultimate rotation θ_u can be determined if an analytical expression for the elastic rotation θ_y is established. The value of the elastic rotation θ_y corresponding to the plastic bending moment capacity can be directly calculated from the elastic rotation of the beam or estimated from the deflection formulae and the lever arm (L_r) for simple structural configurations similar to that adopted herein. In this study, the latter approach is proposed to be consistent with the method adopted in the determination of the numerical rotations, as described in Section 6.3.1, and the analytical elastic rotation $\theta_{y,an}$ is given in Eq. 6.4, where L is the total length of the beam and I is the moment of inertia. Eq. 6.4 is derived from the elastic deflection equation for a beam loaded under four-point bending conditions and assumes that the elastic part of the rotation is the ratio between the elastic deflection at the loading point for a load equivalent to the plastic moment capacity M_{pl} and the distance between the loading point and the support (i.e., the lever arm L_r).

$$\theta_{y,an} = \frac{M_{pl}}{6EI}(3L - 4L_r) \qquad \text{Eq. 6.4}$$

The comparison between the analytical elastic rotations calculated from Eq. 6.4 and the corresponding numerical elastic rotations obtained graphically from the skeleton curves is presented in Figure 6.12, which shows that the estimated and numerical elastic rotations are in good agreement. For members subjected to loading conditions other than four-point configurations, alternative expressions for $\theta_{y,an}$ should be derived using the appropriate elastic deflection formulae, but the remaining steps of the procedure would be analogous to those described herein.

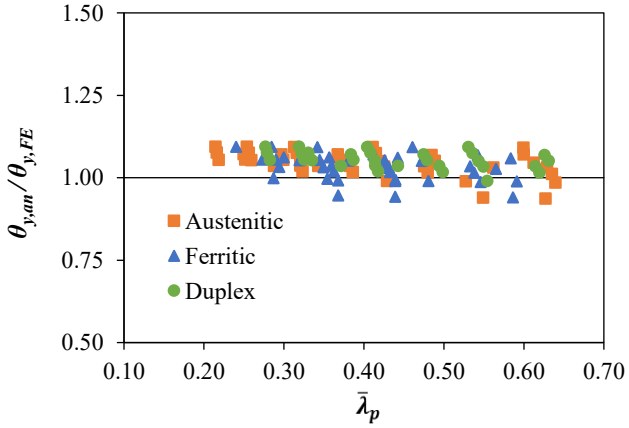

Figure 6.12. Comparison of the analytical elastic rotations obtained from Eq. 6.4 and numerically.

Figure 6.13 compares the moment-rotation responses predicted using the proposed model with the corresponding numerical responses for some typical austenitic, ferritic and duplex RHS beams with different local slenderness values under cyclic loading. As shown in Figure 6.13, the estimated moment-rotation curves are in good agreement with the numerical results. Moderate overpredictions of the rotation values before reaching the plastic bending moment M_{pl} are obtained due to the definition of the elastic rotation θ_y given in prEN 1998-1-2 (2021) and adopted in this study (Section 6.3.2) and the nonlinear response exhibited by stainless steel beams. Nevertheless, the tri-linear models shown in Figure 6.13 demonstrate the accuracy of the proposed expressions for predicting the rotation capacities in general, as well as for the proposed analytical procedure to calculate the elastic rotation and the convenience of assuming that the ultimate bending moment capacity under cyclic loading is equal to the CSM bending resistance.

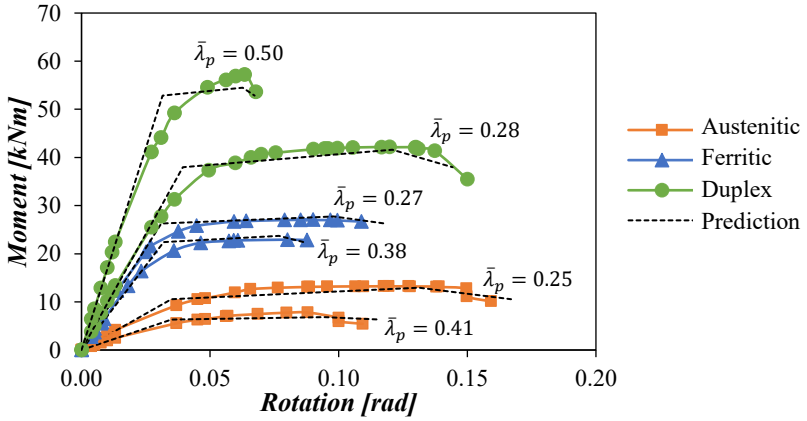

Figure 6.13. Comparison of the moment-rotation responses obtained numerically and estimated using the proposed tri-linear model and rotation capacity functions.

6.5. Concluding remarks

This chapter presents a numerical study on 120 austenitic, ferritic and duplex stainless steel rectangular hollow section beams under cyclic loading with the aim of proposing expressions to estimate the maximum bending moment and rotation capacity of these members that can be useful for computing the actual capacity of stainless steel structures and for predicting the overstrength parameters for the application of capacity design principles. The results have shown that the ultimate strength and rotation capacities of the beams are dependent on the local slenderness of the cross-section and the strain hardening characteristics of the material, and that the ultimate bending moment capacity under cyclic loading can be accurately predicted by the Continuous Strength Method equation for stainless steel beams. For both the stable part and the total plastic rotation capacity of stainless steel beams under cyclic loading, simple power functions depending only on the local slenderness and the elastic rotation are proposed. Based on the derived equations for the estimation of the rotation capacities, a tri-linear model that describes the full moment-rotation curves of stainless steel beams under cyclic loads is

proposed, which can be implemented into existing analysis software to define the behaviour of concentrated plastic hinges.

Corresponding publication: González-de-León I., Arrayago I., Real E. and Nastri E. (2022). Rotation capacity of cold-formed stainless steel RHS beams under cyclic loading. *Journal of Constructional Steel Research*, 192, 107199. https://doi.org/10.1016/j.jcsr.2022.107199

CHAPTER 7

Experimental study on stainless steel tubular members under cyclic loading

7.1. Introduction

In light of the scarce experimental research devoted to the hysteretic behaviour of stainless steel members, the Universitat Politècnica de Catalunya (Spain) has recently promoted a collaboration with the Università degli Studi di Salerno (Italy) to conduct a series of cyclic tests on austenitic hollow section elements. A total of nine specimens with different local and member slenderness values were tested. This chapter describes the experimental programme, including information about the loading protocol and the experimental set-up, and the relevant results obtained from the cyclic tests – failure modes, load-displacement and moment-rotation histories, evolution of the secant stiffnesses and accumulative energy dissipation. The aims of this study are to assist the research community in planning similar experimental programmes and to contribute to the experimental data pool available in the literature for validating numerical models of stainless steel members and frames under cyclic loading.

7.2. Experimental programme

This section describes the experimental programme on stainless steel rectangular hollow section members under cyclic bending promoted by the Universitat Politècnica de Catalunya and conducted at the STRuctural ENGineering Test Hall (STRENGTH) laboratory of the Università degli Studi di Salerno. The geometric properties of the specimens, material characterisation, test set-up configuration and the loading protocol assumed are described herein.

7.2.1. Description of the specimens

The experimental programme comprised nine cold-formed rectangular hollow section members made from EN 1.4301 austenitic stainless steel. The specimens were acquired and prepared by the Universitat Politècnica de Catalunya and were part of an extensive experimental programme carried out at the same university comprising tensile tests on coupons, stub columns, beams and columns, and the subsequent tests on stainless steel frames under vertical and horizontal loading, all of which have been reported in (Arrayago et al. 2020b, 2020c), i.e., Chapters 3 and 4 of this thesis. Thus, the geometric measurements of all cross-sections and the results from the tensile tests reported in Table 3.1 and Table 3.2, respectively, are applicable to the specimens investigated in this study.

Three different cross-sections were tested under cyclic conditions, referred to as: S1-120×80×6, S2-100×80×4 and S3-120×40×4. Table 7.1 summarises the geometric properties of the cross-sections measured before testing, where H is the total height, B is the total width, t is the wall thickness of the cross-sections and R_{ext} is the external corner radius. Note that the cross-sectional measurements reported in Table 7.1 correspond to average values of the CS1, CS2 and CS3 cross-sections published in Table 3.1. Table 7.1 also provides the cross-section classification according to prEN 1993-1-4 (2021) and the local slenderness $\bar{\lambda}_p$ values, calculated as given in Section 2.4.2. As shown in Table 7.1, all cross-sections are categorised as class 1 in bending. According to prEN 1998-1-2 (2021), in a high dissipative structural behaviour (Ductility Class 3 (DC3)), the cross-sections of elements where plastic hinges are expected to form must be class 1. Cantilevers with three different total lengths were covered, referred to as $L1_t$ =1730 mm, $L2_t$ = 1440 mm and $L3_t$ = 860 mm, although the corresponding effective lengths, to which all the results of this study refer, were L1 = 1650 mm, L2 = 1360 mm and L3 = 780 mm. As described in Section 7.2.3, the effective length was measured from the top of the base stiffeners to the loading section. Throughout this study, specimens are identified by their cross-section and effective length, e.g., S1-L1 corresponds to the specimen with the cross-section S1-120×80×6 and an effective length L1 = 1650 mm. Noted that measured initial local and member imperfection magnitudes reported in Table 3.1 are not relevant in this study because they have a negligible effect on the strength and stiffness of members when specimens are loaded transversally.

Table 7.1. Average cross-section dimensions for the investigated RHS.

Cross-section	Cross-section dimensions [mm]				Local slenderness $\bar{\lambda}_p$ in bending	Cross-section class in bending
	H	B	t	R_{ext}		
S1	120.0	80.0	6.0	20.1	0.27	Class 1
S2	99.8	80.2	3.9	12.6	0.42	Class 1
S3	120.1	41.1	3.9	12.1	0.32	Class 1

7.2.2. Material characterisation

The key material parameters relevant for this study correspond to those obtained from flat (F) and corner (Co) coupon tests cut from CS1, CS2 and CS3 cross-sections reported in Table 3.2.

7.2.3. Test set-up

The tests were carried out at the STRENGTH laboratory of the Department of Civil Engineering of the Università degli Studi di Salerno, with experience in testing steel structural members under cyclic loading (D'Aniello et al. 2012; Mitsui et al. 2018). Specimens were tested under cyclic bending around their major axis in an internal reaction frame. Figure 7.1 shows the general set-up of the L1 tests and provides a graphical definition of the effective length (L1, L2, L3), which is the distance between the top of the stiffeners and the centre of the loading section, as mentioned before. As described below, for the L2 and L3 tests the experimental set-up was identical to the one shown in Figure 7.1, but the specimens were raised 300 mm by anchoring a second steel element to the base. In the case of the L3 tests, the auxiliary structure was removed.

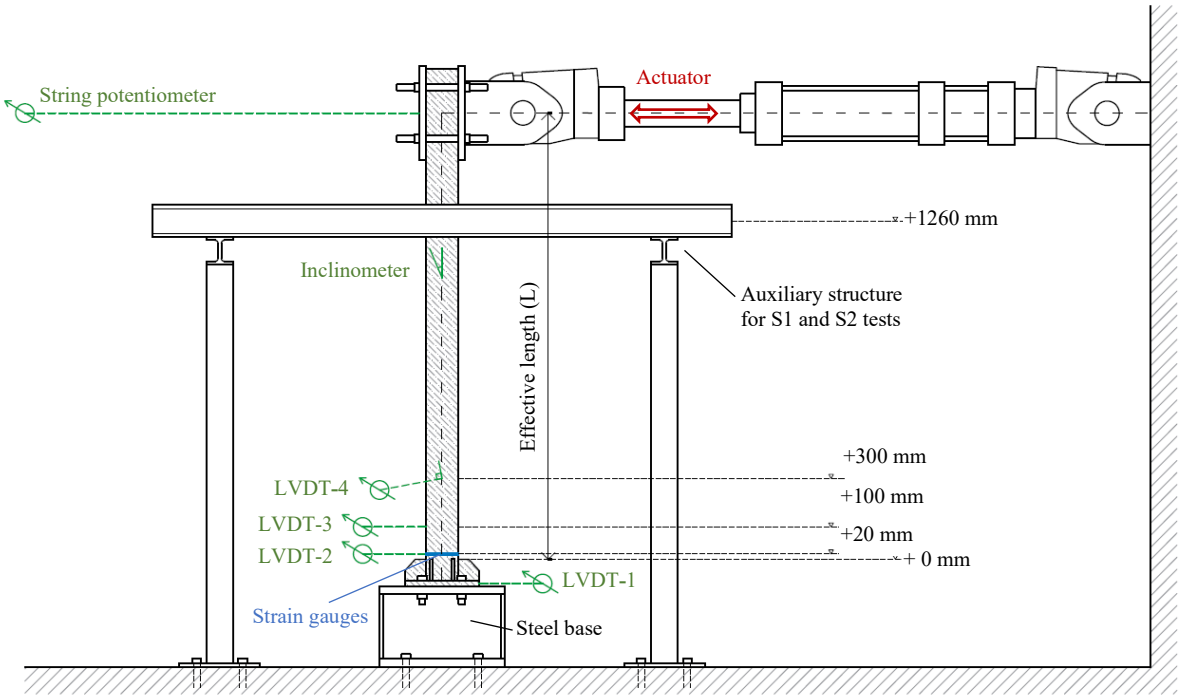

Figure 7.1. General set-up of stainless steel cyclic bending tests.

The cyclic bending tests were conducted following a cantilever loading scheme like the test configuration reported in (Fang et al. 2018), i.e., the bottom end of the specimens was fixed while the top end was free. The loading was applied at the top end of the specimens by imposing a horizontal displacement controlled by a MTS 243.60-02 hydraulic actuator. It should be mentioned that, unlike the loading scheme given in (Fang et al. 2018), no axial load was applied at the top of the specimens because the aim of this work is the investigation of the cyclic response under pure bending, which had not been investigated before to the best of the authors' knowledge – note that the tests conducted by Nip et al. (2010b), Zhou et al. (2018) and Kim et al. (2021) were under cyclic axial loading and those conducted by Fang et al. (2018) were under axial loads and cyclic bending. The loading section was carefully designed to prevent local failure. As shown in Figure 7.2(a), specimens were clamped between two 25 mm-thick steel plates held together by four bolts. One of these plates was, in turn, welded to the free end of the piston. Both ends of the piston were equipped with hinges (see Figure 7.1), thus ensuring that the actuator did not impose a bending moment on the top of the specimens. As shown in Figure 7.2(b), displacements and rotations were restrained at the support of the members by means of 20 mm-thick steel plates welded at the bottom edge of the specimens, similar to those used in the frame tests reported in Chapter 3. These plates were provided with four perforations, to be connected to the strong floor. In addition, the fixed-ended boundary conditions were strengthened by additional 80 mm-high steel stiffeners welded to the bottom end of the specimens and to the base steel plates. The configuration and thickness of the stiffeners depended on the cross-section dimensions. Figure 7.3 details the configuration of the end plates and stiffeners for the three cross-section geometries, where the thicknesses of the stiffeners A and B adopted values of $a = b = 10$ mm for S1 specimens, $a = b = 5$ mm for S2 specimens, and $a = 10$ mm and $b = 5$ mm for S3 specimens. Finally, the capacity of all welded connections to exceed the plastic bending moment of the cross-sections was verified numerically using IDEAStatiCa (2020).

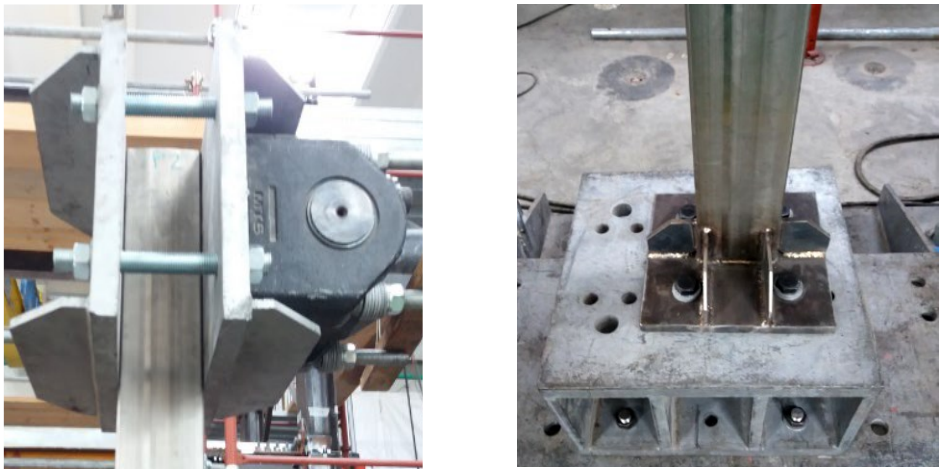

(a) (b)

Figure 7.2. Detailed view of the (a) loading (upper end) and (b) support (bottom end) sections of the specimens.

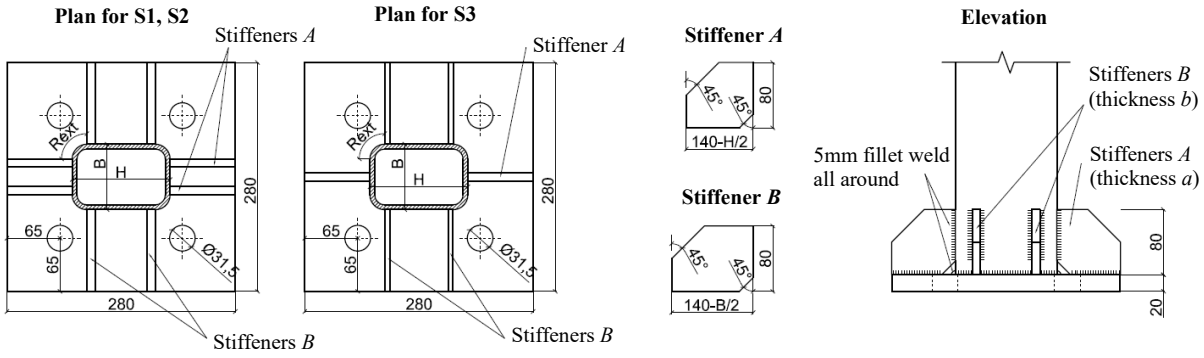

Figure 7.3. End connection details for the tested specimens.

In L1 and L2 tests, the out-of-plane response of the specimens was prevented by guiding the longitudinal displacements through two angular profiles separated by a distance equal to the cross-section width. Details of this auxiliary structure are shown in Figure 7.4. To minimise the friction between the restraining members and the specimens, the faces of the angular profiles in contact with the specimen were coated with petroleum jelly. The angular profiles were welded to two HEB 120 beams located at a height of 1260 mm from the top of the stiffeners for L1 specimens. In turn, these HEB 120 beams were bolted to fixed-ended auxiliary frames in which the rafter and column members were formed by HEB 100 and UPN 100 profiles, respectively. In L2 and L3 tests, the specimens were raised 300 mm above the configuration shown in Figure 7.1 by anchoring a second steel element to the base. Thus, the auxiliary HEB 120 beams were located at a height of 960 mm from the top of the stiffeners for L2 specimens. Note that the auxiliary structure was removed for L3 tests (the shortest specimens) since it obstructed the displacement of the piston.

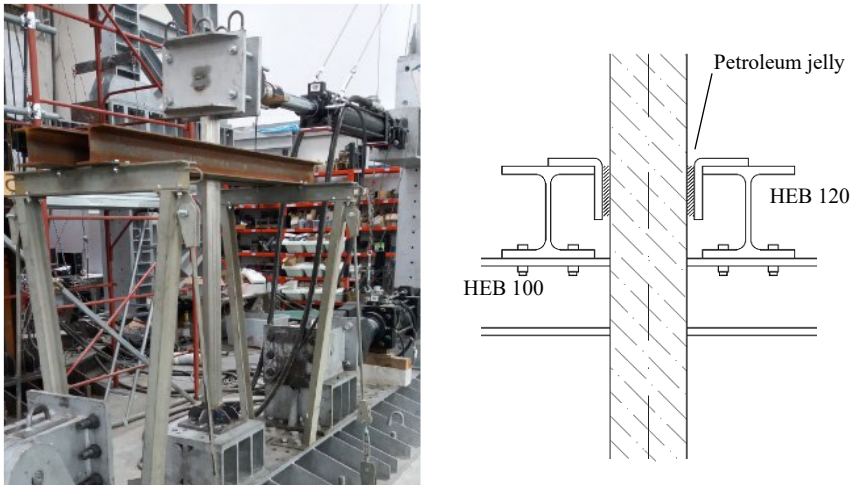

Figure 7.4. General view and detail of the auxiliary structure to avoid out-of-plane displacements.

Several measurement devices were included in the set-up with the aim of acquiring additional information and controlling the correct development of the tests. All measurement devices described below, and their location, are plotted in Figure 7.1. As shown, the horizontal displacement imposed by the actuator at the top end of the specimens was measured by a string potentiometer whose free end was

connected to the centre of the external loading plate. In addition, several LVDT transducers were used to measure short displacements at the support region. Thus, a first LVDT (LVDT-1 in Figure 7.1) was used to measure any in-plane horizontal displacements of the steel plate welded to the specimens at the support to capture any possible settlements of the element connecting the specimen to the strong floor. Hence, the specimen displacement could be obtained as the difference between the horizontal displacement measured by the string potentiometer and the one measured by LVDT-1. In addition, LVDT-2 was used just to check that the base connection was rigid, while LVDT-3 was used to check that the rotation at the base of the specimens was negligible. The last LVDT (LVDT-4) was used to record possible out-of-plane displacements, so it was of paramount importance in L3 tests where the auxiliary structure shown in Figure 7.4 was removed. LVDT-4 was located at the wider flat face of the cross-sections at a height of 300 mm from the top of the stiffeners. The in-plane rotations of the specimens were measured by inclinometers placed at the same face of the specimens at which LVDT-4 devices were located, and at a height from the top of the stiffeners that depended on the length of the member: 1100 mm for L1 tests, 800 mm for L2 tests and 500 mm for L3 tests. The rotations given by the inclinometer were used to double-check the drift angles calculated from the horizontal displacements recorded by the string potentiometer. Finally, strain gauges were attached to the wider flat faces of the specimens at a height of 20 mm above the web stiffeners, i.e., a total of four strain gauges were used per test, to control the strain distribution at the critical sections during the appearance of local buckling.

7.2.4. Loading protocol

The imposed horizontal displacement followed the multi-step loading protocol defined in AISC 341 2016) to qualify cyclic tests of beam-to-column moment connections for special and intermediate moment resisting frames, and already presented in Section 6.2.2. Therefore, the loading protocol shown in Figure 6.3 is also applied in this study, but considering that the lever arm (denoted L_r in the Figure) is equal to the effective lengths given in Section 7.2.1 (L1, L2, L3). The cyclic loading was applied until the collapse of the specimens, which was assumed to be reached when the profile was not able to carry the actuator load and a sharp drop in the load occurred. The loading was applied using displacement control at different rates throughout the tests: 0.1 mm/s for cycles with amplitudes of Δ=0.00375L, 0.25 mm/s for cycles with amplitudes up to Δ=0.04L, and a constant rate of 0.5 mm/s for the following amplitudes.

7.3. Test results and discussion

In this section, a detailed description of the results obtained from the nine tests is provided, which includes the observed failure modes, the resulting force-displacement and moment-rotation skeleton curves, the assessment of the degradation of stiffness, and the evaluation of the energy dissipation

capability of the specimens. It should be noted that only one experiment was performed for each combination of local and global slenderness, so the results presented herein may be slightly affected by factors typical of mechanical testing, such as inhomogeneity of the raw material, specimen processing and random errors during the experiments, whose influence may only be determined by repetitive testing. Therefore, the results reported in this study regarding the values of the ultimate load and number of cycles should be considered in relative terms rather than as absolute final values for the variables investigated herein, such as the local slenderness and specimen length.

7.3.1. Description of failure modes

The specimens were tested under cyclic bending by applying a cyclic load at their top end. Figure 7.5 shows the load-displacement curves obtained for S1 specimens with lengths of (a) L1 = 1650 mm, (b) L2 = 1360 mm and (c) L3 = 780 mm. Likewise, Figure 7.6 and Figure 7.7 display the load-displacement responses for S2 and S3 specimens, respectively, for L1, L2 and L3 lengths. It is important to note that the specimens exhibited the same behaviour during the individual cycles of the same amplitude up to the maximum load, so many hysteretic loops shown in Figure 7.5-Figure 7.7 are overlapped. The specimens were assumed to collapse when crack openings were evident and the profiles were not able to carry the actuator loads, as described in Section 7.2.4. Two modes of failure were observed: S1 and S3 specimens cracked at the corner regions without exhibiting previous signs of deformation, while S2 specimens clearly exhibited local buckling prior to the appearance of cracks at the corner regions and failing. As expected, no global instabilities or out-of-plane displacements were observed during the tests.

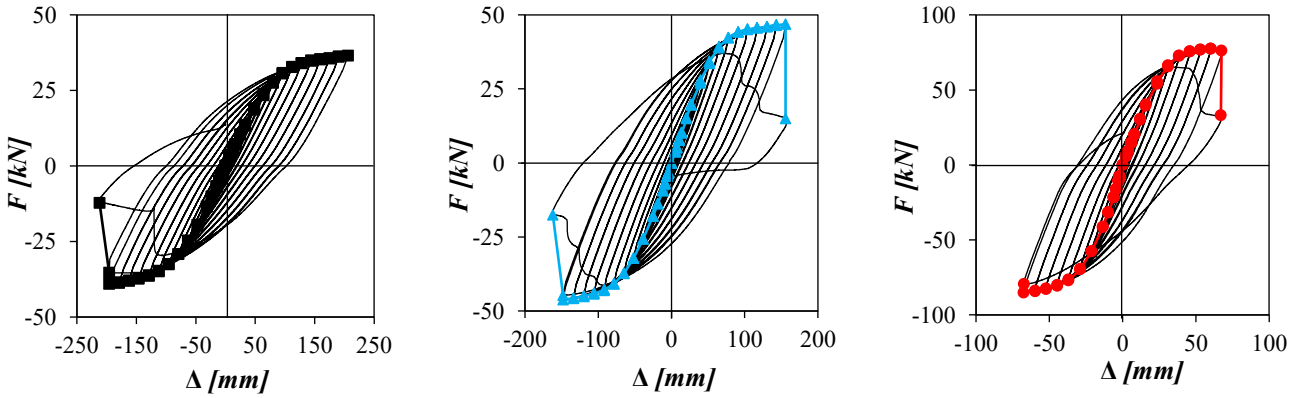

Figure 7.5. Load-displacement hysteretic curves for the studied (a) S1-L1, (b) S1-L2 and (c) S1-L3 austenitic stainless steel beams under cyclic loading.

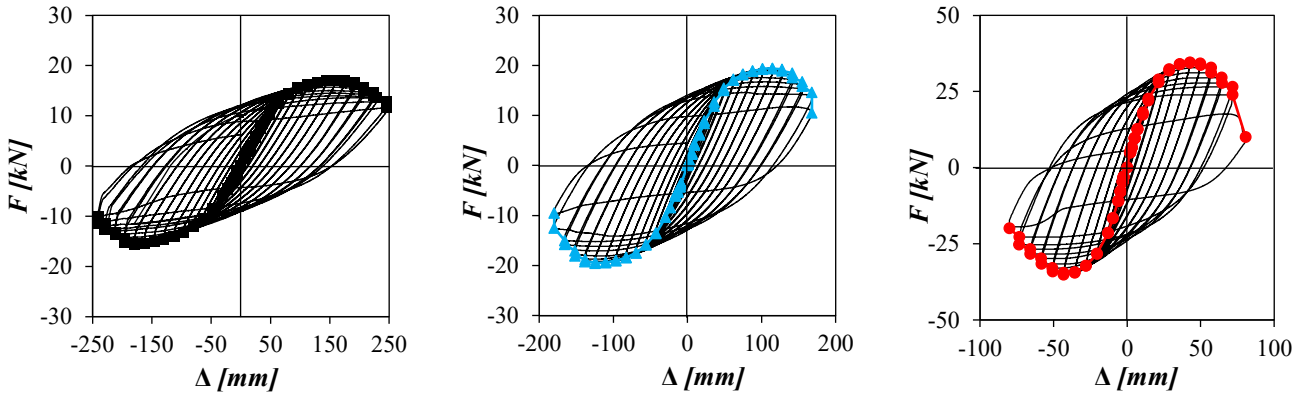

Figure 7.6. Load-displacement hysteretic curves for the studied (a) S2-L1, (b) S2-L2 and (c) S2-L3 austenitic stainless steel beams under cyclic loading.

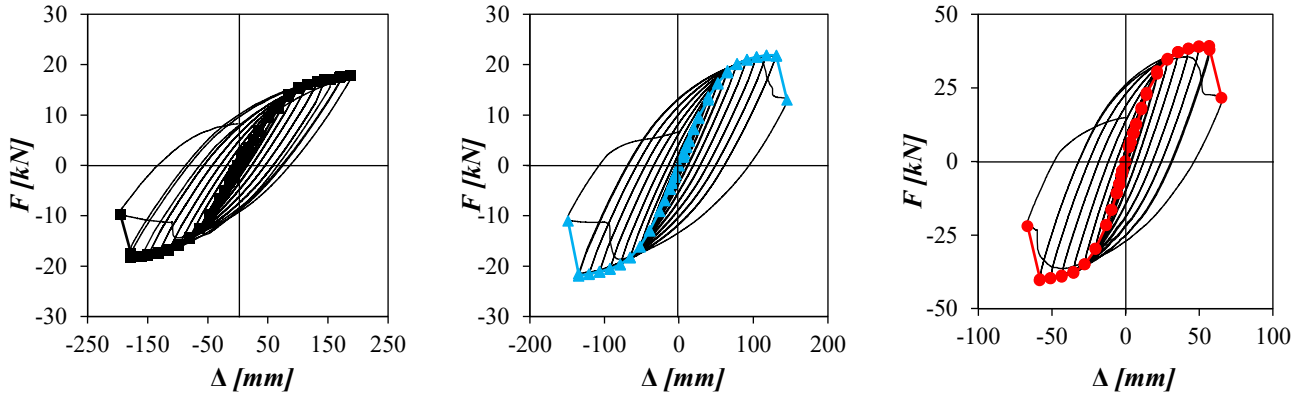

Figure 7.7. Load-displacement hysteretic curves for the studied (a) S3-L1, (b) S3-L2 and (c) S3-L3 austenitic stainless steel beams under cyclic loading.

The failure modes for S1 and S3 specimens, regardless the length, were induced by premature corner failures (i.e., cracks) at the height where the strain gauges were located (20 mm above the top of the stiffeners). It is important to note that no weld failure was observed. The corner fractures occurred at consecutive cycles or even at the same cycle, under tensile loading: the first fractures opened at the corners of the faces furthest from the actuator, and during the next half-cycle, second fractures opened at the same height in the opposite corners. The opening of the second set of cracks led to the immediate collapse of the specimens. Similar failure modes were reported in the literature for cold-formed stainless steel hollow section members under cyclic axial loading (Nip et al. 2010b). It is well known that the heat of the welding process can introduce some imperfections in the specimens, affecting the ductility of the stainless steel material and making regions close to the stiffeners more susceptible to fail (Nip et al. 2010b; Arrayago et al. 2020b). Table 7.2 summarises the number of cycles before the occurrence of the first corner fracture and failure (second corner fracture) for S1 and S3 specimens. The information reported in Table 7.2 coincides with the sequence of failure described above, i.e., S1 and S3 tests were stopped during the same (or the next) cycle at which the first corner cracks occurred. Only the S1-L1 specimen collapsed four cycles after the first crack opening occurred because the second fracture never developed. The S3-L1 specimen also exhibited corner cracks on one side, but this was enough to induce its failure immediately. It is important to highlight that in this study the failure of the specimens was determined

by the loss of resistance, although in practice failure would be associated to the first signals of cracking (Nip et al. 2010b).

Table 7.2. Summary of stainless steel beam test results under cyclic loading.

Specimen	Number of cycles for			F_{u+}	F_{u-}	F_{end}
	Local buckling	Corner opening	Failure	[kN]	[kN]	[kN]
S1-L1	-	43	47	36.4	-39.1	-12.3
S1-L2	-	44	45	46.9	-46.2	-17.5
S1-L3	-	40	40	77.5	-85.2	33.0
S2-L1	26	53	53	17.0	-15.7	11.6
S2-L2	27	48	48	19.4	-19.5	10.5
S2-L3	28	43	43	34.4	-35.2	23.9
S3-L1	-	52	52	17.8	-18.3	-9.9
S3-L2	-	42	43	21.9	-21.9	13.0
S3-L3	-	38	39	39.3	-40.4	21.6

Alternatively, S2 specimens failed after exhibiting local buckling failure and the subsequent fractures at the corners. The first signals of local buckling developed on the faces furthest from the actuator and were propagated to the opposite side and the widest faces of the specimens in the subsequent cycles. As expected, the initial local buckling was located at the critical sections comprised between the stiffeners and heights of 20 mm and 100 mm from the top of the stiffeners. A few cycles after, strength degradation was noticeable in all S2 specimens, and the tests were considered completed. It should be noted that, in the cycles prior to the end of the S2 tests, hairline cracks appeared in the corners furthest from the actuator under tensile forces, and the opposite corners fractured during the next half cycle. However, no sudden drops in strength were observed as per samples S1 and S3. Figure 7.8 shows the development of the local buckling failure for the S2-L2 specimen, which is representative of the failure modes of all S2 specimens. Table 7.2 reports the number of cycles before the occurrence of local buckling, first corner fracture and failure (second corner fracture) for S2 specimens. As shown in the table, several cycles elapsed between the onset of the initial local buckling and the first corner opening. Conversely, the first corner openings and failure of the specimens occurred at the same cycle. Note that the onsets of local buckling and initial corner opening are based on visual observations, while the final fracture cycle was identified in the hysteretic curves as a sharp drop in load.

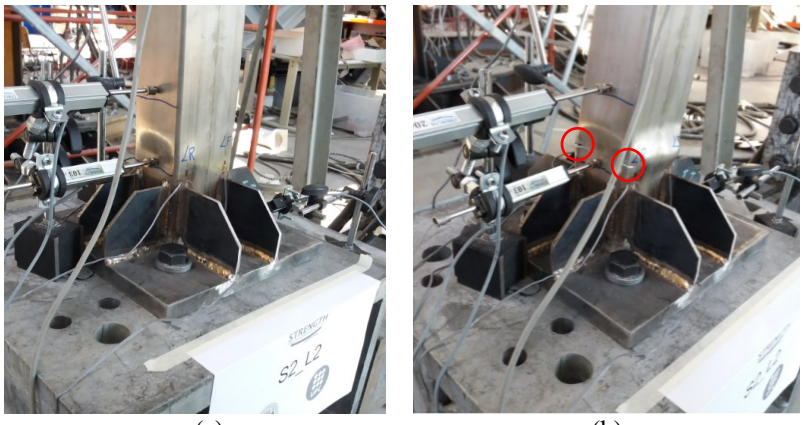

(a) (b)

Figure 7.8. Local buckling failure for the S2-L2 specimen: (a) initial local buckling deformations and (b) corner openings after test completion.

The influence of the local and global slenderness values on the number of cycles can be inferred from the results reported in Table 7.2. Consistent with the findings reported in (Nip et al. 2010b), the number of cycles before failure increases in general as the global slenderness of the member increases, and as the local slenderness of the sections decreases. Regarding the number of cycles for the onset of local buckling (in S2 specimens), it was found to decrease with increasing global slenderness values. This is because the structural behaviour of very short specimens tends to benefit from a higher stability induced by the proximity of the boundary conditions, assuming a cross-section structural behaviour rather than a member structural behaviour.

Finally, Table 7.2 also reports the ultimate horizontal load values F_u applied by the actuator, i.e., the peak load in the load-displacement curves (see Figure 7.5-Figure 7.7). Since the loading followed a tension-compression protocol, two values of the ultimate horizontal load are given for each test. Taking Figure 7.1 as reference, the horizontal loading applied by the actuator is considered positive F_{u+} when directed towards the left (the actuator was in tension) and negative F_{u-} when directed towards the right (the actuator was in compression). As shown in Table 7.2, the ultimate load values, both in tension and compression, increased with decreasing global slenderness values. In addition, Table 7.2 reports the load when the specimen was assumed to fail, F_{end}. As mentioned before, the tests were stopped when the profile was not able to carry the actuator load. In Table 7.2, a positive value of F_{end} indicates that the failure occurred with the actuator in tension, and therefore the strength degradation at failure is calculated by comparing the load values reached when the actuator was in tension F_{end} with F_{u+}. In contrast, a negative value of F_{end} indicates that the ultimate load was first reached when the actuator was in compression. According to the results reported in Table 7.2, the strength abruptly degraded below 40% F_u for S1 specimens, while for S3 specimens the failure load F_{end} dropped to values close to 60% F_u. Finally, S2 specimens showed a gradual loss of resistance and first signals of cracking appeared at a stage when the load resistance degraded to 70% F_u.

7.3.2. Force-displacement and moment-drift skeleton curves

Figure 7.9 presents the load-displacement skeleton curves for (a) S1, (b) S2 and (c) S3 specimens. The skeleton curves plotted in Figure 7.9 were obtained by connecting the peak displacement points of all load-displacement hysteretic loops (see Figure 7.5-Figure 7.7) as per (Ye et al. 2006; prEN 1998-1-2 2021). As mentioned in Section 7.3.1, the profiles usually exhibited a stable behaviour during the individual cycles of the same amplitude, which resulted in the superposition of the corresponding hysteretic loops. As shown in Figure 7.9, the shortest specimens exhibited the highest stiffness, as expected according to the theory of elasticity. Likewise, the shortest specimens, i.e., specimens with the shortest shear length, also showed the highest strength capacity values because the compressed flange in the buckled zone is subjected to a longitudinal stress gradient which depends on the length of

the specimen. Figure 7.10 shows the stress distribution at the compressed bottom flange over the buckling length L_b for a (a) long and (b) short cantilever beam. As shown, different normal stresses develop on both sides of the buckling length of the compressed part of the RHS section: while the normal stresses are equal to σ at the embedment zone, the stresses exhibit a value equal to $\psi\sigma$ at the other end of the buckling length, being ψ lower than unity. Shear stresses τ also develop as a consequence of the differences between the two stress distributions. If the length of the cantilever is reduced ($L_1 >> L_2$), the value of ψ is lower ($\psi_1 >> \psi_2$), i.e., the stress gradient is higher. Because of the longitudinal stress gradient, the average normal stress in the buckled zone is less than the maximum value occurring at the end of embedment zone. The difference between this maximum stress and the average stress in the buckled zone increases as the shear length decreases. Hence, the occurrence of local buckling in the compressed flange is delayed and the maximum flexural resistance of the section increases leading to the increase of the maximum force supported by the specimen. This phenomenon has been already reported for steel members (Mazzolani and Piluso 1996).

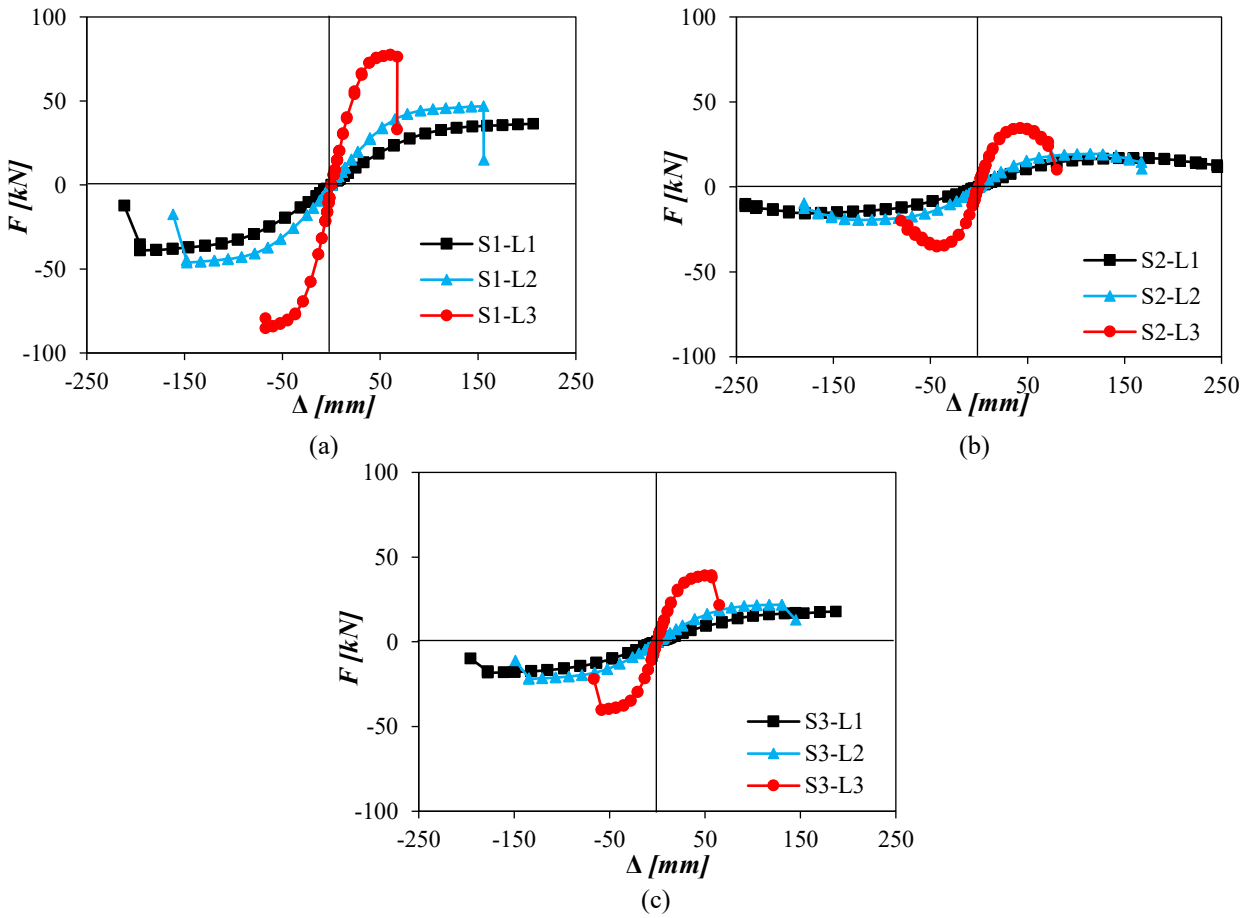

Figure 7.9. Load-displacement skeleton curves for the studied (a) S1, (b) S2 and (c) S3 austenitic stainless steel beams under cyclic loading.

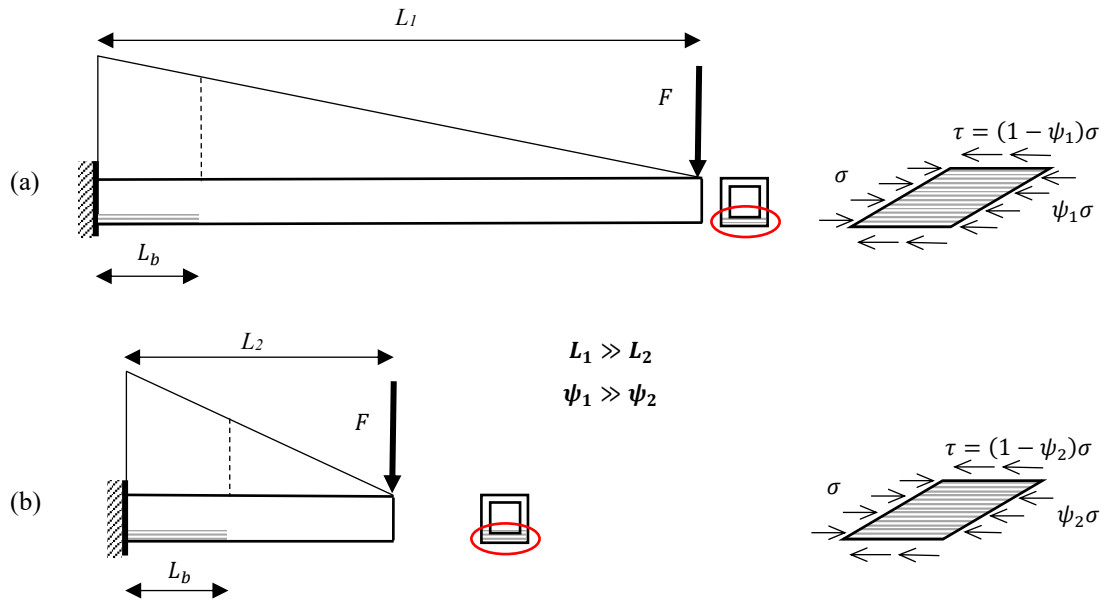

Figure 7.10. Comparison of the stress distributions at the bottom compressed flange over the buckling length L_b for a (a) long and (b) short cantilever.

Additionally, and aligned with the observations reported in Section 7.3.1, S2 specimens show a smooth strength degradation in Figure 7.9, which is an indicator of their ductile behaviour and the formation of plastic hinges, while S1 and S3 specimens exhibited sudden drops in load, indicating that failures were originated by crack openings without previous signs of local buckling. According to the skeleton curves reported in Figure 7.9, all specimens showed almost symmetrical branches on the first and third quadrants, i.e., all specimens experienced similar fractures on both faces, except S1-L1 and S3-L1 specimens which failed due to corner openings on just one side. In addition, S1 specimens exhibited the longest drops in load, which are consistent with the strength degradations of 40% F_u discussed in Section 7.3.1.

Similarly, Figure 7.11 presents the moment-rotation skeleton curves for (a) S1, (b) S2 and (c) S3 specimens. To be consistent with the loading protocol described in Section 7.2.4, the moment values were calculated as the product of the horizontal loads applied by the actuator and the effective lengths, while the rotations were calculated as the ratios between the horizontal displacements recorded at the top of the specimens by the string potentiometer and the effective lengths. As shown in Figure 7.11, similar responses were obtained for the three lengths analysed for each cross-section. For comparison purposes, the moment-rotation curves obtained from the monotonic tests on the same cross-sections published in (Arrayago and Rasmussen 2021b) are also plotted in Figure 7.11 (green dashed curves), as well as the plastic bending moments M_{pl}, computed as the product of the plastic section modulus W_{pl} and the yield stress f_y. As expected, for a given cross-section, the initial stiffness values of the monotonic and cyclic loading tests are equivalent, while the ultimate bending capacity for the monotonic tests is lower due to the hardening of the material under cyclic loading.

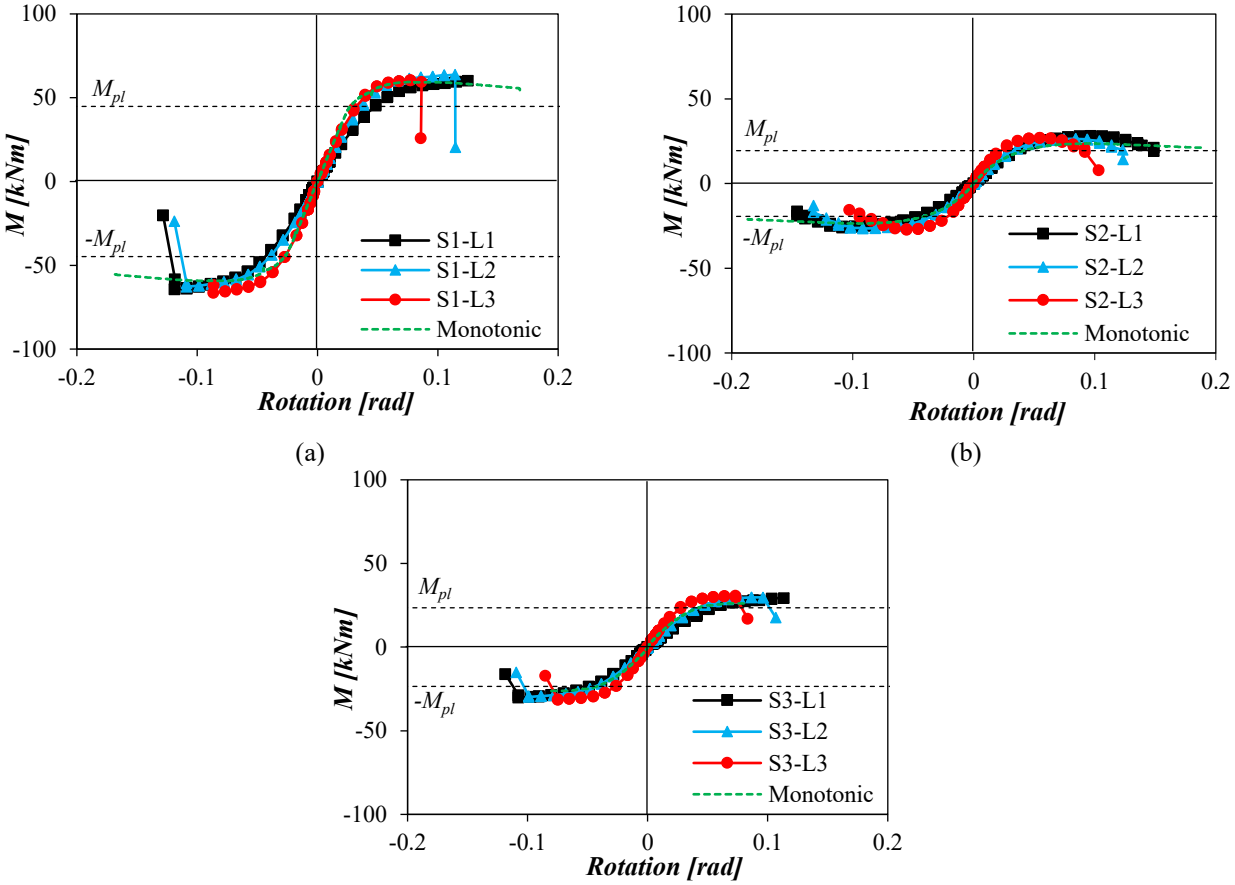

Figure 7.11. Moment-rotation skeleton curves for the studied (a) S1, (b) S2 and (c) S3 austenitic stainless steel beams under cyclic loading.

Finally, Table 7.3 reports the experimental elastic θ_y and ultimate θ_u rotation values according to the criteria given in prEN 1998-1-2 (2021) and plotted in Figure 6.6 for the definition of the plastic rotation, as well as the rotation corresponding to the ultimate bending moment θ_{Mu} and the maximum recorded rotation θ_{rec}. As for the ultimate load values F_{u+} and F_{u-}, two sets of rotation values are given in Table 7.3, one for positive (considering the actuator in tension) and one for negative (actuator in compression) loading. θ_u values are not reported in Table 7.3 for S1 and S3 specimens because the sudden fracture of these specimens made it impossible to record rotation values in the descending branch of the moment-rotation curves.

Table 7.3. Rotation values obtained from test results according to prEN 1998-1-2 (2021).

Specimen	M_{pl}	Actuator in tension [rad]						Actuator in compression [rad]					
	[kNm]	θ_y	θ_{Mu}	θ_u	θ_{rec}	R_0	R	θ_y	θ_{Mu}	θ_u	θ_{rec}	R_0	R
S1-L1	44.8	0.037	0.125	-	0.125	2.38	-	-0.036	-0.119	-	-0.128	2.27	-
S1-L2	44.8	0.033	0.114	-	0.114	2.49	-	-0.031	-0.109	-	-0.119	2.54	-
S1-L3	44.8	0.029	0.077	-	0.086	1.67	-	-0.024	-0.086	-	-0.086	2.62	-
S2-L1	19.4	0.033	0.097	0.149	0.149	1.97	3.57	-0.038	-0.109	-0.138	-0.146	1.85	2.63
S2-L2	19.4	0.029	0.084	0.123	0.124	1.96	3.32	-0.030	-0.092	-0.125	-0.132	2.04	3.15
S2-L3	19.4	0.020	0.055	0.092	0.103	1.78	3.67	-0.020	-0.055	-0.094	-0.103	1.78	3.72
S3-L1	23.5	0.042	0.113	-	0.113	1.73	-	-0.029	-0.091	-	-0.118	2.12	-
S3-L2	23.5	0.034	0.096	-	0.107	1.86	-	-0.032	-0.099	-	-0.109	2.09	-
S3-L3	23.5	0.023	0.073	-	0.083	2.18	-	-0.023	-0.075	-	-0.085	2.19	-

Results reported in Table 7.3 highlight that, in most of the cases, similar rotations were obtained when the specimens were under compressive and tensile forces, which is an indicator of the correct performance of the tests. It was found that the values of the θ_y, θ_{Mu}, θ_u and θ_{rec} rotations generally increased with increasing global slenderness values. An upward trend was also observed in the θ_y and θ_{Mu} values for decreasing local slendernesses. However, no conclusions could be drawn about the relationship between θ_u and the local slenderness values due to the lack of data, since θ_u values could only be determined for S2 specimens. Values of the θ_{rec} rotations were almost equal to those corresponding to the ultimate bending moment θ_{Mu} for S1 and S3 specimens, while for S2 specimens higher values of the θ_{rec} rotations were obtained, showing the ductile behaviour of these specimens. By relating the rotation results from Table 7.3 to the ultimate strength values reported in Table 7.2, it can be inferred that the shortest specimens exhibited the highest stiffness values, which is consistent with the responses plotted in Figure 7.9. The values for the stable part R_0 and total R plastic rotation capacities, determined from the predictive expressions given in Eq. 6.1 and Eq. 6.2, respectively, are also given in Table 7.3. As shown in this table, the values for the stable part of the rotation capacity R_0 for all specimens are comparable and show a slight tendency to increase as the local slenderness decreases. However, once again, no conclusions could be drawn on the relationship between the rotation capacities, both R_0 and R, and the global slenderness. This could be explained by the lack of additional data and the fact that the formulae for estimating the rotation capacities minimise the effect of the specimen length because they are normalised by the elastic rotations θ_y (see Section 6.3.4).

7.3.3. Stiffness degradation

The stiffness of the specimens during the tests has been studied attending to the degradation of the secant stiffness K, which is computed as the ratio of the sum of the maximum positive $F_{\Delta+}$ and negative $F_{\Delta-}$ horizontal loads for each cycle, in absolute values, and the sum of the corresponding total horizontal displacements, Δ_+ and Δ_-, as per (Jiang and Bai 2020). The formulation for the secant stiffness K is given in Eq. 7.1. Figure 7.12 shows the resulting secant stiffnesses against the number of cycles for (a) S1, (b) S2 and (c) S3 specimens. As shown in these curves, the shortest specimens (L3) exhibited the highest values of secant stiffness, and since the collapse of the specimen was reached sooner, the stiffness degradation was more noticeable. In addition, the specimens with the stockiest cross-section, i.e., S1, showed 50% higher secant stiffness values than the corresponding S2 and S3 specimens. S2 and S3 specimens exhibited similar responses. Finally, as reported in Table 7.2, it can be appreciated that all tests with the same length ended after a comparable number of cycles.

$$K = \frac{|F_{\Delta+}| + |F_{\Delta-}|}{|\Delta_+| + |\Delta_-|} \qquad \text{Eq. 7.1}$$

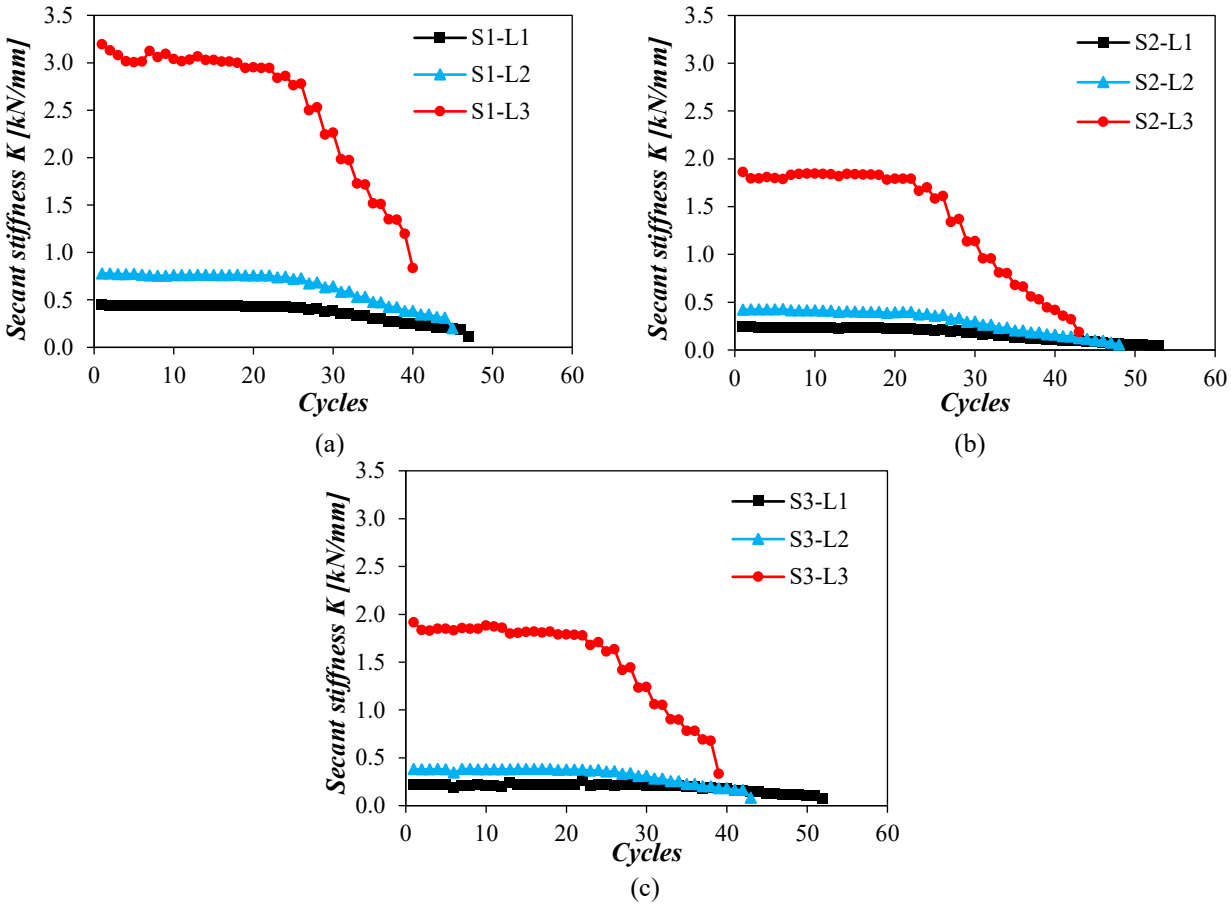

Figure 7.12. Secant stiffness *K* degradation against the number of cycles for the studied (a) S1, (b) S2 and (c) S3 austenitic stainless steel beams under cyclic loading.

7.3.4. Energy dissipation

The computation of the energy dissipation capability of steel structural elements is of paramount importance in seismic design, since most of the energy introduced into steel structures in a seismic event is dissipated through the inelastic deformation of their members (Fang et al. 2018). The accumulated energy absorption (dissipation) capacity of a specimen during a cyclic test is assumed to be the area enclosed by the load-displacement hysteretic loops (see Figure 7.5-Figure 7.7) (Nip et al. 2010; Fang et al. 2018; Kim et al. 2021). Figure 7.13 shows the accumulated energy dissipation, measured in kJ, calculated for (a) S1, (b) S2 and (c) S3 specimens against the number of cycles. As shown in Figure 7.13, the values of the dissipated energy during the first 30 cycles are really low for all specimens as the material deformations are still elastic. This is in agreement with the findings reported in (Fang et al. 2018) for austenitic hollow section specimens under strong-axis cyclic bending. After then, the ductility, i.e., inelastic behaviour, of the members becomes more evident and the accumulated energy absorption capacity increases significantly until the fracture of the specimens. As it can be seen in Figure 7.13, S1 specimens were found to exhibit the highest values of energy dissipation, followed by S2 and S3 specimens. According to (Nip et al. 2010b), the accumulated energy dissipation increases as the local slenderness of the cross-section decreases. However, S2 specimens showed a higher energy dissipation

capacity than S3 specimens despite being slenderer because they reached higher values of maximum recorded rotation θ_{rec} (see Table 7.3), and S3 specimens failed prematurely. Finally, for the same local slenderness (or cross-section), the longest specimens (L1) exhibited higher values of energy dissipation prior to failure due to the higher number of cycles before failure, although the accumulated energy dissipation per cycle increased with decreasing global slenderness values, as also reported in (Nip et al. 2010b).

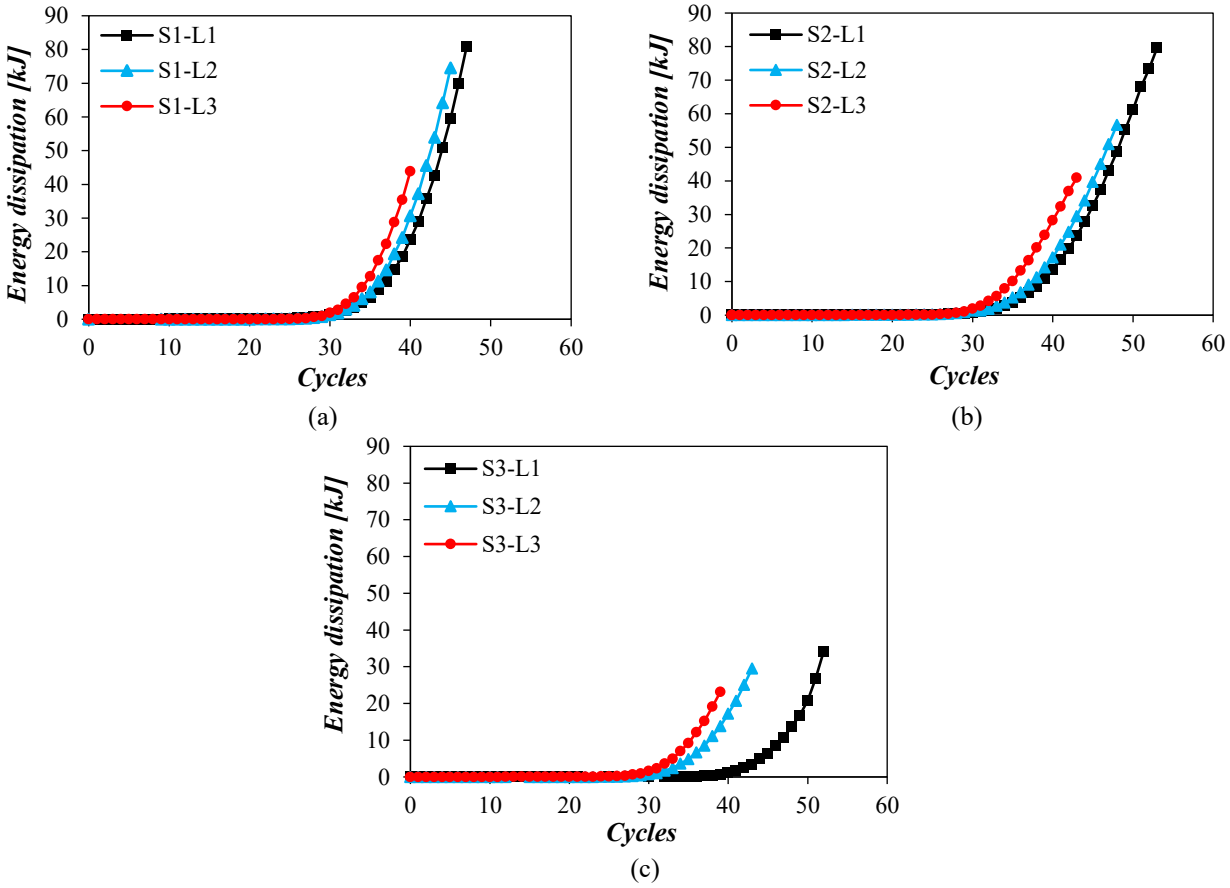

Figure 7.13. Accumulative energy dissipation against the number of cycles for the studied (a) S1, (b) S2 and (c) S3 austenitic stainless steel beams under cyclic loading.

7.4. Concluding remarks

This chapter presents an experimental programme on nine austenitic stainless steel hollow section elements subjected to cyclic loading, covering three different local and member slenderness values, promoted by the Universitat Politècnica de Catalunya and carried out at the Università degli Studi di Salerno. Two different failure modes were observed: the sudden crack of corners without exhibiting previous signs of deformation at the flat regions of the cross-sections, and the development of local buckling deformations prior to failure. Consistent with the findings reported in the literature, it was found that the ultimate load values decreased with increasing global slenderness values. In addition, the number of cycles before failure and the rotation values rose with increasing values of the global slenderness. For those specimens that exhibited a smooth strength degradation, the number of cycles before local buckling occurred decreased with increasing global slenderness values. The total energy

dissipation prior to failure trended upward as the global slenderness increased due to the higher number of cycles achieved. Finally, the shortest specimens exhibited the highest values of ultimate load and failed sooner, leading to a more noticeable degradation, while the stockiest cross-sections exhibited the highest ultimate load, rotation and secant stiffness values. It is expected that the results provided in this study will promote the understanding of stainless steel members under cyclic loading and may help researchers to conduct similar experimental programmes.

Corresponding publication: González-de-León I., Nastri E., Arrayago I., Montuori R., Piluso V. and Real E. (2022). Experimental study on stainless steel tubular members under cyclic loading. *Thin-Walled Structures*, 181, 109969. https://doi.org/10.1016/j.tws.2022.109969

CHAPTER 8

Design of stainless steel moment resisting frames according to the second generation of Eurocode 8

8.1. Introduction

Stainless steel has an excellent potential in seismic design due to its ductility, strain hardening, energy dissipation capacity and fire resistance properties (SCI 2017). However, the number of studies devoted to the understanding of the seismic behaviour of stainless steel is very limited (see Section 2.6), so it is understandable that the future edition of the European standard for the design of structures for earthquake resistance prEN 1998-1-2 (2021) does not include specific rules for stainless steel structures, although it should be noted that recommendations for stainless steel already exist in the Japanese code (BCJ 2016).

Among the typologies of steel structures, steel Moment Resisting Frames (MRFs) are very popular for low and medium-rise buildings for architectural reasons and ease of construction, and most structural codes published in Europe, Japan and the US include provisions to design steel MRFs. Steel MRFs are known to be very flexible framing solutions, and their design is generally governed by their performance against lateral loads. In Eurocode 8, the most extended approach for the seismic design of steel MRFs

is the force-based approach. As mentioned in Section 2.6.2, the force-based approach is based on the performance of an elastic analysis of the structure, where the nonlinear deformations and energy dissipation are considered by reducing the design seismic forces by tabulated behaviour factors, and the resistance of the frame is guaranteed by the fulfilment of several requirements related to the lateral stability, drift limitations and the application of certain capacity design rules (prEN 1998-1-1 2021). Even if this design procedure for steel MRFs is kept, the new version of Eurocode 8 significantly modifies the definition of the ductility classes, behaviour factors, material randomness factors, interstorey drift sensitivity index, local hierarchy criteria and design rules for non-dissipative members (prEN 1998-1-1 2021), among other changes. The effect of these modifications on the design of steel MRFs, making special emphasis on the tabulated values of the behaviour factor, have been already assessed by Lemma et al. (2022) and Tartaglia et al. (2022) for common steel frames. Lemma et al. (2022) studied numerically the performance of 96 steel MRFs designed according to both the current version of Eurocode 8 and the updated prEN 1998-1-2 (2021) specification, covering two carbon steel grades, four plan configurations and three different elevations. The parametric study was performed using OpenSEES (2006), and the comparison of the prescribed behaviour factors with the actual values estimated from nonlinear static analyses revealed that the overall behaviour factors is strongly dependent on the value of its overstrength component. Similarly, Tartaglia et al. (2022) performed, using SeismoStruct (2016), a parametric study of 48 steel MRFs designed according the current and revised versions of Eurocode 8, as well as the US code (ASCE 7 2016). Tartaglia et al. also assessed the actual behaviour factors, which were estimated attending a different criterion to that considered by Lemma et al. (2022). For all 48 frames, the behaviour factors obtained by Tartaglia et al. (2022) were higher than the values given in prEN 1998-1-2 (2021). Both studies concluded that the revised Eurocode 8 promotes lighter structures than the current standard.

In light of the potential of stainless steel alloys for seismic design, this work aims to study, for the first time, the behaviour of stainless steel structures (austenitic, ferritic and duplex) designed according to the provisions for highly dissipative structures (i.e., Ductility Class 3 structures – DC3) given in the forthcoming prEN 1998-1-1 (2021) and prEN 1998-1-2 (2021) specifications. The goals of this study are (1) to evaluate the suitability of the design rules for carbon steel on the design of stainless steel structures, and (2) to estimate the actual behaviour factors for stainless steel MRFs. The study has been performed using the finite element software ABAQUS (2016), which allows to accurately reproduce the nonlinear stress-strain response of stainless steel alloys (Arrayago et al. 2015a), and following the methodology reported in (Lemma et al. 2022).

8.2. Principal provisions for steel MRFs in the revised version of Eurocode 8

This section summarises the provisions of prEN 1998-1-1 (2021) and prEN 1998-1-2 (2021) that apply to this study. Note that these standards refer to carbon steel structures and that, in some cases,

assumptions have been made in this study to adapt them to stainless steel structures. These assumptions, where applicable, are indicated at the end of each sub-section. Finally, it should be highlighted that an important modification of the formula for controlling the second order effects in stainless steel structures subjected to seismic actions is proposed in this study in order to take into account the additional loss of stiffness due to material nonlinearities, which can be found in Section 8.2.5.

8.2.1. Consequence classes, limit states, ductility classes, random material variability and strain hardening overstrength factors

The second generation of Eurocode 8 has introduced important changes to the terminology in an effort to harmonise it with that of other Eurocodes. In line with prEN 1990 (2022), prEN 1998-1-1 (2021) distinguishes between four consequence classes (CC1, CC2, CC3a and CC3b) depending on the importance category of the building. Structures should be regarded as belonging to consequence class CC2 if not otherwise specified. The definition of limit states has also been revised to be consistent to prEN 1990 (2022) and, according to prEN 1998-1-1 (2021), there are two limit states related to the Ultimate Limit State (Near Collapse and Significant Damage, NC and SD, respectively) and two limit states related to the Serviceability Limit State (Damage Limitation and Fully Operational, DL and OP, respectively). In an attempt to simplify the design procedure, only SD limit state verification is mandatory for new structures (prEN 1998-1-1 2021).

Moreover, prEN 1998-1-1 (2021) distinguishes between three ductility classes depending on the dissipative capacity exhibited by the structure: low (DC1), medium (DC2) and high (DC3). In this study, frames have been designed according to the provisions given for DC3 structures. Design for DC3 considers that the structure is expected to show local overstrength, deformation and energy dissipation capacities, and to form a global plastic mechanism at the SD limit state. Each ductility class is associated with a limit of the seismic action index, which depends on the seismic action and the consequence class of the structure, but there is no limit for the seismic action of DC3 structures in prEN 1998-1-1 (2021). Finally, the elastic response spectrum, which represents the seismic forces, is redefined on the basis of the maximum response spectral acceleration and the response spectral acceleration at the vibration period of 1 s instead of the design ground acceleration.

Regarding the overstrength exhibited by the material, prEN 1998-1-1 (2021) differentiates between (1) the material overstrength factor ω_{rm}, which considers the actual (and enhanced) yield stress of the steel and whose values can be found in prEN 1998-1-2 (2021) depending on the carbon steel grade, and (2) the overstrength factor accounting for the hardening of the dissipative zones ω_{sh}, which depends on the plastic mechanism and is a function of the yield stress f_y and the ultimate f_u strength. For DC3 moment resisting frames, ω_{sh} is computed using Eq. 8.1, where C is a cut-off value equal to 1.2 in the case of carbon steel alloys (prEN 1998-1-2 2021). In this study, the material overstrength factors ω_{rm} adopt

the values proposed by Arrayago et al. (2020a) for stainless steel plates, while the hardening overstrength factor ω_{sh} has been computed using Eq. 8.1, assuming the values of f_y and f_u calibrated by Afshan et al. (2019) for stainless steel hot-rolled sections and sheet material (see Table 8.4) and a value of C consistent with the strain hardening of each type of stainless steel. Table 8.1 summarises the values of ω_{rm} and ω_{sh} considered in this study for stainless steel MRFs.

$$\omega_{sh} = \frac{(f_y + f_u)}{2f_y} \leq C \qquad \text{Eq. 8.1}$$

Table 8.1. Material and hardening overstrength factors adopted in the study.

Stainless steel	Material overstrength factor ω_{rm} (Arrayago et al. 2020a)	Hardening overstrength factor ω_{sh} using data given in (Afshan et al. 2019)
Austenitic	1.22	1.4
Ferritic	1.22	1.2
Duplex	1.11	1.2

8.2.2. Behaviour factors

Due to computational reasons, one of the main approaches considered in prEN 1998-1-1 (2021) to verify the adequate combination of strength, deformation capacity and cumulative energy dissipation capacity is the force-based approach. The force-based approach may be used for verification to SD limit state, and may be implemented through the lateral force method and the modal response spectrum method. The approach employs a linear analysis where the design forces are obtained from the superposition of gravity loads and seismic forces, and the overstrength and the nonlinear response of the structure (associated with the material, the structural system and the design procedure) are implicitly and approximately accounted for by a behaviour factor, which in the Eurocode framework is represented by q. Similar approaches are found in other standards, such as the US code, where the corresponding reduction factor is known as the response modification factor R (ASCE 7 2016). Since the values of the reduction (or modification) factors (q, R) determine the seismic design forces, their assessment has been a constant research topic (Lemma et al. 2022; Ferraioli et al. 2014).

The computation of the overall behaviour factor q has been revised and split into three components in prEN 1998-1-1 (2021), as shown in Eq. 8.2, where q_R is the behaviour factor component accounting for the overstrength due to the redistribution of seismic action effects in redundant structures, q_D is the behaviour factor component accounting for the deformation capacity and energy dissipation capacity of the structure, and q_S is the behaviour factor component accounting for the overstrength due to all other sources – such as the strength reserve resulting from the overstrength of individual members (Ferraioli et al. 2014). According to prEN 1998-1-1 (2021), the value of q_S should be adopted equal to 1.5, while different values of q_R and q_D are given in prEN 1998-1-2 (2021) depending on the material,

framing system and the ductility class considered. Thus, Table 8.2 summarised the tabulated values of q_R, q_D and q_S for steel moment resisting multi-storey frames designed to DC3. Note that the overall behaviour factor q, also reported in Table 8.2, approximatively values the product of the three components. In the absence of specific behaviour factors for stainless steel prescribed by the code, this study has assumed the values given in Table 8.2 for the design of the stainless steel MRFs.

$$q = q_R \cdot q_D \cdot q_S \quad \text{Eq. 8.2}$$

Table 8.2. Behaviour factors reported in prEN 1998-1-2 (2021) for DC3 multi-storey steel MRFs.

q_R	q_D	q_S	q
1.3	3.3	1.5	6.5

8.2.3. Drift limitation and second order effects at the Significant Damage limit state

As stated in prEN 1998-1-2 (2021), the global plastic mechanisms should be controlled through the limitation of the drift and second order effects, as well as through the capacity design rules presented in Section 8.2.4. prEN 1998-1-2 (2021) defines the design interstorey drift d_r as the difference of the average lateral displacements d_s at the top and bottom of the storey under consideration induced by the seismic action. The lateral displacements d_s should be calculated using Eq. 8.3 (prEN 1998-1-1 2021), where d_e is the displacement of the same point of the structural model calculated under the reduced spectrum associated to the design seismic action, and q_{disp} depends on the ratio of the fundamental period of the structure T_1 and the corner period of the spectrum T_C, and is calculated as given in Eq. 8.4.

$$d_s = d_e \cdot q_{disp} \quad \text{Eq. 8.3}$$

$$\begin{aligned} q_{disp} &= q && \text{if } T_1 \geq T_C \\ q_{disp} &= 1 + (q-1) \cdot T_C/T_1 \leq 3q && \text{if } T_1 < T_C \end{aligned} \quad \text{Eq. 8.4}$$

According to prEN 1998-1-2 (2021), the design interstorey drift at the Significant Damage limit state $d_{r,SD}$ in moment resisting frames should satisfy the requirement given in Eq. 8.5, where $d_{s,top}$ and $d_{s,bottom}$ are the lateral displacements of the top and bottom points of the considered storey, and h_s is the interstorey height.

$$d_{r,SD} = d_{s,top} - d_{s,bottom} \leq 0.02 \cdot h_s \quad \text{Eq. 8.5}$$

prEN 1998-1-2 (2021) evaluates the sensitivity to second order effects at all stories through the computation of the interstorey drift sensitivity coefficient θ, the formulation of which has been recently revised to properly consider the secant stiffness of structures in the SD limit state (Vigh et al. 2016). In the case of DC3 steel structures, the interstorey drift sensitivity coefficient θ is calculated as given in

Eq. 8.6, where P_{tot} is the total gravity load at and above the storey under consideration due to the masses considered in the seismic analysis of the structure, V_{tot} is the total storey shear in the seismic design situation, and Ω_d is the design overstrength ratio, given in Eq. 8.7. Ω_d is computed as the minimum of $\Omega_{d,i} = \left(M_{pl,Rd,i} - M_{Ed,G,i}\right)/M_{Ed,E,i}$ of all beams in which dissipative zones are expected (when full connections are used), where $M_{pl,Rd,i}$ is the plastic moment at the "i" beam, and $M_{Ed,G,i}$ and $M_{Ed,E,i}$ are the corresponding design moments due to gravity loads and seismic actions, respectively. Ω_d assumes a value higher than 1.0. Note that prEN 1998-1-2 (2021) has also revised the formulation for Ω_d – currently $M_{pl,Rd}/\left(M_{Ed,G} + M_{Ed,E}\right)$ is considered –, and has adopted the formula for beam overstrength factor proposed by Elghazouli (2010). Eq. 8.7 efficiently accounts for the effects of gravity loads on the actual overstrength of the beams, leading to higher values of Ω_d than the current formulation, especially in structures susceptible to collapse due to a soft storey mechanism, i.e., low-rise structures with relatively small column cross-sections and structures with large beam spans subjected to significant gravity loads (Elghazouli 2010).

$$\theta = \frac{P_{tot} \cdot d_{r,SD}}{\omega_{rm} \cdot q_S \cdot V_{tot} \cdot h_s} \quad \text{if } q_S \geq \Omega_d \cdot q_R$$
$$\theta = \frac{P_{tot} \cdot d_{r,SD}}{\omega_{rm} \cdot \Omega_d \cdot q_R \cdot V_{tot} \cdot h_s} \quad \text{if } q_S < \Omega_d \cdot q_R \qquad \text{Eq. 8.6}$$

$$\Omega_d = \left(M_{pl,Rd} - M_{Ed,G}\right)/M_{Ed,E} \qquad \text{Eq. 8.7}$$

According to prEN 1998-1-2 (2021), second order effects may be neglected if the sensitivity coefficient $\theta \leq 0.1$. When relevant, second order effects may approximately be taken into account by multiplying the relevant seismic action effects by a factor equal to $1/(1-\theta)$ if $0.1 < \theta \leq 0.2$, and should be taken into account directly by using the established methods of second order analysis by considering geometric nonlinearities if $0.2 < \theta < 0.3$. The value of θ should not exceed 0.3.

This study limits the maximum design interstorey drift at the Significant Damage limit state $d_{r,SD}$ to 2%, and proposes a new expression to control the second order effects in stainless steel structures based on the expressions shown in Eq. 8.6 (see Section 8.2.5), which allows the adoption of the same limiting values of θ for consideration of geometrical nonlinearities.

8.2.4. Design actions for non-dissipative members and local hierarchy rule for columns

prEN 1998-1-2 (2021) prescribes rules to ensure the weak beam-strong column criterion is met. Thus, steel columns in DC3 should be verified in compression, bending and shear under the most unfavourable combination of design actions N_{Ed}, M_{Ed} and V_{Ed} computed as given in Eq. 8.8, where the subscripts "G" and "E" refer to the internal actions due to gravity loads and seismic actions, respectively. As

shown, internal forces resulting from the seismic action, which are obtained from a modal response spectrum analysis, are magnified by the factor $\omega_{rm} \cdot \omega_{sh} \cdot \Omega_d$, which accounts for the overstrength due to the material randomness, the strain hardening and the overdesign of the dissipative members.

$$\begin{aligned} N_{Ed} &= N_{Ed,G} + \omega_{rm} \cdot \omega_{sh} \cdot \Omega_d \cdot N_{Ed,E} \\ V_{Ed} &= V_{Ed,G} + \omega_{rm} \cdot \omega_{sh} \cdot \Omega_d \cdot V_{Ed,E} \\ M_{Ed} &= M_{Ed,G} + \omega_{rm} \cdot \omega_{rm} \cdot \Omega_d \cdot M_{Ed,E} \end{aligned} \quad \text{Eq. 8.8}$$

In addition, the sum of resistances of the columns that concur at any particular joint should satisfy Eq. 8.9, where $\sum M_{c,pl,Rd}(N_{Ed})$ is the sum of the design moment resistances of the columns at the joint, taking into account the axial load in the seismic design situation, $\sum M_{b,pl,Rd}$ is the sum of the design moment resistances of the connected beams, $V_{Ed,M}$ is the shear force due to the formation of plastic hinges at both beam ends, $V_{Ed,G}$ is the shear force due to the non-seismic actions in the seismic design situation, and s_h is the distance between the centre of the expected plastic hinge and the column axis.

$$\sum M_{c,pl,Rd}(N_{Ed}) \geq \sum \left[\omega_{rm} \cdot \omega_{sh} \cdot \left(M_{b,pl,Rd} + s_h \cdot V_{Ed,M}\right) + s_h \cdot V_{Ed,G}\right] \quad \text{Eq. 8.9}$$

In this study, the resistance verifications were done considering that the cross-sectional resistance is limited to its design plastic resistance value, as recommended by prEN 1998-1-2 (2021). Design plastic axial $N_{pl,Rd}$, shear $V_{pl,Rd}$ and moment $M_{pl,Rd}$ resistances were calculated and combined, if applicable, according to prEN 1993-1-4 (2021). Partial safety factors for resistance (i.e., γ_{M0} and γ_{M1}) have been assumed equal to 1.0.

8.2.5. Derivation of a new second order sensitivity index for stainless steel MRFs

The approach given in prEN 1998-1-2 (2021) for accounting for second order effects in steel MRFs in the seismic design situation is equivalent to prescribed for the static situation in prEN 1993-1-1 (2021). As mentioned in Section 2.5.1, multi-storey steel MRFs governed by the in-plane sway mode can be designed performing a first order elastic analysis (LA) if $\alpha_{cr,sw} \geq 10$. In case of $10 > \alpha_{cr,sw} \geq 3$, second order effects can be accounted for in an elastic analysis by amplifying the horizontal forces by the factor k_{sw} given in Eq. 2.10. In case of $\alpha_{cr,sw} < 3$, it is mandatory to carry out a second order analysis. The value of $\alpha_{cr,sw}$ can be obtained from a linear buckling analysis (LBA) or estimated from Eq. 8.10 (prEN 1993-1-1 2021), where H_f is a fictitious horizontal load applied at the top of the columns of the storey, Δ_f is the interstorey horizontal displacement due to H_f, and $\sum N_{Ed}$ is the sum of the axial forces in the columns within the storey under consideration.

$$\alpha_{cr,sw} = \frac{H_f \cdot h_s}{\Delta_f \cdot \sum N_{Ed}} \qquad \text{Eq. 8.10}$$

This approach is also valid for designing stainless steel MRFs subjected to vertical and horizontal forces, but prEN 1993-1-4 modifies the computation of the $\alpha_{cr,sw}$ factor to take into account the additional losses in stiffness that arise due to material nonlinearities, as proposed by Walport et al. (2021a). Eq. 2.11 shows $\alpha_{cr,sw,ss}$ as prescribed in prEN 1993-1-4 (2021). As for carbon steel structures, stainless steel in-plane MRFs with $10 > \alpha_{cr,sw,ss} \geq 3$ can be designed considering the second order effects by performing a first order MNA analysis if the horizontal forces are magnified by the factor given in Eq. 2.12. Similarly, second order effects can be neglected if $\alpha_{cr,sw,ss} \geq 10$, and may be explicitly considered when $\alpha_{cr,sw,ss} < 3$.

As it can be deduced from comparing Eq. 8.6 and Eq. 8.10, the index θ for evaluating second order effects in the seismic performance of steel MRFs proposed in prEN 1998-1-2 is formulated based on the $\alpha_{cr,sw}$ (note that P_{tot}, $d_{r,SD}$, V_{tot} and h_s in Eq. 8.6 correspond to $\sum N_{Ed}$, Δ_f, H_f and h_s in Eq. 8.10), but considers the beneficial effects of the material overstrength and the overdesign of the structure due to the redundancy and oversizing of the members. In the case of stainless steel structures, this formula should also include the detrimental effect of material nonlinearities in the lateral stability of the structure, as $\alpha_{cr,sw,ss}$ does, and therefore a new definition of the sensitivity factor for stainless steel structures θ_{ss} is required. Considering the analogy between Eq. 8.6 and Eq. 8.10, it is proposed that the index for evaluating second order effects on the seismic performance of stainless steel MRFs may be calculated as given in Eq. 8.11. The values of the Y factor depend on the number of storeys and stainless steel grade and are given in Table 2.1.

$$\theta_{ss} = \frac{P_{tot} \cdot d_{r,SD}}{\omega_{rm} \cdot q_S \cdot V_{tot} \cdot h_s \cdot Y \cdot (K_s/K)} \quad \text{if } q_S \geq \Omega_d \cdot q_R$$

$$\theta_{ss} = \frac{P_{tot} \cdot d_{r,SD}}{\omega_{rm} \cdot \Omega_d \cdot q_R \cdot V_{tot} \cdot h_s \cdot Y \cdot (K_s/K)} \quad \text{if } q_S < \Omega_d \cdot q_R \qquad \text{Eq. 8.11}$$

Note that this definition of the θ_{ss} index allows the adoption of the same limiting values prescribed in prEN 1998-1-2 (2021) for consideration of second order effects in seismic design: second order effects may be neglected if $\theta_{ss} \leq 0.1$, may approximately be taken into account by multiplying the relevant seismic action effects by a Merchant-Rankine factor equal to $1/(1-\theta_{ss})$ if $0.1 < \theta_{ss} \leq 0.2$, and should be taken into account explicitly by performing second order analyses when $0.2 < \theta_{ss} < 0.3$. The value of θ_{ss} should be also limited to 0.3.

8.3. Case studies and design procedure

This section describes the characteristics of the stainless steel Moment Resisting Frames (MRFs) analysed in this study and the steps followed to achieve an efficient design according to the second revision of the Eurocodes. It should be noted that the portal frames analysed in this study, including the design gravity loads and seismic forces, are based on those studied by Lemma et al. and have been designed following a similar procedure. More details of the parametric study performed by Lemma et al. can be found in (Lemma et al. 2022).

8.3.1. Characteristics of the MRFs

A parametric study was conducted to investigate the influence of three variables (i.e., stainless steel grade, number of floors and width of the bays) on the seismic behaviour of stainless steel moment resisting multi-storey frames. The frames were designed according to DC3 prescriptions given in the second revision of the Eurocodes. Only class 1 (prEN 1993-1-4 2021) European standardised sections were used: IPE sections for the beams and HEB or HEM sections for the columns – note that class 1 cross-sections meet the requirement for designing steel MRFs in DC3 (prEN 1998-1-2 2021). A total of 36 structures were analysed. Table 8.3 summarises the variables of the parametric study, which are discussed below.

Table 8.3. Parameters modified in the study cases.

Stainless steel	Plan view: width of bays [m]	Elevation view: no. of storeys
Austenitic	T1: 6, 6, 6, 6	3
Ferritic	T2: 8, 8, 8, 8	6
Duplex	T3: 4, 8, 8, 4	9
	T4: 8, 6, 6, 8	

In order to have a general overview of the influence of the varying ductility and strain hardening characteristics of the most common stainless steel grades, this study included structures on austenitic, ferritic and duplex stainless steels. The whole structure was made for the same stainless steel grade for each particular case. Even if it can be assumed that the initial stiffness of the three material is equal (Afshan et al. 2019), the stress-strain responses of each stainless steel family reveal that austenitic alloys tend to behave in a very ductile manner and have an important strain hardening, while duplex grades provide the highest resistances, with higher values for the nominal yield stress. On the contrary, the resistance and behaviour exhibited by ferritic stainless steel alloys are comparable to those shown by carbon steels (SCI 2017). Table 8.4 reports the properties of the austenitic, ferritic and duplex stainless steels proposed by Afshan et al. (2019) for hot-rolled open sections and considered herein. Note that these parameters are not nominal values; they were proposed based on extensive measurements from actual coupon tests.

Table 8.4. Two-stage Ramberg-Osgood material model parameters from Afshan et al. (2019) used in this study.

Stainless steel	E [GPa]	f_y [MPa]	f_u [MPa]	ε_u [mm/mm]	n	m
Austenitic	200	280	580	0.50	9.1	2.3
Ferritic	200	320	480	0.16	17.2	2.8
Duplex	200	530	770	0.30	9.3	3.6

Figure 8.1 and Figure 8.2 show the plan configurations and generic elevations, respectively, covered in this study, which are identical to those proposed in (Lemma et al. 2022). As it can be seen, four plan typologies (T1, T2, T3, T4) of four bays per side were studied. In the X-direction, the bays were 6 meters long, while in the Y-direction, the bay lengths varied between 4, 6 and 8 meters. Similarly, three total heights were studied – structures of 3 (3S), 6 (6S) and 9 (9S) storeys – to cover low, medium and high multi-storey frames. The storey height assumed a constant value of 3.5 m for all frames.

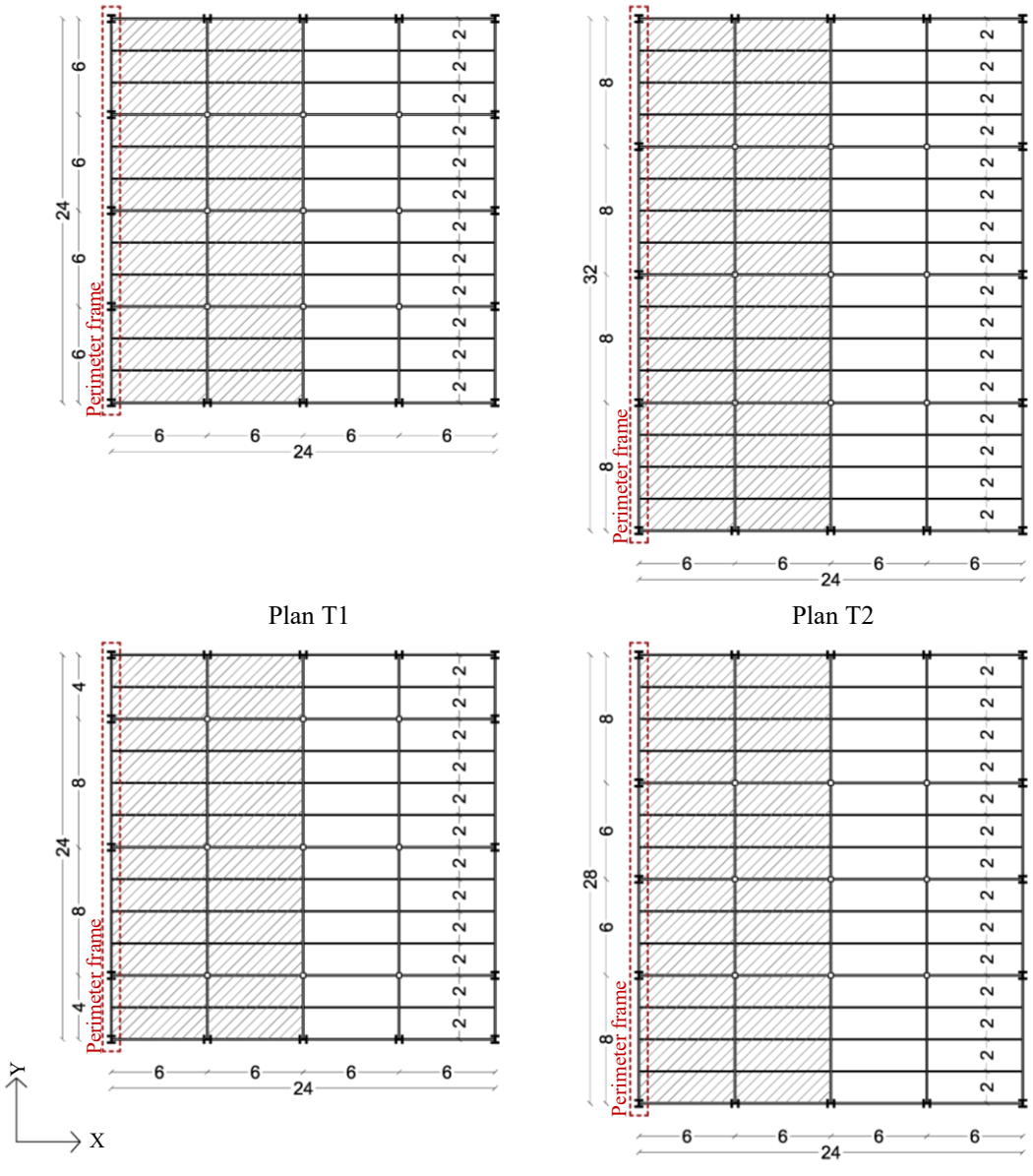

Figure 8.1. Plan typologies covered in this study – equivalent to those reported by Lemma et al. (2022).

Plan	L1	L2	L3	L4
T1	6 m	6 m	6 m	6 m
T2	8 m	8 m	8 m	8 m
T3	4 m	8 m	8 m	4 m
T4	8 m	6 m	6 m	8 m

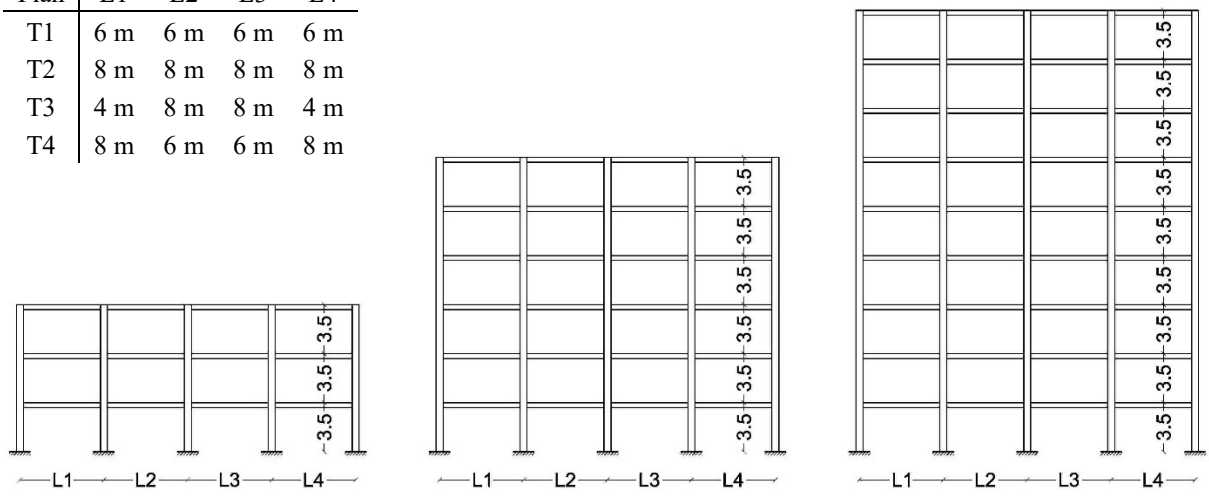

Figure 8.2. Elevations covered in this study – equivalent to those reported by Lemma et al. (2022).

Following the design considerations reported in (Lemma et al. 2022), the seismic actions were assumed to be resisted by the moment resisting perimeter frames, and 2D frame analyses were performed accordingly. Only the perimeter frames in the Y-direction were considered in this study. The tributary areas corresponding to the Y moment resisting frames, which are the half of the plan, are highlighted in Figure 8.1. A leaning column was used to consider, in a planar analysis, the second order effects of the gravity loads applied to the inner resisting part on the perimeter frame. It was also assumed that braced frames existed in the X-direction. Two further considerations were taken into account following the approach in (Lemma et al. 2022): full strength beam-column joints and the diaphragm effect at each floor level.

8.3.2. Gravity loading and seismic mass considerations

Perimeter resistant frames were designed to support the gravity loads reported in (Lemma et al. 2022), i.e., a permanent load of $G_k = 3$ kN/m^2 and a live load of $Q_k = 3$ kN/m^2. Following the loading scheme given in (Lemma et al. 2022), the moment resisting perimeter frames directly supported the loads transmitted by the secondary and main beams in the X-direction corresponding to an area equal to the total length of the portal frame in the Y-direction multiplied by half of the span in the X-direction (6/2 = 3 m), while the leaning column directly supported the loads corresponding to an area equal to the length of the portal frame in the Y-direction multiplied by 1.5 times the span length in the X-direction (6·1.5 = 9 m). Likewise, the seismic masses derived from the gravity loads adopted the same distribution as that given in (Lemma et al. 2022), i.e., the masses were considered lumped at the nodes of the structural model, so those corresponding to the vertical loads of the secondary beams and leaning columns were distributed proportionally to the external and internal nodes of the perimeter resistant frames.

Vertical loads were applied as concentrated. Table 8.5 reports the characteristic values of the concentrated permanent G_k and live Q_k loads assigned to the perimeter frames at each floor and for each plan typology, where $F_{b,conc}$ refers to the concentrated loads transferred from the secondary beams and applied on the main beams, $F_{c,ext}$ and $F_{c,int}$ to the concentrated loads at the external and internal beam-column nodes, and $F_{lean,col}$ to the concentrated loads applied at the leaning column. Table 8.5 also summarises the total mass assigned at each floor and for each plan typology, and its distribution at the external and internal nodes. Note that the seismic masses were computed as $G_k + \psi_{e,i} Q_k$ (prEN 1998-1-1 2021), being $\psi_{e,i} = \psi_2$ (prEN 1998-1-2 2021) and $\psi_2 = 0.3$ (prEN 1990 2022) in the case of structures with occupancy category equal to B (offices). Moreover, it should be noted that the masses reported in Table 8.5 were derived from the gravity loads, i.e., the masses derived from the self-weight of the structure were not included.

Table 8.5. Vertical loads and masses assigned to the perimeter frames.

Plan	Permanent vertical loads [kN]				Live vertical loads [kN]				Seismic masses [Tonnes]		
	$F_{b,conc}$	$F_{c,ext}$	$F_{c,int}$	$F_{lean,col}$	$F_{b,conc}$	$F_{c,ext}$	$F_{c,int}$	$F_{lean,col}$	Tributed to frame	Ext. node	Int. node
T1	18.0	9.0	18.0	648.0	18.0	9.0	18.0	648.0	101.32	12.66	25.33
T2	18.0	9.0	18.0	864.0	18.0	9.0	18.0	864.0	135.09	16.89	33.77
T3	18.0	9.0	18.0	648.0	18.0	9.0	18.0	648.0	101.32	9.50	27.44
T4	18.0	9.0	18.0	756.0	18.0	9.0	18.0	756.0	118.21	11.61	31.66

8.3.3. Seismic force considerations

All case studies were designed to resist the same seismic action. The seismic action was calculated according to the second revision of the Eurocode 8 but to be equivalent to that considered in the study of Lemma et al. (2022) – and computed as prescribed in the current version of Eurocode 8. According to prEN 1998-1-1 (2021), the seismic action should be represented by a pseudo-absolute acceleration response spectrum. The elastic response spectrum was computed assuming a CC2 consequence class, a site category B, a topography amplification factor F_T equal to 1.0, a reference seismic hazard $S_{\alpha,ref}$ of 8.5 m/s^2, and a 5% damping ratio. The resulting seismic action index S_δ was 10.11 m/s^2. As stated in prEN 1998-1-1 (2021), MRFs were designed attending to the Significant Damage (SD) limit state and assuming a return period of 475 years. The resulting elastic spectrum, shown in Figure 8.3. Figure 8.3 also shows the reduced spectra for the application of the force-based approach for SD limit state with and without lower bounds (adopting a value of β = 0.08 given in prEN 1998-1-2 (2021)). It should be noted that MRFs studied by Lemma et al. (2022) were also designed to meet the interstorey drift limitation at the Damage Limitation (DL) limit state. This is no longer a requirement in prEN 1998-1-2 (2021), since the return period for DL has changed from 95 to 60 years, which leads to more severe limitations in SD than in DL. In any event, drift controls at SD according to prEN 1998-1-2 (2021) are similar to those at DL according to the current version of Eurocode 8 (Tartaglia et al. 2022).

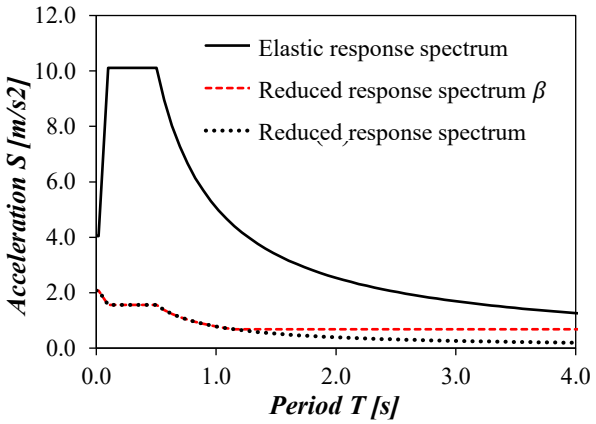

Figure 8.3. Elastic and reduced (with and without lower bound β) response spectra at SD limit state.

8.3.4. Design procedure and analysis considerations

Perimeter frames were designed according to prEN 1990 (2022), prEN 1993-1-1 (2021), prEN 1993-1-4 (2021), prEN 1998-1-1 (2021) and prEN 1998-1-2 (2021), following an iterative process. The design process is outlined in Figure 8.4, which is based on the design phases proposed by Lemma et al. (2022). DC3-S235 frame designs proposed by Lemma et al. were used as a starting point, being the austenitic MRFs the first case studies to be modelled.

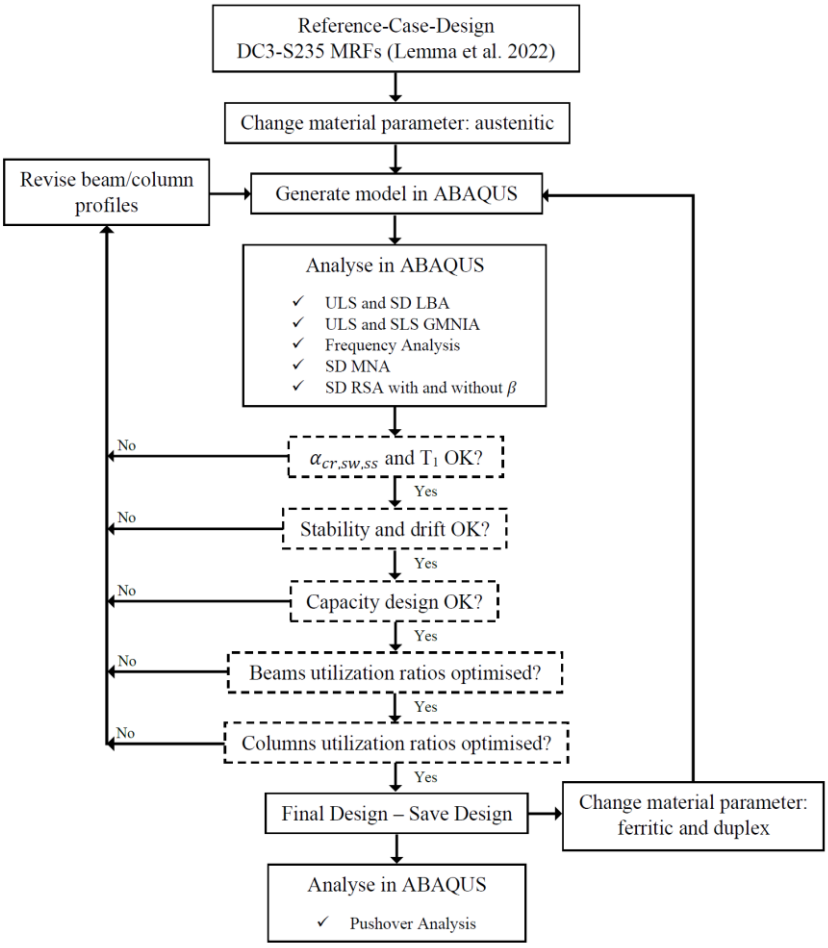

Figure 8.4. Design process adopted in this study.

The structure (i.e., dimensions, material, cross-sections, boundary conditions) and actions (i.e., sway imperfections, masses and loads) were modelled in ABAQUS (2016), as explained in Section 8.4 with more detail. The optimisation of the final design was achieved by checking its stability (interstorey drift values close to, but below, the 2% limit for $d_{r,SD}$ were sought, and the second order sensitivity index for stainless steel MRFs θ_{ss} was limited to 0.3) and member resistance in accordance with the requirements of the second revision of the Eurocodes.

The following analyses were carried out: Linear Buckling Analysis (LBA) with the gravity load combinations at Ultimate Limit State (ULS) and at the Significant Damage limit state (SD) in seismic condition, Geometrical and Material Nonlinear Analysis with Imperfections (GMNIA) at ULS and Serviceability Limit State (SLS), frequency analysis, Material Nonlinear Analysis (MNA) for gravity loads at SD, and reduced Response Spectrum Analysis (RSA) at SD with and without lower bound.

Regarding the static design of the stainless steel frames considered, LBA analyses with the gravity load combination at Ultimate Limit State (ULS) were performed to determine the instability susceptibility of the design $\alpha_{cr,sw,ss}$ (note that structures remained in the elastic range for the considered gravity actions, so K_s/K = 1.0). GMNIA analyses (with ULS and SLS gravity load combinations) were conducted to obtain the values of the internal forces and deflections needed to verify the design requirements prescribed in prEN 1993-1-1 (2021) and prEN 1993-1-4 (2021). Initial sway imperfections were introduced by means of a system of equivalent horizontal forces (i.e., notional loads).

Regarding the seismic design, LBA analyses were performed for the gravity loads at SD limit state to determine the amplification factor $k_{sw,ss}$ given in Eq. 2.12 by which the horizontal forces (initial imperfections) should be multiplied to consider the second order effects in a MNA for gravity loads at SD analysis (prEN 1993-1-4 2021). It is worth mentioning that, technically, it is not necessary to calculate the $k_{sw,ss}$ factor when second order effects are directly taken into account by performing a GMNA, but the amplification of horizontal forces (1) is the most widespread approach of those given in prEN 1993-1-1 (2021) to consider second order effects in in-plane structures, and (2) it is in line with the approach given in prEN 1998-1-2 (2021) to account for second order effects due to seismic actions. Note that for relatively low values of the vertical loads, where second order effects are not triggered, as is the case, performing a GMNA analysis tends to be less detrimental. MNA analyses were performed for gravity loads at SD combination, with the amplified equivalent sway imperfection loads combined with the gravity loads, to determine the design internal forces derived from the gravity loads at the seismic condition necessary for the resistance verifications. Frequency analyses allowed obtaining the fundamental period of the structures. Finally, Response Spectrum Analyses (RSA) were performed to determine (1) the design interstorey drifts at the significant damage limit state $d_{r,SD}$ (using the reduced

spectra at SD without lower bound), and (2) the design internal forces derived from the seismic action necessary to determine the second order effect index and perform resistance verifications (using the reduced spectra at SD with lower bound).

The gravity loads were combined according to prEN 1990 (2022). Eq. 8.12, Eq. 8.13 and Eq. 8.14 show the gravity load combinations considered for Ultimate Limit State (ULS), Serviceability Limit State (SLS) and Significant Damage (SD) limit state for the seismic condition, respectively.

$$1.35G_k + 1.5Q_k \quad \text{Eq. 8.12}$$

$$1.0G_k + 1.0Q_k \quad \text{Eq. 8.13}$$

$$1.0G_k + 0.3Q_k \quad \text{Eq. 8.14}$$

The design that fulfilled all the requirements was adopted as the final design for austenitic stainless steel. It was then re-analysed by changing the material properties to those of ferritic and duplex alloys, and making the required cross-section size modifications to achieve efficient and safe designs for these stainless steels as well.

8.4. Numerical modelling

The characteristics of the numerical models used in this study are described in this section. Unlike other software for seismic design reported in the literature (OpenSEES 2006; SeismoStruct 2016), this study was performed using the general purpose software ABAQUS (2016), which is widely used in stainless steel investigations because the nonlinear stress-strain behaviour can be directly and accurately implemented.

8.4.1. Finite element models

The models were performed using the general-purpose software ABAQUS (2016). The 2D moment resisting frames were designed using 2-noded linear Timoshenko beam elements B21 to ensure computational efficiency. An element size of 50 mm was used to discretise the mesh and realistically capture the behaviour of the plastic hinges, which is consistent with meshes reported in the literature for similar studies (Walport et al. 2019a, 2019b), although a much smaller number of elements per structural element may be sufficient to capture the overall behaviour, as mentioned in Section 5.2.1.3. Figure 8.5 provides a schematic representation of the finite element models used in this study. As shown, the columns were fixed at their bases. The X- and Y-displacements and the relative rotations at all beam-to-columns joints were constrained providing full continuity between members. European standard IPE and HEB/HEM cross-sections were assigned to the beams and columns, respectively.

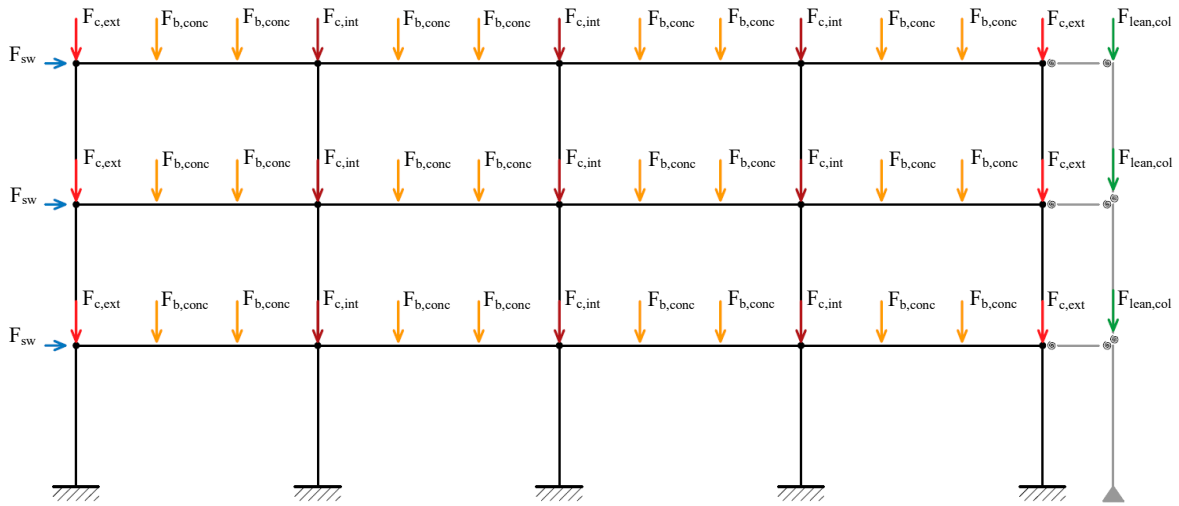

Figure 8.5. Schematic representation of the 2D FE model and loading scheme used in this study.

The gravity loads from the tributary area were applied to the moment resisting frame by means of a leaning column and represented in grey in Figure 8.5. The leaning column was pin-ended at its base, and it was subdivided into as many elastic beam elements as the number of storeys. These elastic beam elements were hinged at each end and connected to the adjacent elements through the spring elements available in ABAQUS. These spring elements were assigned high stiffness values for the X- and Y-directions, and very small stiffness values for rotations so that the elements did not transfer any significant moments to the frames. The effects from the gravity loads applied at the leaning column were transferred to the main structure by elastic beam elements with spring elements at both ends. The spring elements assured that the connecting beams worked as axially rigid. A box-section element available in ABAQUS was assigned to all auxiliary elements, providing moments of inertia and areas much larger at the leaning column and the links than at the frame columns. As in the principal frame, the leaning column and the connecting beams were discretized into 50 mm-long B21 elements. To simulate the effect of a rigid diaphragm, the horizontal displacements of all the nodes at a given floor were constrained to the beam-column joint node located at the left using the kinematic coupling constraint available in ABAQUS.

Initial sway imperfections were added to all load combinations by defining a system of equivalent horizontal forces (F_{sw} in Figure 8.5). The out-of-plumbness considered was computed as given in prEN 1993-1-1 (2021), and forces were amplified as explained in Section 8.3.4. The effects of bow imperfections were disregarded, as well as the effects of residual stresses, since their effect was implicitly considered in the member verifications carried out according to prEN 1993-1-4 (2021).

8.4.2. Material models

The engineering stress-strain curves assigned to the main structure were estimated using the two-stage Ramberg-Osgood material model provided in Section 2.3. Table 8.4 summarised the values of the

parameters for hot-rolled stainless steels adopted in this study, which were obtained from (Afshan et al. 2019). A Poisson's ratio v of 0.3 and a density equal to 7930 kg/cm^3 were assigned to all the stainless steel grades. Engineering stress-strain curves were converted into true stress-strain relationships, as per in prEN 1993-1-14 (2021), and cyclic degradation was not taken into account, as it is not relevant for new structures (prEN 1998-1-1 2021).

As mentioned before, the leaning column and the connecting beams behaved elastically. A perfectly elastic material with E = 210 GPa, v = 0.3 was assigned to these members.

8.4.3. Input actions and analyses

Concentrated gravity loads reported in Table 8.5 were combined according to the suitable load combinations (see Eq. 8.12-Eq. 8.14) and introduced in the model following the loading scheme reported in Figure 8.5. The modified Static General method (ABAQUS 2016) was used to obtain the internal forces and drifts of the frames under the gravity loads at the static (ULS, SLS) and seismic (SD) situations.

Likewise, masses reported in Table 8.5 were included in the finite element model as concentrated masses. A number of modes equal to the number of storeys of the structure, i.e., 3, 6 and 9 modes, were considered in the Response Spectrum Analysis (RSA) to assure a minimum cumulative modal participation ratio of 90% (prEN 1998-1-1 2021). The modes were summed applying the square-root-of-sum-of-squares approach (prEN 1998-1-1 2021), and a single direction of the excitation was studied. Reduced response spectra (with and without lower bound) were defined in terms of acceleration (mm/s^2) and frequency (Hz), and input through the acceleration spectra option available in ABAQUS (2016). A damping value equal to 0.05 was considered (prEN 1998-1-1 2021).

8.5. Design results

The final designs and verification results are presented and assessed in this section. The final designs for each material were labelled as [Typology]-[Storeys]-[Stainless steel grade], e.g., "T1-3S-Aus" refers to a 3-storey portal frame with a T1 floor typology and all structural elements made of austenitic stainless steel.

8.5.1. Design sections

Table 8.6, Table 8.7 and Table 8.8 show the selected hot-rolled European sections for austenitic, ferritic and duplex stainless steel MRFs, respectively. The profiles are listed per storey and are ordered starting from the lowest storey, i.e., from the first to the last storey. For T1 and T2 configurations, all beams of the same storey (in both external and internal spans) were designed with the same cross-section, while

in cases T3 and T4 the beams of the outermost spans had different cross-sections than the beams of the internal spans and are distinguished as (ext) and (int) in the Tables.

Table 8.6. Design sections for austenitic frame cases.

Case	Beams	Exterior columns	Interior columns
T1-3S	IPE 360; IPE 300; IPE 270	HEB 240; HEB 240; HEB 240	HEB 400; HEB 400; HEB 400
T2-3S	IPE 400; IPE 360; IPE 330	HEB 400; HEB 360; HEB 320	HEM 300; HEM 300; HEM 280
T3-3S	IPE 300; IPE 270; IPE 270 (ext); IPE 360; IPE 360; IPE 330 (int)	HEB 240; HEB 240; HEB 240	HEB 450; HEB 400; HEB 400
T4-3S	IPE 450; IPE 360; IPE 360 (ext); IPE 330; IPE 300; IPE 300 (int)	HEB 360; HEB 300; HEB 260	HEB 450; HEB 450; HEB 320
T1-6S	IPE 450; IPE 450; IPE 360; IPE 360; IPE 330; IPE 330	HEB 320; HEB 320; HEB 280; HEB 280; HEB 260; HEB 260	HEM 320; HEM 320; HEM 300; HEM 300; HEM 280; HEM 280
T2-6S	IPE 500; IPE 500; IPE 400; IPE 400; IPE 360; IPE 360	HEB 450; HEB 450; HEB 400; HEB 400; HEB 360; HEB 360	HEM 340; HEM 340; HEM 340; HEM 340; HEM 300; HEM 300
T3-6S	IPE 360; IPE 360; IPE 330; IPE 330; IPE 300; IPE 300 (ext); IPE 500; IPE 500; IPE 400; IPE 400; IPE 360; IPE 360 (int)	HEB 300; HEB 300; HEB 280; HEB 280; HEB 240; HEB 240	HEM 360; HEM 360; HEM 340; HEM 340; HEM 300; HEM 300
T4-6S	IPE 500; IPE 500; IPE 450; IPE 450; IPE 360; IPE 360 (ext); IPE 400; IPE 400; IPE 360; IPE 360; IPE 360; IPE 360 (int)	HEB 450; HEB 450; HEB 450; HEB 450; HEB 360; HEB 360	HEM 340; HEM 340; HEM 320; HEM 320; HEM 300; HEM 300
T1-9S	IPE 450; IPE 450; IPE 450; IPE 400; IPE 400; IPE 400; IPE 360; IPE 360; IPE 360	HEB 320; HEB 320; HEB 320; HEB 300; HEB 300; HEB 300; HEB 280; HEB 280; HEB 280	HEM 340; HEM 340; HEM 340; HEM 320; HEM 320; HEM 320; HEM 300; HEM 300; HEM 300
T2-9S	IPE 550; IPE 550; IPE 550; IPE 450; IPE 450; IPE 450; IPE 400; IPE 400; IPE 400	HEB 450; HEB 450; HEB 450; HEB 400; HEB 400; HEB 400; HEB 360; HEB 360; HEB 360	HEM 400; HEM 400; HEM 400; HEM 360; HEM 360; HEM 360; HEM 300; HEM 300; HEM 300
T3-9S	IPE 400; IPE 400; IPE 400; IPE 360; IPE 360; IPE 360; IPE 330; IPE 330; IPE 330 (ext); IPE 550; IPE 550; IPE 550; IPE 450; IPE 450; IPE 450; IPE 400; IPE 400; IPE 400 (int)	HEB 280; HEB 280; HEB 280; HEB 260; HEB 260; HEB 260; HEB 240; HEB 240; HEB 240	HEM 360; HEM 360; HEM 360; HEM 320; HEM 320; HEM 320; HEM 300; HEM 300; HEM 300
T4-9S	IPE 500; IPE 500; IPE 500; IPE 450; IPE 450; IPE 450; IPE 400; IPE 400; IPE 400 (ext); IPE 450; IPE 450; IPE 450; IPE 400; IPE 400; IPE 400; IPE 360; IPE 360; IPE 360 (int)	HEB 450; HEB 450; HEB 450; HEB 360; HEB 360; HEB 360; HEB 320; HEB 320; HEB 320	HEM 400; HEM 400; HEM 400; HEM 360; HEM 360; HEM 360; HEM 300; HEM 300; HEM 300

Table 8.7. Design sections for ferritic frame cases.

Case	Beams	Exterior columns	Interior columns
T1-3S	IPE 360; IPE 300; IPE 270	HEB 240; HEB 240; HEB 240	HEB 400; HEB 400; HEB 400
T2-3S	IPE 400; IPE 360; IPE 330	HEB 400; HEB 360; HEB 320	HEM 300; HEM 300; HEM 280
T3-3S	IPE 300; IPE 270; IPE 270 (ext); IPE 360; IPE 360; IPE 330 (int)	HEB 240; HEB 240; HEB 240	HEB 450; HEB 400; HEB 400
T4-3S	IPE 400; IPE 360; IPE 360 (ext); IPE 300; IPE 300; IPE 300 (int)	HEB 300; HEB 300; HEB 260	HEB 450; HEB 450; HEB 320
T1-6S	IPE 400; IPE 400; IPE 360; IPE 360; IPE 360; IPE 360	HEB 300; HEB 300; HEB 280; HEB 280; HEB 260; HEB 260	HEB 450; HEB 450; HEB 400; HEB 400; HEB 360; HEB 360
T2-6S	IPE 500; IPE 500; IPE 400; IPE 400; IPE 360; IPE 360	HEB 320; HEB 320; HEB 300; HEB 300; HEB 300; HEB 300	HEM 340; HEM 340; HEM 340; HEM 340; HEM 340; HEM 340
T3-6S	IPE 330; IPE 330; IPE 300; IPE 300; IPE 300; IPE 300 (ext); IPE 500; IPE 500; IPE 400; IPE 400; IPE 360; IPE 360 (int)	HEB 300; HEB 300; HEB 280; HEB 280; HEB 240; HEB 240	HEM 320; HEM 320; HEM 320; HEM 320; HEM 300; HEM 300
T4-6S	IPE 500; IPE 500; IPE 400; IPE 400; IPE 360; IPE 360 (ext); IPE 400; IPE 400; IPE 360; IPE 360; IPE 360; IPE 360 (int)	HEB 450; HEB 450; HEB 400; HEB 400; HEB 360; HEB 360	HEB 400; HEB 400; HEB 400; HEB 400; HEB 400; HEB 400

Table 8.7. Design sections for ferritic frame cases (continued).

Case	Beams	Exterior columns	Interior columns
T1-9S	IPE 450; IPE 450; IPE 450; IPE 400; IPE 400; IPE 400; IPE 360; IPE 360; IPE 360	HEB 320; HEB 320; HEB 320; HEB 300; HEB 300; HEB 300; HEB 280; HEB 280; HEB 280	HEM 320; HEM 320; HEM 320; HEM 320; HEM 320; HEM 320; HEM 300; HEM 300; HEM 300
T2-9S	IPE 550; IPE 550; IPE 550; IPE 450; IPE 450; IPE 450; IPE 400; IPE 400; IPE 400	HEB 400; HEB 400; HEB 400; HEB 360; HEB 360; HEB 360; HEB 320; HEB 320; HEB 320	HEM 400; HEM 400; HEM 400; HEM 340; HEM 340; HEM 340; HEM 300; HEM 300; HEM 300
T3-9S	IPE 400; IPE 400; IPE 400; IPE 360; IPE 360; IPE 360; IPE 330; IPE 330; IPE 330 (ext); IPE 550; IPE 550; IPE 550; IPE 450; IPE 450; IPE 450; IPE 400; IPE 400; IPE 400 (int)	HEB 280; HEB 280; HEB 280; HEB 260; HEB 260; HEB 260; HEB 240; HEB 240; HEB 240	HEM 360; HEM 360; HEM 360; HEM 320; HEM 320; HEM 320; HEM 300; HEM 300; HEM 300
T4-9S	IPE 500; IPE 500; IPE 500; IPE 450; IPE 450; IPE 450; IPE 400; IPE 400; IPE 400 (ext); IPE 450; IPE 450; IPE 450; IPE 400; IPE 400; IPE 400; IPE 360; IPE 360; IPE 360 (int)	HEB 400; HEB 400; HEB 400; HEB 340; HEB 340; HEB 340; HEB 320; HEB 320; HEB 320	HEM 360; HEM 360; HEM 360; HEM 340; HEM 340; HEM 340; HEM 300; HEM 300; HEM 300

Table 8.8. Design sections for duplex frame cases.

Case	Beams	Exterior columns	Interior columns
T1-3S	IPE 360; IPE 300; IPE 300	HEB 320; HEB 320; HEB 320	HEB 360; HEB 360; HEB 360
T2-3S	IPE 400; IPE 360; IPE 330	HEB 360; HEB 360; HEB 320	HEM 300; HEM 300; HEM 280
T3-3S	IPE 300; IPE 270; IPE 270 (ext); IPE 360; IPE 360; IPE 330 (int)	HEB 320; HEB 320; HEB 260	HEB 360; HEB 360; HEB 360
T4-3S	IPE 360; IPE 360; IPE 360 (ext); IPE 330; IPE 330; IPE 300 (int)	HEB 320; HEB 320; HEB 320	HEM 300; HEM 300; HEM 260
T1-6S	IPE 360; IPE 360; IPE 360; IPE 360; IPE 300; IPE 300	HEB 360; HEB 360; HEB 320; HEB 320; HEB 260; HEB 260	HEB 360; HEB 360; HEB 360; HEB 360; HEB 320; HEB 320
T2-6S	IPE 450; IPE 450; IPE 400; IPE 400; IPE 360; IPE 360	HEB 320; HEB 320; HEB 320; HEB 320; HEB 320; HEB 320	HEM 320; HEM 320; HEM 300; HEM 300; HEM 280; HEM 280
T3-6S	IPE 300; IPE 300; IPE 270; IPE 270; IPE 270; IPE 270 (ext); IPE 450; IPE 450; IPE 400; IPE 400; IPE 360; IPE 360 (int)	HEB 320; HEB 320; HEB 320; HEB 320; HEB 240; HEB 240	HEM 300; HEM 300; HEM 300; HEM 300; HEM 260; HEM 260
T4-6S	IPE 450; IPE 450; IPE 400; IPE 400; IPE 360; IPE 360 (ext); IPE 360; IPE 360; IPE 330; IPE 330; IPE 300; IPE 300 (int)	HEB 360; HEB 360; HEB 360; HEB 360; HEB 320; HEB 320	HEM 300; HEM 300; HEM 300; HEM 300; HEM 260; HEM 260
T1-9S	IPE 450; IPE 450; IPE 450; IPE 360; IPE 360; IPE 360; IPE 330; IPE 330; IPE 330	HEB 360; HEB 360; HEB 360; HEB 340; HEB 340; HEB 340; HEB 320; HEB 320; HEB 320	HEM 300; HEM 300; HEM 300; HEM 300; HEM 300; HEM 300; HEM 280; HEM 280; HEM 280
T2-9S	IPE 500; IPE 500; IPE 500; IPE 450; IPE 450; IPE 450; IPE 360; IPE 360; IPE 360	HEB 360; HEB 360; HEB 360; HEB 360; HEB 360; HEB 360; HEB 320; HEB 320; HEB 320	HEM 320; HEM 320; HEM 320; HEM 300; HEM 300; HEM 300; HEM 280; HEM 280; HEM 280
T3-9S	IPE 360; IPE 360; IPE 360; IPE 360; IPE 360; IPE 360; IPE 300; IPE 300; IPE 300 (ext); IPE 500; IPE 500; IPE 500; IPE 400; IPE 400; IPE 400; IPE 360; IPE 360; IPE 360 (int)	HEB 320; HEB 320; HEB 320; HEB 260; HEB 260; HEB 260; HEB 240; HEB 240; HEB 240	HEM 320; HEM 320; HEM 320; HEM 300; HEM 300; HEM 300; HEM 280; HEM 280; HEM 280
T4-9S	IPE 500; IPE 500; IPE 500; IPE 450; IPE 450; IPE 450; IPE 400; IPE 400; IPE 400 (ext); IPE 400; IPE 400; IPE 400; IPE 360; IPE 360; IPE 360; IPE 360; IPE 360; IPE 360 (int)	HEB 360; HEB 360; HEB 360; HEB 360; HEB 360; HEB 360; HEB 320; HEB 320; HEB 320	HEM 320; HEM 320; HEM 320; HEM 320; HEM 320; HEM 320; HEM 280; HEM 280; HEM 280

The design of the analysed frames is governed by the stability criteria and, as a general rule, the aim has been to reduce the dimensions of the beams considered in the reference cases (i.e., carbon steel frames reported by Lemma et al. (2022)) as much as possible, since the yield stress of stainless steels is higher than that of carbon steel considered as reference, and to increase the column sizes to compensate for the lower stiffness of stainless steels. In spite of this, the beams that resulted from the design tended

to be significantly oversized because the total stiffness of the frames was greatly affected by the stiffness provided by the floors. The final selected cross-sections for austenitic and ferritic low-rise MRFs are in line with those reported in (Lemma et al. 2022) for equivalent carbon steel MRFs, since the analyses remained in their elastic range and the elastic parameters of stainless and carbon steels are similar, and these designs were unaffected by second order effects. However, the design of medium- and high-rise structures was affected by second order effects, being more detrimental in the austenitic cases, which explains the differences observed in the profiles for the 6S and 9S cases. Finally, the most notable differences with respect to the reference profiles were found in the duplex cases: the significantly higher yield stress of this material makes several HEB profiles to be no longer classified as class 1, forcing their replacement with HEM profiles.

8.5.2. Results from the seismic analyses

Table 8.9, Table 8.10 and Table 8.11 show the relevant seismic results obtained from the numerical analyses for austenitic, ferritic and duplex MRFs, respectively. In the Tables, T_1 is the fundamental period, V_d is the design base shear force, $\alpha_{cr,sw,ss}$ and $k_{sw,ss}$ are the instability factor and corresponding amplification factor at the SD load combination, $ISDR_{SD}$ is the interstorey drift at the SD limit state, Ω_d is the overdesign factor, θ_{ss} is the maximum interstorey drift sensitivity index, $ISDR_{SD,2^o}$ is the interstorey drift at the SD limit state considering second order effects, UR_c is the maximum utilisation ratio for columns, and "Requir." refers to the design requirement that conditioned the selection of the profiles. Note that all cases satisfied the local hierarchy requirement given in Eq. 8.9, because the governing design rule was the interstorey drift and the required lateral stiffness of the structures was achieved by increasing the inertia of the columns once the weak beam-strong column criterion was verified (Tartaglia et al. 2022).

Table 8.9. Fundamental seismic results for austenitic MRFs.

Case	T_1 [s]	V_d [kN]	$\alpha_{cr,sw,ss}$	$k_{sw,ss}$	$ISDR_{SD}$ [%]	Ω_d	θ_{ss}	$\frac{1}{(1-\theta_{ss})}$	$ISDR_{SD,2^o}$ [%]	UR_c	Requir.
T1-3S	1.09	224	14.89	1.00	2.04	3.03	0.09	1.00	2.04	1.00	SD, UR
T2-3S	1.08	299	14.97	1.00	2.01	3.38	0.07	1.00	2.01	0.94	SD, UR
T3-3S	1.04	233	16.54	1.00	1.98	2.92	0.09	1.00	1.98	0.97	SD, UR
T4-3S	1.02	272	16.95	1.00	1.96	3.21	0.08	1.00	1.96	0.99	SD, UR
T1-6S	1.74	400	10.67	1.00	1.77	2.20	0.12	1.13	2.00	0.90	SD, UR
T2-6S	1.79	535	10.07	1.00	1.79	2.26	0.12	1.14	2.04	1.02	SD, UR
T3-6S	1.72	404	10.98	1.00	1.70	1.99	0.13	1.15	1.96	0.87	SD, UR
T4-6S	1.72	484	10.91	1.00	1.72	2.35	0.11	1.13	1.94	0.99	SD, UR
T1-9S	2.43	592	7.74	1.15	1.63	1.65	0.14	1.16	1.90	1.02	SD, UR
T2-9S	2.47	766	7.65	1.15	1.73	1.75	0.14	1.16	2.02	1.04	SD, UR
T3-9S	2.37	585	8.32	1.14	1.65	1.68	0.15	1.18	1.95	1.00	SD, UR
T4-9S	2.45	681	7.65	1.15	1.67	1.56	0.17	1.21	2.02	0.95	SD, UR

Table 8.10. Fundamental seismic results for ferritic MRFs.

Case	T_1 [s]	V_d [kN]	$\alpha_{cr,sw,ss}$	$k_{sw,ss}$	$ISDR_{SD}$ [%]	Ω_d	θ_{ss}	$\frac{1}{(1-\theta_{ss})}$	$ISDR_{SD,2^o}$ [%]	UR_c	Requir.
T1-3S	1.09	224	17.59	1.00	2.04	3.55	0.07	1.00	2.04	0.89	SD, UR
T2-3S	1.08	299	17.69	1.00	2.01	3.99	0.05	1.00	2.01	0.83	SD
T3-3S	1.04	233	19.54	1.00	1.98	3.38	0.07	1.00	1.98	0.84	SD
T4-3S	1.08	261	18.15	1.00	2.01	3.68	0.07	1.00	2.01	0.97	SD, UR
T1-6S	1.81	401	11.22	1.00	1.90	2.40	0.10	1.00	1.90	0.88	SD, UR
T2-6S	1.90	533	10.69	1.00	1.91	2.40	0.10	1.00	1.91	0.82	SD
T3-6S	1.81	405	11.60	1.00	1.80	2.08	0.11	1.13	2.03	0.73	SD
T4-6S	1.82	469	11.38	1.00	1.83	2.38	0.10	1.11	2.03	0.92	SD, UR
T1-9S	2.44	594	9.01	1.12	1.63	1.91	0.12	1.14	1.86	0.88	SD, UR
T2-9S	2.47	766	9.04	1.12	1.76	2.01	0.11	1.12	1.98	0.90	SD, UR
T3-9S	2.37	585	9.84	1.11	1.65	1.94	0.11	1.13	1.86	0.83	SD
T4-9S	2.50	686	8.65	1.13	1.69	1.78	0.13	1.15	1.95	0.84	SD

Table 8.11. Fundamental seismic results for duplex MRFs.

Case	T_1 [s]	V_d [kN]	$\alpha_{cr,sw,ss}$	$k_{sw,ss}$	$ISDR_{SD}$ [%]	Ω_d	θ_{ss}	$\frac{1}{(1-\theta_{ss})}$	$ISDR_{SD,2^o}$ [%]	UR_c	Requir.
T1-3S	1.06	229	17.24	1.00	1.99	6.61	0.04	1.00	1.99	0.88	SD, UR
T2-3S	1.10	297	16.07	1.00	2.02	7.17	0.03	1.00	2.02	0.86	SD, UR
T3-3S	1.08	226	16.89	1.00	2.03	5.59	0.05	1.00	2.03	0.76	SD
T4-3S	1.09	262	16.56	1.00	2.05	6.60	0.04	1.00	2.05	0.80	SD
T1-6S	2.02	400	8.34	1.14	2.03	3.53	0.10	1.00	2.03	0.80	SD
T2-6S	2.05	535	8.35	1.14	1.99	3.94	0.08	1.00	1.99	0.78	SD
T3-6S	2.00	399	8.79	1.13	1.98	3.17	0.10	1.00	1.98	0.58	SD
T4-6S	2.04	465	8.42	1.13	2.01	3.54	0.09	1.00	2.01	0.67	SD
T1-9S	2.62	575	7.44	1.16	1.86	2.87	0.10	1.00	1.86	0.60	SD
T2-9S	2.73	771	6.84	1.17	1.74	3.26	0.10	1.11	1.94	0.88	SD, UR
T3-9S	2.64	577	7.33	1.16	1.78	2.66	0.11	1.12	2.00	0.68	SD
T4-9S	2.69	687	6.81	1.17	1.80	2.82	0.11	1.13	2.02	0.80	SD

The obtained values of the fundamental periods and the design base shear forces are reasonable, and in the range of those published by Lemma et al. (2022). The fundamental periods ranged from 1.02 to 2.73 s, with the highest values being aligned with the tallest structures. As expected, the frames designed with the same profiles, i.e., the austenitic and ferritic T1-3S, T2-3S and T3-3S structures, showed the same T_1 and V_d values. The lowest values of the fundamental period were obtained for the austenitic cases since these structures were the ones with the lowest lateral stiffness. Furthermore, higher values for V_d were associated with high values of fundamental periods and masses, which explains the fact that the highest values of V_d were exhibited by the austenitic and ferritic T2-9S cases, but not by T2-9S-Dup, as it has a lower amount of mass due to a lower self-weight.

In the 3S cases, the highest values of $\alpha_{cr,sw,ss}$ were exhibited by the ferritic MRFs, followed by the duplex and the austenitic MRFs, which is in line with the values that the Y factor assumed for each stainless steel. In the 6S and 9S MRFs, the ferritic cases still exhibited the highest values of $\alpha_{cr,sw,ss}$,

followed by the austenitic and duplex MRFs, which showed the lowest values. It should be noted that the stability and resistance verifications at duplex frames were rarely affected by the Merchant-Rankine amplification factor $1/(1-\theta_{ss})$ due to the high values of ω_{rm} and Ω_d.

As explained in Section 8.3.4, interstorey drifts between 1.9 and 2.0 % were sought during the design process (see $ISDR_{SD,2^o}$ values). Note that the $ISDR_{SD}$ values reported in the Tables were obtained from the RSA analyses, and do not consider second order effects, while the $ISDR_{SD,2^o}$ values correspond to the actual interstorey drift indices, i.e., they were obtained by multiplying the $ISDR_{SD}$ values by the factor $1/(1-\theta_{ss})$, as prescribed in prEN 1998-1-2 (2021).

The value of the beam-overdesign factor Ω_d indicates the oversizing of the structure in terms of resistance. As shown in the Tables, the values of Ω_d ranged from 1.56 to 3.38 for the austenitic cases, from 1.63 to 3.99 for the ferritic frames, and from 1.74 to 7.17 for duplex MRFs. As expected, the highest values were usually obtained for the structures with the lowest height (3S) and longest spans (T2). The values of Ω_d for austenitic frames were in line with those reported in (Lemma et al. 2022) for DC3 carbon steel MRFs designed according to prEN 1998-1-2 (2021), where Ω_d adopts values between 1.50 and 3.0, approximately. Alternatively, ASCE 7 (2016) considers a constant value of Ω_d = 3.0. Since the design of the frames was governed by the interstorey drift calculated in the elastic regime, and the lateral stiffness of the structure is actually influenced by the inertia of the beams, slightly higher values of Ω_d were obtained for the ferritic cases, while Ω_d adopted overly conservative values for duplex structures.

Second order effects, which are evaluated by the stability index θ_{ss}, were negligible in all 3S cases, as well as in 6S-Dup cases ($\theta_{ss} < 0.1$). The highest values of θ_{ss} were obtained for 9S-Aus structures. For all cases, $\theta_{ss} < 0.2$, so the second order effects were considered by multiplying the seismic action effects by the Merchant-Rankine factor $1/(1-\theta_{ss})$. A trend between the $k_{sw,ss}$ and the $1/(1-\theta_{ss})$ factor can be drawn, even if a clear relationship cannot be established because θ_{ss} depends on the beam-overdesign factor Ω_d and the displacement $d_{r,SD}$. The obtained θ_{ss} values were in line with the values published in recent studies for carbon steel MRFs (Tartaglia et al. 2019, 2022; Lemma et al. 2022). It should be highlighted that if the Y factor is not considered (i.e., Eq. 8.6 is used instead of the proposed expression Eq. 8.11), the resulting stability indexes θ_{ss} would be below 0.1 in all cases, which would be unsafe and unreasonable since stainless steels are more affected by second order effects than carbon steels.

Finally, regarding the verification of column resistance, it is worth noting that austenitic cases were the most optimised ones, with utilisation ratio UR_c values close to unity – and never higher than 1.05%. Obviously, the governing design requirement was the interstorey drift at the SD limit state in all cases, but the verification of column resistance UR_c was also observed to be at the limit (i.e., $UR_c > 0.85$) in

all austenitic cases and in several ferritic cases, while the high strength capabilities exhibited by duplex stainless steels explain why the UR_c requirements rarely conditioned the final design in these cases.

8.6. Performance assessment: behaviour factors for stainless steel

The actual behaviour factors of the case studies have been estimated in this study to assess the suitability of carbon steel behaviour factors proposed by prEN 1998-1-2 (2021) for stainless steel structures. This section presents the assumptions considered in this study for the calculation of the individual behaviour factors (q_R, q_S, q_D), as well as the corresponding results.

8.6.1. Overview of the decomposition of the behaviour factor

It is well-assumed that the behaviour factor should consider the reserve of strength due to the redundancy of the structure and the oversizing in the elements, the energy dissipation capacity of the structure (ductility), and the structural damping (Uang et al. 1991; Whittaker et al. 1999; Zeris et al. 2014; Ferraioli et al. 2014; Castiglioni et al. 2017; Vamvatsikos et al. 2020). Based on this definition, the overall behaviour factor can be expressed as shown in Eq. 8.15, where q_Ω is the general overstrength factor – q_Ω can be split into the q_R factor, which accounts for the overstrength due to the redistribution of seismic action effects in redundant structures, and the q_S factor, which accounts for the overstrength due to other sources –, q_D is the factor pertinent to ductility, and q_ζ is the factor that reflects the influence of damping effects. It should be noted that the same damping values are generally considered for elastic and inelastic analyses (q_ζ=1) (Whittaker et al. 1999; Zeris et al. 2014; Ferraioli et al. 2014; Castiglioni et al. 2017), which results in the computation of the behaviour factor proposed by prEN 1998-1-2 (2021) (see Eq. 8.2).

$$q = q_\Omega \cdot q_D \cdot q_\zeta = (q_R \cdot q_S) \cdot q_D \cdot q_\zeta \quad \text{Eq. 8.15}$$

Due to the impact of the behaviour factor in seismic design, significant research has been devoted to the accurate formulation of each individual factor expressed in Eq. 8.15. According to Newmark and Hall (1982), the overdesign factor q_R can be estimated as per in Eq. 8.16 as the ratio of the shear force at which the global inelastic behaviour initiates V_y and the shear force at which the first local yielding occurs at any member $V_{1,y}$. In addition, when the fundamental period is higher than 0.5 s (Castiglioni et al. 2017), the ductility factor q_D can be defined in terms of the horizontal displacements as given in Eq. 8.17, i.e., as the ratio of the inelastic Δ_u and elastic Δ_y drift values at the ultimate resistance.

$$q_R = \frac{V_y}{V_{1,y}} \quad \text{Eq. 8.16}$$

$$q_D = \frac{\Delta_u}{\Delta_y} \quad \text{Eq. 8.17}$$

Considering that the general overstrength behaviour factor q_Ω may account for the reserve in resistance from the ultimate state V_u to the design base shear V_d, and that $q_\Omega = q_R \cdot q_S$, the estimation of the term pertinent to the overstrength due to other sources q_S can be computed as given in Eq. 8.18, i.e., as the ratio of the resistance at which the first local yielding occurs at any member and the design base shear (Lemma et al. 2022; Tartaglia et al. 2022).

$$q_S = \frac{V_{1,y}}{V_d} \qquad \text{Eq. 8.18}$$

Consequently, the overall behaviour factor can be computed as given in Eq. 8.19.

$$q = q_R \cdot q_D \cdot q_S \cdot q_\zeta = \frac{V_y}{V_{1,y}} \cdot \frac{\Delta_u}{\Delta_y} \cdot \frac{V_{1,y}}{V_d} \qquad \text{Eq. 8.19}$$

prEN 1998-1-2 (2021) explicitly defines the q_R factor as the ratio of the resistance value by which the horizontal seismic design action needs to be multiplied in order to first reach the resistance of a dissipative zone in any member in the structure and the resistance value by which the horizontal seismic design action needs to be multiplied, in order to form dissipative zones in a number of sections sufficient for the development of overall structural (plastic) instability, which may be obtained from a nonlinear static analysis. In other words, Eurocode adopts the definition proposed by Newmark and Hall (1982) for q_R. However, the second revision of Eurocodes does not prescribe any formulae for estimating the values of q_D and q_S.

8.6.2. Nonlinear static response and criteria for the bilinear approximation

Several approaches are available in the literature to estimate the actual behaviour factor of structures (Mazzolani and Piluso 1996). Among the most common are the nonlinear static (pushover) analyses and nonlinear time-history analyses, which generally lead to similar results (Lemma et al. 2022; Tartaglia et al. 2022). Nonlinear static analyses are carried out under constant vertical loads and monotonically increasing lateral loads. prEN 1998-1-1 (2021) states that the lateral loads should be distributed according to the pattern of the fundamental mode of vibration and calculated as functions of the total mass of each storey. Although the assumptions that the response of structures is governed by a single mode and that the mode shape remains constant through the whole-time history response are not completely accurate, the resulting resistance-displacement responses can be considered as accurate for regular medium-height structures (Krawinkler and Seneviratna 1998). To compute the behaviour factor value, the inelastic resistance-displacement response obtained from the pushover analysis may be idealised into a bilinear response defined by the three pair of points shown in Eq. 8.19, i.e., the first local yielding point $V_{1,y}$, the yielding point V_y and the ultimate state point V_u. However, there is no

consensus on the definition of these points from the results of the pushover analysis (Castiglioni et al. 2017). prEN 1998-1-1 (2021) states that the force-deformation capacity curve may be idealised into a bilinear relationship similar to that shown in Figure 8.6. In Figure 8.6, the elastic stiffness k^* is the secant stiffness to the point of the capacity curve where the first yielding of the primary structure occurs, and the yielding displacement Δ_y is computed as given in Eq. 8.20, where V_u is the force at ultimate state, Δ_u is the displacement that corresponds to V_u and E^* is the area under the transformed curve up to V_u. According to prEN 1998-1-1 (2021), the ultimate state (V_u, Δ_u) may correspond in any primary member, to ultimate local deformation in a ductile post-elastic mechanism, or to a brittle failure, or a failure governed by the instability of the whole structure, whichever occurs first. Instability can be assumed to occur when interstorey drift exceeds 4%.

$$\Delta_y = \frac{2E^* - V_u \cdot \Delta_u}{k^* \cdot \Delta_u - V_u} \qquad \text{Eq. 8.20}$$

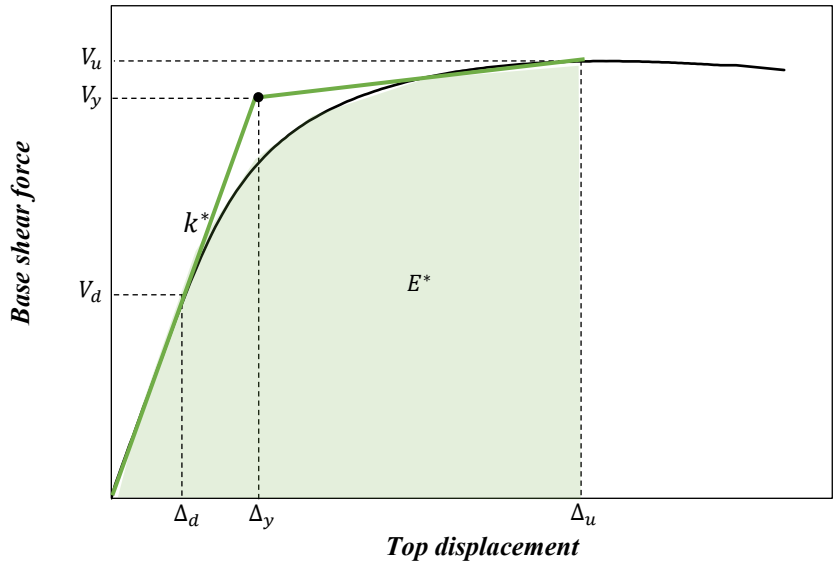

Figure 8.6. Pushover curve bilinear idealisation prescribed in prEN 1998-1-1 (2021).

The idealisation prescribed by prEN 1998-1-1 (2021) has been simplified in recent studies, where performance factors for SMRF design according to the second generation of Eurocode 8 were evaluated. Thus, Figure 8.7 shows a typical pushover curve and the bilinear idealisation responses proposed by Lemma et al. (2022) and Tartaglia et al. (2022). At shown, in both studies the first significant yielding point is the point where the inelastic behaviour onsets, and the yielding point is the intersection point of the initial tangent slope and the shear force at the ultimate limit state ($V_y = V_u$). The ultimate limit state in the first model (Lemma et al. 2022) is reached when one of these phenomena occurs: the columns buckle, the ultimate shear capacity is reached ($V_{u,max}$), or the 4% maximum interstorey drift is exceeded ($V_{u,4\%}$). The ultimate limit state in (Tartaglia et al. 2022), which is based on work reported in (FEMA P-695 2016), is determined by the ultimate base shear capacity $V_{u,max}$, and q_D is the ratio of the horizontal displacement corresponding to a base shear resistance equal to $0.8V_{u,max}$ and the elastic displacement at the ultimate resistance.

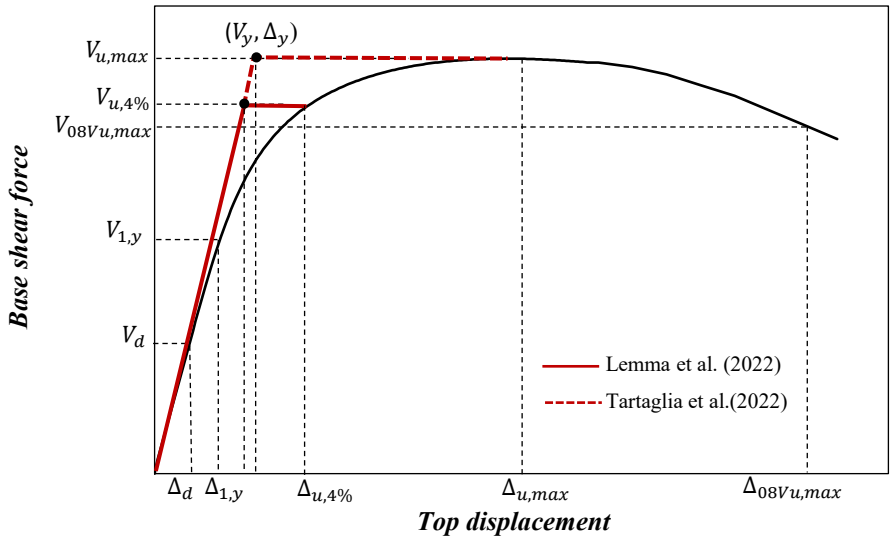

Figure 8.7. Pushover curve bilinear idealisations followed by Lemma et al. (2022) and Tartaglia et al. (2022).

8.6.3. Criteria adopted for the estimation of the actual behaviour factors for stainless steel MRFs

In this study, the actual behaviour factors of stainless steel frames were estimated by performing pushover analyses in ABAQUS (2016). In these analyses, the loading was applied in two steps: first, the structures were subjected to gravity loads (and sway imperfections); second, the lateral forces were applied and amplified monotonically until the ultimate base shear capacity was reached. The lateral forces were distributed among the floors following the modal pattern, i.e., the first mode of vibration, as established in prEN 1998-1-1 (2021). A modified Riks method available in ABAQUS (2016) was used to plot the full shear force-top displacement responses of the MRFs. As a sample, Figure 8.8 shows the pushover responses obtained for T1-3S cases. The pushover curves were idealised in bilinear responses assuming the criteria considered by Lemma et al. (2022). To this purpose, it was necessary to identify the load levels at which the design strength was reached, the first yielding of any member happened, and the structure collapsed. While the first state was easy to identify, the last two may be subject to discussion.

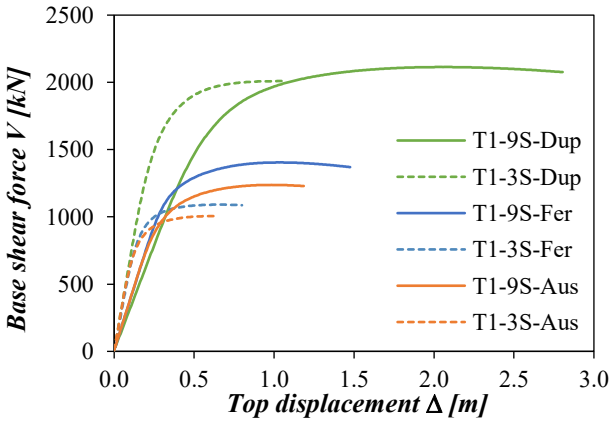

Figure 8.8. Pushover responses for T1-3S cases.

According to prEN 1998-1-1 (2021), for structures other than reinforced concrete and steel, given a force-deformation relationship, the first yielding of the primary structures denotes the point where the first member enters in the nonlinear range. However, the nonlinear behaviour of stainless steels complicates the determination of yielding in stainless steel cross-sections (see Section 5.4.1). According to the literature, a stainless steel section can be considered to yield when it reaches one of the following bending moment values: M_{el}, M_{02} and M_{pl}. The elastic bending moment resistance M_{el} is computed as $M_{el} = W_{el} \cdot f_y$, being W_{el} is the elastic section modulus, while M_{02} is the moment at which the maximum normal tensile stress is equal to the yield stress f_y. For carbon steel M_{02} is equal to M_{el}, but in materials showing nonlinear stress-strain responses such as stainless steels, it has to be estimated by integrating the nonlinear stress distribution of the cross-section (Real and Mirambell 2005). Finally, the plastic bending moment resistance M_{pl} is computed as $M_{pl} = W_{pl} \cdot f_y$, being W_{pl} the plastic section modulus. In an effort to be consistent with the carbon steel approach, two first yielding states were identified in this study: the first time the elastic moment M_{el} is reached at any member, and the first time the plastic bending moment M_{pl} is reached at any member. However, it should be remembered that the identification of the first yielding state ($V_{1,y}, \Delta_{1,y}$) does not influence the value of the global behaviour factor (see Eq. 8.19).

Similarly, two different ultimate states were identified in the pushover curves: the first ultimate state was associated with the limitation of the interstorey drift to 4%, while the second ultimate state was associated with achieving the ultimate base shear capacity (Tartaglia et al. 2022). Note that class 1 cross-sections guarantee the redistribution of internal forces up to high action levels, but cross-sections are susceptible to buckle once their capacity is exceeded – and local buckling is one of the reasons to consider the ultimate limit state of frames (prEN 1998-1-1 2021). Beam-type finite elements (ABAQUS 2016) are unable to reproduce local buckling, so in this study the strain limit method (see Section 2.4.2) was adopted to estimate the local failure of the structural members.

8.6.4. Results of the actual behaviour factors for stainless steel MRFs

Table 8.12, Table 8.13 and Table 8.14 show the relevant values of the force-displacement results obtained from the pushover analyses for austenitic, ferritic and duplex MRFs, respectively. In the Tables, V_d and Δ_d are the design base shear force and corresponding displacement (V_d), $V_{1,Mel}$ and $\Delta_{1,Mel}$ are the shear base force and corresponding displacement when the first member reaches its M_{el} capacity, $V_{1,Mpl}$ and $\Delta_{1,Mpl}$ are the shear base force and corresponding displacement when the first member reaches its M_{pl} capacity, $V_{u,4\%}$ and $\Delta_{u,4\%}$ are the shear base force and corresponding displacement when the interstorey drift reaches the 4% limit ($ISDR_{4\%}$), and $V_{u,max}$, $\Delta_{u,max}$ and $ISDR_{max}$ are the shear base force, corresponding displacement and corresponding interstorey drift when the ultimate base shear capacity is reached. As shown, the design state V_d was reached significantly before the state associated with the first yielding M_{el} for all frames, and hence M_{pl}, while the state associated with the first yielding M_{pl} was remarkably close to

the ultimate state associated to the $ISDR_{4\%}$, with $V_{1,Mpl}/V_{u,4\%}$ ratios ranging from 0.71 to 0.93. In all the cases analysed, ultimate base shear capacity was reached after exceeding the ultimate state recommended in the standard ($ISDR_{4\%}$): while the austenitic and ferritic cases exhibited $ISDR_{max}$ values close to 4%, with mean values of 6.2% and 6.3%, duplex MRFs exhibited $ISDR_{max}$ values close to 10%. For the ultimate limit state associated with the $ISDR_{4\%}$, reasonable values were obtained for both compressive and tensile strains, much smaller than the strain limit defined by the CSM, ε_{csm}, with maximum compressive strains of $1.62\varepsilon_y$ observed in T1-3S-Dup and maximum tensile strains of $6.37\varepsilon_y$ observed in T1-9S-Dup. Similarly, for the ultimate limit state associated with $ISDR_{max}$, the compressive strains were lower than ε_{csm}, with maximum a compressive strain of $4.13\varepsilon_y$ observed in T1-3S-Dup, and a maximum tensile strain of $9.43\varepsilon_y$ observed in T1-9S-Dup. Note that the strain limit values commonly adopted for class 1 cross-sections are $6\varepsilon_y$ in the case of compression and 2% in the case of tension for plastic design. In the accidental case of fire, the Eurocode limits the maximum tensile strain to 2% as well.

Table 8.12. Fundamental resistance-displacement pushover results for austenitic MRFs.

Case	V_d [kN]	Δ_d [mm]	$V_{1,Mel}$ [kN]	$\Delta_{1,Mel}$ [mm]	$V_{1,Mpl}$ [kN]	$\Delta_{1,Mpl}$ [mm]	$V_{u,4\%}$ [kN]	$\Delta_{u,4\%}$ [mm]	$V_{u,max}$ [kN]	$\Delta_{u,max}$ [mm]	$ISDR_{max}$
T1-3S	224	32	642	102	848	176	981	365	1006	645	6.8%
T2-3S	299	34	867	108	1099	159	1383	345	1450	705	7.7%
T3-3S	233	31	662	96	975	221	1061	365	1094	686	7.2%
T4-3S	272	30	805	95	1098	156	1358	365	1409	759	7.9%
T1-6S	400	81	784	171	955	240	1245	590	1297	1019	6.5%
T2-6S	535	88	1039	184	1300	268	1647	644	1682	962	5.7%
T3-6S	404	79	724	150	912	213	1278	625	1315	989	5.9%
T4-6S	484	80	957	171	1167	239	1531	653	1557	940	5.5%
T1-9S	592	155	859	242	1027	339	1229	807	1238	977	4.8%
T2-9S	766	160	1153	257	1390	354	1740	837	1779	1221	5.8%
T3-9S	585	147	871	228	1053	305	1365	786	1390	1108	5.5%
T4-9S	681	159	1020	238	1244	333	1442	834	1457	1059	5.0%

Table 8.13. Fundamental resistance-displacement pushover results for ferritic MRFs.

Case	V_d [kN]	Δ_d [mm]	$V_{1,Mel}$ [kN]	$\Delta_{1,Mel}$ [mm]	$V_{1,Mpl}$ [kN]	$\Delta_{1,Mpl}$ [mm]	$V_{u,4\%}$ [kN]	$\Delta_{u,4\%}$ [mm]	$V_{u,max}$ [kN]	$\Delta_{u,max}$ [mm]	$ISDR_{max}$
T1-3S	224	35	660	107	920	190	1053	342	1091	654	7.1%
T2-3S	299	34	986	117	1283	175	1574	342	1654	728	7.9%
T3-3S	233	31	725	99	1145	254	1206	361	1246	702	7.4%
T4-3S	261	32	772	97	1079	150	1379	363	1420	680	7.1%
T1-6S	401	85	819	179	1012	250	1280	576	1309	866	5.8%
T2-6S	533	98	1061	202	1349	289	1701	603	1758	968	6.0%
T3-6S	405	87	730	161	955	230	1332	608	1381	989	6.0%
T4-6S	469	88	941	181	1183	249	1561	626	1593	923	5.6%
T1-9S	594	156	979	266	1183	370	1389	799	1405	1032	5.1%
T2-9S	766	163	1267	276	1589	388	1917	750	2001	1270	6.9%
T3-9S	585	146	978	248	1229	338	1555	777	1599	1190	5.9%
T4-9S	686	164	1062	262	1315	365	1591	816	1611	1059	5.1%

Table 8.14. Fundamental resistance-displacement pushover results for duplex MRFs.

Case	V_d [kN]	Δ_d [mm]	$V_{1,Mel}$ [kN]	$\Delta_{1,Mel}$ [mm]	$V_{1,Mpl}$ [kN]	$\Delta_{1,Mpl}$ [mm]	$V_{u,4\%}$ [kN]	$\Delta_{u,4\%}$ [mm]	$V_{u,max}$ [kN]	$\Delta_{u,max}$ [mm]	$ISDR_{max}$
T1-3S	229	33	1259	193	1564	273	1732	348	2009	1016	10.8%
T2-3S	297	34	1773	222	2132	297	2298	348	2771	1037	11.4%
T3-3S	226	32	1185	176	1523	259	1732	344	2008	988	10.5%
T4-3S	262	32	1506	196	1858	266	2115	344	2522	1064	11.3%
T1-6S	400	109	1217	352	1520	509	1641	620	1827	1270	8.1%
T2-6S	535	114	1710	387	2024	504	2240	629	2586	1427	9.1%
T3-6S	399	106	1103	304	1346	399	1674	621	1994	1605	10.2%
T4-6S	465	111	1390	352	1664	461	1920	628	2254	1519	9.5%
T1-9S	575	182	1399	469	1627	591	1870	816	2114	2056	10.5%
T2-9S	771	204	2029	570	2360	722	2632	936	2849	1725	7.9%
T3-9S	577	183	1316	432	1560	538	1974	886	2159	1861	9.2%
T4-9S	687	191	1620	473	1903	601	2209	857	2403	1663	8.2%

The values of the design resistance (V_d), first yielding resistances at M_{el} and M_{pl} ($V_{1,Mel}$,$V_{1,Mpl}$) and ultimate state resistance at $ISDR_{4\%}$ ($V_{u,4\%}$) reported in Table 8.12, Table 8.13 and Table 8.14 were used to compute the individual overstrength (q_R and q_S) behaviour factors using Eq. 8.16 and Eq. 8.18. Figure 8.9 shows the calculated values of q_R and q_S for (a) austenitic, (b) ferritic and (c) duplex MRFs. Values prescribed by prEN 1998-1-2 (2021), i.e., q_R=1.3 and q_S=1.5 are also plotted. As shown, the scatter in q_R is low compared to the scatter observed in q_S values. It should be remembered that q_R depends on the structure typology, while q_S is associated with the oversizing of the structural members. In fact, those case studies that showed notable higher q_S values were the one with values of Ω_d> 3.0 (i.e., 3S cases). Based on the results shown in Figure 8.9, it can be concluded that the values of q_R and q_S resulting from the consideration of the first yielding state when achieving M_{el} at any beam for the first time are more consistent with the values prescribed in the Eurocode for carbon steel frames than those considering the first yielding state for M_{pl}. Thus, the first yield state is hereafter referred to as the first time any member reaches its M_{el} capacity.

Table 8.15 presents the values of the individual and general behaviour factors obtained for all the case studies. The values were estimated as indicated in Eq. 8.19, and using the V_d, $V_{1,Mel}$, $V_{u,4\%}$, $\Delta_{1,Mel}$, $\Delta_{u,4\%}$ values reported in Table 8.13-Table 8.14. V_y and Δ_y were estimated as indicated in Figure 8.7, i.e., as the intersection point of the initial tangent slope and a horizontal line at the ultimate limit state. Table 8.15 also provides the mean values and coefficients of variation (COV) for the different components of q.

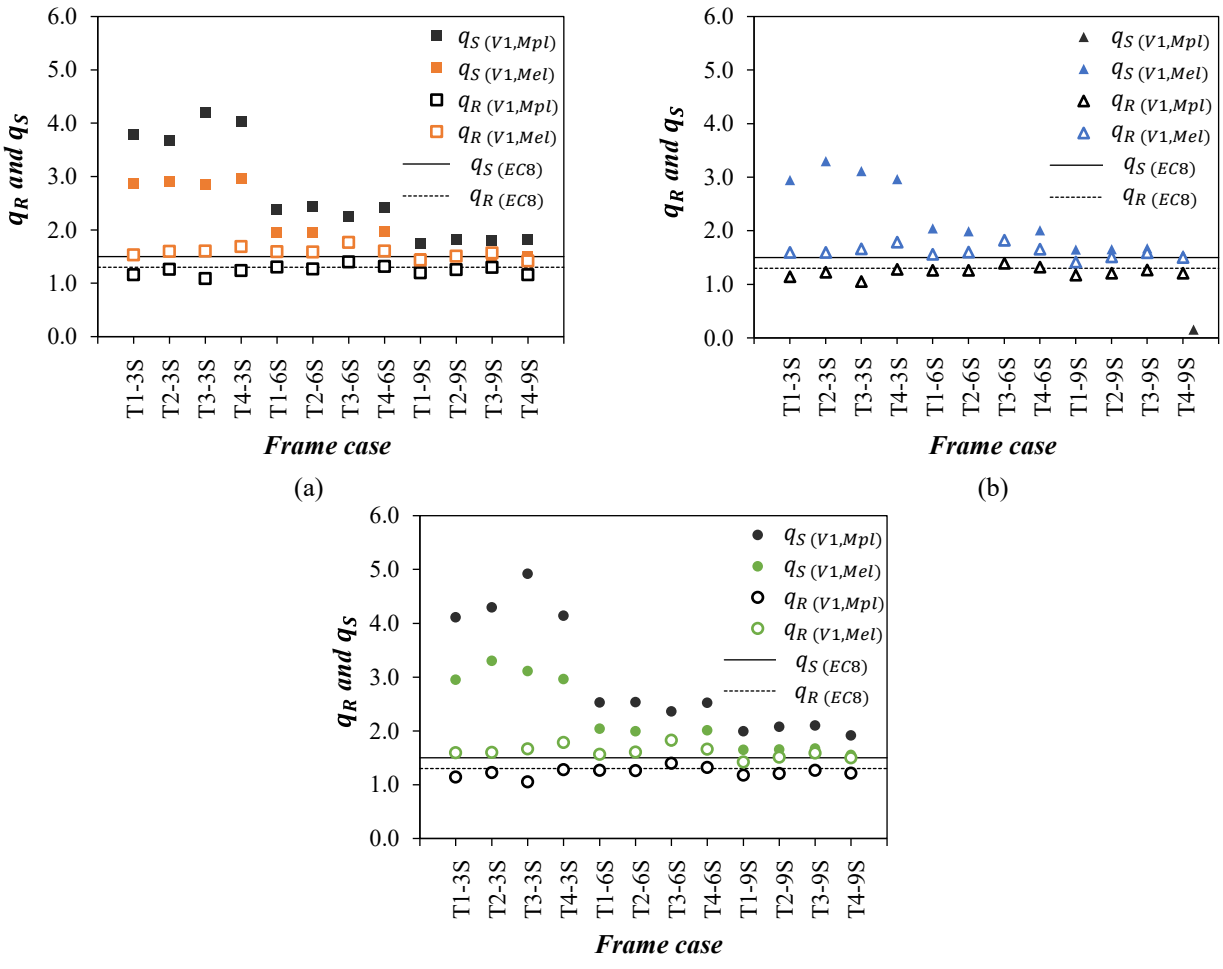

Figure 8.9. Numerical q_R and q_S behaviour factors for (a) austenitic, (b) ferritic and (c) duplex stainless steel frames and tabulated values given in prEN 1998-1-2 (2021).

Table 8.15. Behaviour factor values from pushover analyses (up to $ISDR_{4\%}$).

Case	Austenitic				Ferritic				Duplex			
	q_R	q_D	q_S	q	q_R	q_D	q_S	q	q_R	q_D	q_S	q
T1-3S	1.53	2.57	2.87	11.29	1.60	2.10	2.95	9.90	1.38	1.40	5.49	10.58
T2-3S	1.60	2.19	2.90	10.14	1.60	1.91	3.30	10.06	1.30	1.30	5.97	10.10
T3-3S	1.60	2.61	2.84	11.88	1.66	2.27	3.11	11.77	1.46	1.41	5.23	10.75
T4-3S	1.69	2.41	2.95	12.02	1.79	2.13	2.96	11.28	1.40	1.32	5.75	10.65
T1-6S	1.59	2.34	1.96	7.29	1.56	2.12	2.04	6.78	1.35	1.39	3.04	5.70
T2-6S	1.59	2.37	1.94	7.30	1.60	1.92	1.99	6.12	1.31	1.32	3.20	5.53
T3-6S	1.77	2.50	1.79	7.89	1.82	2.11	1.81	6.95	1.52	1.40	2.76	5.88
T4-6S	1.60	2.57	1.98	8.14	1.66	2.14	2.01	7.13	1.38	1.37	2.99	5.65
T1-9S	1.43	2.51	1.45	5.22	1.42	2.19	1.65	5.12	1.34	1.38	2.43	4.49
T2-9S	1.51	2.31	1.51	5.24	1.51	1.84	1.66	4.60	1.30	1.34	2.63	4.58
T3-9S	1.57	2.30	1.49	5.36	1.59	2.00	1.67	5.32	1.50	1.41	2.28	4.83
T4-9S	1.41	2.48	1.50	5.26	1.50	2.14	1.55	4.97	1.36	1.40	2.36	4.49
Mean	1.57	2.43	2.10	8.09	1.61	2.07	2.22	7.50	1.38	1.37	3.68	6.94
COV	0.059	0.052	0.281	0.314	0.068	0.060	0.283	0.329	0.052	0.027	0.381	0.372

As discussed above, q_R depends on the typology of the steel MRF. In the case of multi-storey moment resisting steel frames, for both DC2 and DC3 designs and even for aluminium MRFs, prEN 1998-1-2 (2021) proposes a value of q_R =1.3. In the case studies, the factor q_R exhibited a low dispersion (regardless the height of the structure) and showed similar values for austenitic and ferritic frames, but lower values for duplex structures. Nevertheless, all values obtained are higher than 1.3, being the mean values 1.57, 1.61 and 1.38 for austenitic, ferritic and duplex frames, respectively. These values of q_R are consistent with the stress-strain behaviour of the different grades. The austenitic grades are the most ductile stainless steels and have the lowest yield stress. The latter condition favours a more coherent relationship between the conventional design (governed by the vertical load resistance) and the seismic design (governed by the lateral stiffness). The achievement of $V_{u,4\%}$ occurred sooner for the austenitic cases than for the ferritic ones (with higher f_y values), which explains the slightly lower values of q_R for the austenitic frames than for the ferritic MRFs. The design of the duplex MRFs (which have the highest f_y values) was conditioned by the lateral stiffness, so their members were oversized for vertical actions, showing the highest values of $V_{1,Mel}$. This, together with the definition of the ultimate limit state at $ISDR_{4\%}$ and not at the maximum capacity of the structure, explains why the $V_{u,4\%}$ values are closer to the $V_{1,Mel}$ values and, consequently, the q_R values for duplex are notably lower than for the other stainless steel types.

The trend observed for the ductility factor q_D is also consistent with the typical behaviour of each stainless steel family. As shown in Table 8.15, the highest values of q_D are displayed by the austenitic cases, followed by the ferritic frames and, lastly, the duplex MRFs. Table 8.4 shows that austenitic is the most ductile alloy, followed by duplex and finally ferritic grades. The fact that the lowest q_D values are exhibited by the duplex cases, and not by the ferritic ones, is due to the smaller ratios between the fictional point Δ_y and the ultimate displacement $\Delta_{u,4\%}$.

The individual behaviour factor q_S is related to the oversizing of the structure and, as shown in Table 8.15, there is a clear relationship between the q_S values and the Ω_d values given in Table 8.12, Table 8.13 and Table 8.14. Focusing on the frame typology, the highest values of q_S are aligned with the lowest buildings and the T2 typology cases. Focusing on the material, the highest values of q_S are found for duplex cases. Despite the variability observed, prEN 1998-1-1 (2021) prescribes a constant value of q_S equal to 1.5. In the case of stainless steel structures, with lower initial stiffness and significantly affected by second order effects, the beams (and consequently the columns, to meet the weak beam-strong column criterion) need to be oversized, resulting in higher values of q_S than those given in the standard.

It should be noted that the values given in Table 8.15 are consistent with those reported in the reference study (Lemma et al. 2022) for S335 and S235 steels. As illustrated in (Lemma et al. 2022), the values

of q_R were higher than 1.3 for all cases, ranging between 1.3 and 2.0 for both steels, with slightly higher values for S235 steel. The q_D values showed a lower scatter, being approximately 1.5 for S335 MRFs, and between 2.0 and 2.5 for S235 MRFs. The highest variability was observed for the q_S factor, which ranged between 1.5 and 3.5 for S355, and between 1.0 and 2.0 for S235.

Finally, the individual behaviour factors were also calculated considering the ultimate state associated with the maximum capacity of the structure, since the limit strain method showed that for the ultimate state associated with the $ISDR_{4\%}$ the members were far from failure. Table 8.16 presents the values of the behaviour factors estimated using Eq. 8.19 and the $V_d, V_{1,Mel}, V_{u,max}, \Delta_{1,Mel}, \Delta_{u,max}$ values reported in Table 8.13-Table 8.14. V_y and Δ_y were estimated as indicated in Figure 8.7, i.e., as the intersection point of the initial tangent slope and a horizontal line at the ultimate limit state ($V_{u,max}, \Delta_{u,max}$). The mean and COV values of the behaviour factors are also given in Table 8.16.

Table 8.16. Behaviour factor values from pushover analyses (up to ultimate base shear capacity).

Case	Austenitic				Ferritic				Duplex			
	q_R	q_D	q_S	q	q_R	q_D	q_S	q	q_R	q_D	q_S	q
T1-3S	1.57	4.44	2.87	19.96	1.65	3.89	2.95	18.96	1.60	3.53	5.49	30.93
T2-3S	1.67	4.28	2.90	20.75	1.68	3.87	3.30	21.40	1.56	3.22	5.97	30.10
T3-3S	1.65	4.76	2.84	22.34	1.72	4.28	3.11	22.87	1.69	3.48	5.23	30.88
T4-3S	1.75	4.83	2.95	24.99	1.84	3.89	2.96	21.17	1.67	3.42	5.75	32.95
T1-6S	1.65	3.89	1.96	12.59	1.60	3.12	2.04	10.19	1.50	2.56	3.04	11.68
T2-6S	1.62	3.47	1.94	10.91	1.66	2.98	1.99	9.83	1.51	2.59	3.20	12.54
T3-6S	1.82	3.84	1.79	12.50	1.89	3.31	1.81	11.30	1.81	3.04	2.76	15.19
T4-6S	1.63	3.65	1.98	11.73	1.69	3.10	2.01	10.52	1.62	2.82	2.99	13.67
T1-9S	1.44	3.02	1.45	6.32	1.44	2.80	1.65	6.62	1.51	3.08	2.43	11.32
T2-9S	1.54	3.29	1.51	7.64	1.58	2.98	1.66	7.80	1.40	2.28	2.63	8.44
T3-9S	1.60	3.18	1.49	7.55	1.64	2.98	1.67	8.15	1.64	2.71	2.28	10.14
T4-9S	1.43	3.12	1.50	6.68	1.52	2.74	1.55	6.44	1.48	2.49	2.36	8.72
Mean	1.61	3.81	2.10	13.66	1.66	3.33	2.22	12.94	1.58	2.94	3.68	18.05
COV	0.066	0.160	0.281	0.465	0.072	0.148	0.283	0.464	0.067	0.137	0.381	0.527

As expected, the values reported in Table 8.16 are remarkably higher than those given in Table 8.15, especially for the low-rise buildings. The values of the overall behaviour factor q ranged from 6.32 (T2-9S-Aus) to 30.93 (T1-32-Dup). As shown herein, the values for each individual behaviour factor obtained from considering the ultimate state ($V_{u,max}, \Delta_{u,max}$) follows the trend observed when limiting the ultimate state to $ISDR_{4\%}$, except for the q_R factor, which adopts similar values in all cases, with an average value of approximately 1.6. The product $q_R \cdot q_S$ results in similar values when using the factors given in Table 8.16 to those reported by Tartaglia et al. (2022) for steel MRFs designed according to prEN 1998-1-2 (2021), as Tartaglia et al. considered the state associated with the maximum resistance of the portal frame as the ultimate state to calculate q_R and q_S. Thus, for the 3-storey cases studied by Tartaglia et al. (2022), the $q_R \cdot q_S$ values are between 6.5 and 7.2, and for the 6-storey cases, between 5.4 and 6.6. In (Tartaglia et al. 2022), q_D values were estimated considering a different criterion (q_D =

$\Delta_{0.8V_{u,max}}/\Delta_y$), with q_D values higher than those obtained in this study, and ranging from 3.4 to 5.9, approximately. Although the values of q_R, q_D, q_S and q given in Table 8.16 are in line with those published by Tartaglia et al. (2022), and the strain limit method showed that the beams did not suffer from local buckling even when the structures achieved their maximum resistance capacity, they should be treated with caution since the corresponding drift was too high in some of the cases, especially in the most oversized frames (i.e., 3S cases).

8.7. Proposal of behaviour factor for stainless steel MRFs: European and US design frameworks and comparison to the Japanese factors

This section presents the values for the European behaviour factor q for stainless steel MRFs proposed in this study. The equivalent response modification factors R, overstrength factors Ω_0 and the deflection amplification factors C_d corresponding to the US design framework (ASCE 7 2016) are calculated, and a comparison to the equivalent factor $1/D_s$ prescribed in the Japanese code (BCJ 2016) is also provided.

8.7.1. European design framework

Based on the results presented in the previous section, this research proposes individual behaviour factor values for austenitic, ferritic and duplex MRFs for their seismic design in the Eurocode framework. The values are based on the results reported in Table 8.15, which were obtained following the criteria recommended by the second revision of Eurocode 8, i.e., considering a maximum interstorey drift of 4%. The recommended behaviour factor values are summarised in Table 8.17, which depend on the stainless steel grade. The values for q_R are higher than that proposed in prEN 1998-1-2 (2021) for carbon steel (1.3) as the stainless steel alloys exhibit signs of yielding earlier, and consequently show higher $V_{u,4\%}/V_y$ ratios. Likewise, the values of q_S for stainless steels are higher than for carbon steel (1.5) because stainless steel MRFs tend to be more oversized due to the lower lateral stiffness of the systems. As mentioned before, in MRFs the lateral stiffness is defined by the Young's modulus and nonlinear material effects, and thus the design is governed by the interstorey drift rather than by the resistance of the members. This condition is particularly pronounced in duplex frames, which exhibit a remarkably high yield stress, much higher than the yield stress of carbon steels covered in prEN 1998-1-2 (2012). Alternatively, the proposed q_D values for stainless steel are lower than the value given for carbon steel MRFs (3.3). As mentioned in Section 8.6.1, Eurocode does not state explicitly the conditions to determine q_D, and it is reasonable to assume, in view of the results reported herein and in the literature (Lemma et al. 2022; Tartaglia et al. 2022), that the q_D value of the code was defined as $\Delta_{0.8V_{u,max}}/\Delta_y$ (Tartaglia et al. 2022). In view of this, the values of q_D proposed in Table 8.17 for stainless steels lie between the average values obtained from the two ultimate states considered in this study. Finally, the resulting values of the overall behaviour factor q for stainless steel are higher than

those for carbon steel, as one may expect due to the higher ductility and strain hardening characteristics of stainless steels. Overall q values are lower than the mean values reported in Table 8.15, except for duplex frames. For this grade, the values have been slightly increased as it was found that the capacity of the structures was notably underestimated when limiting the ultimate state to $ISDR_{4\%}$.

Table 8.17. Recommended behaviour factors for DC3 multi-storey stainless steel MRFs.

Stainless steel	European framework				US framework	
	q_R	q_D	q_S	q	R	Ω_0
Austenitic	1.5	2.4	2.1	7.5	12.0	3.0
Ferritic	1.5	2.1	2.2	7.0	12.0	3.0
Duplex	1.4	1.4	3.5	7.0	12.0	3.0

Moreover, it should be noted that the values recommended in Table 8.17 are conservative for the stainless steel MRFs made with class 1 sections studied in this research, as the assessment of the strains at the ultimate state considered showed that the selected cross-sections were far from local buckling failure. Therefore, it is reasonable to assume that the values given in Table 8.17 can be equally valid for stainless steel MRFs with non-dissipative members made of class 2 cross-sections (dissipative members are required to be class 1 (prEN 1998-1-2 2021).

8.7.2. US design framework

In the North American design framework, FEMA P-695 (2016) reports a detailed procedure for estimating the denominated "seismic performance factors", i.e., the response modification factor R, the overstrength factor Ω_0, and the deflection amplification factor C_d. These factors comply with the US seismic provisions in (ASCE 7 2016) and other standards such as (AISC 341 2016). As in the European design framework, R, Ω_0 and C_d assume different values depending on the structural archetype, and can be estimated from global inelastic responses. Thus, for special steel moment resisting frames, which can be considered equivalent to DC3 designs, R, Ω_0 and C_d values are equal to 8, 3 and 5.5, respectively (ASCE 7 2016). The R factor is the ratio of the force level that would be developed in the system for design earthquake ground motions (if the system remained entirely linear and elastic) to the base shear prescribed for design, Ω_0 is the ratio of the maximum strength of the fully-yielded system to the design base shear, and C_d is some fraction of the R factor (typically less than 1.0). C_d is estimated as the ratio of the roof drift of the seismic-force resisting system corresponding to design base shear, assuming that the system remains essentially elastic for this level of force, and the roof drift of the yielded system corresponding to design earthquake ground motions, multiplied by the R factor. Based on the Newmark rule, the value of C_d is equal to the value of R when assuming a damping factor equal to 5%.

Since the North American standards ASCE 7 (2016) and AISC 341 (2016) propose seismic design equations similar to those prescribed in prEN 1998-1-2 (2021) – see (Tartaglia et al. 2022) for a detailed overview of the US design requirements –, and the equations proposed in AISC 370 (2021) for stainless

steel are based on the equations given in prEN 1993-1-4 (2021), it can be recommended that for special stainless steel moment resisting frames R (C_d) and Ω_0 adopt the values of q and $q_R \cdot q_S$ given in Table 8.16. Based on the mean values of q and $q_R \cdot q_S$, Table 8.17 also includes approximate and conservative recommended values for R and Ω_0. It should be noted that the mean values of Ω_0 for austenitic, ferritic and duplex systems were close to 3.5, 3.5, and 5.5, respectively, but following the indications given in (FEMA P-695 2016), Ω_0 was limited to 3.0. Obviously, values for R and Ω_0 are indicative. To obtain more accurate values of the seismic performance factors, archetypes, analyses and idealisations of the force-displacement curves must meet all the requirements given in FEMA P-695 (2016).

8.7.3. Japanese design framework

Finally, the recommended values and results are compared with the values prescribed in the Japanese code (BCJ 2016) for stainless steel structures. Currently, the Japanese code is the only international specification that includes specific recommendations for the design of stainless steel portal frames under seismic conditions. Similar to the European and US standards, the Japanese code (BCJ 2016) prescribes values of performance factors to take advantage of the ductility of the structural member in the ultimate limit state. Not only the elastic analysis but also the plastic analysis is compulsory to check structural safety in this design framework. Thus, the inverse of the ductility reduction factor D_s available in the Japanese code (BCJ 2016) is considered equivalent to the European ductility behaviour factor q_D calculated assuming that the ultimate state is defined by the achievement of the maximum capacity of the structure. The value of $1/D_s$ depends on the cross-section classifications of the columns and beams (and on the effective slenderness ratio of the brace in the case of braced portal frames). The Japanese code covers only three stainless steel alloys, with yield stress and ultimate strength values between 235 and 325 MPa, and between 520 and 690 MPa, respectively; and classifies beams and columns into four groups (A-D), based on the cross-sectional shape and yield stress. Although the stainless steels used in this study are not specifically covered by the Japanese code, it can be assumed that the case studies present class A columns and class B beams. For MRFs without bracings and class B cross-sections, the value of $1/D_s$ prescribed in (BCJ 2016) is 3.33. As it is shown in Table 8.16, the value of $1/D_s$ is in good agreement with the q_D values obtained for the case studies.

8.8. Concluding remarks

The second generation of Eurocode 8 will include remarkable changes, but will not introduce any supplementary rules for stainless steel structures because the lack of studies on the global performance of stainless steel structures under seismic forces. On this context, this chapter presented a numerical research on the seismic performance of 36 stainless steel Moment Resisting Frames (MRFs). The case studies were designed according the codified prescriptions for highly dissipative structures (DC3) given

in prEN 1998-1-1 (2021) and prEN 1998-1-2 (2021). The parametric study was performed in ABAQUS and based on the investigation on carbon steel MRFs by Lemma et al. (2022).

The study cases have been designed according to the force-based approach given in prEN 1998-1-1 (2021) (based on tabulated values of behaviour factors), and the rules prescribed in prEN 1998-1-2 (2021). These provisions refer to carbon steel structures and, in some cases, assumptions have been made to adapt them to stainless steel structures. The design of the analysed frames was governed by the stability criteria and, as a general rule, the final selected cross-sections were similar to those exhibited in the reference cases. The major differences were explained by the lower lateral stiffness, higher yield stress values, and higher susceptibility to second order effects shown by the stainless steels. It was observed that, in order to ensure sufficient lateral stiffness, beams tend to be oversized for gravity loadings. The analysis of the investigated frames led to the proposal of a new expression to assess and consider second order effects on stainless steel structures, which accounts for the effect of material nonlinearities and allows the adoption of the limiting values prescribed in prEN 1998-1-2 (2021) for consideration of geometrical nonlinearities.

In order to assess the suitability of carbon steel behaviour factors for stainless steel structures. The different components of the behaviour factors (q, q_R, q_D, q_S) were estimated from the pushover curves and idealised into bilinear response following recommendations given in the literature. Based on these results, a set of values have been proposed for the behaviour factors to design stainless steel MRFs according to DC3 prescriptions, which have been particularized for each stainless steel family owing to their different behaviour. Thus, values of the structural overstrength factors q_R and q_S and for stainless steels, are higher than that proposed in prEN 1998-1-2 for carbon steel, as stainless steel alloys exhibit signs of yielding earlier, and MRFs tend to be more oversized due to the lower lateral stiffness of the systems, respectively. Alternatively, values of the ductility factor q_D are lower than the value given for carbon steel MRFs, which may seem contradictory, but it is probably due to the criteria – not explicitly mentioned – followed by the Eurocode for the estimation of this factor. The resulting values of the overall behaviour factor q for stainless steel are higher than those for carbon steel (i.e., 7.5 for austenitic frames and 7.0 for ferritic and duplex structures), as one may expect due to the higher ductility and strain hardening characteristics of stainless steels. Finally, the recommended values of q_D have been compared with the corresponding $1/D_s$ factor given in the Japanese code, the only standard that includes seismic rules for stainless steel structures to date, showing a good agreement. Likewise, and due to the similarities between the European and US design frameworks, preliminary values for the seismic performance factors (R, Ω_0 and C_d) prescribed in the US framework have been also recommended in this study.

Corresponding publication: González-de-León I., Arrayago I., Real E. and Sato A. (2023). Design of stainless steel moment resisting frames according to the second generation of Eurocode 8. *Submitted to Engineering Structures*.

PART III

Towards the consideration of material degradation

CHAPTER 9

Ductile fracture simulation of stainless steel coupons under monotonic tensile forces

9.1. Introduction

The failure of stainless steel alloys is ductile and is originated by void growth and coalescense (Zhang et al. 2022). Since 1960, several ductile fracture models have been developed for steels under monotonic loading, however, no specific prescriptions or adaptations have been provided yet to define the ductile fracture of stainless steels under monotonic loading. The accurate definition of ductile fracture models in stainless steels will be essential in the development of new design approaches such as the Direct Design Method (DDM) (Zhang et al. 2016b; Arrayago et al. 2022). Currently, the DDM covers the failure of whole systems and elements, but it does not consider the failure of joints explicitly. Hence, connections need to be verified afterwards using the general provisions in the traditional design codes instead of using advanced numerical simulations. For the implementation of joint checks in the DDM, it is fundamental to include fracture models in the advanced finite element simulations to avoid this additional check. Furthermore, the development of ductile fracture models for stainless steel alloys will contribute to the widespread and strategic use of this material for seismic application, after some adaptations. It is known that the inelastic response under cyclic loading is very sensitive to the material characterisation (Hartloper

et al. 2021). In fact, the European code for the design of structures for earthquake resistance prEN 1998-1-1 (2021) states that, in the case of existing buildings, the cyclic degradation due to the nature of seismic action must be adequately modelled referring to reliable bases and, where possible, to experimental tests. A correct cyclic modelling starts from an accurate monotonic modelling, since the failure mode under the two loading types is ductile and exhibits similar fracture mechanisms (Nip et al. 2010a; Kanvinde 2017), thus cyclic simulations will also benefit from the correct prediction of the failure mode under monotonic loading.

On this context, the aim of this study is to propose a reliable model to reproduce the ductile damage and fracture of stainless steel alloys under monotonic loading in finite element software, using experimental results from monotonic tensile coupon tests on austenitic, ferritic and duplex stainless steels carried out at the Universitat Politècnica de Catalunya as reference.

9.2. Ductile fracture models for steels under monotonic loading

Mechanical fracture models are based on the relationship between the ductile fracture of steels and the void growth, and they can be categorised into coupled and uncoupled models (Zhang et al. 2022). Coupled models, such as the Continuous Damage Mechanics (CDM) model (Lemaitre 1985), implement the ductile fracture by modifying the constitutive material model, so they define a fracture criterion and a damage evolution law. Conversely, uncoupled models only define a failure criterion related to the stress-strain relationship. Examples of uncoupled models are the Void Growth Model (VGM) and the Stress Modified Critical Strain (SMCS) model developed by Kanvinde and Deierlein (Kanvinde and Deierlein 2006), and the Lee and Wierzbicki model (Lee and Wierzbicki 2004).

The Void Growth Model (VGM) and the Stress Modified Critical Strain (SMCS) model relate the initiation of ductile fracture under monotonic loading to the equivalent plastic strain and stress triaxiality (Kanvinde and Deierlein 2006) and are suitable for predicting the failure modes dominated by tension, i.e., subjected to high triaxial stresses $T > 1/3$ (Song et al. 2020). In the VGM model the ductile fracture initiates when the void growth index VGI exceeds a certain critical value VGI_{cr}, which is calculated by integrating the triaxiality and plastic strain history, and it is an inherent property of the material. Much simpler, the SMCS model assumes that the triaxiality remains constant during the loading history (Kanvinde and Deierlein 2006) and considers that the fracture initiates when the equivalent plastic strain $\bar{\varepsilon}_{pl}$ exceeds a critical value $\bar{\varepsilon}_{pl,cr}$, which is calculated as a function of the triaxiality. Eq. 9.1 shows the failure criterion for the SMCS model, where $\bar{\varepsilon}_{pl,cr}$ is the critical equivalent plastic strain, α is the toughness index or fracture parameter and T is the triaxiality computed as the ratio of the mean stress and the von Mises stress. The parameter α is calibrated using experimental data and Finite Element (FE) analyses, and it is a material property (Kanvinde and Deierlein 2006).

$$\bar{\varepsilon}_{pl,cr} = \alpha \exp(-1.5T) \qquad \text{Eq. 9.1}$$

The Lee and Wierzbicki model (Lee and Wierzbicki 2004) is recommended for identifying ductile fracture under full-ranged triaxialities, such as those originated by a combination of tensile and shear forces (Song et al. 2020). Eq. 9.2 shows the computation of the critical equivalent plastic strain $\bar{\varepsilon}_{pl,cr}$ in the Lee and Wierzbicki model, where $T < 0$ triaxiality values correspond to fractures dominated by shear modes, $T > T_0$ to fractures dominated by tensile modes, and triaxiality values between 0 and T_0 correspond to combined tension and shear fracture modes. In Eq. 9.2, T_0 is the stress triaxiality under pure tension, assumed as $1/3$, while C_1 and C_2 are the fracture strains at pure shear ($T = 0$) and pure tension ($T = 1/3$), respectively. These parameters are calibrated through experimental data and FE analyses (Song et al. 2020).

$$\bar{\varepsilon}_{pl,cr} = \begin{cases} \infty, & T \leq -1/3 \\ C_1/(1+3T), & -1/3 < T \leq 0 \\ C_1 + (C_2 - C_1)\,(T/T_0), & 0 < T \leq T_0 \\ C_2 T_0 / T & T > T_0 \end{cases} \qquad \text{Eq. 9.2}$$

The versatility and straightforward implementation of these models in FE analyses have motivated the calibration of the VGI_{cr}, α and C_1 and C_2 parameters for different types of metallic materials, including stainless steel alloys. In addition, they have been adapted for the prediction of ductile fracture under cyclic loading (Kanvinde and Deierlein 2007; Jia and Kuwamura 2015). Thus, Jia and Kuwamura (2015) have adapted the SMCS for cyclic loading, being subsequently calibrated for austenitic stainless steel by Baiguera et al. (2019). As it can be expected from Eq. 9.1 and Eq. 9.2, and visualised in Figure 9.1, the fracture criterion against the stress triaxiality for the SMCS and Lee and Wierzbicki models are similar but follow different mathematical functions.

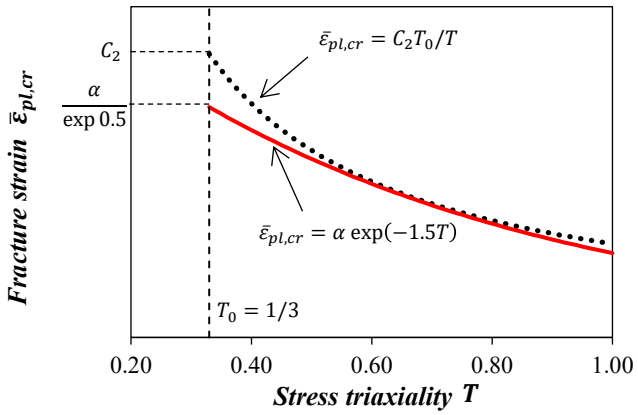

Figure 9.1. Fracture strain-triaxiality relationships of SMCS and Lee and Wierzbicki models.

Table 9.1 reports the values of the toughness index α calibrated for austenitic and duplex stainless steel materials under tensile forces, as published in (Yin et al. 2019) and (Chang et al. 2019; Zhang et al. 2022), respectively. Values of the C_2 parameter calibrated for austenitic stainless steel bolts reported in

(Song et al. 2020) are also provided. Finally, the values of the critical void growth index VGI_{cr} reported in (Baiguera et al. 2019) for duplex stainless steel are also given. Calibrated values for VGI_{cr} and α tend to be very similar, even analogous, but the SMCS model has the advantage of not requiring the integration of the triaxiality and plastic strain history (Zhang et al. 2022). Given that the values reported in Table 9.1 show some scatter, and with the aim of increasing the available data, the values of the α and C_2 parameters are calibrated in this study for austenitic, ferritic and duplex alloys from experimental tensile tests performed at the Universitat Politècnica de Catalunya. The SMCS and Lee and Wierzbicki models have been selected for their simplicity and considering that extensions of these models for predicting ductile fracture under cyclic loading already exist.

Table 9.1. Fracture parameters for austenitic and duplex stainless steels reported in the literature.

Stainless steel	Parameters	Min. value	Max. value	Reference
Austenitic	α	3.0	3.6	Yin et al. (2019)
Duplex	α	5.1	6.8	Zhang et al. (2022)
Duplex	α	2.8	3.3	Chang et al. (2019)
Austenitic	C_2	1.1	2.9	Song et al. (2020)
Duplex	VGI_{cr}	2.7	3.2	Baiguera et al. (2019)

9.3. Experimental results

This study presents the calibration of the fracture parameters for the SMCS and Lee and Wierzbicki ductile damage models by reproducing the behaviour of stainless steel coupons under tensile loading tested at the Universitat Politècnica de Catalunya. A total of eight coupons were simulated: two on the austenitic grade 1.4301, two on the ferritic grade 1.4003, two on the ferritic grade 1.4016, and two on the duplex grade 1.4462. Experimental results used herein belong to three different campaigns published in previous studies: austenitic coupon tests are reported in (Arrayago et al. 2020b), ferritic 1.4003 coupon tests are detailed in (Arrayago and Real 2016) and ferritic 1.4016 and duplex results are given in (Arrayago et al. 2015a). Different stainless steel product types were covered: austenitic and ferritic 1.4003 coupon tests were directly cut from the flat parts of cold-formed (CF) rectangular hollow section (RHS) specimens, while ferritic 1.4016 and duplex coupons were cut from sheet material (SM). Table 9.2 summarises the geometric characteristics of the coupons prior to be tested, where L and W are the total length and width, respectively, and l and w are the length and width of the necked area shown in Figure 9.2, and t is the thickness of the coupon. The cross-section areas A given in Table 9.2 correspond to the areas of the necked sections, where the highest values of stress-strain were expected.

Table 9.2. Geometric properties of the coupons prior to be tested.

Stainless steel	L [mm]	l [mm]	W [mm]	w [mm]	t [mm]	A [mm^2]
Austenitic CF	280	120	35	15	3.80; 3.62	57.0; 54.3
Ferritic CF	280	120	35	15	2.78; 1.96	41.7; 29.4
Ferritic SM	230	94	20	12	3.24; 3.22	38.9; 38.6
Duplex SM	230	94	20	12	3.23; 3.24	38.8; 38.9

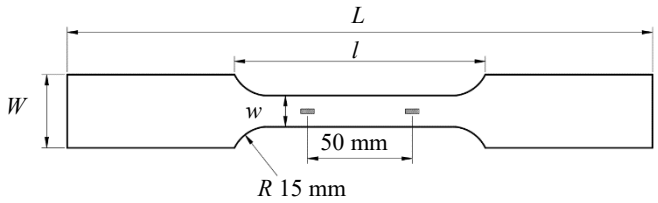

Figure 9.2. Necked coupons for tensile tests and definition of geometric parameters.

A 50 mm gauge length extensometer attached to the coupon to measure the strains, as shown in Figure 9.2. All tensile tests were performed following the requirements prescribed in ISO 6892-1 (2009). In the case of the austenitic coupon tests, the initial strain rate was 0.005 mm/s until 3% of the total strain was reached, and 0.05 mm/s thereafter (Arrayago et al. 2020b). Ferritic cold-formed coupon tests were conducted at an initial strain rate of 0.00025 mm/s and of 0.008 mm/s after the yield stress (Arrayago and Real 2016). Alternatively, ferritic and duplex coupon tests on sheet material were performed following a strain rate of 0.001 mm/s up to approximately 1% of the total strain, and then increased up to 0.037 mm/s (Arrayago et al. 2015a).

For information purposes, Table 9.3 reports the mean values of the two-stage Ramberg-Osgood material model parameters (Arrayago et al. 2015a) from the tests conducted and published in (Arrayago et al. 2015, 2020b; Arrayago and Real 2016). It is worth mentioning that the values of yield stress f_y and ultimate strength f_u reported in Table 9.3 are remarkably higher than the nominal values prescribed in material and structural specifications (prEN 1993-1-4 2021; EN 10088-4 2009). These differences are, however, consistent with the overstrength values reported in the literature for sheet material and cold-formed material in (Afshan et al. 2015; Arrayago et al. 2020a).

Table 9.3. Mean values for the two-stage Ramberg-Osgood material model parameters.

Stainless steel	E [GPa]	$\sigma_{0.05}$ [MPa]	f_y [MPa]	f_u [MPa]	ε_u [%]	n	m
Austenitic CF	190.1	429	481	672	31.0	7.1	3.1
Ferritic CF	178.1	386	424	485	13.0	15.0	2.4
Ferritic SM	213.8	285	316	502	15.6	13.6	3.0
Duplex SM	213.6	532	634	830	21.8	8.1	3.0

Figure 9.3 shows the stress-strain responses for three of the coupon tests studied herein. The stress values were determined as the ratio between the tensile loads recorded by the actuator and the cross-section area, while the strain values were calculated as the relative longitudinal displacement between the two gauges divided by the distance of 50 mm. In Figure 9.3, the ultimate stress f_u and corresponding ultimate strain ε_u, which is also known as the strain at necking, is marked by a vertical line for each curve. As shown, the strain-stress response of austenitic stainless steel is characterised by a high ductility and a high ultimate-to-yield stress ratio, while the highest strengths are found in the duplex stainless steel. It can be also observed that the ferritic and duplex coupons extracted from sheet material exhibited a similar relative value of the post-necking deformation, i.e., $(\varepsilon_f - \varepsilon_u)/\varepsilon_f$ (being ε_f the strain

at fracture), while for the austenitic coupon tests these values were slightly lower. This can be explained by the fact that the austenitic coupons studied herein were cut from cold-formed tubes, a fabrication process that is known to affect the mechanical characteristics by enhancing the strength but reducing the ductility (Rossi et al. 2013).

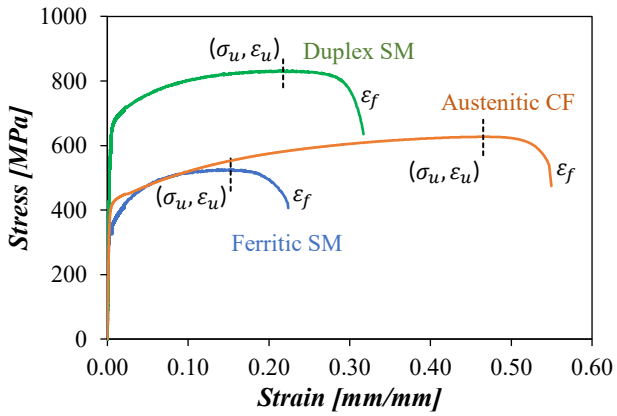

Figure 9.3. Typical stress-strain responses of the stainless steel alloys used in this study.

9.4. Numerical modelling

9.4.1. General

Numerical simulations for the calibration of the fracture parameters have been performed in the general-purpose finite element software ABAQUS (2016). The coupons were modelled according to the geometrical measures described in Table 1 using the incompatible eight-node linear brick elements (C3D8I), as recommended in (Song et al. 2020). Although some studies recommend the use of very dense meshes based on the characteristic length (Yin et al. 2019), after a convergence study, the models were discretised following a 4×4 mm mesh (Xie and Chen 2021), except for the effective length area, where a 1×1 mm mesh was employed, and a four-element mesh was used through the thickness, in line with the recommendations given in (Song et al. 2020). Figure 9.4 shows the finite element model and final adopted mesh for the ferritic coupon test, which is representative of all finite models developed for this study. The end surfaces of the coupons were coupled to centroidal reference points, referred as loading and support reference points in Figure 9.4, and were forced to move as rigid bodies. The loading was imposed as a longitudinal displacement at the loading reference point, while all degrees of freedom were constrained at the support reference point, simulating the fixed-ended boundary conditions described in Section 9.3. To facilitate the output of results, a set conformed by two mid-thickness nodes placed 50 mm apart, i.e., the gauge length of the extensometer used in the tests, was defined. No imperfections were assigned since the coupons were tested under tensile loading. The second order plastic analyses (GMNA) were solved using the Static General method available in ABAQUS (2016).

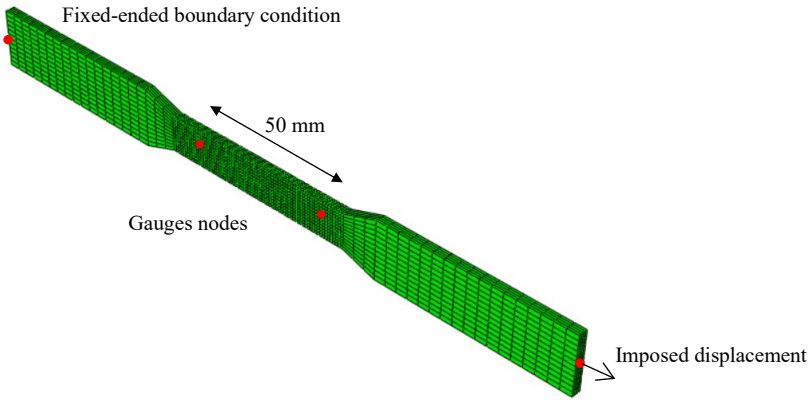

Figure 9.4. Typical finite element model for coupon tests, including mesh discretisation.

9.4.2. Material model

In this study, the material plasticity in ABAQUS (2016) was defined using the stress-strain data obtained from the tensile test results, thus avoiding possible inaccuracies due to the implementation of the two-stage Ramberg-Osgood material model. To consider the material behaviour up to failure, the engineering stress-strain curves shown in Figure 9.2 were converted to true stress-strain responses using Eq. 9.3 and Eq. 9.4, where ε and σ are the engineering strain and stress, respectively, and ε_{true} and σ_{true} are the corresponding true strain and true stress.

$$\varepsilon_{true} = \ln(1 + \varepsilon) \quad \text{Eq. 9.3}$$

$$\sigma_{true} = \sigma(1 + \varepsilon) \quad \text{Eq. 9.4}$$

Eq. 9.3 and Eq. 9.4 are valid if there is a uniform stress-strain relationship, but once the necking starts, the concentration of triaxial stresses and plastic strains increases considerably (Song et al. 2020). When the fracture area is known, the stress-strain behaviour between the necking initiation to failure can be easily estimated, as shown in (Yin et al. 2019). However, and since the fracture areas were not available in this study, the plasticity of the material up to failure was estimated using the weighted average method proposed by Ling (1996), which has been recently used for austenitic stainless steels by Song et al. (2020). The weighted average method, which is graphically defined in Figure 9.5, establishes an upper and a lower bound between which the actual (weighted) true stress-strain curve is comprised. The true stress-strain upper and lower bounds are given in Eq. 9.5 and Eq. 9.6, respectively, where $\varepsilon_{n,true}$ and $\sigma_{n,true}$ are the true strain and true stress at necking.

$$\sigma_{true} = \sigma_{n,true} \exp(\varepsilon_{true} - \varepsilon_{n,true}) \quad \text{for } (\varepsilon_{true} > \varepsilon_{n,true}) \quad \text{Eq. 9.5}$$

$$\sigma_{true} = \sigma_{n,true}(\varepsilon_{true}/\varepsilon_{n,true})^{\varepsilon_{n,true}} \quad \text{for } (\varepsilon_{true} > \varepsilon_{n,true}) \quad \text{Eq. 9.6}$$

The weighted average true stress-strain relationship is given in Eq. 9.7, where w is a weighted average factor to be calibrated by trial and error. Ling (1996) proposed a constant value of the weighted average factor w for carbon steel, whereas Song et al. (2020) proposed a variable w for stainless steels. Eq. 9.8 shows the computation of w as published in (Song et al. 2020) and adopted in this study, where the values of the weighting parameters a_1 and a_2 are calibrated by trial and error.

$$\sigma_{true} = \sigma_{n,true}\left[w\exp\left(\varepsilon_{true} - \varepsilon_{n,true}\right) + (1-w)\left(\varepsilon_{true}/\varepsilon_{n,true}\right)^{\varepsilon_{n,true}}\right] \quad \text{for } (\varepsilon_{true} > \varepsilon_{n,true}) \quad \text{Eq. 9.7}$$

$$w = 1/[1 + a_1\,(\varepsilon_{true}/\varepsilon_{n,true})^{a_2}] \quad \text{with } (0 \le w \le 1) \quad \text{for } (\varepsilon_{true} > \varepsilon_{n,true}) \quad \text{Eq. 9.8}$$

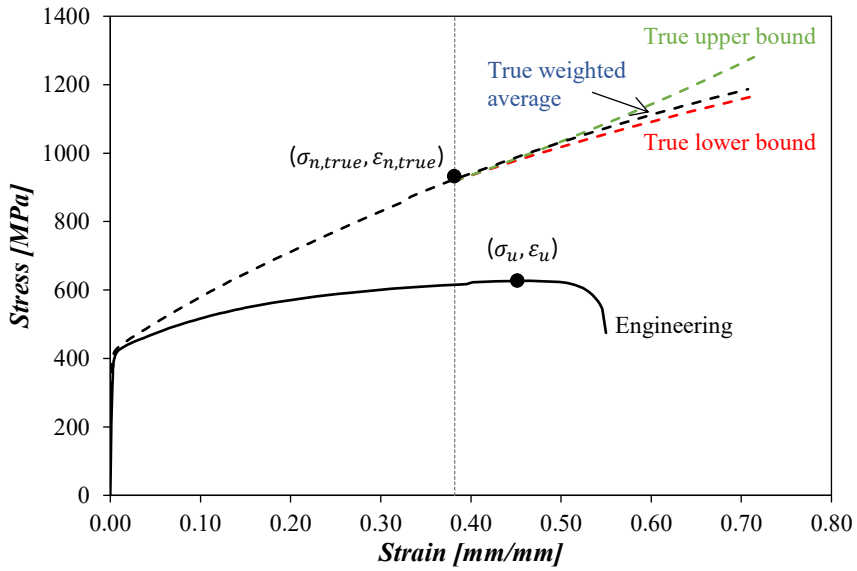

Figure 9.5. Weighted average method for calibrating post-necking stress-strain behaviour.

Regarding the weighting parameters a_1 and a_2, it is important to note that a low value of the a_1 parameter results in an increase of the stresses corresponding to strain values slightly higher than the necking strain, i.e., it raises the resulting weighted average true stress-strain curve towards the upper bound, while a low value of the a_2 parameter decreases the stresses corresponding to large strain values, i.e., the end of the calibrated weighted average true stress-strain curve tends to approach the lower bound. In fact, the weighted average true stress-strain curve calibrated with the pair $a_1 = 100.0$ and $a_2 = 0.0$ (i.e., $w \cong 0.0$) results in almost the lower bound, while with the pair $a_1 = 100.0$ and $a_2 = 100.0$ (i.e., $w = 1.0$) results in the upper bound.

9.4.3. Ductile damage model

In addition to defining the stress-strain material model, a ductile damage criterion needs to be included in the finite element analyses, which affects the stress-strain behaviour after necking (Jia and Kuwamura

2014). To incorporate the Stress Modified Critical Strain (SMCS) and Lee and Wierzbicki fracture models to the FEM analyses, the built-in material option "ductile damage" available in ABAQUS (2016) was used. The ductile criterion for the onset of damage due to nucleation, growth, and coalescence of voids provided in ABAQUS (2016) is given in Eq. 9.9. In Eq. 9.9, ω_D is the criterion for the initiation of fracture and $\bar{\varepsilon}_{pl,cr}(T)$ is the equivalent plastic strain at the onset of damage, which depends on the instantaneous triaxiality value. In the context of ABAQUS (2016), the stress triaxiality is computed as the ratio of the pressure stress p, and the von Mises equivalent stress q, i.e., $T = -p/q$. During the analysis, ω_D increases monotonically with plastic deformation, and when ω_D reaches unity, the fracture initiation occurs. Those elements satisfying the damage criterion were removed by the "element deletion" option. It should be noted that the effect of the strain rate is not considered in this study, following the approach adopted in (Song et al. 2020).

$$\omega_D = \int \frac{d\bar{\varepsilon}_{pl}}{\bar{\varepsilon}_{pl,cr}(T)} = 1 \qquad \text{Eq. 9.9}$$

9.5. Calibration of fracture parameters for stainless steel alloys

The fracture parameters of the SMCS and the Lee and Wierzbicki models were calibrated by fitting the numerical stress-strain data obtained from the GMNA analyses carried out on the FE models described in Section 9.4 to the experimental results described in Section 9.2. To be consistent with the experimental procedure, the numerical stresses were calculated as the ratio of the axial reaction to the necked area, while the numerical strains were calculated as the relative displacement between the two nodes considered as gauges divided by the gauge length of the extensometer. Figure 9.6 shows the numerical failure mode obtained for one of the duplex FE models.

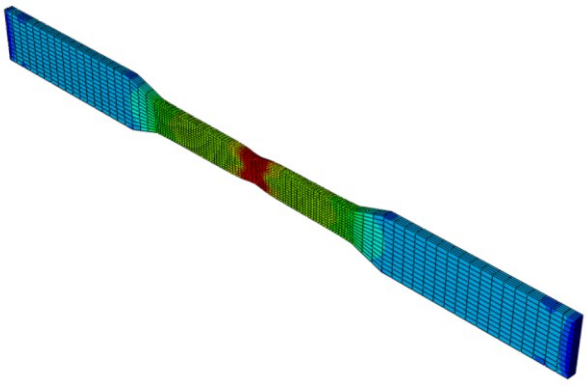

Figure 9.6. Typical finite element model for coupon tests, after failure.

According to Kanvinde and Deierlein (2006), the SMCS fracture parameter α is calibrated by computing Eq. 9.1 with the values of triaxiality and plastic strain obtained from an FE analysis in the critical node at the incremental step where the fracture occurs. Similarly, the Lee and Wierzbicki fracture parameter C_2 can be computed by integrating the fields of plastic strain and triaxiality in the

critical element (Song et al. 2020), also determined from FE analysis. Nevertheless, once the ductile fracture model is included in the FE analysis, the stress-strain behaviour after necking is affected (Jia and Kuwamura 2014), so the computation of the fracture parameter changes. In light of this and in line with the procedure to calibrate the parameter of fracture described in (Jia and Kuwamura 2014), the calibration of the fracture parameters α and C_2 followed an iterative process.

The values of the weighting (a_1 and a_2) and fracture (α and C_2) parameters for the stainless steels covered in this study are summarised in Table 9.4. Since the calibration of the weighting parameters a_1 and a_2 is based on trial and error, the first attempt was based on the pair $a_1 = 30.0$ and $a_2 = 2.0$ reported in (Song et al. 2020). As shown in Table 9.4, for the austenitic cases and the ferritic coupon test SM-1, the values of a_1 and a_2 resulted in true stress-strain curves almost equal to the lower bound (i.e., provided values of $w \cong 0.0$ for strains compressed between $\varepsilon_{n,true}$ and $\varepsilon_{f,true}$). The fact that the lower bound provided a good prediction of the true stress-strain curve without the need to calibrate a weighted average material curve is in line with the findings reported in (Jia and Kuwamura 2014), which also pointed out that even the lower bound of the weighted average method overestimated the behaviour of some steels.

Table 9.4. Calibrated values of the a_1, a_2, α and C_2 parameters for the stainless steel covered in this study.

Stainless steel	a_1	a_2	α	C_2
Austenitic CF-1	100.0	0.0	1.6	1.0
Austenitic CF-2	100.0	0.0	1.4	0.8
Ferritic CF-1	30.0	1.8	1.3	0.9
Ferritic CF-2	30.0	1.3	1.3	0.9
Ferritic SM-1	100.0	1.0	1.8	1.5
Ferritic SM-2	30.0	1.0	1.6	1.2
Duplex SM-1	30.0	1.7	1.9	1.5
Duplex SM-2	30.0	1.0	1.8	1.5

Regarding the fracture parameters α and C_2, the calibrated values reported in Table 9.4 were, as expected, similar for the pair of analysed coupons (i.e., for each specific grade of stainless steel and manufacturing process). This is in line with the assumption of the fracture parameter being a material property (Kanvinde and Deierlein 2006). As it can been seen from the fracture parameters reported in Table 9.4, similar values of α and C_2 were obtained for ferritic and duplex coupons extracted from sheet material, while for the cold-formed austenitic and ferritic stainless steels the α and C_2 values were slightly lower. It should be noted that in the cold forming process the strength is enhanced but the ductility is decreased (Rossi et al. 2013).

A relationship between the ductility capacity of each stainless steel family and the values of the fracture parameters can be also drawn from Table 9.4. Thus, values of the fracture parameters for cold-formed austenitic coupon tests are slightly higher than for the cold-formed ferritic material, while for duplex sheet material the parameters are slightly higher than for ferritic sheet material. It is well-known that

the austenitic stainless steel alloys are those exhibiting the greatest levels of ductility, following by the duplex, while ferritic stainless steel alloys exhibit the less ductile behaviour (Arrayago et al. 2015a). The data presented herein suggests that higher values of the fracture parameters α and C_2 are associated to a more ductile fracture behaviour and, therefore, correspond to more ductile materials.

Figure 9.7 shows the stress-strain curves obtained using the numerical models explained in Section 9.4 with the calibrated fracture parameters and the experimental curves. As shown in these figures, identical stress-strain curves are obtained when adopting the SMCS model and the Lee and Wierzbicki model, and the predicted responses are in very good agreement with the experimental curves for all the stainless steel coupons analysed.

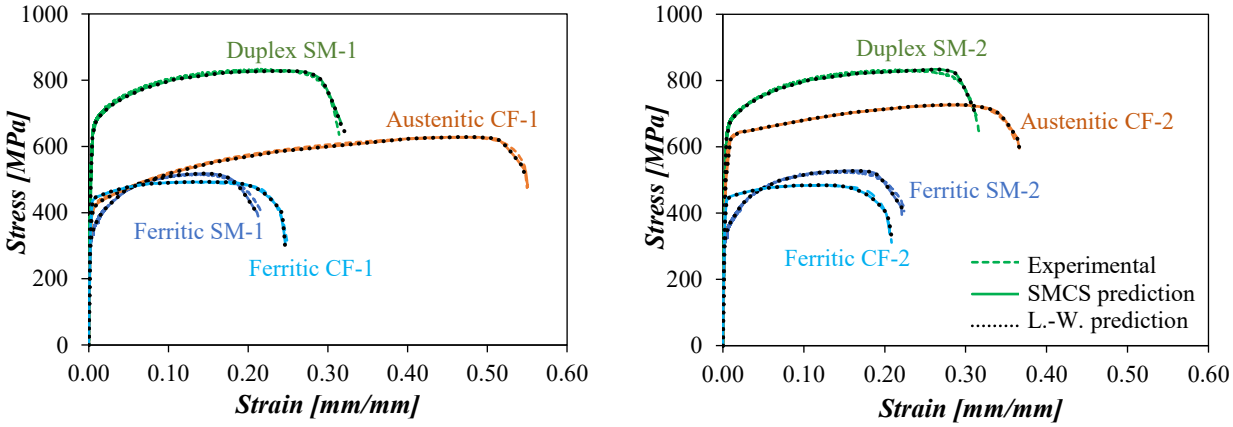

Figure 9.7. Comparison of the experimental and numerical stress-strain responses for the calibrated fracture parameters.

Considering the fracture parameters calibrated and presented in this study, preliminary recommendations for the α and C_2 parameters for different stainless steel materials can be made. A value for the fracture parameter of the SMCS model of α=1.5 is proposed for cold-formed austenitic material, while a value of α=1.8 is recommended for duplex sheet material. In the case of ferritic stainless steel, it is proposed to adopt a value of α=1.3 when the material is cold- formed, and α=1.7 for sheet or unformed material. Likewise, the C_2 parameter values preliminarily recommended for the Lee and Wierzbicki model are C_2=1.0 for cold-formed austenitic material, C_2=0.9 for duplex sheet material, and C_2=1.3 and C_2=1.5 for cold-formed and sheet ferritic material, respectively. It should be underlined that these values are preliminary because they are based on a limited number of results; a more extensive study is necessary for a proper calibration.

9.6. Concluding remarks

In this study, the fracture parameter values of two ductile fracture models, widely used for their simplicity and accuracy, were calibrated: the α parameter for the Stress Modified Critical Strain model (SMCS) and the C_2 parameter of the Lee and Wierzbicki model. The calibrations were based on tensile coupon tests on austenitic, ferritic and duplex stainless steels carried out at the Universitat Politècnica

de Catalunya. Coupons extracted from cold-formed tubes and from sheets were analysed to investigate the effect of cold forming in the fracture parameters. The calibrated parameters were obtained iteratively using numerical finite element simulations and the experimental results. The calibrated values are similar for the two cases of analysed for each type of material, with a slight difference between the different grades analysed, confirming that the fracture parameters for the SMCS and Lee and Wierzbicki models are an inherent property of the material. Higher α and C_2 values were observed for the more ductile alloys, suggesting a direct correlation between the two. Based on the calibrated parameters, average values of the fracture parameters were preliminarily proposed for direct application in finite element simulations.

Corresponding publication: González-de-León I., Arrayago I., Nastri E. and Real E. (2022). Ductile fracture simulation of stainless steel coupons under monotonic tensile forces. *Proceedings of the SDSS, International Colloquia on Stability and Ductility of Steel Structures*, Aveiro, Portugal, 520–526. https://doi.org/10.1002/cepa.1785

CHAPTER 10

Conclusions and suggestions for future research

10.1. General conclusions

Stainless steel is one of the most promising construction materials of the future due to its long service life, low maintenance requirements and high residual value. Research in recent decades has focused on the characterisation of the material, which exhibits a significant nonlinear stress-strain behaviour, on the resistance of cross-sections and on the efficient design of structural members. This research has been based on experimental studies and has used advanced finite element simulation tools to increase the casuistry and improve the accuracy of the available design formulae by developing new approaches. In recent years, research has extended to the analysis of the global behaviour of stainless steel structures, taking advantage of the high accuracy of analysis software and avoiding costly experimental programmes. As a result of these studies, the scope of stainless steel standards has increased considerably recently. However, they are still far from being as comprehensive as carbon steel standards. Some of the topics that need further research are those dealing with the overall behaviour of structures under static loads, the seismic behaviour of stainless steel structures and the simulation of material degradation to take it into account in advanced design, which are the three main issues

addressed in this thesis. In this chapter, the main conclusions derived from the different studies undertaken in the three parts that comprise this thesis are summarised.

Researches included in Part I focused on studying the influence of material and geometric nonlinearities on the global performance of stainless steel portal frames. Bases on numerical studies that demonstrated that the degradation of stiffness due to the nonlinear material response of stainless steel alloys causes greater deformations and increases second order effects (Walport et al. 2019b), the future edition of the Eurocode 3, Part 1-4 prEN 1993-1-4 will prescribe, for first time, global design rules for stainless steel structures considering the effect of material nonlinearities. With the aim of providing experimental evidence of this behaviour, a comprehensive experimental programme on sway and non-sway stainless steel frames with slender and stocky rectangular hollow sections was carried out at the Universitat Politècnica de Catalunya, whose details and results are provided in Chapters 3 and 4. The experience gained in the planning and execution of these tests has been used when carrying out similar experimental programmes by other research groups, including new stainless steel frames. In addition, the reported results have been used to validate the numerical models used in several numerical studies, including independent research works. Finally, the analysis of the experimental results allowed the validation of the design approach to accounts for the influence of material nonlinearities on the global analysis of stainless steel frames to be featured in prEN 1993-1-4 (2021).

With the aim of enhancing the available alternatives for the global design of stainless steel structures in the European framework, a new Stiffness Reduction Method (SRM) based on the cross-section and member resistance formulae given in prEN 1993-1-4 (2021) was developed, which is described in Chapter 5. SRMs are the preferred structural design approaches in the US, but constitute an interesting alternative to the methods traditionally adopted in the Eurocode. The SRM proposed in Chapter 5 allows predicting the ultimate capacity and internal forces in stainless steel structures by performing a second order elastic analysis in which the stiffness of members is reduced by a set of factors to account for the effect of the spread of plasticity, residual stresses and member imperfections. The method only requires that initial out-of-plumbness imperfections be included, and the verification is limited to checking cross-section capacities. The design results obtained from applying the proposed method were found to be in line with those obtained with the Direct Method of Analysis (DM) prescribed in AISC 370 (2021), and very similar to those obtained from a nonlinear material and geometric analysis with imperfections (GMNIA). It should be noted that at the time this research was carried out, the AISC 370 specification had not yet been officially published, so this study can be considered one of the first to validate the DM for stainless steel structures.

Part II of this thesis is comprised by three studies related to the rotation capacity and seismic behaviour of stainless steel structures. The correct estimation of the rotation capacity is of paramount importance from an assessment point of view, because it allows establishing the actual capacity of the structure.

Likewise, an accurate computation of the maximum bending moment that the dissipative member can withstand allows a precise prediction of the overstrength parameters to be considered in the application of the capacity design principles. The study, presented in Chapter 6, showed that the maximum bending moment was comparable to the CSM bending moment. Based on finite element numerical results, a simple expression to estimate the rotation capacities of stainless steel cross-sections subjected to bending in terms of the local slenderness was proposed. With the proposed formula and analytical expressions to predict the elastic rotation, the research carried out in this thesis proved that it is possible to accurately describe the complete moment-rotation response. This can be useful to define the behaviour of plastic hinges and their implementation in seismic calculation software. To the author's knowledge, there is no equivalent formula for the rotation capacities of carbon steel.

Currently, the knowledge on the cyclic behaviour of stainless steel at member level is very limited due to the small number of experimental studies carried out. To enhance the experimental database available in the literature, a series of cyclic tests on stainless steel structural elements, tested for the first time under pure lateral loading, were carried out. The experimental programme was promoted and funded by Universitat Politècnica de Catalunya and tested at the Università degli Studi di Salerno. The details on the specimens, the set-up and the results are given in Chapter 7. The results were found to be in line with the data provided by similar studies, proving a significant rotation capacity and a remarkable energy dissipation capability in stainless steel members, and can be used as reference for calibrating numerical models under cyclic loading in the future.

Finally, Chapter 8 presents a study on the seismic behaviour of multi-storey stainless steel portal frames, proposing new design rules that take into account the nonlinear stress-strain response of stainless steel. It is one of the few studies available to date dedicated to the seismic design of stainless steel systems, and the first to be carried out taking into account the new design framework prescribed by the latest version Eurocode 8 (2021). The study was carried out using advanced finite element software that allowed the definition of the nonlinear stress-strain of stainless steel, and covered three types of alloys, four types of floors with different span widths, and three different heights. A total of 36 stainless steel moment resisting portal frames were designed to meet the high dissipation requirements prescribed in prEN 1998-1-2 (2021) for carbon steel structures. The design approach followed was the force-based method, which is the preferred approach – with slight variations – in the main international seismic design codes. A new formula was proposed to effectively account for the effects of material nonlinearities on the overall stiffness degradation of the system under seismic loads, and the actual values of the behaviour factors were also estimated. These factors were found to be higher than those currently prescribed for carbon steel, as one may expect due to the higher ductility and strain hardening characteristics of stainless steels.

The last study included in this thesis investigates the ductile fracture of stainless steels under monotonic loading (Part III - Chapter 9). Although there is a consensus on the material model to be used to define the behaviour of stainless steels up to the maximum stress, this is not the case for the model that defines the post-fracture behaviour. The extension of the material model until failure is of significant importance at the moment, with one possible application of this material model that defines the complete response of stainless steel up to failure being the explicit simulation of joint failure, which can be implemented in new design approaches that study the response of structures as whole systems, such as the Direct Design Method. Through the comparison of experimental and numerical results, the study carried out the calibration of the fracture parameters for two well-known ductile fracture models under monotonic loading commonly used in carbon steel, and values are proposed for different types of stainless steels.

10.2. Specific conclusions

This section presents the key results, formulae and calibrated parameters that have been developed and proposed in the framework of this thesis, and that may be directly applicable in other research and specifications for the design of stainless steel structures.

10.2.1. Experimental programme on stainless steel frames

The extensive description of the experimental set-up for stainless steel frame tests provided in this study includes strategies to ensure the verticality of the actions representing gravity loads during sway deflections, to avoid out-of-plumb displacement, to define the optimal location of vertical point loads, and to measure all necessary support reactions. These issues are of extreme importance when testing frames, and have been the subject of long hours of discussion due to the lack of similar tests in the literature – it should be recalled that these tests are considered to be the first tests on stainless steel frames subjected under vertical and horizontal loading in the world. Some of the solutions adopted have been achieved with the help of renowned international researchers as well as experts from the industrial sector. The experience gained in the preparation and execution of these complex frame tests has already helped researchers to efficiently plan future experimental programmes on structural systems (Juza and Jandera 2022; Yun et al. 2022), thus increasing the number of available frame tests.

Initial geometric imperfections play a fundamental role in the design of frames under static loads, although their values are often not measured accurately. Thus, the measurement of initial global and local imperfections carried out in the framework of this thesis contribute to the experimental data pool available in the literature.

10.2.2. Analysis and assessment of experimental tests. Second order effects according to prEN 1993-1-4

It is expected that the reported experimental results, as well as the exhaustive description of the finite element model built, serve to validate numerical models of frames by independent researchers in the future. That is the case of the following studies carried out in this thesis (González-de-León et al. 2021, 2022). Accurate advanced finite element models are essential to investigate the influence of geometric and material nonlinearities on the behaviour of stainless steel frames, characterised by a significant nonlinear stress-strain response. Thus, by comparing the responses obtained from different types of analyses (LA, GNA, MNA, GMNA) it is possible to assess the influence of geometric nonlinearities, material nonlinearities and the interaction of both, respectively, on the overall structural behaviour.

The performance of the tested frames has validated the formula for accounting for the influence of second order effects on the global stability of stainless steel frames. This formulation was solely based on numerical research, and was included in the Eurocode without experimental evidence. Based on the test results, the $\alpha_{cr,sw,ss}$ factor proposed by Walport et al. (2019b) to account for the influence of material nonlinearity on the global analysis of stainless steel frames can be considered to be in good agreement with the evidence obtained from the tests. However, this expression only captures the amplification of internal forces due to sway effects, and thus further reductions would be necessary for the case of systems susceptible to local buckling, such as the Frame 4 tested herein, which failed due to a combination of local buckling and sway effects.

10.2.3. A stiffness reduction method for the in-plane design of stainless steel frames according to prEN 1993-1-4

In the framework of this thesis, a Stiffness Reduction Method (SRM) for the in-plane stability design of stainless steel structures with stocky Rectangular Hollow Section (RHS) members has been developed, using the provisions included in the upcoming version of prEN 1993-1-4 (2021). This approach was based on the design method proposed by Kucukler et al. (2014, 2016) for carbon steel frames, and has shown to be equivalent to the Direct Analysis Method proposed in AISC 370 (2021). The proposed approach allows predicting the ultimate capacity and internal forces in stainless steel structures by performing a second order elastic analysis in which the stiffness of members is reduced by a set of factors to account for the effect of the spread of plasticity, residual stresses and member imperfections. The method only requires that initial out-of-plumbness imperfections be included, and the verification is limited to checking cross-section capacities.

The procedure to apply the proposed Stiffness Reduction Method for the in-plane stability design of stainless steel structures with stocky RHS sections is summarised as follows:

(i). Perform a Linear Elastic Analysis (LA) to estimate the maximum internal forces (axial force N_{Ed} and bending moment M_{Ed}) in each member under the design loads.

(ii). Calculate the Stiffness Reduction factors for each member from the proposed formulae:

$$\tau_N = \frac{4\psi^2}{\alpha^2 \frac{N_{Ed}}{N_{pl}} \left[1 + \sqrt{1 - 4\psi \frac{(N_{Ed}/N_{pl} - 1)}{\alpha^2 \, N_{Ed}/N_{pl}}}\right]^2} \quad \text{but} \quad \tau_N \leq 1 \qquad \text{Eq. 10.1}$$

$$\text{where} \quad \psi = 1 + \bar{\lambda}_0 \alpha \frac{N_{Ed}}{N_{pl}} - \frac{N_{Ed}}{N_{pl}} \qquad \text{Eq. 10.2}$$

$$\tau_M = \left[1 + (n-1)\frac{M_{el}}{M_{pl}}\left(\frac{C_m M_{Ed}}{M_{pl}}\right)^{n-2}\right]^{-1} \qquad \text{Eq. 10.3}$$

$$\tau_{NM} = \tau_N \tau_M \left\{1 - \left(\frac{N_{Ed}}{N_{pl}}\right)^{0.8}\left(\frac{C_m M_{Ed}}{M_{pl}}\right)\right\} \qquad \text{Eq. 10.4}$$

$$\text{where } C_m = 0.6 + 0.4\mu \quad \text{but } C_m \geq 0.4 \qquad \text{Eq. 10.5}$$

with N_{pl} and M_{pl} being the plastic resistance of the gross cross-section and the plastic moment resistance of the cross-section, respectively; $\bar{\lambda}_0$ and α being the slenderness plateau and imperfection factor given in next version of prEN 1993-1-4 (2021), respectively; and μ being the ratio between the smaller and larger applied end moments.

(iii). Perform a Geometrically Nonlinear Analysis with Stiffness Reduction (GNA-SR) considering initial global imperfections (out-of-plumbness) only. Note that stiffness reduction factors should affect the flexural stiffnesses, but not the axial stiffnesses, of all the members.

(iv). Check the cross-section capacity using the internal forces determined from the GNA-SR analysis under the design loads through the following strength interaction expression for stocky sections:

$$M_{Ed} \leq M_{N,csm} = M_{csm}\frac{1 - (N_{Ed}/N_{pl})}{1 - 0.5a} \leq M_{csm} \qquad \text{for } \bar{\lambda}_p \leq 0.60 \qquad \text{Eq. 10.6}$$

being $M_{N,csm}$ the plastic moment resistance reduced due to the axial force N_{Ed}, M_{csm} the CSM moment resistance, and $\bar{\lambda}_p$ the local slenderness.

10.2.4. Rotation capacity of cold-formed stainless steel RHS beams under cyclic loading

The numerical study on 120 austenitic, ferritic and duplex stainless steel rectangular hollow section beams under cyclic loading demonstrated that the ultimate bending moment capacity under cyclic

loading can be accurately predicted by the Continuous Strength Method equation for stainless steel beams, and that the exhibited rotation capacity can be directly related to the local slenderness.

The plastic rotation capacities were determined based on the prescriptions given in Eurocode 8 for predicting the plastic rotations θ_{pl} on steel beams, and distinguish between the stable part of the plastic rotation capacity R_0, which is related to the maximum bending moment, and the total plastic rotation capacity R, which also includes the post-buckling behaviour. Equations for determining the stable part R_0 and the total R plastic rotation capacities are given below.

$$R_0 = \frac{\theta_{Mu}}{\theta_y} - 1 \qquad \text{Eq. 10.7}$$

$$R = \frac{\theta_u}{\theta_y} - 1 \qquad \text{Eq. 10.8}$$

Based on these expressions, the following equations were proposed for predicting the rotation capacity of cold-formed stainless steel RHS beams under cyclic loading. Values of the parameters β and ρ are reported in the table below. It should be noted that these parameters were calibrated based on data on fully-effective cross-sections ($\bar{\lambda}_p \leq 0.68$). As shown, the plastic rotation capacity formulae disregard the elastic rotation θ_y, but this can be easily estimated from elastic deflection formulae.

$$R_{i,pred} = \frac{\beta}{\bar{\lambda}_p^{\ \rho}} \qquad \text{for} \quad \bar{\lambda}_p \leq 0.68 \qquad \text{Eq. 10.9}$$

Table 10.1. Coefficients for the proposed expressions to predict the stable part and total plastic rotation capacities of stainless steel beams under cyclic loading.

Stainless steel	Stable part of the rotation capacity $R_{0,pred}$		Total rotation capacity R_{pred}	
	β	ρ	β	ρ
Austenitic	0.7	1.0	0.8	1.2
Ferritic/Duplex	0.4	1.3	0.4	1.5

Based on the proposed equations for the estimation of the rotation capacities, and knowing the elastic rotation and ultimate bending moment values, a tri-linear model that describes the full moment-rotation curves of stainless steel beams under cyclic loads can be proposed, which can be implemented into existing analysis software to define the behaviour of concentrated plastic hinges.

10.2.5. Design of stainless steel moment resisting frames according to the second generation of Eurocode 8

A total of 36 stainless steel Moment Resisting Frames (MRFs) were designed for first time according to the prescription given for carbon steel frames in the upcoming version of prEN 1998-1-1 and prEN

1998-1-2 (2021). The analysis of the investigated frames led to the proposal of a new expression to assess and consider second order effects due to seismic actions on stainless steel structures, which accounts for the effect of material nonlinearities, and allows the adoption of the limiting values currently prescribed in prEN 1998-1-2 (2021) for conventional steel for consideration of geometrical nonlinearities. The proposed formulated in given below, and includes the further degradation of the stiffness due to material nonlinearities through the factor Y, whose values are given in prEN 1993-1-4 (2021). The ratio K_s/K is the comparison between the stiffness of the structure obtained from a first order elastic analysis (LA) and that obtained from a first order plastic analysis (MNA). It should be noted that in seismic design it is common that structures remain in the elastic range for the considered gravity actions, so in general K_s/K = 1.0.

$$\theta_{ss} = \frac{P_{tot} \cdot d_{r,SD}}{\omega_{rm} \cdot q_S \cdot V_{tot} \cdot h_s \cdot Y \cdot (K_s/K)} \quad \text{if } q_S \geq \Omega_d \cdot q_R$$

$$\theta_{ss} = \frac{P_{tot} \cdot d_{r,SD}}{\omega_{rm} \cdot \Omega_d \cdot q_R \cdot V_{tot} \cdot h_s \cdot Y \cdot (K_s/K)} \quad \text{if } q_S < \Omega_d \cdot q_R \qquad \text{Eq. 10.10}$$

Among all the seismic design approaches, the force-based approach is probably the most used. With slightly variations, the force-based approach is included in all the main seismic design standards. The Among all the seismic design approaches, the force-based approach is probably the most used one, and is the one included in most international seismic design standards. The force-based approach implemented through the modal response spectrum method employs a linear analysis, where the design forces are obtained from the superposition of gravity loads and seismic forces, and the overstrength and the nonlinear response of the structure (associated with the material, the structural system and the design procedure) are implicitly and approximately accounted for through a behaviour factor, which in the Eurocode framework is represented by q. The computation of the overall behaviour factor q has been revised and split into three components in the new version of prEN 1998-1-1 (2021), where q_R is the behaviour factor component accounting for the overstrength due to the redistribution of seismic action effects in redundant structures, q_D is the behaviour factor component accounting for the deformation capacity and energy dissipation capacity of the structure, and q_S is the behaviour factor component accounting for the overstrength due to all other sources (such as the strength reserve resulting from the overstrength of individual members).

According to the criteria followed by recent studies the different components of the behaviour factors (q, q_R, q_D, q_S) were estimated from the 36 case studies analysed. The recommended behaviour factor values are summarised in Table 10.2, which depend on the stainless steel type. The values for q_R are higher than that proposed in prEN 1998-1-2 (2021) for carbon steel, as stainless steel alloys exhibit signs of yielding earlier. Likewise, the values of q_S for stainless steels are higher than for carbon steel

because stainless steel MRFs tend to be more oversized due to the lower lateral stiffness of the systems. Alternatively, the proposed q_D values for stainless steel are lower than the value given for carbon steel MRFs, but this is probably due to the criteria used by the Eurocode to define this value. Finally, the resulting values of the overall behaviour factor q for stainless steel are higher than those for carbon steel, as one may expect, due to the higher ductility and strain hardening characteristics of stainless steels. The recommended values of q_D have been compared with the corresponding $1/D_s$ factor given in the Japanese code, the only standard that includes seismic rules for stainless steel structures to date, showing a good agreement.

Table 10.2. Recommended behaviour factors for DC3 multi-storey stainless steel MRFs.

Stainless steel	European framework				US framework	
	q_R	q_D	q_S	q	R	Ω_0
Austenitic	1.5	2.4	2.1	7.5	12.0	3.0
Ferritic	1.5	2.1	2.2	7.0	12.0	3.0
Duplex	1.4	1.4	3.5	7.0	12.0	3.0

Finally, and due to the similarities between the European and US design frameworks, preliminary values for the seismic performance factors (R, Ω_0) prescribed in the US framework have been also recommended in this study (see Table 10.2).

10.2.6. Ductile fracture simulation of stainless steel coupons under monotonic tensile forces

The parameters of two ductile fracture models (α for the Stress Modified Critical Strain model (SMCS) and C_2 for the Lee and Wierzbicki model) were calibrated using the stress-strain curves from a set of tensile coupon tests on austenitic, ferritic and duplex stainless steels extracted from cold-formed (CF) tubes and from sheets (SM). Table 10.3 shows the values recommended for the α and C_2 parameters for different types of stainless steel alloys and materials.

Table 10.3. Values of the α and C_2 parameters for different types of stainless steel alloys and materials.

Stainless steel	α	C_2
Austenitic CF	1.5	1.0
Ferritic CF	1.3	1.3
Ferritic SM	1.7	1.5
Duplex SM	1.8	0.9

In addition to calibrating the ductile fracture parameters, the weighted average method proposed by Song et al. (2020) was applied in this study to estimate the material behaviour up to failure when the fracture area is unknown. This method requires an iterative process to calibrate the two additional parameters that describe the true stress-strain curve once necking is initiated. Calibrated values of these parameters are also presented in this thesis and will serve as a starting point for further investigations that use the weighted average method.

10.3. Future lines of research

This section provides a list of future lines of research that will allow to extend the studies carried out in this thesis on the different research paths addressed.

1.a) The frame tests highlighted the need for carrying out further experimental investigations on connections, including both fixed- and pinned-ended support conditions, and beam-to-column connections. The behaviour of connections is key to the overall performance of the structure and clear guidelines on how to design welded and bolted connections are needed, as well as codified formulae for estimating the strength and redistribution capacity of connections, especially in stainless steel.

1.b) The analysis of the portal frame results also showed that the factor for determining the susceptibility to second order effects $\alpha_{cr,sw,ss}$ is well calibrated in the case of frames with fully-effective cross-sections, but needs adaptations when considering sections susceptible to local buckling. This problem would be extensible to carbon steel frames with slender cross-sections as well. Furthermore, these tests only validated the applicability of the $\alpha_{cr,sw,ss}$ approach prescribed for single-storey frames, which depends on the Y factor that assumes much smaller values for multi-storey portal frames, and further research would be required to experimentally assess the suitability of these factors.

1.c) To fully implement the proposed Stiffness Reduction Method as an alternative approach to simplify the stability design of stainless steel frames according to European provisions, the present study should be extended to other cross-section types, including open sections, slender cross-sections prone to local buckling, other failure modes and load combinations, such as lateral-torsional buckling and axial load plus biaxial bending, respectively, as well as to more complex structures.

2.a) The functions proposed for estimating the rotation capacities of stainless steel structural members subjected to cyclic loading were based on numerical results, so their evaluation against experimental results is needed, as well as their application to other types of loading schemes such as beam-columns and other types of cross-sections, including class 4 cross-sections. A study on the extension of the formulae proposed in this thesis to stainless steel RHS beam-columns is already underway.

2.b) Further experimental studies on the cyclic performance of stainless steel at all levels – material, members, connections, systems – are also necessary. Currently, the number of studies dedicated to this subject is very low, which prevents the full adaptation of the seismic design codes for carbon steel to stainless steel structures. The results from the cyclic tests presented in this thesis can be used to validate numerical models, which in turn can be used in parametric studies that enhance the knowledge on the cyclic behaviour of nonlinear steel structures.

2.c) The study on the global behaviour of stainless steel structures under seismic actions underlined the need to particularise the standards for stainless steel, be it the mathematical expressions to guarantee acceptable strength and stiffness or the design recommendations. Thus, the expression proposed to take into account second order effects has shown that current stability verifications lead to unsafe stainless steel designs. Also, the design of moment resisting frames is generally governed by their performance against lateral loads, and since stainless steel has a lower initial stiffness than carbon steel, structural design typologies including bracings should be recommended when designing in stainless steel.

2.d) The recommended behaviour factor values were based on a relatively low number of structural systems. For a more reliable calibration and implementation in the code, the number of case studies should be increased by modifying the variables presented in this study, but also the intensity of the seismic action, the cross-section classes of the non-dissipative elements or the system typology. In addition, the behaviour factors can also be estimated by incremental dynamic analyses and compared to those proposed herein. Furthermore, this study focused on DC3 structures, but should be extended to DC2 and DC1 structures as well. The recommended values for the seismic performance factors prescribed in the US framework should be also considered as a starting point for a more detailed future investigation. Finally, this study can serve as a call to commercial software developers to include the two-stage Ramberg-Osgood material model in their material model offerings.

3) The fracture parameter values proposed in this thesis can be taken as preliminary, since they were based on a low number of experimental curves. To be of application in finite element simulations, these values will need to be recalibrated based on extensive experimental data. Furthermore, since the SMCS and Lee and Wierzbicki models have already been modified to predict ductile fracture under seismic conditions, the fracture parameters proposed for monotonic loading will also need to be adapted for cyclic loading histories in future studies.

REFERENCES

ABAQUS. (2016). ABAQUS/Standard User's Manual Volumes I-III and ABAQUS CAE Manual, Dassault Systemes Simulia Corporation.

Afshan S. and Gardner L. (2013a). Experimental study of cold-formed ferritic stainless steel hollow sections. *Journal of Structural Engineering (ASCE)*, 139 (5), 717–728.

Afshan S. and Gardner L. (2013b). The continuous strength method for structural stainless steel design. *Thin-Walled Structures*, 68, 42–49.

Afshan S., Francis P., Baddoo N., Gardner L. (2015). Reliability analysis of structural stainless steel design provisions. *Journal of Constructional Steel Research*, 114, 293–304.

Afshan S., Zhao O., Gardner L. (2019) Standardised material properties for numerical parametric studies of stainless steel structures and buckling curves for tubular columns. *Journal of Constructional Steel Research*, 152, 2–11.

American Institute of Steel Construction (AISC). (2016). AISC 341. Seismic Provisions for Structural Steel Buildings. Illinois, USA.

American Institute of Steel Construction (AISC). (2022). AISC 360. Specification for Structural Steel Buildings. Illinois, USA.

American Institute of Steel Construction (AISC). (2021). AISC 370. Specification for Structural Stainless Steel Buildings. Illinois, USA.

American Society of Civil Engineers (ASCE). (2016). ASCE 7. Minimum design loads for buildings and other structures. Reston, USA.

American Society of Civil Engineers (ASCE). (2022). ASCE 8. Specification for the Design of Cold-formed Stainless Steel Structural Members. Reston, USA.

Arrayago I. and Rasmussen K.J.R. (2021). Buckling curves for cold-formed stainless steel columns and beams. *Journal of Structural Engineering (ASCE)*, 147 (10), 04021149.

Arrayago I. and Rasmussen K.J.R. (2021). System-based reliability analysis of stainless steel frames under gravity loads. *Engineering Structures*, 231, 111775.

Arrayago I. and Real E. (2015). Experimental study on ferritic stainless steel RHS and SHS cross-sectional resistance under combined loading. *Structures*, 4, 69–79.

Arrayago I. and Real E. (2016). Experimental study on ferritic stainless steel simply supported and continuous beams. *Journal of Constructional Steel Research*, 119, 50–62.

Arrayago I., Real E., Mirambell E. and Westeel R. (2014). Comparative study of analytical expressions for the modelling of stainless steel behaviour. *Thin-Walled Structures*, 83, 2–11.

Arrayago I., Real E. and Gardner L. (2015a). Description of stress–strain curves for stainless steel alloys. *Materials & Design*, 87, 540–552.

Arrayago I., Picci F., Mirambell E. and Real E. (2015b). Interaction of bending and axial load for ferritic stainless steel RHS columns. *Thin-Walled Structures*, 91, 96–107.

Arrayago I., Real E. and Mirambell E. (2016). Experimental study on ferritic stainless steel RHS and SHS beam-columns. *Thin-Walled Structures*, 100, 93–104.

Arrayago I., Rasmussen K.J.R. and Real E. (2017a). Full slenderness range DSM approach for stainless steel hollow cross-section columns and beam-columns. *Journal of Constructional Steel Research*, 138, 246–263.

Arrayago I., Real E. and Mirambell E. (2017b). Design of stainless steel continuous beams with tubular cross-sections. *Engineering structures*, 151, 422–431.

Arrayago I., Real E., Mirambell E. and Chacón R. (2017c). Global plastic design of stainless steel frames. *Proceedings of the Eurosteel, European Conference on Steel and Composite Structures*, Copenhagen, Denmark, 3463–3471.

Arrayago I., Real E., Mirambell E. and González-de-León I. (2019). Experimental study on the general behaviour of stainless steel frames. *Proceedings of the SDSS, International Colloquia on Stability and Ductility of Steel Structures*, Prague, Czech Republic, 124–132.

Arrayago I., Rasmussen K.J.R. and Real E. (2020a). Statistical analysis of the material, geometrical and imperfection characteristics of structural stainless steels and members. *Journal of Constructional Steel Research*, 175, 106378.

Arrayago I., González-de-León I., Real E. and Mirambell E. (2020b). Tests on stainless steel frames. Part I: Preliminary tests and experimental set-up. *Thin-Walled Structures*, 157, 107005.

Arrayago I., González-de-León I., Real E. and Mirambell E. (2020c). Tests on stainless steel frames. Part II: Results and analysis. *Thin-Walled Structures*, 157, 107006.

Arrayago I., Real E., Mirambell E. and Gardner L. (2020d). The Continuous Strength Method for the design of stainless steel hollow section columns. *Thin-Walled Structures*, 154, 106825.

Arrayago I., Real E., Gardner L. and Mirambell E. (2021). The Continuous Strength Method for the design of stainless steel hollow section beam-columns. *Engineering Structures*, 238, 111981.

Arrayago I., Rasmussen K.J.R. and Zhang H. (2022). System-based reliability analysis of stainless steel frames subjected to gravity and wind loads. *Structural Safety*, 97, 102211.

Ashraf M., Gardner L. and Nethercot D.A. (2005). Strength enhancement of the corner regions of stainless steel cross-sections. *Journal of Constructional Steel Research*, 61 (1), 37–52.

Austin W.J. (1961). Strength and design of metal beam-columns. *Journal of the Structural Division*, 87 (4), 1–32.

Avery P. and Mahendran M. (2000). Large-scale testing of steel frame structures comprising non-compact sections. *Engineering Structures*, 22, 920–936.

Baddoo N.R. (2008). Stainless steel in construction: a review of research, applications, challenges and opportunities. *Journal of Constructional Steel Research*, 64 (11), 1199–1206.

Baiguera M., Vasdravellis G. and Karavasilis T.L. (2019). Ultralow cycle fatigue tests and fracture prediction models for duplex stainless-steel devices of high seismic performance braced frames. *Journal of Structural Engineering (ASCE)*, 145 (1), 04018230.

Barszcz A.M. and Gizejowski M.A. (2007). An equivalent stiffness approach for modelling the behaviour of compression members according to Eurocode 3. *Journal of Constructional Steel Research*, 63 (1), 55–70.

Becque J., Lecce M. and Rasmussen K.J.R. (2008). The direct strength method for stainless steel compression members. *Journal of Constructional Steel Research*, 64, 1231–1238.

Blum H.B. and Rasmussen K.J.R. (2018). Elastic buckling of columns with a discrete elastic torsional restraint. *Thin-Walled Structures*, 129, 502–511.

Bock M., Gardner L. and Real E. (2015). Material and local buckling response of ferritic stainless steel sections. *Thin-walled structures*, 89, 131–141.

Buchanan C., Real E. and Gardner L. (2018). Testing, simulation and design of cold-formed stainless steel CHS columns. *Thin-Walled Structures*, 130, 297–312.

Building Center of Japan (BCJ). (2016). The Building Standard Law of Japan. Tokyo, Japan.

Cashell K.A. and Baddoo N.R. (2014). Ferritic stainless steels in structural applications. *Thin-Walled Structures*, 83, 169–181.

Castiglioni C.A., Alavi A., Brambilla G., Kanyilmaz A. and Brambilla G. (2017). A procedure for the assessment of the behaviour factor for steel MRF systems based on pushover analysis. *Proceedings of the ECCOMAS, Thematic Conference on Computational Methods in Structural Dynamics and Earthquake Engineering*, Rhodes Island, Greece, 15–17.

Centre for Advanced Structural Engineering (CASE). (1990). Compression tests of stainless steel tubular columns. Investigation Rep. S770. University of Sydney, Australia.

Chacón R., de Marco M., Real E. and Arrayago I. (2018). An experimental study on the cyclic response of austenitic stainless steel. *Proceedings of the ICASS, International Conference on Advances in Steel Structures*, Hong Kong, China, 1–12.

Chacón R., Puig-Polo C. and Real E. (2021). On the use of systems for tests on stainless steel members and frames aimed at interoperability. *Proceedings of the Eurosteel, European Conference on Steel and Composite Structures*, Sheffield, United Kingdom, 2999–2307.

Chang X., Yang L., Zong L., Zhao M.H. and Yin, F. (2019). Study on cyclic constitutive model and ultra-low cycle fracture prediction model of duplex stainless steel. *Journal of Constructional Steel Research*, 152, 105–116.

Chen L., Yao X., Sun Z. and Wang D. (2022). Study seismic performance of duplex stainless steel under large strain amplitude by cyclic loading test. *Journal of Constructional Steel Research*, 194, 107332.

Chen Y., Zhou F., Zhang R. and Cai Y. (2022). Experimental study on seismic behaviour of welded H section stainless steel beam-columns. *Engineering Structures*, 259, 114105.

Clark P., Frank K., Krawinkler H. and Shaw R. (1997). Protocol for Fabrication, Inspection, Testing, and Documentation of Beam-Column Connection Tests and Other Experimental Specimens, SAC Report SAC/BD-97/02, SAC Joint Venture.

Cruise R.B and Gardner L. (2008a). Residual stress analysis of structural stainless steel sections. *Journal of Constructional Steel Research*, 64 (3), 352–366.

Cruise R.B. and Gardner L. (2008b). Strength enhancements induced during cold forming of stainless steel sections. *Journal of Constructional Steel Research*, 64 (11), 1310–1316.

D'Aniello M., Landolfo R., Piluso V. and Rizzano G. (2012). Ultimate behavior of steel beams under non-uniform bending. *Journal of Constructional Steel Research*, 78, 144–158.

Di Sarno L., Elnashai A.S. and Nethercot D.A. (2003). Seismic performance assessment of stainless steel frames. *Journal of Constructional Steel Research*, 53, 1289–1319.

Di Sarno L., Elnashai A.S. and Nethercot D.A. (2006). Seismic retrofitting of framed structures with stainless steel. *Journal of Constructional Steel Research*, 62, 93–104.

Di Sarno L., Elnashai A.S. and Nethercot D.A. (2008). Seismic response of stainless steel braced frames. *Journal of Constructional Steel Research*, 64, 914–925.

Elghazouli A.Y. (2010). Assessment of European seismic design procedures for steel frame structures. *Bulletin of Earthquake Engineering*, 8, 65–89.

Euro Inox. (1994). Design Manual for Stainless Steel (Second Edition).

European Committee for Standardization (CEN). (2022). prEN 1990. Eurocode 0: Basis of structural and geotechnical design. Brussels, Belgium.

European Committee for Standardization (CEN). (2005). EN 1993-1-1:2005. European Committee for Standardization Eurocode 3. Design of steel structures. Part 1-1: General rules – General rules and rules for buildings. Brussels, Belgium, 2005.

European Committee for Standardization (CEN). (2021). prEN 1993-1-1. Eurocode 3 – Design of Steel Structures – Part 1-1: General rules and rules for buildings. Brussels, Belgium.

European Committee for Standardization (CEN). (2006). Eurocode 3. EN 1993-1-3:2006. Design of steel structures. Part 1-3: General rules. Supplementary rules for cold-formed members and sheeting. Brussels, Belgium, 2006.

European Committee for Standardization (CEN). (2006). EN 1993-1-4. Eurocode 3: Design of Steel Structures – Part 1-4: General Rules. Supplementary Rules for Stainless Steels. Brussels, Belgium

European Committee for Standardization (CEN). (2015). EN 1993-1-4:2006+A1:2015. Eurocode 3: Design of Steel Structures – Part 1-4: General Rules. Supplementary Rules for Stainless Steels, including amendment A1. Brussels, Belgium.

European Committee for Standardization (CEN). (2021). prEN 1993-1-4. Eurocode 3: Design of Steel Structures – Part 1-4: General Rules. Supplementary Rules for Stainless Steels. Brussels, Belgium.

European Committee for Standardization (CEN). (2005). EN 1993-1-8:2005. European Committee for Standardization. Eurocode 3. Design of steel structures. Part 1–8: Design of joints. Brussels, Belgium, 2005.

European Committee for Standardization (CEN). (2021). prEN 1993-1-14. Eurocode 3: Design of Steel Structures – Part 1-14: Design assisted by finite element analysis. Brussels, Belgium.

European Committee for Standardization (CEN). (2021). prEN 1998-1-1. Eurocode 8: Design of structures for earthquake resistance —Part 1-1: General rules and seismic action. Brussels, Belgium.

European Committee for Standardization (CEN). (2021). prEN 1998-1-2. Eurocode 8: Design of structures for earthquake resistance – Part 1-2: Rules for new buildings. Brussels, Belgium, 2021.

European Committee for Standardization (CEN). (2009). EN 10088-4. Stainless Steels Part 4: Technical 917 Delivery Conditions for Sheet/Plate and Strip of Corrosion Resisting Steels for Construction Purposes. 918 Brussels, Belgium.

European Committee for Standardization (CEN). (2009). EN ISO 6892-1:2009. Metallic Materials – Tensile Testing. Part 1. Method of Test at Room Temperature. Brussels, Belgium.

European Committee for Standardization (CEN). (2018). EN 1090-2:2018. Execution of steel structures and aluminium structures – Part 2: Technical requirements for steel structures. Brussels, Belgium.

Fang C., Zhou F. and Luo C. (2018). Cold-formed stainless steel RHSs/SHSs under combined compression and cyclic bending. *Journal of Constructional Steel Research*, 141, 9–22.

Federal Emergency Management Agency (FEMA). (2009). FEMA P-695. Quantification of Building Seismic Performance Factors, Washington, USA.

Ferraioli M., Lavino A. and Mandara A. (2014). Behaviour factor of code-designed steel moment-resisting frames. *International Journal of Steel Structures*, 14, 243–254.

Fieber A., Gardner L. and Macorini L. (2019). Design of structural steel members by advanced inelastic analysis with strain limits. *Engineering Structures*, 199, 109624.

Gardner L. (2019) Stability and design of stainless steel structures – review and outlook. *Thin-Walled Structures*, 141, 208–216.

Gardner L. and Nethercot D.A. (2004a). Experiments on stainless steel hollow sections—Part 1: Material and cross-sectional behaviour. *Journal of Constructional Steel Research*, 60 (9), 1291–1318.

Gardner L. and Nethercot D.A. (2004b). Numerical modeling of stainless steel structural components – A consistent approach. *Journal of Structural Engineering (ASCE)*, 130 (10), 1586–1601.

Gardner L. and Cruise R.B. (2009). Modeling of residual stresses in structural stainless steel sections. *Journal of Structural Engineering (ASCE)*, 135 (1), 42–53.

Gardner L. and Theofanous M. (2008). Discrete and continuous treatment of local buckling in stainless steel elements. *Journal of Constructional Steel Research*, 64, 1207–1216.

Gardner L., Yun X., Fieber A. and Macorini L. (2019). Steel design by advanced analysis: material modeling and strain limits. *Engineering*, 5, 243–249.

González-de-León I., Arrayago I. and Real E. (2021). Interaction of geometric and material nonlinearities in stainless steel frames. *Proceedings of the Eurosteel, European Conference on Steel and Composite Structures*, Sheffield, United Kingdom, 2149–2157.

González-de-León I., Arrayago I., Real E. and Mirambell E. (2022). A stiffness reduction method for the in-plane design of stainless steel members and frames according with EN 1993-1-4. *Engineering Structures*, 253, 113740.

Hartloper A.R., de Castro e Sousa A. and Lignos D.G. (2021). Constitutive Modeling of Structural Steels: Nonlinear Isotropic/Kinematic Hardening Material Model and Its Calibration. *Journal of Structural Engineering (ASCE)*, 147, 04021031.

Hradil P. and Talja A. (2013). Investigating the role of gradual yielding in stainless steel columns and beams by virtual testing. *Proceedings of the SEMC, International Conference on Structural Engineering, Mechanics and Computation*, Cape Town, South Africa, 1459–1464.

Huang Y. and Young B. (2013). Experimental and numerical investigation of cold-formed lean duplex stainless steel flexural members. *Thin-Walled Structures*, 73, 216–228.

Huang Y. and Young B. (2014). The art of coupon tests. *Journal of Constructional Steel Research*, 96, 159–175.

IDEAStatiCa. (2020). User guide. *South-Moravian Innovation Centre*, Czech Republic, www.ideastatica.com.

Jandera M., Gardner L. and Machacek J. (2008). Residual stresses in cold-rolled stainless steel hollow sections. *Journal of Constructional Steel Research*, 64 (11), 1255–1263.

Jia L.J. and Kuwamura H. (2014). Ductile fracture simulation of structural steels under monotonic tension. *Journal of Structural Engineering (ASCE),* 140 (5), 04013115.

Jia L.J. and Kuwamura H. (2015). Ductile fracture model for structural steels under cyclic large strain loading. *Journal of Constructional Steel Research*, 106, 110–121.

Jiang L. and Bai G. (2020). Experimental Study on Cumulative Damage Behavior of Steel-Reinforced Concrete Columns. *Advances in Civil Engineering*, 6, 1–16.

Juza J. and Jandera M. (2022). Stainless Steel Portal Frame Tests. *Proceedings of the SDSS, International Colloquia on Stability and Ductility of Steel Structures*, Aveiro, Portugal, 500–505.

Kanvinde A.M. (2017). Predicting fracture in civil engineering steel structures: State of the art. *Journal of Structural Engineering (ASCE)*, 143 (3), 03116001.

Kanvinde A.M. and Deierlein G.G. (2006). Void growth model and stress modified critical strain model to predict ductile fracture in structural steels. *Journal of Structural Engineering (ASCE)*, 132, 1907–1918.

Kanvinde A.M. and Deierlein G.G. (2007). Cyclic void growth model to assess ductile fracture initiation in structural steels due to ultra-low cycle fatigue. *Journal of Engineering Mechanics*, 133 (6), 701–712.

Kaufmann E.J., Metrovich B.R. and Pense A.W. (2001). Characterization of cyclic inelastic strain behavior on properties of A572 Gr. 50 and A913 Gr. 50 rolled sections. ATLSS report no. 01–13. Bethlehem, Pa: Lehigh University.

Kim R.H., Kim T.S., Im S.H. and Xi Y. (2021). Hysteretic behavior comparison of austenitic and lean duplex stainless steel square hollow section members under cyclic axial loading. *Engineering Structures*, 237, 112227.

Kim S.E. and Chen W.F. (1996a). Practical advanced analysis for unbraced steel frame design. *Journal of Structural Engineering (ASCE)*, 122 (11), 1259–1265.

Kim S.E. and Chen W.F. (1996b). Practical advanced analysis for braced steel frame design. *Journal of Structural Engineering (ASCE)*, 122 (11), 1266–1274.

Krawinkler H. and Seneviratna G.D.P.K. (1998). Pros and cons of a pushover analysis of seismic performance evaluation. *Engineering Structures*, 20, 452–464.

Kucukler M., Gardner L. and Macorini L. (2014). A stiffness reduction method for the in-plane design of structural steel elements. *Engineering Structures*, 73, 72–84.

Kucukler M., Gardner L. and Macorini L. (2016). Development and assessment of a practical stiffness reduction method for the in-plane design of steel frames. *Journal of Constructional Steel Research*, 126, 187–200.

Landesmann A. and Batista E.M. (2005). Advanced analysis of steel framed buildings using the Brazilian standard and Eurocode-3. *Journal of Constructional Steel Research*, 61 (8), 1051–74.

Lázaro L. and Chacon R. (2022) Material behaviour of austenitic stainless steel subjected to cyclic and arbitrary loading. *Journal of Constructional Steel Research*, 189, 107113.

Lee Y.W. and Wierzbicki T. (2004). Quick Fracture Calibration for Industrial Use, No. 115. Impact and Crashworthiness Laboratory, Massachusetts Institute of Technology.

Lemaitre J. (1985). A continuous damage mechanics model for ductile fracture. *Journal of Engineering Materials and Technology, Transactions of the ASME,* 107, 83–89.

Lemma M.S., Rebelo C. and Silva L.S. da. (2022). Eurocode 8 revision - Implications on the design and performance of steel moment-resisting frames: Case study. *Soil Dynamics and Earthquake Engineering*, 161, 107411.

Li H.T. and Young B. (2018). Web crippling of cold-formed ferritic stainless steel square and rectangular hollow sections. *Engineering Structures*, 176, 968–980.

Li Z. and Schafer B.W. (2010). Buckling analysis of cold-formed steel members with general boundary conditions using CUFSM: conventional and constrained finite strip methods. *Proceedings of the International Speciality Conference on Cold-Formed Steel Structures*. Saint Louis, Missouri, USA.

Liew J.Y.R., White D.W. and Chen W.F. (1993a). Second-order refined plastic-hinge analysis for frame design. Part I. *Journal of Structural Engineering (ASCE)*, 119 (11), 3196–3216.

Liew J.Y.R., White D.W. and Chen W.F. (1993b). Second-order refined plastic-hinge analysis for frame design. Part II. *Journal of Structural Engineering (ASCE)*, 119 (11), 3217–3236.

Lim J.B.P., King C.M., Rathbone A.J., Davies J.M. and Edmondson V. (2005). Eurocode 3 and the in-plane stability of portal frames. *The Structural Engineer*, 83 (21), 43–8.

Ling Y. (1996). Uniaxial true stress-strain after necking. AMP J. Technol, 5 (1), 37–48.

Maquoi R. and Rondal J. (1978). Mise en équation des nouvelles courbes Européennes deflambement. *Construction Métallique*, 1, 17–30.

Mazzolani F.M. and Piluso V. (1996). Theory and design of seismic resistant steel frames. CRC Press.

Mazzolani F.M. and Piluso V. (1997). Prediction of the rotation capacity of aluminium alloy beams. *Thin-Walled Structures*, 27 (1), 103–116.

Meza F.J., Baddoo N.R. and Gardner L. (2021). Development of Flexural Buckling Rules for the New AISC Stainless Steel Design Specification. *Proceedings of the Eurosteel, European Conference on Steel and Composite Structures*, Sheffield, United Kingdom, 1537–1542.

Mitsui K., Latour M., Rizzano G., Sato A. and Piluso V. (2018). Experimental and numerical analysis of the ultimate behaviour of square hollow sections under combined axial and bending loads. *Ingegneria Sismica*, 35 (2), 5–22.

Nastri E. and Piluso V. (2020). The influence of strain-hardening on the ultimate behaviour of aluminium RHS-beams under moment gradient. *Thin-Walled Structures*, 157, 107091.

Newmark N. and Hall W. (1982). Earthquake spectra and design. Earthquake Engineering Research Institute.

Nip K.H., Gardner L., Davies C.M. and Elghazouli A.Y. (2010a). Extremely low cycle fatigue tests on structural carbon steel and stainless steel. *Journal of Constructional Steel Research*, 66 (1), 96–110.

Nip K.H., Gardner L. and Elghazouli A.Y. (2010b). Cyclic testing and numerical modelling of carbon steel and stainless steel tubular bracing members. *Engineering Structures*, 32, 424–441.

OpenSEES. (2006). Open System for Earthquake Engineering Simulation. Pacific Earthquake Engineering Research Center, University of California, US.

Packer J.A., Wardenier J., Kurobane Y., Dutta D. and Yeomans N. (1992). Design guide for rectangular hollow section (RHS) joints under predominantly static loading. CIDECT Design Guide No. 3. Verlag TÜV Rheinland GmbH, Köln, Germany.

Rasmussen K.J.R. (2003). Full-range stress-strain curves for stainless steel alloys. *Journal of Constructional Steel Research*, 59, 47–61.

Rasmussen K.J.R. and Hancock, G.J. (1993a). Design of cold-formed stainless steel tubular members. I: Columns. *Journal of Structural Engineering (ASCE)*, 119 (8), 2349–2367.

Rasmussen K.J.R. and Hancock G.J. (1993b). Design of cold formed stainless steel structural members. II: beams. *Journal of Structural Engineering (ASCE)*, 119 (8), 2368–2386.

Real E. and Mirambell E. (2005). Flexural behaviour of stainless steel beams. *Engineering Structures*, 27, 1465–1475.

Rossi B., Afshan S. and Gardner L. (2013). Strength enhancements in cold-formed structural sections – Part II: Predictive models. *Journal of Constructional Steel Research*, 83, 189–196.

Sarquis F.R., Lima L.R.O., S. da Vellasco P.C.G. and Rodrigues M.C. (2020). Experimental and numerical investigation of hot-rolled stainless steel equal leg angles under compression. *Thin-Walled Structures*, 151, 106742.

Segura G., Pournaghshband A., Afshan S. and Mirambell E. (2021). Numerical simulation and analysis of stainless steel frames at high temperature. *Engineering Structures*, 227, 111446.

SeismoStruct. (2016). Seismosoft – A computer program for static and dynamic nonlinear analysis of framed structures.

Shen Y.F. and Chacón R. (2020). Geometrically Nonlinear Analysis with stiffness reduction for the stability design of stainless steel structures: application to members and planar frames. *Thin-Walled Structures*, 148, 106581.

Song Y., Wang J., Uy B. and Li D. (2020). Experimental behaviour and fracture prediction of austenitic stainless steel bolts under combined tension and shear. *Journal of Constructional Steel Research*, 166, 105916.

Steel Construction Institute (SCI). (2017). Design Manual for Structural Stainless Steel, 4th Edition.

Su M., Young B. and Gardner L. (2014) Deformation-based design of aluminium alloy beams. *Engineering Structures*, 80, 339–349.

Surovek-Maleck A.E. and White D.W. (2004a). Alternative approaches for elastic analysis and design of steel frames. I: overview. *Journal of Structural Engineering (ASCE)*, 130 (8), 1186–1196.

Surovek-Maleck A.E. and White D.W. (2004b). Alternative approaches for elastic analysis and design of steel frames. II: verification studies. *Journal of Structural Engineering (ASCE)*, 130 (8), 1197–1205.

Tartaglia R., D'Aniello M., Di Lorenzo G., De Martino A. and Landolfo R. (2019). Comparison of different design requirements on P-delta effects for steel moment resisting frames. *Proceedings of the*

ECCOMAS, Thematic Conference on Computational Methods in Structural Dynamics and Earthquake Engineering, Crete, Greece, 5730–5740.

Tartaglia R., D'Aniello M. and Landolfo M. (2022). Seismic performance of Eurocode-compliant ductile steel MRFs. *Earthquake Engineering & Structural Dynamics*, 51, 2527– 2552.

Theofanous M. and Gardner L. (2009). Testing and numerical modelling of lean duplex stainless steel hollow section columns. *Engineering Structures*, 31(12), 3047–3058.

Uang C.M. (1991). Establishing R (Or Rw) and Cd factors for building seismic provisions. *Journal of Structural Engineering*, 117, 19–28.

Vamvatsikos D., Bakalis K., Kohrangi M., Pyrza S., Castiglioni C.A., Kanyilmaz A., et al. (2020). A risk-consistent approach to determine EN1998 behaviour factors for lateral load resisting systems. *Soil Dynamics and Earthquake Engineering*, 131, 106008.

Vigh L.G., Zsarnoczay A., Balogh J.M. and Castro J.M. (2016). P-Delta effect and pushover analysis: Review of Eurocode 8-1. Report N.1 of WG2 CEN/TC 250/SC 8.

Walport F., Gardner L. and Nethercot D.A. (2019a). A method for the treatment of second order effects in plastically-designed steel frames. *Engineering Structures*, 200, 109516.

Walport F., Gardner L., Real E. and Arrayago I. (2019b). Nethercot D.A. Effects of material nonlinearity on the global analysis and stability of stainless steel frames. *Journal of Constructional Steel Research*, 152, 173–182.

Walport F., Arrayago I., Gardner L. and Nethercot D.A. (2021a). Influence of geometric and material nonlinearities on the behaviour and design of stainless steel frames. *Journal of Constructional Steel Research*, 187, 106981.

Walport F., Kucukler M. and Gardner L. (2021b). Stability design of stainless steel structures. *Journal of Structural Engineering (ASCE)*, 148 (1), 04021225.

Walport F., Gardner L. and Nethercot D.A. (2021c). Design of structural stainless steel members by second order inelastic analysis with CSM strain limits. *Thin-Walled Structures*, 159, 107267.

Walport F., Chan H.U., Nethercot D.A. and Gardner L. (2023). Design of stainless steel structural systems by GMNIA with strain limits. *Engineering Structures*, 276, 115339.

Wang Y.Q., Chang T., Shi Y.J., Yuan H.X., Yang L. and Liao D.F. (2014). Experimental study on the constitutive relation of austenitic steel S31608 under monotonic and cyclic loading. *Thin-Walled Structures*, 83, 19–27.

Wang Z., Wang Y., Beibei Li B. and Zhang Y. (2022). Experimental and numerical study on seismic behaviour of aluminium alloy frames. *Journal of Building Engineering*, 50, 104231.

Whittaker A., Hart G. and Rojahn C. (1999). Seismic response modification factors. *Journal of Structural Engineering*, 125, 438–44.

Wilkinson T. and Hancock G.J. (1999). Tests of cold-formed rectangular hollow section portal frames, Research Report No. R783, University of Sydney, Australia.

Wilkinson T. and Hancock G.J. (2000). Tests to examine plastic behavior of knee joints in cold-formed RHS. *Journal of Structural Engineering (ASCE)*, 126 (3), 297–305.

Xie Z. and Chen Y. (2021). Experimental and modeling study of cyclic plasticity and ductile fracture of thin structural steel sheets. *Thin-Walled Structures*, 162, 107658.

Ye D., Matsuoka S., Nagashima N. and Suzuki N. (2006). The low-cycle fatigue, deformation and final fracture behaviour of an austenitic stainless steel. *Material Science and Engineering*, 415 (1-2), 104–117.

Yin F., Yang L., Wang M., Zong L. and Chang X. (2019). Study on ultra-low cycle fatigue behavior of austenitic stainless steel. *Thin-Walled Structures*, 143, 106205.

Young B. and Rasmussen K.J.R. (2003). Measurement techniques in the testing of thin-walled structural members. *Experimental Mechanics*, 43, 32–38.

Yun X., Zhu Y., Wang Z. and Gardner L. (2022). Benchmark tests on high strength steel frames. *Engineering Structures*, 258, 114108.

Zeris C. (2014). Behavior factor and ductility. Encyclopedia of Earthquake Engineering. 260–280.

Zhang H., Shayan S., Rasmussen K.J.R. and Ellingwood B.R. (2016a). System-based design of planar steel frames, I: Reliability framework. *Journal of Constructional Steel Research*, 123, 135–143.

Zhang H., Shayan S., Rasmussen K.J.R. and Ellingwood B.R. (2016b). System-based design of planar steel frames, II: Reliability results and design recommendations. *Journal of Constructional Steel Research*, 123, 154–161.

Zhang X., Rasmussen K.J.R. and Zhang H. (2016c). Experimental investigation of locally and distortionally buckled portal frames. *Journal of Constructional Steel Research*, 122, 571–583.

Zhang M., Zheng B., Wang J., Wu B. and Shu G. (2022). Study on fracture properties of duplex stainless steel and its weld based on micromechanical models. *Journal of Constructional Steel Research*, 190, 107115.

Zhao O., Gardner L. and Young B. (2016a). Behaviour and design of stainless steel SHS and RHS beam-columns. *Journal of Constructional Steel Research*, 106, 330–345.

Zhao O., Gardner L. and Young B. (2016b). Experimental study of ferritic stainless steel tubular beam-column members subjected to unequal end moments. *Journal of Structural Engineering (ASCE)*, 142 (11), 04016091.

Zhao O., Afshan S. and Gardner L. (2017). Structural response and continuous strength method design of slender stainless steel cross-sections. *Engineering Structures* 2017, 140, 14–25.

Zheng S., Zhou F., Cheng J., Li H.-T. and Rong R. (2022). Experimental study on cyclic hardening characteristics of structural stainless steels. *Journal of Constructional Steel Research*, 191, 107196.

Zhou F. and Li L. (2016). Experimental study on hysteretic behavior of structural stainless steels under cyclic loading. *Journal of Constructional Steel Research*, 122, 94–109.

Zhou F. and Young B. (2005). Tests of cold-formed stainless steel tubular flexural members. *Thin-Walled Structures*, 43, 1325–1337.

Zhou F., Fang C. and Chen Y. (2018). Experimental and numerical studies on stainless steel tubular members under axial cyclic loading. *Engineering Structures*, 171, 72–85.

Ziemian R.D. (2010). Guide to stability design criteria for metal structures. *John Wiley & Sons*.

Ziemian R.D. and McGuire W. (2002). Modified tangent modulus approach, a contribution to plastic hinge analysis. *Journal of Structural Engineering (ASCE)*, 128 (10), 1301–1307.

Zubydan A.H. (2010). A simplified model for inelastic second order analysis of planar frames. *Engineering Structures*, 32 (10), 3258–3268.

Zubydan A.H. (2011). Inelastic second order analysis of steel frame elements flexed about minor axis. *Engineering Structures*, 33 (4), 1240–1250.